DISS. ETH NO. 28143

Experimental Evaluation of Gas Retention in Two-Phase Flows relevant to Pool Scrubbing in FCVS

A thesis submitted to attain the degree of

DOCTOR OF SCIENCES

(Dr. sc. ETH Zürich)

presented by

Petros Papadopoulos

MSc in Nuclear Engineering
ETH Zürich / EPF Lausanne

born on 30.03.1988

citizen of Oberlunkhofen

accepted on the recommendation of

Prof. Dr. Horst-Michael Prasser (ETH Zürich), examiner
Prof. Dr. Philipp Rudolf von Rohr (ETH Zürich), co-examiner
Prof. Dr. Luis E. Herranz (CIEMAT), co-examiner

2022

To my beloved wife
Sandra

ACKNOWLEDGMENT

A doctoral thesis holds one author on the front page but the work would have never been possible without the endless support of a lot of people. As with many bigger projects, there are phases were anything is possible and moments where the aim seems unreachable. This is where support is needed not only on a technical level to proceed with the problem, but also with guiding assistance or motivational talks, coffees or during later hours also more fortified beverages.

Many thanks go to all the student projects that I was honored to supervise. Many ideas came forward, some better than others and after overcoming all the pit faults on our ways, there was always some sort of reward at the end of every student work. Namely, chronologically, I would like to thank Karl Baur, Laura Perez, Robin Streich, Markus Schmid, Gabriel Tomic, Bernhard Roth and Tim Willibald. Mohamed Ramadame I would like to thank for his technical aid on the coding part with his computer science background that he preferred to invest a summer into an internship than enjoying his well-deserved time after the examination period. Special thanks go to our KONIKOF exchange student, Yugyung Kim, that performed a number of experiments during one of the warmest summer periods in the lab. It was also a big pleasure to collaborate with our two exchange PhD students from overseas and inspire them with our knowledge on two-phase flow measurements to solve their issues in their home institutes, Casey Tompkins from the University of Wisconsin and Corey Clifford from Texas A&M. David Breitenmoser deserves a special mentioning who, after his semester project, further developed our ideas on the droplet detection which led to a very nice journal publication.

At this stage, I would also like to acknowledge the support of Farhad Sadough from AMD who contributed to my work by providing me a Radeon Pro WX8200 graphics card to accelerate my calculations.

My friends and colleagues at ETH Zürich and Paul Scherrer Institut that were always there to have a good laugh on our problems and keeping ourselves always positive and motivated. At ETH Zürich, this was mainly Christian Bolesch, Lukas Robers, Nathan Lafferty, Heiko Kromer, Xiaorong Li and Robert Adams. Jovo Vidic should also be mentioned here who always found time to help in electronic matters despite him working for a different institute. At Paul Scherrer Institut, I had the pleasure to work with Filip Janasz, Leticia Moguel Fernandez, Adolf Rydl, Bernd Jäckel, Detlef Suckow, Hauke Schütt, Wilhelm Bissels and our two technicians Francesco Pumilia and Huseyin Mutlukal. Unforgotten the times with my office mate and friend Jarmo Kalilainen with whom with shared the “fun” office of the floor where people would always find us having an ear for everyone’s troubles and jokes. My two predecessors, Torsten Betschart and Vladimir Brankov who handed me over in many hours their codes, facility and knowledge. I would have lost so many hours if they would not have had the patience to guide me through the instructions and little tricks of operating TRISTAN or processing wire-mesh sensor data.

I cannot express my gratitude with words to my supervisor Dr. Terttaliisa Lind for her constant guidance, her encouragement, her availability, her trust in me and my work, the patience and generous help at any time throughout my thesis. Her door was always open for me and my crazy ambitions and works, whether in the office or at home.

I would like to express my sincere gratitude to my supervisor Prof. Dr. Horst-Michael Prasser for the privilege to pursue my PhD in his lab, for his advice and trust in my work and the continuous support even when this support made his life sometimes difficult. I had the chance to dive into the wide field of two-phase flows, to give lectures and exercises for students, travel to conferences and learned how to present and discuss results in an objective and critical way.

At this point I would like to thank my family and especially my parents, who made it possible for me to follow my heart and achieve my goals. I am also thankful to all my close-by and far-away friends for good times outside of the university routine, namely Moritz Vischer, Francesco D’Aleo, Durie Suh, Daniel Seiler, Mirjam Rohrbach, Shilpi Singh and Angela Mühlenbroich. Last, but most certainly not least, I would like to thank my wonderful wife who never lost faith in me even in the darkest times. She made sure that I never lost heart and that my chocolate and coffee supply never ran out. I thank her for her understanding even when my dissertation became a constant travel companion on our holidays.

ABSTRACT

The safe operation of a nuclear power plant (NPP) has the highest priority for the owning utility. Therefore, safety measures must be in place for the anticipation of different, sometimes very challenging or even severe, accident scenarios. As part of the installations to mitigate the consequences of severe accidents, filtered containment venting systems have been developed in the past and installed to protect the containment from integrity failure due to over pressurization after a core damage. The designs of nowadays filters rely either on dry filters (sand bed, metal fiber or zeolite filters) or wet scrubbers. In case of wet scrubbers, the efficiency for scrubbing contaminants from the gas stream is depending, among other parameters, on the hydrodynamic properties of the flow, chemical composition of the scrubber solution and additional internal structures for enhancement of the mixing.

The removal of iodine species has not been an easy task for wet scrubbers so far. Several studies tried lately to link the removal efficiency of iodine to different quantities like gas injection velocity, bubble residence time and iodine concentration in the contaminated gas stream or gas temperature applied to different gas inlet nozzle designs. In the field of the soluble gas models, which are part of the models dealing with the retention of gaseous iodine variations, the available data set were rather scarce to validate the codes, which use those correlations. Furthermore, the tests conducted to benchmark these codes laid their focus on suppression pools, i.e. rather simple nozzles, and using a high share of steam where condensation is having a big impact on the flow field and trapping. In the bubble rising zone, the regime of a homogeneous bubble column is assumed to establish after the injection. In reality, especially for filtered containment venting systems, the high volumetric flow rates can lead to very heterogeneous and chaotic flow behavior that is not well captured by the existing models.

The aim of this work was to characterize the established two-phase flow structure for two typical filtered containment venting system nozzles, i.e. a Venturi design and a simple converging nozzle with impaction plates combined with a bubble breaker. The main instrumentation utilized for this purpose were wire-mesh sensors in two different facilities, TRISTAN and ISOLDE, at the Paul Scherrer Institut. Furthermore, a new methodology for high-speed shadowgraphy was proposed and applied to measure droplet sizes inside the throat of self-priming Venturi nozzles. The adiabatic conditions and non-condensable gases, dry nitrogen or compressed air, were chosen on purpose to disentangle the very complex mechanisms of pool scrubbing and focus on the pure soluble gas diffusion.

The measured droplet sizes and the corresponding Sauter mean diameter in the Venturi design suggest to rather focus on annular flow based correlations than common Venturi correlations from the chemical field due to the unique self-priming operation mode. In the pool, the heterogeneous flow fields that came forth in both nozzle designs at the most probable flow rates made a closer look at mass transfer phenomena necessary.

Carbon dioxide was used as a substitute for inside a small-scale bubble column with 50 x 50 mm^2 cross-section at ETH Zürich to investigate the effect of the flow structure on the mass transfer. For these tests, a new methodology for mass transfer experiments was developed, using wire-mesh sensors for both, two-phase flow structure characterization and measurement of the scrubbed gas concentration in the liquid. The results showed a high contribution from smaller bubbles in the mass transfer process whereas Taylor bubbles are not strongly participative. The new gained data on the spatio-temporal evolution of the concentration of the dissolved gas was used to extract mass transfer coefficients with the help of a one-dimensional code based on the continuous stirred tank and the axial dispersion model. The simultaneous measurement of mass transfer and interfacial area allowed to separate mass transfer coefficients from the interfacial area concentrations. The model could be further developed in the future with more experimental data especially at lower gas concentrations relevant to pool scrubbing and eventually molecular iodine tests.

ZUSAMMENFASSUNG

Der sichere Betrieb eines Kernkraftwerks hat die höchste Priorität für den Betreiber. Deshalb werden Sicherheitssysteme benötigt, die es ermöglichen, unterschiedlichste, auch schwerste Störfallszenarien beherrschen. Ein Teilsystem zur Begrenzung der Auswirkungen von schweren Störfällen sind gefilterte Druckentlastungssysteme. Sie wurden in der Vergangenheit entwickelt und installiert, um das Containment der Anlage vor einem Überdruck zu schützen, der infolge eines Kernschadens auftreten kann. Hierbei kommen entweder sogenannte trockene Filter (Sandbett-, Metallfaser- oder Zeolithfilter) oder Nasswäscher zum Einsatz, oder auch eine Kombination aus beidem. Bei Nasswäschern hängt die Effizienz der Beseitigung von Kontamination aus dem Gasstrom unter anderem von hydrodynamischen Parametern der Strömung, der chemischen Zusammensetzung der Flüssigkeitsvorlarge im Filter und der Geometrie von zusätzlichen internen Strukturen zur besseren Durchmischung ab, wie z.B. Mischer oder Tröpfchenabscheider.

Die Auswaschung der unterschiedlichen Iodverbindungen ist für Nasswäscher immer noch keine leichte Aufgabe. Eine Reihe von aktuellen Studien versuchte, die Effizienz der Iodrückhaltung mit unterschiedlichen Parametern zu verbinden, wie z.B. mit der Injektionsgeschwindigkeit des Gases, der Blasenverweilzeit und der Iodkonzentration im Gasstrom, sowie der Temperatur. Auf dem Gebiet der Modelle für lösliche Gase, welche als Teil der Modellierung für die Bestimmung der Rückhaltewerte von gasförmigen Iodverbindungen relevant sind, gibt es nur wenig experimentelle Daten, mit denen, angewandt auf verschiedene Düsenformen, Rechenprogramme validiert werden können. Weiterhin wurden viele Tests auf die Rückhaltung der Druckentlastungskammern in Siedewasserreaktoren fokusiert, in denen aufgrund der Kondensierung des hohen Dampfanteils nur teilweise Rückschlüsse auf die Diffusionsmodelle gezogen werden können. In der Blasenaufstiegszone wird angenommen, dass sich fern von der Düse das Regime einer homogene Blasensäule herausbildet. In der Realität, besonders in Systemen zur gefilterten Druckentlastung, sind die Volumenströme jedoch hoch, was zu einer heterogenen und letztlich chaotischen Strömungsstruktur führen kann, die durch die existierenden Modelle nicht korrekt erfasst wird.

Die vorliegende Arbeit hatte das Ziel, die Struktur der sich einstellende Zweiphasenströmung bei Verwendung von zwei für die gefilterte Druckentlastung typischen Düsenformen zu charakterisieren, namentlich für eine Venturidüse und eine einfache Düse mit Prallplatten unter Einsatz eines statischen Mischers. Die wichtigste Instrumentierung bestand aus einem Gittersensor, der in zwei unterschiedlichen Testanlagen, TRISTAN und ISOLDE am Paul Scherrer Institut, eingesetzt wurden. Zudem wurde eine neue Methode zur Messung von Tröpfchengrössen in der Umgebung des engsten Querschnitts einer selbstansaugenden Venturidüse vorgeschlagen und eingesetzt. Die Versuche wurden unter adiabatischen Bedingungen mit trockenem Stickstoff oder Druckluft durchgeführt, um zunächst die Komplexität, die bei Vorhandensein von Dampf auftritt, zu vermeiden und auf die Mechanismen des Auswaschprozesses und den Diffusionsvorgängen von reinen wasserlöslichen Gasen zu fokussieren.

Die in der Venturidüse gemessenen Tröpfchengrössen und die dazugehörigen Sauterdurchmessern erlauben den Schluss, dass Korrelationen für den Tröpfchenmitriss in einer Ringströmung besser geeignet sind, als die aus der chemischen Verfahrenstechnik stammenden empirischen Formeln für Venturidüsen. Dies ist auf die Besonderheit der Selbtansaugung der Waschflüssigkeit zurückzuführen. Im Volumen oberhalb der Düse erfordert die sich einstellende heterogene Strömung eine besondere Aufmerksamkeit hinsichtlich der Bestimmung des Massentransfers.

In eigenen Versuchen zum Massenübergang wurde anstelle von Iod Kohlendioxid als Modellgas eingesetzt. Hierfür wurde eine kleinmassstäbliche Blasensäukle mit einem Strömungsquerschnitt von 50 x 50 mm^2 an der ETH Zürich verwendet. Für diese Tests wurde basierend auf Gittersensoren eine neuartige Methode entwickelt, die eine gleichzeitige Charakterisierung der Strömungsstruktur und Messung der Konzentration des bereits im Wasser gelösten Gases ermöglicht. Die Ergebnisse zeigen einen relativ hohen Anteil kleinerer Blasen am Massenübergang, während grosse Taylor-Blasen kaum dazu beitragen. Die neuen Daten der räumlich-zeitlichen Entwicklung der

Konzentrationsverteilung des gelösten Gases wurde dazu verwendet, die Massentransferkoeffizienten zu ermitteln. Dies geschah mit Hilfe eines eindimensionalen Rechenmodells, das die Säule über die Höhe in Kontrollvolumen unterteilt, wobei die axiale Rückvermischung berücksichtigt wurde. Die simultane Messung von Massenübergang und Zweiphasengrenzfläche ermöglichen eine Separation des Massenübergangskoeffizienten von der Konzentration der Zwischenphasengrenzfläche. Das Model könnte in Zukunft bei Vorliegen umfangreicherer experimenteller Daten weiterentwickelt werden, speziell im Hinblick auf die niedrigen realen Konzentrationen von Iod im Gesamtmassenstrom des Gases und zur Auswertung von Versuchen mit elementarem Iod herangezogen werden.

Table of Contents

List of Figures

List of Tables

Nomenclature

Abbreviations

BWR	Boiling Water Reactor
FCVS	Filtered Containment Venting System
HSC	High-Speed Camera
IAD	Interfacial Area Density
IAEA	International Atomic Energy Agency
LDA	Laser Doppler Anemometry
LWR	Light Water Reactor
PCB	Printed Circuit Board
PIV	Particle Image Velocimetry
PWR	Pressurized Water Reactor
WMS	Wire-Mesh Sensor

Latin Alphabet

a	Interfacial area density [1/m]
A	Interfacial area [m^2]
c	Concentration of dissolved gas in liquid [ppm]
d	Diameter [m]
D_z	Axial dispersion coefficient [m^2/s]
D_L	Liquid-side diffusion coefficient [m^2/s]
d_{32}	Sauter mean diameter [m]
DF	Decontamination Factor [-]
e	Eccentricity [-]
Eö	Eötvös number [-]
CDF	Cumulative density function [-]
f	Frequency [Hz]
g	Gravity constant [m/s^2] Normalized conductivity [-]
Ga	Galileo number [-]
h	Height [m]
He	Henry constant [$mol/(m^3 \cdot Pa)$]
j	Superficial velocity [m/s]
k	Mass transfer coefficient [m/s]
k_La	Volumetric mass transfer coefficient [1/s]
K	Overall Mass transfer coefficient [m/s]
m	Mass [kg]
n	Number [-]
P	Perimeter [mm^2s]
pdf	Probability density function [-]
r	Radius [m]
Re	Reynolds Number [-]
Sc	Schmidt Number [-]
t	Time [s]
u	Measured conductance by the wire-mesh sensor [-]
v	Velocity [m/s]
V	Volume [m^3]
We	Weber Number [-]

Subscript

0	Number weighted
2	Area weighted
3	Volume weighted
b	Bubble
ch	Channel
eq	Equivalent
g, G	Gas
H	Hydraulic
in	Incoming
int	Interphase
l, L	Liquid
i,j,k	WMS node (i,j) at frame k
m	Mean
out	Outgoing

Greek Alphabet

ε	Void fraction [-]
η	Collection efficiency [-]
μ	Dynamic Viscosity [kg /m·s]
ν	Kinematic viscocity [m^2/s]
ρ	Density [kg/m^3]
σ	Standard Deviation [-] Surface tension [N/m] Conductivity [S/m]
τ	Residence time [s]
φ	Electrical potential [V]

1 INTRODUCTION

Energy production is facing one of its biggest challenges of the past two centuries. A growing demand for electricity and mobility are heavily contributing to the overall greenhouse gas emissions in the world due to the use of fossil energy sources. New ways have to be found until mid-century to limit the emissions to a fraction of nowadays values, the so-called net zero targets [1]. Nuclear power can and is contributing to the solution of this problem. With carbon emissions comparable to other renewable energy sources, it is besides run-off hydro stations the only energy production method that can generate baseload electricity. The International Energy Agency has acknowledged the important role of nuclear energy in the future by expecting a minimum 20% share of the electricity generation by 2050 [2]. This means an immense upscaling of the existing fleet, resulting in at least 1000 GW of new nuclear energy to meet the targets.

The safe operation of nuclear power plants goes together with certain safety standards, being it design specific installations or operational guidelines and training. The International Atomic Energy Agency (IAEA) is keeping track on the regulations of its members and helps extend the world-wide safety standards. One of the most profound pillars of nuclear safety is the so-called *defense in depth* philosophy. It helps to prevent the progression of accident scenarios by deploying guidelines for the operators, training and safety installations [3]. In terms of design specific measures, three barriers are already in place in light water reactors (LWR) to mitigate the release of radioactivity to the environment. The fuel cladding forms the first layer, containing the fuel ceramic matrix and the fission products produced during operation. The primary cooling water and the reactor pressure vessel belong to the second barrier and hold back fission products in case of fuel damage. The third and last safety barrier is the containment, which in some countries consists of two shells to protect either the environment from hazardous events inside the containment or the reactor pressure vessel from outside events. Whereas some existing power plants have already double shell containments, they became standard with the introduction of the generation III nuclear reactor designs. Despite the small risk of a severe accident with radiological releases, i.e. currently around 1e-5 or less per reactor year, the accident at the Fukushima Daiichi site in Japan has shown the heavy consequences. Even with the retention of fission products in the suppression pool of the units, radioactivity was still released to the environment during depressurization events to maintain the integrity of the containment.

In order to avoid the pressure buildup inside the containment and the release of radioactivity due to venting, filtered containment venting systems (FCVS) were designed in the past. By venting at an earlier state, the probability of an integrity failure of the containment can be lowered. Nuclear power plants in a number of countries are equipped with dedicated FCVS. The time of installation in some of these countries predates the disaster in Japan, other countries implemented them as part of the lessons learnt from the accident. The concept of those systems is to pass the vent gas through a filter before releasing it to the environment as schematically illustrated in Figure 1.

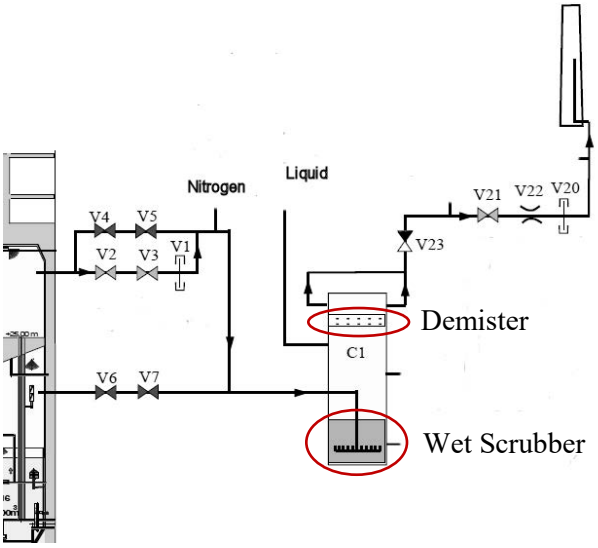

Figure 1: Simplified diagram of an FCVS from Olkiluoto 1 & 2 taken from [4]. The vent lines from the containment enter the wet scrubber and exit after the demister to the chimney.

As part of the accident analysis and the postprocessing, the status of existing filter systems, national regulations and installations was reviewed and summarized by Jacquemain et al. [4]. Yet, the task to

retain the radioactive releases in those filters is a challenging one. The chemical complexity of the source term after a core damage makes the design of such filters very demanding. Different aerosols with different size distributions as well as radioactive gas phase species like elemental iodine gases can interact with all the plant inventory under high temperatures and radiation levels. The developed FCVS designs so far can be divided into two different types, dry filters, e.g. sand bed or zeolite filters, and wet scrubbers with the possibility to combine wet and dry solutions in one FCVS. Depending on the vendor, the FCVS work with different principles to retain the active particles or gases. Jacquemain et al. [4] commented wet scrubbers as a proven technique to filter aerosols and gases and on their additional benefit of serving as a heat sink at the beginning of the venting phase and hence help to decrease the pressure. The scrubbers sparge the contaminated gas stream through a nozzle into a liquid pool which are usually equipped with internals and chemical additives to enhance the retention efficiency. At the pool surface, droplets are formed either by bubble breakup or entrainment which is why wet scrubbers have a demister upstream of the outlet to retain the liquid back to the pool. The demister can also be seen in the schematic in Figure 1.

Pool scrubbing processes are not only taking place in FCVS but also in other bigger pools in both light water reactor designs, e.g. in the suppression pools in boiling water reactors or at the secondary side of the steam generators in pressurized water reactors. Though these pools are designed for normal operation (steam generator) or design basis accidents (suppression pools) of the power plant, they can contribute to the reduction of the radioactive releases and can serve as scrubbing pools during postulated severe accident events. Thus, it is not surprising, that, as a direct consequence of the Fukushima accident, there has been an increase in research for a more profound understanding and accurate modeling of the scrubbing processes.

From all the volatile fission products that have a significant health impact, the iodine species have turned out to be a rather challenging fission product in terms of retention due to the high volatility and reactivity of iodine. Iodine releases are also among the most contributing ones in the beginning phase of an accident regarding dose to the public as studied by Soffer et al. [5]. Collins et al. [6] studied different formation possibilities of iodine with other elements under light water reactor accident conditions and concluded that under a steam environment, the majority of the iodine is bound as the hygroscopic aerosol CsI but the presence of molecular iodine in gas form cannot be excluded. Under the harsh environment during core damage, iodine can also react with other organic compounds inside the containment or reactor to form organic iodides such as methyl iodide (CH_3I) and other similar organic compounds often sub summarized as OrgI. CH_3I is a hazardous chemical even in its none active form. It is very volatile and hardly soluble in an aqueous scrubbing fluid. Its retention is much more difficult than the filtering of the molecular form of iodine or aerosols. Hillrichs et al. [7] collected the regulations of different European countries in 2012 which typically require decontamination factors (DF) of elemental iodine from 10 to 100. The DF is defined as the ratio of the total mass flowing into a pool to the total mass leaving the pool as presented in (1.1). To put the elemental iodine requirements into perspective, the wet scrubber designs of vendors like Westinghouse and AREVA deliver decontamination factors for aerosols in the order of 1’000 to 10’000 [4].

$$DF = \frac{m_{in}}{m_{out}} \tag{1.1}$$

The difficulty of trapping volatile radioactive gases such as iodine was already known since the Windscale fire in 1957. Crick and Linsley [8] identified this in their assessment on the radiological impact of the accident. I-131 contribute to a large extend to the total collective dose. A decade after the accident, Diffey et al. [9] reported their study on the decontamination factors of a suppression pool mockup for elemental iodine, methyl iodide and 6 µm particles in steam-air mixtures or pure air streams. The results of this work revealed a big impact of the ratio of steam to air on the DF. A lower air content in the gas mixture resulted in higher decontamination factors for elemental iodine which came from a better condensing effect in the pool. For the experiments conducted without steam with a constant iodine inlet concentration in the air stream, Diffey et al. fitted their experimental data to the correlation (1.2) where x is defined in (1.3) with the

volumetric flow rate $\dot{V}_g$, the measuring time t_{meas}, the Henry constant He and pool volume V_l.

$$DF = \left(1 - \frac{1-e^{-x}}{x}\right)^{-1} \quad (1.2)$$

$$x = \frac{\dot{V}_g * t_{meas} * He}{V_l} \quad (1.3)$$

The tests with the 6 µm sized Ni/Cr particles showed a similar trend in the steam-air ratio and its effect on the retention. The higher steam fraction in the gas had not as such of an effect as expected but would lead still to slightly better decontamination factors. Two interesting observations were made with the iodine tests in the big pool and the methyl iodide tests. Due to the weak binding of molecular iodine in water, it can also be rereleased from the pool, which is referred to as revolatilization. The observed revolatilization of iodine was mostly dependent on the concentration in the pool and the time elapsed since it was added to the pool. The additional time in the pool would presumably allow the iodine to form some stronger chemical bonds with the water or pollutants inside the liquid that are more soluble in water. This assumption was not further specified and left open. Regarding methyl iodide, no significant filtering could be measured that was not easily revolatilized by sparging air through the pool. The addition of thiosulfate only had a positive effect on the retention and trapping of molecular iodine.

The work of Hillary et al. [10] confirmed the results of Diffey et al. [9] on the higher steam fraction giving higher molecular iodine DFs. Contrary observations were made on particle loaded gas stream with higher steam fraction leading to lower filtration but the biggest activity in the air rich gas stream was found in the demister of the facility. In an additional work, Hillary et al. [11] further investigated the trapping mechanisms of methyl iodide in charcoal filters at dry and slightly humid conditions which were very promising if the flow direction is kept downwards and the filter is properly sealed.

A couple of years later, Stanford and Webster [12] studied the influence of degassed water on the pressure suppression but also the retention of elemental iodine in suppression pools. Unlike Diffey et al. [9] or Hillary et al. [13], they saw an increase by a factor of 5 or greater in the retention efficiency of iodine by adding 2 weight-% of air into the steam flow. No explanation was given to what could have increased the rather poor retention. Diffey and Hillary concluded a strong condensation retention which is reduced in a steam-non-condensable flow mix.

Siegwarth and Siegler [14] looked once more into methyl iodide retention in suppression pools and its dependencies on the nozzle position, water pH or feeding concentration. None of them showed big variances, only the pool temperature made a difference worth noting.

The POSEIDON tests reported by Güntay [15] were conducted some years later at Paul Scherrer Institute using various injection nozzles and studying the effect of the nozzle diameter and submergence of the pool of an iodine loaded nitrogen gas stream. The results showed an increase in the decontamination factor with increasing pool height and decreasing nozzle diameter. The bigger pool submergence lead to higher residence times inside the pool whereas the smaller nozzle diameter was assumed to sparge finer bubbles which would increase the interfacial area in the two-phase flow field. Unfortunately, the tests were performed as integral tests with no hydrodynamic information on the flow regime inside the POSEIDON tank.

Such experimental test series are an important element in the development of models for simulation tools. The derived models in the codes can be benched against a variety of test data in order to gain less uncertainty in the simulation of real-life accident scenarios. Three of the more widely used severe accident codes are SUPRA [16], BUSCA [17] and SPARC [18]. Herranz et al. [19] reviewed the three different codes with the existing empirical data at that time. In terms of iodine vapor retention in aqueous solution, the two codes BUSCA and SPARC were compared against the data of Diffey et al. [9]. Two major limitations were apparent in the BUSCA code. First, BUSCA could only handle the molecular iodine but not the methyl iodide retention. On top of that, no revolatilization was implemented in the code. Both codes suffered from a missing water chemistry that is affecting the pH level which is essential in keeping iodine in a dissolved state.

One other issue comes from the hydrodynamic modeling side. The description of the flow regime at

different conditions in the pools is an ongoing process. Taking as an example the bubble swarm formation in the SPARC manual, which is pictured in Figure 2, the injected gas stream is modeled in three stages. The first is the globule formation region after the nozzle. The big gas globules are breaking up in the second stage, the bubble breakup region, and rise up to the surface in the bubble rising zone. The third and final stage is the pool surface. At all three stages, mass is being transferred at the gas-liquid interface. The bubble rising zone is modeled as a bubble swarm with equal diameter. In BUSCA, the bubbles are either spherical, ellipsoid or elliptical caps whereas SPARC is limited to spheres and ellipsoids only. None of the codes takes into account a transition into churn-turbulent flow conditions, predominant at high gas flow rates.

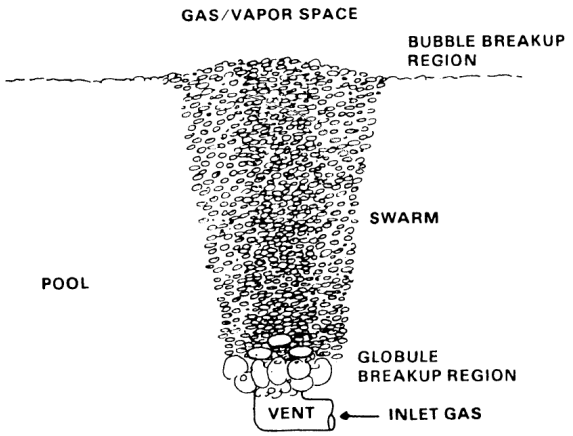

Figure 2: Bubble swarm formation in pool scrubbing codes as exemplary displayed in the SPARC-90 manual [18].

Around the same time as the work of Herranz et al. [19], Fischer [20] looked into the differences of the computer codes from a modelling aspect. The differences are summed up in Table 1. There are major differences between the codes regarding the species considered in the scrubbing process but also the zone in which the scrubbing takes place.

In BUSCA, basically only molecular iodine is modeled in the bubble rise zone. The decontamination factor results from a semi-analytical solution for the diffusion equation. The first solution applies for spherical caps (1.4), the second for spherical bubbles (1.5). The variables λ and τ_D are depending on the Henry constant *He*, the liquid and gaseous diffusivity constant D_L and D_G respectively and the shape of the bubbles given by the radius r_B and the bubble semi-angle φ.

$$DF_{I2} = \frac{2\pi^{\frac{1}{2}}}{\lambda}\left(\frac{t_{rise}}{\tau_D}\right)^{\frac{3}{2}} \tag{1.4}$$

$$DF_{I2} = e^{\frac{t_{rise}}{\tau_D}} \tag{1.5}$$

$$\tau_D = \frac{\pi^{\frac{1}{2}}\cdot\beta\cdot r_B^{\frac{5}{4}}\left(He+\left(\frac{D_L}{D_G}\right)^{\frac{1}{2}}\right)}{6D_L^{\frac{1}{2}}\cdot g^{\frac{1}{4}}\cdot f(\alpha)} \tag{1.6}$$

$$\beta = 1-\frac{3}{2}\cos(\alpha)+\frac{1}{2}\cos^3(\alpha) \tag{1.7}$$

$$f(\alpha) = \left(\frac{2}{3}+\frac{1}{3}\cos(\alpha)\right)^{\frac{1}{2}}(1-\cos(\alpha)) \tag{1.8}$$

$$\tau_D = \frac{3}{2}\frac{\sin^2(\alpha)\cdot D_L^{\frac{1}{2}}\cdot\tau_D^{\frac{1}{2}}}{\beta\cdot r_B\left(He+\left(\frac{D_L}{D_G}\right)^{\frac{1}{2}}\right)} \tag{1.9}$$

Table 1: Species and Zones Considered in the Codes according to Fischer [21]

Species	BUSCA	SPARC	SUPRA
Molecular Iodine I_2	• Bubble Rise Zone	• Primary System • Injection Zone • Bubble Rise Zone • Pool Surface Zone	• Bubble Rise Zone • Pool Surface Zone
Methyl Iodide CH_3I		• Injection Zone • Bubble Rise Zone	• Bubble Rise Zone • Pool Surface Zone
CsI_{gas}			• Bubble Rise Zone • Pool Surface Zone
HI	Non-soluble		

In SPARC, the bubble rise zone is modeled using the diffusive volumetric diffusion flow φ_{I2} (1.12) which is made of the diffusion velocity u_D (1.13), the factor accounting for vaporization θ_{I2} and the surface area of the bubbles A_B. The decontamination factor for the fine bubbles DF_B (1.11) is then combined with the share of globules f_G to get the total decontamination factor DF_{I2}. The share of the globule bubbles is thereby decreasing the overall DF_{I2} which means that the code assumes no interaction of the bigger bubbles.

$$DF_{I2} = \frac{1}{f_G + \frac{f_B}{DF_B}} \tag{1.10}$$

$$DF_B = e^{\frac{6\phi_{I2} t_{rise}}{\pi d_B^3}} \tag{1.11}$$

$$\phi_{I2} = u_{D,I2}\theta_{I2}A_B \tag{1.12}$$

$$u_{D,I2} = u_{D,G}\frac{c_g - c_{int}}{c_g} \tag{1.13}$$

$$c_{int} = \frac{c_l^{eq} \cdot u_{D,L} + c_g \cdot u_{D,G}}{He \cdot u_{D,L} + u_{D,G}} \tag{1.14}$$

$$u_{D,L/G} = \sqrt{\frac{D_{L/G}}{\pi \cdot t_{rise}}} \tag{1.15}$$

Due to the share of globules f_G and the share of bubbles f_B, SPARC sort of takes two different bubble sizes into account. The decontamination factor for methyl iodide is calculated the same way with the corresponding diffusion and Henry constants. The model of SUPRA is built similar to SPARC and BUSCA but more dependent on hydrodynamics and difficult to be isolated for the soluble gas model. Nonetheless, an insight is given by Wassel et al. [16] with a code validation for mostly aerosol retention and the methyl iodide tests of Diffey et al. [9].

As mentioned earlier, the predominant form of iodine during a severe accident is its aerosol form CsI. This makes a small excursion into the research of aerosol retention noteworthy. Beside CsI, numerous other aerosol species can be formed in a damaged reactor core that react with the reactor pressure vessel, the internals or the concrete of the reactor building. It is not surprising that there were various experimental programs to investigate fission product transport and retention, e.g. the ACE, EPRI, JAERI or LACA-Espana tests. These test campaigns were summarized by Ramsdale et al. [21] in their work.

The retention phenomena that are responsible for the filtering of the particles and gases are numerous which makes the experimental studying and validation of models very complex and cumbersome. The most important particle transport processes from a gas bubble to liquid are diffusion, inertial deposition and gravitational deposition as described by the model presented by Fuchs et al. [22]. In order to calculate the transport by these different processes, particle size and density, as well as the bubble size and the velocity of the bubble relative to the liquid need to be known, in addition to the gas and liquid properties. More recent works focused their research work on the aerosol retention on the secondary side of the steam generator during a steam generator tube rupture case.

During the ARTIST project, a height scaled steam generator tube bundle was assembled to study the flow paths of aerosols after a tube break. Lind et al. [23] found a strong retention close to the break which highlighted the importance of the jet-bundle interaction even at smallest submergence levels. Also, a higher submergence lead to higher retention values as well as a bigger particle size due to inertial effects. The CFD simulations of Dehbi et al. [24] were able to replicate the experimental results of the ARTIST project, using LES models. Kim et al. [25] started at KAERI another campaign on studying aerosol retention effects on a short steam generator bundle. The first tests were performed with a dried tube bundle, i.e. no water submergence on the secondary side. In their first tests, most of the aerosol deposition was not found closest to the break but further downstream. This was explained by resuspension at high velocities which dragged the aerosols further. They also found most of the mass being deposited on the neighboring tubes due to impaction.

Another region relevant for aerosol trapping is the suppression pool. These nozzles usually inject the gas in different directions due to their branching design. Diao et al. [26] focused on analyzing the impact of the inlet pressure and the injection direction on particle scrubbing efficiencies in pressure suppression pools. They concluded that the increase of inlet pressure is beneficial for the retention of aerosols, especially while staying at subcritical flow conditions. The injection direction becomes unimportant ones the flow reaches

critical flow conditions. At this stage, due to the increase of the relative velocity, high retention values can be reached.

Herranz et al. [27] worked on a more fundamental level and looked into the jet scrubbing of aerosols. Their studies found for particle velocities that lead to Stokes number bigger than 0.01, even without steam condensation, particle removal efficiencies of 90 % or higher. This was attributed most probably to the inertial impaction of the aerosols at these thermal-hydraulic conditions. The importance of the hydrodynamics was stretched as well, as the two-phase dynamics will affect the retention. They even built up a new correlation for the jet scrubbing conditions.

In the validation study of Fujiwara et al. [28], the analytical results from MELCOR simulations were compared with measurements of single bubbles containing particles. An interesting finding of their work was the effect of CsI on the bubble shape. The soluble aerosol acted like a surfactant which resulted in more spherically shaped bubbles than with non-soluble aerosols. This conclusion was the reason for most of the deviation between the MELCOR calculations and their results as a different bubble shape would lead to different bubble rising velocities and different interfacial area.

Regarding gas retention, most of the work on pool scrubbing related specifically to iodine retention was carried out in the later 1980s and early 1990s. This topic received renewed attention after the Fukushima Daiichi accident in 2011 as it was realized that more efficient mitigation methods for fission product release from a severe accident scenario would be needed. In Europe, the PASSAM (Passive and Active Systems on Severe Accident source term Mitigation) project was launched to further investigate open questions in pool scrubbing. The research targets were summarized by Herranz et al. [29] with focus being laid on the jet injection regime, high gas flow rates rising through pools, bubble hydrodynamics and long-term behavior of the iodine trapped in FCVS pools. The outcomes were summarized by Albiol et al. [30]. Most experimental work was done to improve the understanding of aerosol particle trapping and retention with a limited number of tests done to investigate the methyl iodide trapping in wet scrubbers, with the conclusion that no further enhancement could be reached by optimizing the performance of the pool.

Around the same time, the 1:1 height scale VEFITA (Venting Filter Assessment) facility was assembled at PSI as described by Suckow et al. [31]. The experiments aimed to characterize the thermal-hydraulic quantities relevant for FCVS and study the retention of aerosols, iodine and organic iodide using typical industrial scrubber additives like sodium thiosulfate to bind iodine and sodium hydroxide or sodium carbonate to control the pH of the pool water. As part of the research program, new methods were investigated to improve the retention of organic iodides.

Earlier tests at PSI as described by Lind et al. [32] confirmed the results of Siegwart and Siegler [14] regarding the pH dependency of the gaseous iodine retention. Like in the POSEIDON tests, a higher nozzle submergence would lead to higher decontamination factors due to the longer exposure of the gas. The organic iodides again showed very weak retention values inside the wet scrubber which dropped significantly if the pool temperature was decreased below 70°C. Again, except for the level swell which is linked to the void fraction, little information was given on the flow structure.

Beghi et al. [33] studied in the small-scale facility Mini-VEFITA the retention of elemental iodine with a commercial scrubber setup using the nozzle design of the CCI filter [4]. Thanks to the borosilicate glass walls of the facility, visual observations could be made to estimate the flow conditions inside the scrubber. The work found a strong dependency of the retention quality of gaseous iodine on the flow regime as shown in Figure 3. The retention in the churned-turbulent regime was mostly taking place in the injection zone. The jet regime at these high flow rates forms a large interfacial area due to the droplet formation which are only limited by the concentration gradient between the gas and the liquid. Thus, the DF increased with an increase of the iodine concentration in the gas inlet stream. These new insights made the characterization of the two-phase flow inside scrubbers even more important but also rendered the conservatism of experimental data questionable. Too high iodine loading is used to achieve a better detection efficiency by chemical sensors, which would result in non-conservatively high DFs. However,

the experiments agreed very well with the two-film theory in the bubble rise zone.

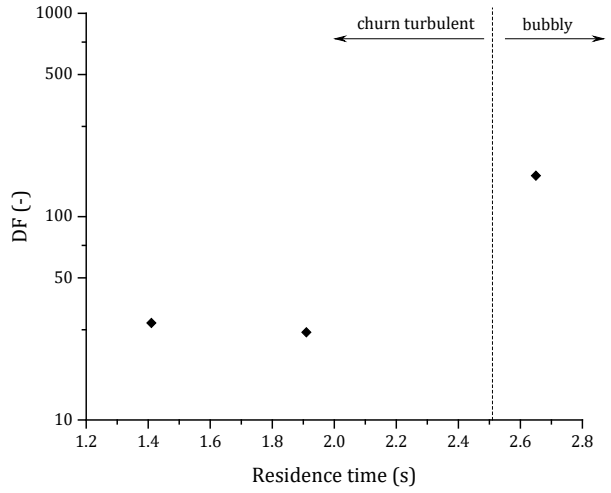

Figure 3: DF as a function of residence time showing significant change in the flow regime transition using the injector and mixing element from CCI-IMI-Nuclear and loaded with 0.06 M $Na_2S_2O_3$ and 0.1 M NaOH at 21°C in the Mini-VEFITA test facility [33]

Another nozzle geometry that gained a lot of interest in recent years is the self-priming Venturi design. Majid et al. [34], [35] studied the effect of the gas injection flow rate, iodine concentration in the gas inlet and the effect of the operating the Venturi in submerged or unsubmerged mode on the filter efficiency. The studies first started in the unsubmerged mode, i.e. the Venturi nozzle was submerged only to the liquid suction position to focus on the performance of the nozzle. In this operation mode, a higher inlet concentration of iodine in the gas gained higher decontamination factors. Furthermore, with increasing the injection gas flow rate (240 m^3/h to 340 m^3/h), more iodine was scrubbed out of the gas stream. The higher gas flow rate would create finer droplets inside the throat which would mean a higher interfacial area density. This assumption was supported with the fact that the removal efficiency was nearly unaffected by the iodine inlet concentration at the highest volumetric flow rate. The very high interfacial area would make up for a lower concentration difference between the droplet interphase and the gas stream. In a second step, the Venturi nozzle was operated in a fully submerged mode. Due to the now present bubble rising zone, a higher DF was in general observed for the fully submerged nozzle. The dependency of the iodine inlet concentration or the gas flow rate disappears compared to the unsubmerged operation mode. The additional scrubbing in the pool allows to retain all the remaining iodine in the gas stream after being injected into the liquid bulk.

Zhou et al. [36] did not observe any dependency on the entering iodine gas concentration in their studies with an unsubmerged Venturi nozzle, although in their work, they stayed at relatively small concentrations (up to 35 mg/m^3) compared to Majid et al. (up to 300 mg/m^3). The reason for the used inlet concentrations was not documented but it could be related to the detection limit of their instrumentation. Both works sampled at the inlet at outlet using an unspecified spectrophotometer but Zhou et al. had no droplet separator installed upstream the sampling line. Gulhane et al. [37] looked again into the pH dependency of the iodine trapping and tried to verify existing pressure drop models with their setup. A higher pH lead to higher DFs which agrees with the research reported by Lind et al. [32] and Siegwarth and Siegler [14].

With the injection and the bubble rise regime being covered, Herranz et al. [38] and Fischer et al. [39] investigated the iodine mass transfer at the pool surface. The atmosphere of suppression pools or FCVS can still interact with the pool surface in either direction, leading to either more retention or more revolatilization. Both works used the two-film theory to derive mass transfer coefficients to benchmark them against their experimental data. However, despite their values being within good error margins, due to the scarce availability of pool surface tests, both agreed that more validation work would be required before implementing their models in a system code.

A lot of studies have been performed in the past to understand the mechanisms of gaseous iodine filtering. Most of them were done in an integral way and single dependencies could be identified, e.g. the pH of the pool or the pool temperature. Nonetheless, in terms of modelling, the hydrodynamic aspect of the mass transfer, i.e. interfacial area density, two-phase flow structure and void fraction, were either determined over assumptions or neglected. The phenomenon of pool scrubbing during postulated severe accidents, be it in suppression pools, FCVS or on the secondary side of a

steam generator in case of a tube rupture with fuel damage is anything but easy. The optimal retention values for elemental iodine could cause major drawbacks for the aerosol retention and vice versa.

Betschart [40] was one of the first to perform studies in a large diameter facility with and without tube bundles in a wide range of injection flow rates to investigate the effect of a tube bundle on the sizes and shapes of the bubbles, the void fraction and the interfacial area density that are being formed after a tube rupture. He found that large bubbles exist even after long distances of the injection point which does not agree with the bubble swarm formation theory of the system codes.

The interest in replicating pool scrubbing phenomena with calculations is one of the main objectives of the Integration of Pool scrubbing Research to Enhance Source-term Calculations (IPRESCA) project that was launched recently as firstly presented by Gupta et al. [41]. The experimental data of various international partners should be made available for better model development and remaining issues should be addressed by institutes with the capabilities to perform experiments on them. Beside simplified experiments, also more complex ones closer to real accident conditions are foreseen under this framework.

The aim of this work is to support the severe accident research domain by characterizing two typical commercial scrubber nozzles with accurate hydrodynamic data. For this purpose, two different measuring techniques were required to evaluate both, bubble hydrodynamics like interfacial area density and bubble sizes, and droplet sizes. The wire-mesh sensor with its tomographic capabilities was used for the heterogeneous bubbles in the pool and high-speed shadowgraphy for the estimation of droplet sizes inside a Venturi throat. The methodology of the wire-mesh sensor data analysis was further developed to obtain results for the (quasi) stagnant liquid flow regime. Regarding the droplet sizes, a new analysis method was proposed. The results in the higher flow ranges showed a heterogeneous flow behavior which made further mass transfer investigations necessary. A model gas, i.e. carbon dioxide, was chosen at various concentrations with nitrogen as an inert gas to study general two-phase flow mass transfer effects with non-condensable gases. The wire-mesh sensor was again used to measure two quantities simultaneously, the bubble sizes and the dissolved gas content. The analysis was adjusted for an environment with a changing liquid conductivity and additional calibration steps had to be introduced for the segregation of liquid and gas and the dissolved gas quantification. A one-dimensional model was drafted to interpret the results of this new developed measurement methodology and to compare the obtained mass transfer coefficient with existing literature. The results of the model indicated that the idea deserves further study which would need more experimental data in the low gas concentration region, also to be relevant for iodine pool scrubbing situations.

2 INSTRUMENTATION AND METHODOLOGY

Measurements in two-phase flows is even nowadays a challenging task in terms of optimal instrumentation. The characterization of the flow should be done with as much information and as non-intrusive as possible. In gas-liquid flow, void fraction, bubble size distribution, bubble velocities and interfacial area are important targets for a high-resolution instrumentation in order to understand the driving mechanisms in two-phase heat and mass transfer. High temporal and spatial resolutions are necessary to obtain the desired quantities inside a two-phase flow field. In the past, many intrusive and non-intrusive instrumentation methods have been developed and established in the recent research environment. The list starts with direct imaging techniques with or without the addition of particle image velocimetry (PIV) or laser doppler anemometry (LDA), continues to instruments based on the electrical properties like electrical impedance tomography, electrical probes and wire-mesh sensors (WMS), goes over to optical probes and ultrasonic transmitters and ends with radiation-based solutions like x-ray or neutron tomography. Instinctively, non-intrusive methods would be preferred due to their nature of not disturbing the dynamics of the flow. Unfortunately, not all non-intrusive techniques offer the necessary amount of details for the description of the flow. Thus, a closer look also at intrusive measuring equipment is noteworthy.

One of the first non-intrusive measuring technique applied for the study of two-phase flow is the direct photography. The work of Rosenberg [42] was one of the earliest records on the investigation of bubble drag coefficients, bubble shapes and bubble terminal velocities. Single air bubbles of different sizes were produced and recorded in their flow path with a 35 mm camera with up to 60 frames per second. The frame rate allowed a quantitative imaging of the bubble movement of spherical bubbles, oblate spheroids and spherical caps. Levenspiel [43] studied the collapse of steam bubbles for the estimation of the heat transfer coefficient using in his work a high-speed camera with 1000 frames per second. Kintner et al. [44] summarized existing studies at that time in two-phase flows with direct photography and mentioning first works using cameras with frequencies of up to 8000 Hz and particle tracing methods. The digital cameras and analysis with computer codes brought forward more possibilities. Nishino et al. [45] tried to improve the accuracy of the direct photography by using stereoscopic imaging to overcome the problem with the missing third dimension. In order to properly calibrate their methodology, fixed sized particles were used. The results were satisfying with focus being lied to the new gained information of the spatial position of the tracked particles. Murai et al. [46] continued with the stereoscopic approach and applied it in bubble plums up to void fractions of 12 % for the estimation of the 3D void distribution. The overlapping bubbles were dealt with by statistically assuming that a shadow is covering one or two bubbles in the line of sight at different void fractions. It was Honkanen et al. [47] who proposed a detection algorithm of highly overlapping bubbles by following the bubble curvature and applying the so called breakline method. The method tracks the curvature of a recognized boundary and sets segmentation points where the curvature suddenly peaks. Broeder and Sommerfeld [48] characterized a turbulent bubbly flow in a bubble column with the help of planar imaging, PIV for the liquid velocity field and particle tracking of the bubbles for the bubble velocities. In their approach, if 85% of the contour is detected, only one bubble is validated whereas both were considered if this value dropped to 75%. This should address the high uncertainty observed by Honkanen et al. with wobbling bubbles. Oblate ellipsoids in the flow can change their shape and curvature which would result in an artificial fragmentation of the bubble. A novel shadowgraphic optical probe was developed by Lichti and Bart [49] to be installed between two pipe segements to obtain bubble size distributions and average void fraction in bubbly flow. They used a watershed transformation as described by Beucher [50] to deal with overlapping bubbles. The design of the probe is shielding the tube segment from light other than the installed source which gives very good shadowgraphic images. A similar filtering technique was used by Nunno et al. [51] with four different cameras to describe the 3D position of bubbles in bubbly flow and in a plunging jet, including

bubble rise velocity, bubble size and trajectories. Murai et al. [52] moved away from bubbly flow and tried to characterize plugs inside helical tubes with a backlight tomographic technique they designed with different angled mirrors. They described the shape and speed of Taylor bubbles in horizontal and helicoil tubes but no information was obtained on the interface or the equivalent bubble size. Dasgupta et al. [53] also aimed to study churned-turbulent and annular flow regimes by means of image analysis with their focus being the disturbance waves in both flow regimes.

The direct photography is relatively simple in terms of experimental setup, but one major drawback was found to be the limited depth of field. The scale of droplets and bubbles would require a fine film and camera resolution in the sub millimeter region which would affect the depth of field accordingly due to the laws of optics. Thompson [54] proposed a method based on diffraction by opaque and transparent particles which would turn out to be very much appreciated in the two-phase flow studies. Thomson himself continued to further develop his principle to the holographic particle technique [55]. Within a short time period, the interest in performing studies with holographic measurements grew and first tests were conducted to characterize particle sizes like droplets in gas-liquid or liquid-liquid flows [56]. As Thompson mentions in his summarizing work [56], the off-axis holograms were being investigated in their usefulness which needed higher resolution recording films for the additional benefit of not needing to capture the full transmitted light. It was Hausmann and Lauterborn [57] who proposed a reconstruction technique of three-dimensional off-axis holographic images to determine bubble sizes and position. Unfortunately, the computational power at the time did not allow to quantify a big number of bubbles. Nonetheless, Lauterborn continued his research and validated the direct camera imaging technique [58] with holography [59]. The holographic imaging remained though more preferred for the droplet analysis than bubble dynamics as Lee and Kim showed in their review [60]. Bubble swarms would disturb the light path more than droplet sprays which would result in blurred holograms. Feldmann [61] combined short-time holography in a stereoscopic setup to measure bubble sizes in a stirred aerated bubble column at different impeller speeds. The possibility to estimate the void fraction and the interfacial area was left open with little additional computational effort. Shao et al. [62] used digital inline holography with a modified watershed filter to obtain bubble size and droplet size distributions from artificial data but also experimental bubble data from a cavitation water tunnel.

The optical methods like direct photography or holography with support of PIV or LDA to quantify the velocity fields have reached a high level of accuracy and scientific acceptance for their applications. Unfortunately, they remain useful in low void applications with a limitation to the bubbly and the jet flow regime near nozzles. As mentioned earlier, the blockage of the line of sight by bigger plumes or churns poses a major challenge. Hence, different methods had to be developed to work in all various flow regions.

In the chronology of non-intrusive two-phase flow instrumentation, the use of x-ray was also one of the earlier techniques. Hewitt and Roberts [63] compared x-ray photographs taken with conventional flash photography to study the different two-phase flow patterns. They started with bubbly and slug flow and traversed the churn-turbulent regime to annular flow. The x-ray photographs revealed some flow structures that were hidden behind the turbulent structure. Jones et al. [64] continued to quantitively measure void fraction and link it to the different flow regimes. The probability density function of the void could be assigned to three different flow structures, bubbly, slug and annular flow. Bubbly and annular flow gave unimodal distributions in the probability density function in the low and high void fraction region respectively. The slug flow regime was the only bimodal distribution observed at different liquid superficial velocities. The statistical behavior of the void could be correlated to the flow structure.

The best available technology today giving the highest accuracy and resolution would be the high-speed x-ray tomography which achieves high measuring frequencies with a very high resolution as invented by Prasser and Hampel [65] and further used in the works of Fischer et al. [66] and Hampel et al. [67]. Unfortunately, the ultrafast x-ray gun has not only a size limitation in terms of facility size as the aforementioned had up to 180 mm inner diameter with bigger inner

diameters mentioned to be in development. The use of x-ray techniques requires radiation shielding around the facility and proper training for the personnel handling the x-ray machines. Furthermore, an x-ray device is even without these limitations a rather expensive measuring technique.

In terms of radiation, neutrons are attractive for void fraction measurements as the liquid, usually water, has a high sensitivity for hydrogenous molecules and a low one for metal components. Banerjee et al. [68] performed first tests with aluminum phantoms to simulate (inverted) annular flow and stratified flow. The aluminum phantoms would block the flow passage where the gaseous phase would be in the real two-phase flow. The aluminum was necessary to compare the experiments with Monte Carlo simulations. The neutron scattering technique was also used with air-water tests where the void fraction was measured in parallel with fast closing valves. Banerjee et al. concluded that the neutron scattering technique would be a robust instrumentation method to determine void fraction. Bossi et al. [69] increased the framerate of their neutron radiograph to 2000 to 10000 frames per second for two-phase flow events that take place within 1 to 10 ms. The neutron pulse was generated by a TRIGA reactor with the neutrons being converted with a LiF-ZnS screen. A high-speed camera was recording the image on the screen with first qualitative images of a gas injector being presented in their work.

The work of Chang and Harvel [70] applied real-time neutron radiography to characterize a bubble column. The signal was used to determine void fraction and mean bubble diameters by applying an image technique with pixel to pixel analysis. The interfacial area could be estimated through the mean diameter and the assumption of a homogeneous flow structure. Mishima et al. [71] visualized slug and annular flow in a rectangular duct with frame rates up to 1000 frames per second and measured the void fraction profile of slugs and waves along the longitudinal axis. In the annular flow region, the disturbance waves could be observed and quantified in height.

Zboray and Prasser [72] used a cold neutron source to quantify liquid film thicknesses in more complex flow channels like fuel element sub channels with a pixel resolution of 60 to 90 μm. Unlike the previous works, the subchannel was placed on a turn table to get a tomographic image of the cross section. The drawback was a time averaged image. Zboray and Trtik [73, 74] continued their research with cold neutron radiography with a narrow channel and achieved recording frequencies of 800 frames per second. With their setup, they were able to reconstruct 3D renderings as no obscuring of overlapping bubbles took place. Last but not least, Lani and Zboray [75] took another look to the TRIGA pulse with a narrow channel and were able to ramp up the frequency to 4000 frames per second with a pulse length of 20 to 40 ms.

Neutron tomography and radiography as a non-intrusive measuring technique is becoming very interesting when looking into pressurized metal tanks but for adiabatic unpressurized situations, the drawback of one single line of site and the required investment into a neutron generator and appropriate shielding made it not an attractive solution. Other techniques like electric impedance tomography as first presented by Price [76] for the study of two phase flows or ultrasound imaging as presented by Lattimer et al. [77] would conclude the non-intrusive techniques that have also been used in bubbly flow regimes but have yet not been widely used in more heterogeneous flow situations.

The wire-mesh sensor (WMS) as described by Prasser et al. [78] solved the spatial information problem in the cross section of the test section and is a good compromise in terms of accuracy of the measurement, resolution and applicability for the determination of two-phase flow characteristics. The drawback of the intrusiveness of the sensor is outweighed by the flexibility and easy modification on the sensor itself without changing the data acquisition system and most of the analytical part.

2.1 Bubble measurements using Wire-Mesh Sensors

The WMS, as it was presented for the first time in Prasser et al. [78], has been used in the past two decades in multiple areas for multiphase flow applications. A comprehensive description of the technology, the possible ways of signal processing and a summary of the numerous applications is given by Prasser [79]. Peña and Rodriguez [80] also looked into the different shapes and application fields of the WMS and its usage

so far. The WMS has been used in the past to study water and gas mixing phenomena, to characterize gas-liquid two-phase flows but also liquid-liquid and even three-phase flows. It is an intrusive measuring technique that determines in its original idea the instant local void fraction distribution as presented by Prasser et al. [78] by measuring the electrical conductivity or capacity between two or three wire planes, normally one transmitting and up to two receiving ones. In principle, two different phases can be distinguished as long as the difference in the electrical conductivity or capacitance is significantly bigger than the noise level. Thus, when looking on conductive WMS, gas-liquid two-phase flows provide the optimal setup with the gas phase having no electrical conductivity in an unionized state, as long as the liquid has a detectable conductivity.

By applying a high frequent alternating voltage pulse on the transmitters, the incoming electrical current is measured simultaneously by all receiver electrodes. A simplified electrical scheme is depicted in Figure 4. The WMS200 [81] data acquisition box converts the electrical current into 12-bit long integer values which are stored in a compressed format in 32-bit long integers. One transmitting pulse detected by 16 receiver electrodes results in 6 32-bit unsigned integers. The frequency of the sensor array can be set from 10'000 Hz for the smallest configuration, i.e. 16 transmitters x 16 receivers, down to 1'024 Hz for a maximum of a 128x128 mesh. Doubling the transmitter number, starting from a minimum of 16 transmitter electrodes, leads each time to halving the frequency due to the longer waiting time for the alternating pulse to run through all transmitting electrodes.

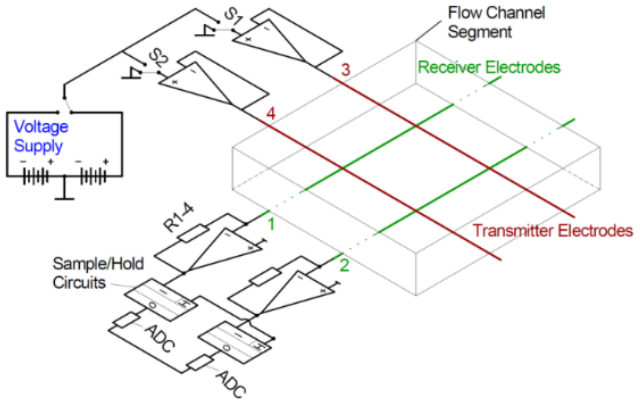

Figure 4: Electrical schematic of the wire-mesh sensor as presented in the work of Betschart [40].

The main disadvantage of the sensor lies in its intrusive nature. The intrusiveness of the wire array increases with an increasing amount of wires or bigger wire diameters. The reason can be found in the bigger cross-section area that is covered by the wires and disturbing the actual flow. Decreasing the wire diameter to a minimum size would be the consequence to reduce the effect of the blocked area by the wires. However, there is a limit in the wire sizes coming from structural limitations. During the measurements in the various flow fields, the wires will be stressed by the flow disturbance and the pressure buildup. The strain limitation of the wire material will consequently not allow for infinitely thin wires. From a manufacturing point of view, wires with smaller diameters below 100 µm are also more prone to form permanent bends while crafting the sensor which will be more susceptible for breaks. In previous works, like Prasser et al. [82], Betschart et al. [40], or Ito et al. [83], a wire diameter of around 100 µm in their facilities lead to good results. Stainless steel, i.e. AISI 316L and AISI 304, is the material of choice as a good compromise between good soldering properties, low electrical resistivity, a relatively good elasticity reaction on strain stress and corrosion resistance in a wet environment. The lateral pitch in most designed sensors used in this work was around 3 mm, another compromise between hinderance of the flow, i.e. pressure drop, and spatial resolution. The axial pitch was kept as small as possible with a lower limit of half the lateral pitch. Most of the times, the axial pitch was a result of the sealing dimensions inside the facility to avoid leakage flow paths at the wire connection points to the data acquisition unit outside the facility.

Calibration of the raw data

Once the acquired conductance $u_{i,j,k}$ is measured and stored, is has to be calibrated to get the void fraction information $\varepsilon_{i,j,k}$ of each node *(i,j)* at the frame *k*. In the first work presented by Prasser et al. [78], the conversion was done by linear interpolation of the instantaneous conductance $u_{i,j,k}$ against the liquid and gas conductivity, u_{liquid} and u_{gas} respectively, as described in (2.1).

$$\varepsilon_{i,j,k} = 1 - \frac{u_{i,j,k} - u_{gas}}{u_{liquid} - u_{gas}} \qquad (2.1)$$

Given the fact that gases used in two-phase flow studies can be considered as electrical insulators and have a conductivity value very close to 0, leads to the simplification in (2.2).

$$\varepsilon_{i,j,k} = 1 - \frac{u_{i,j,k}}{u_{liquid}} \tag{2.2}$$

Later studies reported an overestimation of the bubble volumes due to an overestimation of the void fraction with the given calibration method. Sigrist et al. [84] proposed to use the theory of Maxwell to quantify the void fraction. In later works, George et al. [85] also described in their studies using electrical-impedance tomography the application of what they called the Maxwell-Hewitt relation (Maxwell [86], Hewitt [87]) which was derived for dispersed nonconductive media in a conducting phase. In a first step, the conductance of each node $u_{i,j,k}$ is normalized with the liquid conductivity value u_{liquid} as before, but forming the relative conductivity value $g_{i,j,k}$ as described in (2.3).

$$g_{i,j,k} = \frac{u_{i,j,k}}{u_{liquid}} \tag{2.3}$$

The Maxwell-Hewitt relation can be applied in a second step which yields the gas fraction $\varepsilon_{i,j,k}$ as a function of the normalized conductivity $g_{i,j,k}$ as stated in (2.4) for each node in the sensor plane.

$$\varepsilon_{i,j,k} = \frac{1-g_{i,j,k}}{1+\frac{g_{i,j,k}}{2}} \tag{2.4}$$

De La Rue and Tobias [88] reported that the Maxwell void correlation is only accurate up to 25 % void fraction. Beyond this value, the Bruggemann relation would be more suitable. Prasser et al. [89] performed studies on synthetic WMS data and concluded that using (2.4) yields good void and bubble size results down to the resolution limit of the wire-mesh sensor with a very good accuracy. The application of the Maxwell-Hewitt relation promises better results in detecting the bubble boundary, which lies at low void fractions and led previously to an overestimation of the bubble volume. The curves in Figure 5 illustrate both calibration methods graphically. The difference between both calibration curve is highest at 50% void and shows why the linear interpolation method suffers from too big void values at the bubble boundary.

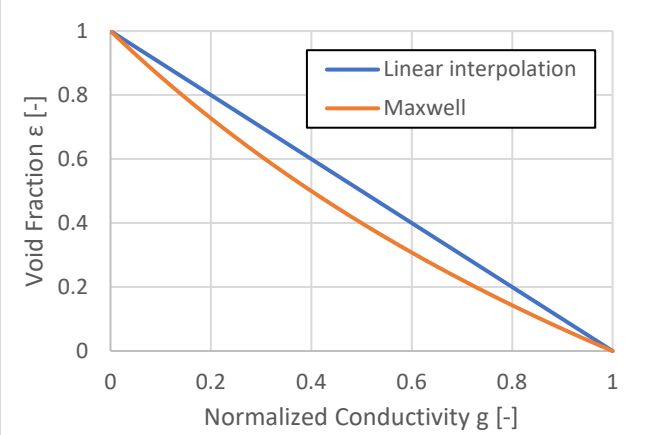

Figure 5: Comparison of linear interpolation vs Maxwell calibration method for normalized conductivity values between 0 and 1 using the linear relation and the Maxwell-Hewitt relation.

One of the bigger challenges in calibrating the data is obtaining the reference value u_{liquid}. Depending on the installation, a reference measurement can be taken by filling the facility with the liquid phase only. The mean value over the measuring time gives a robust result on the liquid conductivity. The drawback of this method is the assumption that the liquid phase does not undergo changes during the experiment, e.g. temperature decrease due to the forced evaporation from injected dry gas or variations of the dissolved gas in the water. Both phenomena can have an effect on the electrical conductivity of the liquid phase.

A more versatile approach is using the time histogram of each node to find the liquid reference value over a predefined sample time. This method comes from the digital imaging technique and is used there to discretize between background and the objects of interest. By using a time sample, a new liquid reference value is obtained after each sample window with the creation of a new histogram of the signal. This method was applied by Betschart [40] for the WMS analysis and showed a good behavior for many measurement conditions. Taking for instance Figure 6, the histogram indicates two distinctive peaks of the signal of node (32,32), the center node of the WMS of the ISOLDE test facility at PSI which will be described later. The first peak at 0 is an attribute of the gas phase which will grow with higher gas flow rates. The second peak gives the liquid conductivity value which varies from node to node. The reasons for the variation can be

manufacturing tolerances, e.g. slight shifts in the wire distance, the oxidation state of the wires or the aging of the data acquisition amplifiers. Thus, each node is calibrated with its own time series. If the fluctuations of the liquid conductivity were high, for example because of temperature changes or chemical reactions in the mass transfer experiments, the sample length was reduced to a minimum of 10'000 frames to get a decent statistical distribution and a high sampling of liquid references.

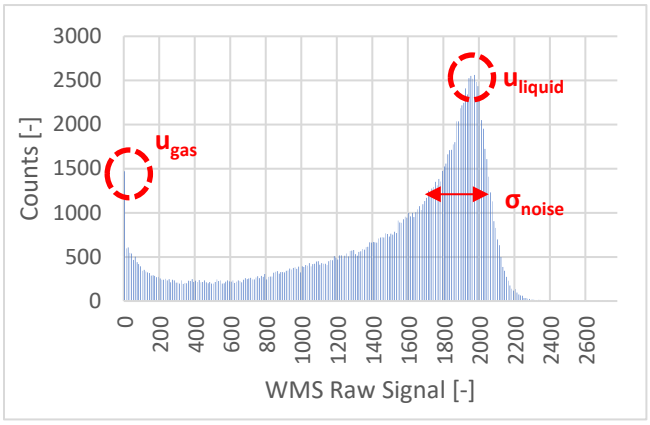

Figure 6: Signal histogram of the ISOLDE WMS at central node (32,32) with 150 ln/min injection flow rate and an injection nozzle of 6 mm inner diameter.

An additional preconditioning step was lately presented by Prasser et al. [90] to further take into account the electrical field disturbance at the bubble interface. The asymmetric distribution of the electrical current at bubble interfaces leads to so-called overshoots in the liquid phase. Overshoots are defined by showing a higher conducting value than the liquid reference conductivity, leading to a negative value in the void fraction calculation. In Figure 6, a part of the signal is clearly bigger than the liquid peak which is partially coming from this effect. The other effects are the distance disturbance during a bubble traversing through the sensor and electrical fields in the air (e.g. WiFi or cell phone signals) or a disturbed voltage pulse due to noise in the electrical grid.

The outcome of the work of Prasser et al. [90] was named overshoot compensation and deals with the relative conductance values $g_{i,j,k}$ as described in (2.3). An algorithm goes through the acquired measurement matrix and aims to find values that are bigger than 1.00. If a value is found, the 9 Moore neighbor cells in the same time frame are compared to find the void fraction value with the smallest $g_{i,j,k}$. Figure 7 is giving an example for a fictive 4x5 mesh array. The nodes (1,3), (2,2), (3,1) and (3,2) have relative conductance values that are above 1.0. The next step is to find the local minima. Taking the node (1,3) with a value of 1.1, the neighbor with the smallest conductance value is node (2,4) with a value of 0.55. The overshoot difference of 0.1 is now transferred to the cell (2,4).

	1	2	3	4	5
1	1.00	1.00	1.10	0.70	0.40
2	1.00	1.35	0.75	0.55	0.05
3	1.02	1.25	0.40	0.05	0.00
4	1.00	1.00	0.90	0.10	0.00

Figure 7: 4x5 mesh with overshoots at the boundary.

In Figure 8, the algorithm compensated all values above 1.0 that had a Moore neighbor with a value less than 1.0 with the described method. This is why cell (3,1) still lies above 1.0. Moreover, as exemplary described before, the cell (2,4) has a value of 0.65, taking the difference of 0.1 from cell (1,3). This fictive sample of a WMS segment does though not fully replicate real world conditions. The noise overlay of the sensor is not only coming from the electrical field distortion. For real measurement data, the values are corrected only above a defined noise threshold, e.g. if the noise is 5%, the values above 1.05 will be adjusted to the boundary of 1.05.

	1	2	3	4	5
1	1.00	1.00	1.00	0.70	0.40
2	1.00	1.00	0.75	0.65	0.05
3	1.02	1.00	1.00	0.05	0.00
4	1.00	1.00	0.90	0.10	0.00

Figure 8: Corrected conductance array with overshoot compensation.

With the corrected $g_{i,j,k}$, the data can be calibrated to void fraction data $\varepsilon_{i,j,k}$ with the Maxwell-Hewitt equation as derived in (2.4). At this point, the bubble recognition and bubble reconstruction could be initiated to gather the information on bubble volumes and surfaces. To improve the robustness of the recognition and the reconstruction algorithm, a last preconditioning step has to be performed. As mentioned before, the noise signal which is received as well, will deform the void fraction data. The symmetric filter which was presented in the studies of Betschart [40] was further improved with a phenomenon observed in the data.

Signal Filtering Technique

The easiest way of filtering data would be to define a low threshold value, e.g. 5%, and replace all the values below this threshold value with a void fraction of 0%. This method will artificially decrease the bubble size since the bubble boundaries can have low values that are close to the threshold value. The next step which was adapted in Betschart [40] would be to define a threshold value and check also the values of the von Neumann neighbors. If one of the neighbors has a value that is significantly higher, it belongs to the bubble and is not altered. Otherwise, the value is set to 0% as before. This method, the so-called symmetric filtering method, works very well for measuring conditions with noise levels up to 10%. There are though cases, which were observed in the TRISTAN facility and will be presented in Section 3.2, where the wires are spanned over 0.5 m of channel width. At very high turbulence, the wires start to oscillate in the flow and lead to overlaid noise signals of more than 30%. Applying the symmetric filter would remove smaller bubbles that have relatively small void maxima and shift the bubble size distribution towards bigger bubbles.

The final method, which was used in this work, is an adapted version of the symmetric filter. As before, the von Neumann neighbors of the measuring points that are smaller than the defined noise threshold are being considered. In the new version of the filter, the absolute difference of each neighbor to the reference cell is obtained. If the difference is smaller than a predefined differential threshold, the value is being set to 0% void. Otherwise, it is assumed that the cell belongs to a bubble in the field. This method is very effective against synchronic wire vibrations. A decent differential threshold is enough to eliminate a void plateau of noise values independent of their effective void value.

The determination of the noise threshold is an important step in this procedure. The value is used for the symmetric differential filtering but serves also as the threshold for the recognition algorithm. As marked in Figure 6, the standard deviation of the second peak σ_{noise} is calculated. The threshold for the bubble boundary ε_{tr} is set to 1.5 times the standard deviation σ_{noise} with the value σ_{noise} being capped at 30 %. The differential threshold for the filter is defined as 3/4 of ε_{tr}. These values were found empirically with the various data sets from the facilities and turned out to be quite robust in their application independent of the used sensor or facility.

Figure 9 illustrates the above described calibration, overshoot compensation and symmetric differential filter methods on a frame of a 12 mm oblate bubble. At this stage, the void data is ready and preconditioned for the bubble reconstruction where the connected void elements are labeled as an independent bubble to determine the size and interface.

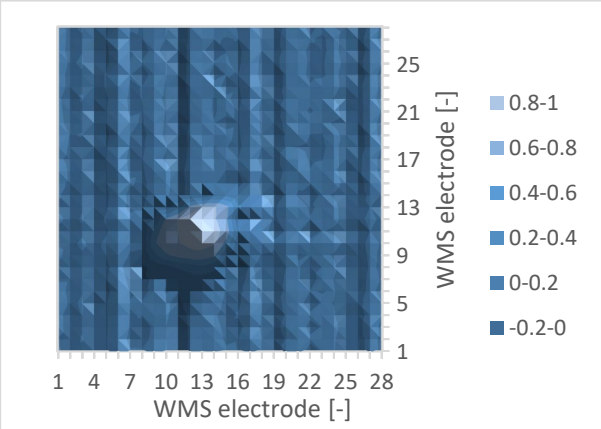

a) Raw void data calibrated with Maxwell-Hewitt

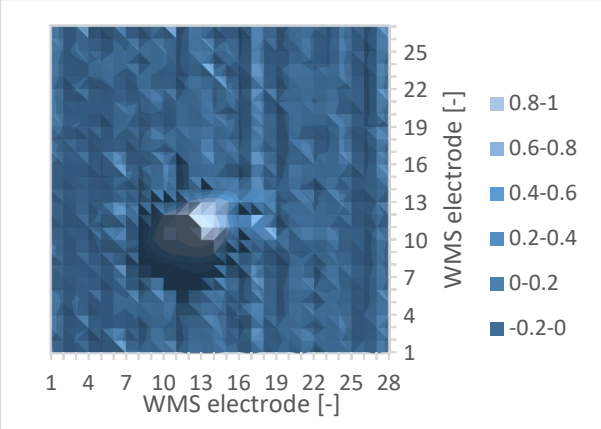

b) Void data with overshoot compensation

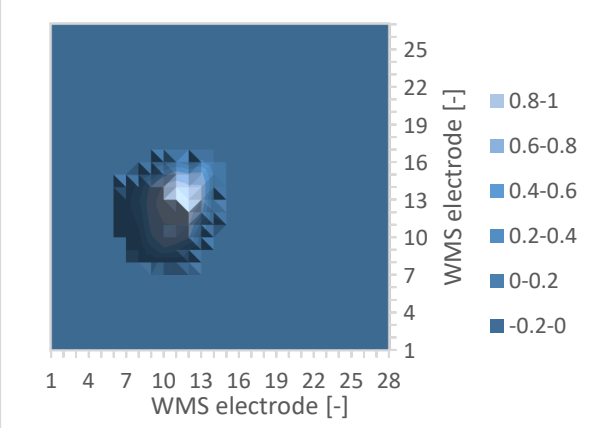

c) Void data with overshoot compensation and symmetric differential filter

Figure 9: The three different calibration steps for a bubble in a 28x28 WMS with 1.5 mm pitch and a superficial velocity of 0.4 cm/s.

Methodology of the bubble reconstruction

The algorithms used for the bubble recognition and reconstruction have been documented in Prasser and Beyer [91] and Brankov [92]. The first step is to create a new measurement matrix that holds the bubble ID values. The bubble IDs are assigned with the extended decremental recursive flood fill algorithm as specified in the work of Prasser and Beyer [91]. The algorithm iterates through the measurement matrix until the void of a cell (i,j,k) $\varepsilon_{i,j,k}$ exceeds the noise threshold value ε_{tr} previously described for the filtering. As a next step, the process starts searching for the maximum void within any interconnected void fraction that exceeds the threshold value $\varepsilon_{tr.}$ Starting from the maximum void in the bubble, the extended decremental flood fill checks its neighboring cells for voids smaller than the maximum and bigger than ε_{tr}. If a neighbor is found at a certain instance that has a higher void fraction, the flood fill is stopped. This mechanism makes sure that two bubbles that are very close to each other are not accidently unified. Once the initiated flood fill of the neighboring bubble is running, the process compares the stopping value, the assumed bubble boundary, with the smaller of the two void maxima of the two apparent bubbles. If the difference between the bubble boundary and the smaller void maximum is smaller than the differential threshold value $\Delta\varepsilon_{tr}$, the two bubble IDs are merged. This last step addresses the issue that arises from the noise signal inside the bubble that can create an artificial local plateau. According to Prasser and Beyer [91], the differential threshold $\Delta\varepsilon_{tr}$ should be selected as double the threshold value ε_{tr} for noise levels less than 15%.

The further processing, the bubble reconstruction, rebuilds the bubble interface by using an arc interpolation scheme as presented in the work of Betschart [40]. The bubble interface boundary is initially set to 50%. The reconstruction algorithm interpolates with three-point arcs a circumference for each frame and point of each bubble. The sum of all areas enclosed by the perimeter multiplied by the height of each frame, i.e. 1 frame, should be equal to the volume determined by summing the void fractions of the same bubble ID. If not, the bubble boundary value is adjusted to a bigger or smaller value depending if the found volume was too big or too small with a bisection

method. This step is repeated until the two volumes, the total sum of the voids and the calculated volume by the arc reconstruction converge. With the final value, the interface can be estimated by calculating all the circumferences P_i from each frame of the same bubble. The correction of the units from electrodes and frames to the WMS typical [mm²s] is resolved in the final step with the wire pitch and the framerate before storing the values.

Betschart [40] used the truncated cone approximation which is drawn schematically in Figure 10. The expressions for calculating the volume and interphase of two consecutive frames with perimeters P_1 and P_2 and the areas A_1 and A_2 are described in (2.5) and (2.6) respectively. The height of the cone is represented by h_{cone}.

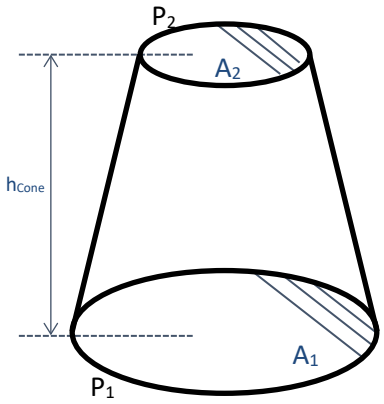

Figure 10: Schematic of the truncated cone approach as seen in the work of Betschart [40].

The benefit of the cone approximation is a good accuracy as it takes the tilt of the two consecutive areas of the surface into account but it comes at a higher computational cost. The height h_{cone} is depending on the bubble velocity v_{bub} (2.7) and cannot be factorized out of the equation (2.6) for the estimation of the bubble interface. Each perimeter P_i would need to be stored separately and converted in a much later step with the height h_{cone}, i.e. after the bubble velocity calculation.

$$V_{cone} = \frac{h_{cone}}{3} * (A_1 + \sqrt{A_1 * A_2} + A_2) \quad (2.5)$$

$$A_{cone} = \frac{P_1+P_2}{2} * \sqrt{A_1^2 + A_2^2 + \sqrt{A_1 A_2} + h_{cone}^2} \quad (2.6)$$

$$h_{cone} = \frac{1\,frame}{f} * \frac{d_{axial}}{v_{bub}} \quad (2.7)$$

In the cylinder approach, the cone height h_{cone} is always exactly 1 frame long. The above seen volume and surface in Figure 10 would correspond to (2.8) and (2.9). A small error is introduced with this approximation but thanks to the high frequency of the WMS, the error is accepted for the gain in computational speed.

$$V_{cylinder} = h_{cone} * A_1 \quad (2.8)$$

$$A_{cylinder} = h_{cone} * P_1 \quad (2.9)$$

Using the simpler cylinder approach gives the possibility to sum up the perimeters P_i of each frame of a bubble and store the sum of the areas and the perimeters before converting them with h_{cone} to the proper bubble volume and bubble surface as shown in (2.10) and (2.11).

$$V_{bubble} = h_{cone} * \sum_i A_i \quad (2.10)$$

$$A_{bubble} = h_{cone} * \sum_i P_i \quad (2.11)$$

Bubble Velocity

The bubble velocity is an important parameter for the analysis of the WMS data but also for the velocity field characterization. Many works have studied methods to quantify the bubble velocity for each independent bubble [93, 94, 95, 96, 97]. The methods all rely on either using two consequent WMS or three-layer designs where two layers receive simultaneously the signal of the transmitter layer between them Even with the information of two different layers, the difficult part lies in finding the same bubble on both WMS layers. The intrusiveness of the sensor disturbs the bubble shape when traversing the first layer. In case of small bubbles or low liquid recirculation flow rates, the bubbles can change their shape. A shape shift might lead to a relocation of the calculated center of mass which can lead to an artificially high bubble velocity. Ito et al. [83] used a three-layer WMS and two cross-correlation calculations, one coarse and one fine to obtain the bubble velocity. In their comparison with high-speed camera observations upstream the sensor, the WMS lead to a deceleration of the bubbles at the sensor position for liquid superficial velocities below 0.5 m/s and to an acceleration of the bubbles above 0.8 m/s as highlighted in Figure 11. Thus, a discrepancy between the observed oblates by high-speed camera and the WMS was expected. The bubble count on the first

and second layer also showed the expected bubble fragmentation which makes a bubble assignment between both layers difficult.

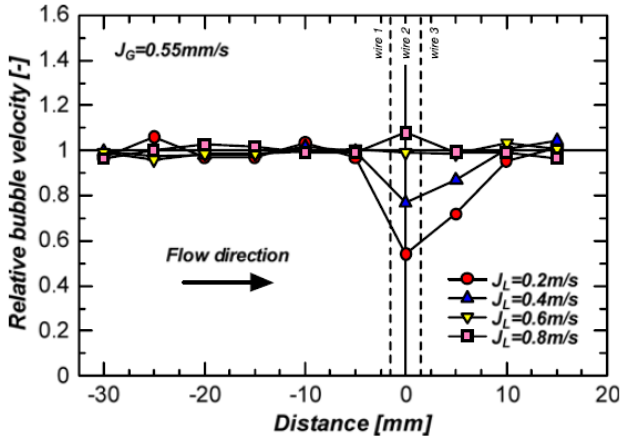

Figure 11: Intrusive effect of the WMS on the bubble velocity as seen by Ito et al. [83]

Kanai et al. [96] used two consequently installed WMS and a cross-correlation algorithm on the void fraction data to get the phasic gas velocity in the two-phase flow field. Furuya et al. [98] continued to improve this algorithm to get individual bubble velocities. They identified all bubbles on both WMS and estimated the volume of each bubble. Within a predefined time span, the volume change index was calculated for each bubble pair, which is the relative difference between the volumes. The two bubbles with the smallest difference in volume on both layers were matched together and the velocity calculated. The index was capped to 20% where the bubbles were then discarded from the analysis. No statistics were given on how many bubbles were not considered in the analysis if no matching bubble was found on the second layer. While empirically trying to find a good method for the determination of the bubble velocity within the previous mentioned, the best one working in stagnant pool conditions was a modified version of Ito et al. [83].

After identifying all bubbles on the first layer, the void fraction data of both layers are used for cross-correlation. At the WMS node of the center of mass of each bubble, e.g. of a bubble lying on coordinate (*i,j,k*), the void data is cross-correlated on both layers within a time window, i.e. (*i,j,k-dt*) to (*i,j,k+dt*). If the cross-correlation does either not yield anything or the value is higher than twice the gas injection velocity, the average gas phase velocity is assigned to the bubble. So far, this method showed good results for a time span *dt* of 100 times the frame length of each individual bubble. The individual bubble velocity is required to translate the bubble volume V_i* [mm^{2}s] to V_i [mm^3] and the bubble interface A_i* [mms] to A_i [mm^2]. The equivalent bubble diameter d_{eq} is later on calculated by the bubble volume V_i, assuming spherical bubbles as shown in (2.12).

$$d_{i,eq} = \sqrt[3]{\frac{6\,V_i}{\pi}} \qquad (2.12)$$

The equivalent bubble diameter has been used in many works and is an efficient parameter to create comparable bubble size distributions.

Interfacial Area Density

One of the strengths of the WMS is the recognition of the bubble interface, which leads to well estimated interfacial area densities. There are two basic approaches to obtain the area of gas-liquid interphase from primary measuring information coming from wire-mesh sensors. The first one published by Prasser [99] uses a reconstruction of the bubble boundary from corner points found by comparing the local instantaneous void fraction with a threshold. This can be done in a number of different ways, e.g. in the 2D geometry of each recoded frame with a successive extension to the third dimension perpendicular to the measuring plane or directly in 3D. There are also different options in approximating the bubble boundary, such as linear or curved lines or surfaces as documented by Brankov [92]. Later on, Prasser et al. [100] proposed a so-called gradient method, which is based on the fundamental concept of the local instantaneous interfacial area density being equal to the gradient of the phase indicator function. On the finite resolution of the measuring grid of the wire-mesh sensor, this can be approximated by a void fraction gradient calculated with a differential stencil. This method is not yet fully established. It has been validated so far against artificial wire-mesh sensor data. The method has been used only preliminary with real data, as validation in the different flow regimes requires a reference technique, which was not available. Two more issues would be faced relevant to this work. First, it also suffers on the difficulty to determine the void

fraction gradient in flow direction which once more has to be converted from a difference of void fractions related to a time interval between successive frames by a quantity that is related to an axial distance, for which a bubble velocity has to be known. Second, the gradient method did not perform very well in the region with bubbles that had the size of the lateral wire pitch or less. As it later turned out in many of the experiments, this was often the case with the designed WMS.

The work of Prasser [99] suggested to convert the interfacial area into the interfacial area density using the approximation presented in (2.13). The summed up interfacial areas A_i of all measured bubbles are divided against the total volume in the facility, i.e. the measuring time t_m multiplied with both summed superficial velocities j_L and j_G and the cross-section area A_{fch} of the test channel.

$$a_{tot} = \frac{\sum_i^n A_i}{t_m * A_{ch} * (j_L + j_G)} \tag{2.13}$$

In this work, many experiments were performed with quasi zero or zero liquid circulation. Assuming no liquid circulation in the facility, the expression (2.13) would become (2.14) with V_{liquid} being the collapsed level volume of the liquid.

$$a_{tot} = \frac{\sum_i^n A_i}{t_m * A_{ch} * j_G + V_{liquid}} \tag{2.14}$$

With a longer measuring time, the volume of the liquid would have less weight in the denominator and would thus falsify the results. A different approach was required and developed to get better accuracy for low liquid circulation experiments. The total average interface present in a column at a given time can be estimated by (2.15).

$$A_{tot} = \frac{1}{\mathrm{t_m}} \sum \tau_i A_i \tag{2.15}$$

The measuring time t_m is scaling the sum of all interfaces A_i which are present during the time window τ_i. The time τ_i can be derived with the height L_{ch} of the facility and the bubble velocity v_i to $\tau_i = L_{ch}/v_i$. Inserting this modification into (2.15) leads to (2.16).

$$A_{tot} = \frac{1}{\mathrm{t_m}} \sum \frac{L_{ch}}{v_i} A_i \tag{2.16}$$

The interfacial area density is defined as the total bubble interface divided by the total volume of the two-phase mixture. The total mixture is the height L_{ch} multiplied with the cross-section A_{ch} of the channel. Thus, the interfacial area a_{tot} can be calculated using (2.16) to obtain the total interface and the facility dimension for the total volume, hence forming (2.17).

$$a_{tot}[1/\mathrm{m}] = \frac{\mathrm{A_{tot}}}{\mathrm{L_{ch} A_{ch}}} = \frac{1}{t_m L_{ch} A_{ch}} \sum \frac{L_{ch}}{v_i} A_i \tag{2.17}$$

Assuming that the bubble velocity does not change during the transition through the sensor, the interfacial area of the bubble is defined as the product of the WMS derived interface A_i^* multiplied with the bubble velocity v_i (2.18).

$$A_i = \mathrm{A_i^*} v_i \tag{2.18}$$

Using (2.18) in (2.17), the height L_{ch} is canceled out and the value A_i^* can be directly used as shown in (2.19).

$$a_{tot} = \frac{1}{t_m * A_{ch}} \sum_i^n A_i^* \tag{2.19}$$

The new proposed method (2.19) is computationally a very cheap solution. The need of the bubble velocity for the interfacial area density is no longer given and according to (2.11), the total sum of all perimeters P_i of the bubbles will suffice to quantify a_{tot}. Furthermore, it should also work at conditions with an induced superficial liquid velocity.

Benchmark of the methodology using artificial data

New analytical methods need to be validated against reliable data to verify their performance or be compared against the same data analyzed by another established measuring technique. In case of the WMS, the works of Clifford et al. [101], Prasser [99] and Simiano and Prasser [93] have demonstrated how to create synthetic WMS data by solving the electroquasi-static approximation of the electric field equations in a charge-free environment (2.20) for predefined bubble sizes where σ is the electrical conductivity and φ is the electrical potential.

$$\nabla \cdot (\sigma \nabla \varphi) = 0 \tag{2.20}$$

The bubble is virtually pushed through a sensor with a known velocity, i.e. 100 mm/s to create conductivity values for each slice with a sampling frequency of 1000 Hz. Stacking all the slices results in the known 3D matrices with the x and y axis as the lateral and the z axis as the temporal axis.

In the WaterLoop facility at ETH Zürich and the ISOLDE facility at PSI, the lateral pitch of the sensors was designed to be 3.0 mm whereas the TRISTAN facility has a lateral distance of 3.4. Since the sensor of TRISTAN was already studied by Betschart [40], the virtual data had a lateral distance of 3.0 mm in a 6 x 6 array. The axial pitch was set to 3.5 mm as in the ISOLDE sensor, which is the most limiting for small bubble sizes compared to the 1.5 mm of the WaterLoop sensor or the 2.0 mm of the TRISTAN sensor. The artificial bubble size distribution was uniform between 0.5 and 4 mm. The bubble radii were rather small considering the flow regime of interest being the churned-turbulent region with big gas volumes. A previous study of Prasser et al. [82] has shown that bigger bubbles that are at least two wire pitches in diameter are less of an issue to be properly detected by the sensor than the ones that are about a wire pitch in diameter. Thus, the aim of this data set was to study the lower end recognition quality of the sensor and the analytical methodology. Furthermore, it is quite challenging to create artificial data for slugs or churn-turbulent bubble fragments, which would require additional efforts in modeling and presumably the support of CFD. So, for this work, three independent data sets were generated. Perfect spherical bubbles, oblate spheroids with the axial semi axis c being half of the lateral axis a and ellipsoid spheroids with the lateral semi axis b being half the size of the other two equal axes a and c as depicted exemplary in Figure 12.

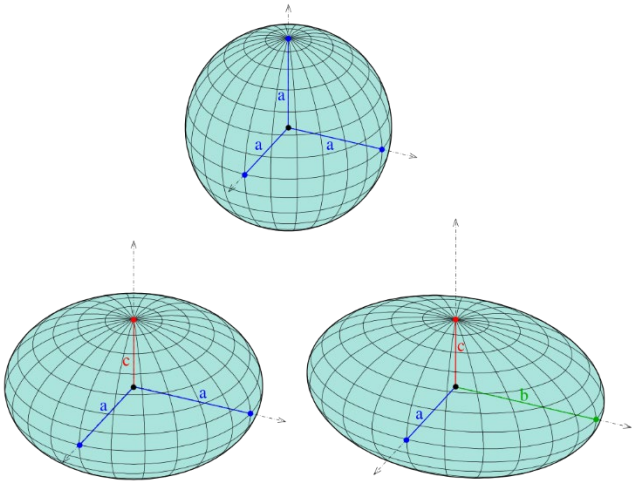

Figure 12: A sphere, an oblate spheroid and an ellipsoid spheroid with the semi axis as presented in wikimedia [102].

The data was analyzed with the new proposed algorithm. In the output file of the analyzed data, 80 % of the spherical bubbles, 78 % of the oblate spheroid ones and 72 % of the ellipsoids were recognized. In a second step, the bubble velocity was calculated with the aforementioned methodology. Since the bubble velocity is needed to determine the bubble volume and its surface, it has a big impact on the obtained quantities and their uncertainty. Hence, the first quantity to be examined is the bubble velocity of the three data sets. Figure 13 shows the bubble velocity statistics of the different spheroids. The recognized spheres and oblates show a good statistic with a mean value of 88 and 90 mm/s respectively, which is roughly 10% off the real value. The ellipsoids performed worse which required some further investigations.

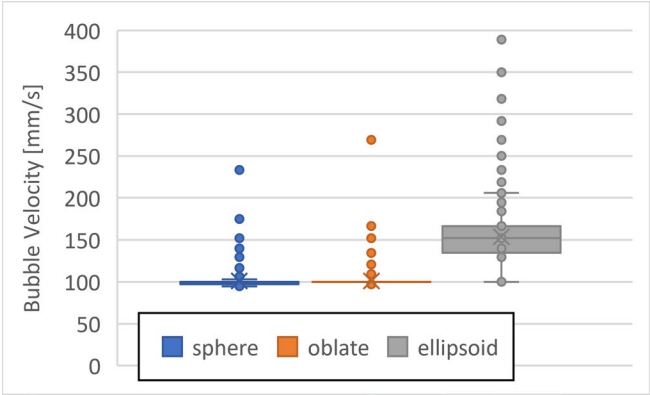

Figure 13: Bubble velocity statistics of the three artificial data set with the 25th and 75th percentile as box boundary and marked outliers.

The probability to detect a bubble as an entity as displayed in Figure 14 is 100 % for bubble radii down to 2 mm, which would correspond to 2/3 of the wire distances. For smaller bubbles, it decreases progressively, whereby the oblate spheroid bubbles suffer a bit more from their small extension in axial direction, which is half of the height of the spherical bubbles. The big axial distance between the electrode planes is showing here its weakness. However, it is surprising that still 80 % of the spherical bubbles of 1 mm diameter are detected. Almost none of the bubbles are detected for the bubble sizes of 0.5 mm. At this size, the spheres and ellipsoids are still relatively well detected but the oblates again underperform, this time significantly. Note that the term “detection” is here the ability to identify the bubble, which does not tell

anything on the achievable accuracy of the bubble size and surface measurements.

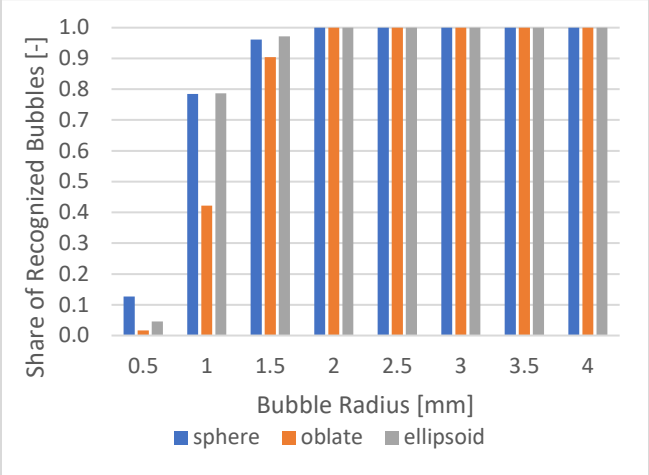

Figure 14: Recognition limitation of the designed WMS with 3 mm lateral and 3.5 mm axial pitch at different bubble radii with the presented data analysis for the three artificial data sets – spheres, oblate spheroids and ellipsoids.

The average quality of the hydrodynamic parameters of the bubbles is summarized in Table 2. Each quantity of every recognized bubble, i.e. the bubble volume, the bubble surface and the bubble radius, are compared against the input parameter of the artificial data generation. The thereby created relative values are in second step averaged over all recognized bubbles. The interfacial area density is obtained using (2.19) and compared against the total interfacial area density of the input data.

Table 2: Average reconstruction quality of artificial WMS data sets comparing interfacial area density (IAD), bubble volume, bubble interfacial area and bubble radius with standard deviation against the real values.

	IAD	**V_{bub}**	**A_{bub}**	**R_{bub}**	**σ_{Rbub}**
Sphere	1.11	1.11	0.97	1.02	0.09
Oblate	0.98	1.37	0.95	0.83	0.12
Ellipsoids	0.76	1.58	1.34	0.89	0.19

The spheres and oblates show a very good recognition performance with offsets of up to 17 % except for the volume of the oblates. The interfacial area density achieves an even smaller deviation of 11 %. The radius is underrated for oblates and agrees better for the other two with good standard deviation values. The ellipsoids show here a small weak spot in terms of bubble volume and interface. This has mostly to do with breaking up the signal of one bubble into multiple fragments if the signal was too weak.

The evaluated bubble radius is compared with the effective radius in Figure 15. The comparison reveals a good agreement for all the bubbles with a radius that lies between 1.5 mm and 2.5 mm. The bubbles bigger than 2.5 mm are showing a trend to be underestimated within a small uncertainty. The constant underestimation can be explained by the bubble velocity. The reconstructed bubbles are multiplied with a bubble velocity that is roughly 10 % below the artificially set velocity, leading to 10 % less bubble volume and thus to 5 % less bubble radius. It is therefore necessary to work on getting a higher accuracy in the determination of the bubble velocity.

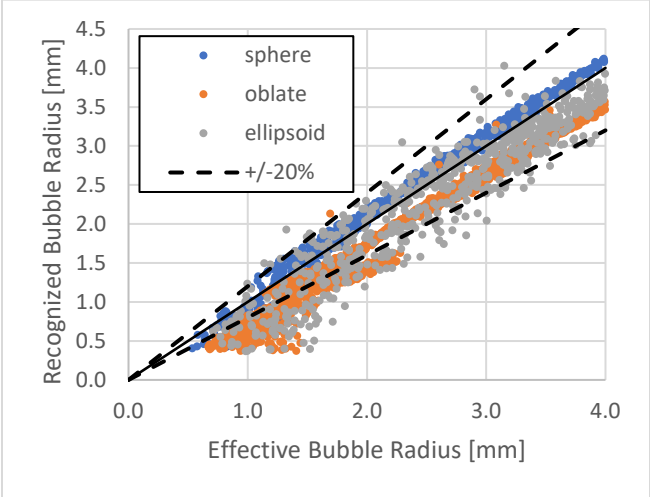

Figure 15: Recognition limitation of the data analysis in terms of bubble radius and an uncertainty of ± 20%.

The reason for the bad detection of small bubbles can be found in Figure 16. The data points depict the maximum instantaneous void fraction sampled during the passage of each individual bubble for different bubble sizes as it was presented in Richter et al. [103] and in Betschart [40]. A first theoretical explanation is given by Prasser and Beyer [104]. The maximum void in small bubbles is decreasing with size as expected, leading to bubbles with less than 1 mm radius having a peak void signal of 10%. This comes very close to the filtering threshold. At 20 %, double this boundary, the bubble radius is found to be 1.5 mm. With the presented methodology and a mesh with 3 mm lateral and axial pitch, the lowest detected bubble sizes with good

confidence are at least 1.5 mm in radius. It is worth noting that the large scatter of the data in this figure is due to the effect of the position of the bubble with regard to the electrode wires. A bubble hitting a crossing point of wires generates a larger signal amplitude, whereas a bubble flowing through the mesh between the electrode wires causes only a small decrease of the measured conductance.

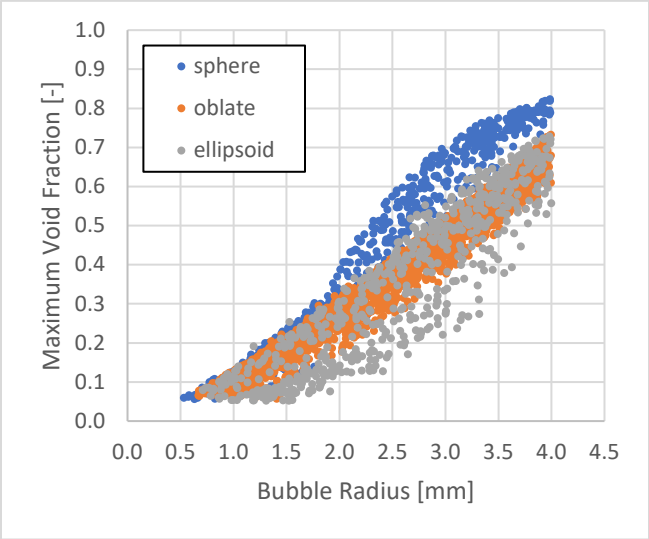

Figure 16: Maximum void of the artificial spheres and oblates as recognized by the presented WMS analysis.

Benchmark of the methodology using facility data

Another way to bench an updated algorithm is to use it against a data set with known parameters. In the comparison work of Baur [105], a small data set was recorded with a denser sensor array. This 3-layer WMS was designed with wires of only 50 µm thickness with a lateral and axial distance of 1.5 mm and an array size of 28 x 28 electrodes. The aim was to compare WMS data with high-speed camera recordings as it was done earlier in Prasser et al. [82] to further develop the gradient method with small electrode distances. The construction of a WMS with wires this thin and a good optical access was achieved by sacrificing on the endurance of the sensor. Thus, only three reliable measurements in the test matrix were generated with oblate spheroids as exemplary displayed from a high-speed camera image in Figure 17. The superficial liquid velocity was constant for all three signal samples at 0.5 ± 0.05 m/s.

Figure 17: High-speed camera greyscale image of oblates passing through a 3-layer 28x28x28 WMS from the work of Baur [105].

The induced liquid velocity was required on the one hand for the optimal operating point of the WMS and the bubble formation at the nozzle. As mentioned earlier, the work of Ito et al. [83] has shown that the bubble velocity stays the most constant through the wire-mesh at liquid flow rates around 0.6 m/s. The liquid velocity also helps to induce a constant bubble breakaway at the nozzle and thereby form uniform sized bubble volumes which allowed keeping the determination of the average bubble volume relatively simple. Since the gas flow rate, the bubble count and the bubble formation time were all known parameters, the average bubble volume could be derived. To verify the uniformity of the sizes, the bubble generation at the nozzle was observed and analyzed with high speed shadowgraphy as illustrated in Figure 18. The two images show one binarized bubble in the creation process attached to the nozzle. On the second image, the bubble detached and started flowing upwards in the image direction.

Figure 18: HSC shadowgraphy at the inlet nozzle before and after bubble breakaway from the work of Baur [105] after binarization.

If the bubbles are to share same volumes, the time difference between two rip-offs of two bubbles at the nozzle should be the same. For the determination of the bubble generation times, the binarized shadow images as presented in Figure 18 were analyzed. The circularity of the white area could be estimated for each bubble at the nozzle for each frame. Plotting the time dependency of the circularity revealed a sharp increase of a factor of at least three in value immediately after detachment as plotted in Figure 19. The time between two of those peaks indicates the bubble generation time at the nozzle tip with the given gas flow rate. Therefore, the bubble volume can be deduced by measuring the generation time and multiplying it with the volumetric flow rate.

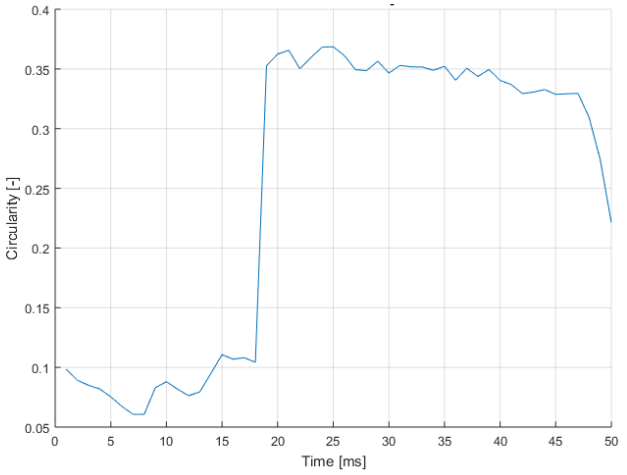

Figure 19: Bubble breakaway at the nozzle at the WaterLoop facility at ETH from the work of Baur [105].

The maximum measuring time of the used high-speed camera was 2 seconds at a measuring frequency of 2500 Hz. The statistical values of the estimated time between two rip-offs for each measurement as well as the implicated average bubble volume and the standard deviation are summarized in Table 3. The slightly higher standard deviation for the lowest gas flow rate is most probably a result from the lower end limitation of the mass flow controller. The flow area of the mass flow controller is almost closed, leading to nervous controlling behavior to keep the flow rate constant.

Table 3: Measured bubble generation times with high-speed shadowgraphy at the gas nozzle inlet and the calculated bubble volume.

Gas Rate [l_n/min]	Mean Generation Time [ms]	Estimated Volume [mm^3]	Standard Deviation [%]
0.25	33.12	148.1	5.25
0.4	30.65	219.3	3.56
0.55	28.92	284.5	3.18

Since the bubble volumes were constant within a good margin, the average bubble velocity had to be the same constant for all bubbles. The bubble volumes derived from the WMS, V_i* with the unit [mm^{2}s], had very small deviations among each other with a standard deviation of 3 % and less. The total gas volume corresponds to the number of recognized bubbles times the average volume of a bubble at the given gas flow rate. The total gas volume can then be divided by the sum of all bubble volumes V_i*, consequently giving an average bubble velocity for all bubbles. The average velocities for the gas flow rates of 0.25 ln/min, 0.4 ln/min and 0.55 ln/min would correspond with this approach to 1270 ± 40 mm/s, 1190 ± 25 mm/s and 1152 ± 9 mm/s respectively. The supposed deceleration of the bubble velocity with increasing size is a product of the pump that was set to a constant frequency and not to a constant flow rate. The liquid flow meter showed deviations of ± 0.5 l/min at a flow rate of 93 l/min.

The bubble velocities determined by cross-correlating sensor signals and their statistics are shown in Figure 20. The values are within bounds of ± 100 mm/s except for the highest flow rate that is within bounds of ± 150 mm/s. For the two higher gas flow rates, i.e. 0.4 ln/min and 0.55 ln/min, the average gas velocity and the analyzed velocities from the WMS data overlap with their uncertainty areas with the WMS lying slightly below the average gas velocity. For the lowest gas flow rate, the average velocity lies even above uncertainty range. The reason for the poor performance at this flow rate could be a combination of the mass flow controller as it also had the highest standard deviation in the bubble generation times with the effect of the liquid recirculation.

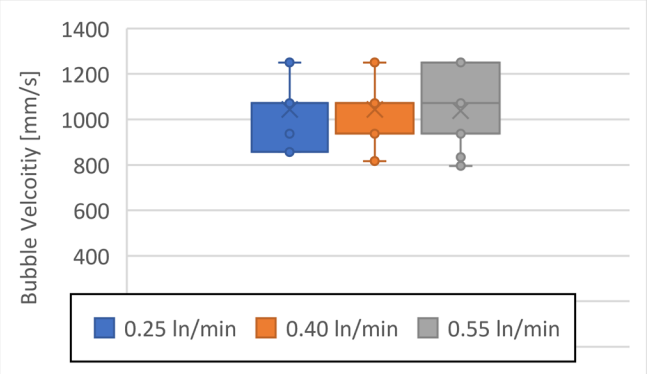

Figure 20: Statistics of the bubble velocities of the three different flow rates at the WaterLoop facility with the 25th and 75th quartile as box boundaries.

The aforementioned estimation of the number of frames used for the cross-correlation was found empirically. In Table 4, the three frame lengths that produced the most reasonable results are shown. Below 2000 frames, the bubble size distribution was distorted and above 3000 frames, the average gas phase velocity was mostly used. The Sauter-mean diameter (d_{32}), which is an important parameter in modelling in heat and mass transfer, and the ratio of the total recognized bubble volume to the injected gas volume were used as validation parameters. The average bubble volume was also used as a check parameter. While performing the calculation, a minor dependency was observed on the number of frames the bubble was visible in the WMS data and the additional frames required for a good cross-correlation of the signal. The choice of the number of frames in which the interrogated bubble is present, multiplied by a factor of 100 seemed a good compromise.

The bubble sizes could now be obtained with the calculated bubble velocity. The bubble size distributions in Figure 21, with the average bubble radius marked for each flow rate, show an underestimation of the average radius measured by the WMS. The underestimation is between 4 and 7 %. The size distributions also show for 0.55 ln/min that a couple of smaller bubbles broke off and create a very small bump at around 3 mm which could be observed too in the high-speed camera recordings and the raw data of the WMS. The widening of the size distribution is mainly contributed to the bubble velocity estimation since the bubble volumes V_i* determined by the WMS show a finer peak. The correct estimation of the bubble velocity has a strong impact on the accuracy of the results and should be further improved in future research.

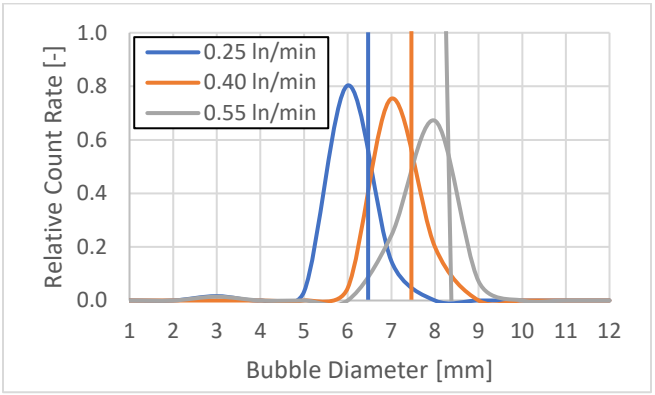

Figure 21: Bubble size distribution of the three gas flow rates with indicators (vertical lines) for the average bubble volume based on the rip-off times.

Tompkins et al. [106] also focused on collecting existing research literature and estimate the uncertainty of the WMS. The multiple calculation steps to get to the bubble size make an error propagation calculation starting from the primary conductance values very difficult. Nonetheless, with all the data and research he was able to assess, certain boundaries could be

Table 4: Sensitivity study on the frame length of the void signal used to cross-correlate between both sensor layers

	0.25 ln/min		**0.40 ln/min**		**0.55 ln/min**	
Avg. Diameter [mm]	**6.56**		**7.5**		**8.16**	
	d_{32} [mm]	Recog. Volume [-]	d_{32} [mm]	Recog. Volume [-]	d_{32} [mm]	Recog. Volume [-]
2000 frames	6.26	0.84	7.26	0.89	7.80	0.87
2500 frames	6.23	0.83	7.27	0.89	7.87	0.89
3000 frames	6.20	0.82	7.26	0.89	7.86	0.89
100 · (frame length of bubble)	6.22	0.82	7.20	0.87	7.88	0.90

obtained. The void fraction for example was quantified with an uncertainty of 11 % compared to other instrumentation techniques throughout all flow regimes. For bubbles smaller than 1.2 the wire pitch, an uncertainty of 20 % was measured whereas for bubbles bigger than 2.4 times the wire pitch, the error lies within 10 %. These results, that were backed by Banowski et al. [67], suggested a liquid superficial velocity of at least 0.4 m/s and a gas mean velocity greater than 0.5 m/s for high accuracy bubble size estimations from the wire-mesh sensor. Still, they can be used as a basic orientation to get an idea of the error of the results in the following sections. Taking these boundaries together with the results from the synthetic data and the HSC comparison data of Baur, the uncertainty values can be summed up to the values in Table 5.

Table 5: Uncertainty qualification for bubbly flows using WMS sensor technology

	Upper Boundary	**Lower Boundary**
Interfacial area density	+ 11 %	- 24 %
Bubble Radius	+ 21 %	- 17 %
Bubble Velocity	+ 50 %	- 12 %
Void [106]	+ 11 %	- 11 %
Bubble Diameter [106]	+ 20 %	- 20 %

2.2 Droplet Measurements in Annular Flows

The methods that are presented in here were published by Breitenmoser et al. [107] with only the parts highlighted that are relevant for the FCVS Venturi design.

Looking into scrubbing activities, the bubble rise zone is not the only relevant area. As mentioned earlier, the near field of the injection nozzle needs also to be modeled, since it can be quite relevant for the retention of especially aerosols, but also gaseous radioactive compounds. In the jet regime of the nozzle or inside a Venturi scrubber for example, high retention values are achieved by intensive turbulent mixing, a high interfacial area density due to strong bubble breakup and ripples, if liquid films are present, whereby droplets become a very important element of further enhancement of the retention. As part of the flow characterization, the droplet size distribution is therefore relevant for a correct modelling and the successive code validation. The WMS is not a suitable instrument for droplet detection as they are formed in the sub millimeter region. Optical imaging methods have shown much better performances in this area of the two-phase flow research field. Based on the work of York et al. [108], analog high-speed photography was successfully applied to measure droplet sizes in Venturi scrubbers with liquid jet and spray injection by Atkinson and Strauss [109] and Roberts and Hill [110]. With the emerging of digital high-speed imaging and image processing, repeatability and reproducibility of droplet size measurements significantly improved, which allowed Gamisans et al. [111] to iterate their measurements to find a proper illumination for the measurement of droplet sizes with a CCD camera. The water film present at the throat wall of self-priming Venturi scrubbers makes the direct imaging analysis more challenging and requires some adaption of already existing image processing algorithms used for droplet size analysis of liquid jets and sprays, as presented by Blaisot and Yon [112], Fdida et al. [113], Lecuona et al. [114], Lee and Kim [115], Rezayat et al. [116] and W. Zhou et al. [117].

Droplet Size Description

In order to quantify the droplet sizes inside a commercial Venturi nozzle used for FCVS, an imagine analysis method was developed to determine the droplet sizes. In comparison with other optical techniques such as Phase Doppler Particle Analysis (PDPA) or Laser Doppler Anemometry (LDA), the direct image analysis is robust against multi-scattering effects. Inside the Venturi nozzle, a varying water film thickness between the light source and the imaging device would make the analysis with PDPA or LDA very cumbersome. Moreover, direct imaging offers two additional advantages regarding droplet size measurements. This method allows to capture not only spherical objects but any non-spherical shapes due to the direct visualization as shown by Lee and Kim [115]. Especially for large unstable droplets that according to Azzopardi et al. [118] can be present in Venturi nozzles, a non-spherical approach can result in a higher droplet size accuracy.

Furthermore, direct imaging provides a much larger dynamic range compared to the other two aforementioned methods, which is ideal for size distributions with high variance and skewness. However, given the available measurement equipment for this work, there is a limitation on the spatial resolution compared to the other techniques. The spatial resolution in this study is limited to 42 µm. With the laser diffraction technique, Alonso et al. [119] was able to detect droplets with an equivalent diameter of 6 µm.

The image preparation consists of three pre-processing steps to condition the data for an easier analysis. First, the raw grayscale images as seen in Figure 22 are binarized by Otsu's method [120]. After the binarization, bright spots are visbile in the center of bigger droplets which is where the light was reflected perpendicularly to the droplet surface. The second step, a filling operation, is carried out to remove these spots, as it can be seen in Figure 23a. To account for the depth-of-field effect, defocused droplets are in a last step removed by the gray-level gradient method as it was also performed by Lee and Kim [115]. The gradient threshold was set to 25% of the local maximum intensity, which was suggested by previous studies by Honkanen et al. [47]. A small section of an exemplary filtered and filled binarized image is shown in Figure 23b. It is worth mentioning that the depth-of-field effect will lead to a bias towards larger droplets. A thorough analysis of the various experimental uncertainties associated with the results of this study is added in the Appendix A.

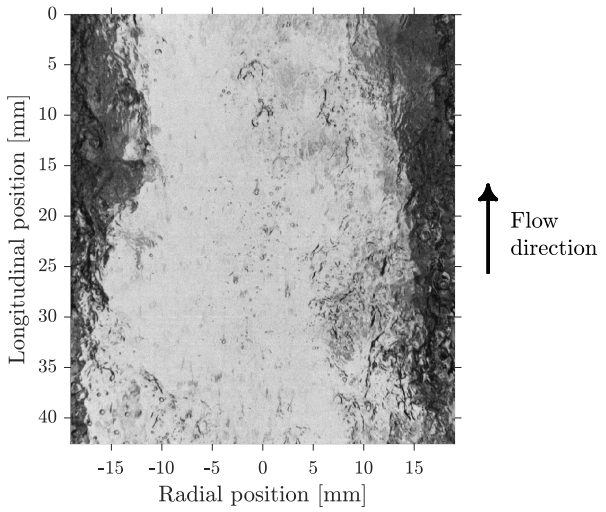

Figure 22: Raw grayscale image of the Venturi throat with the two liquid films (dark areas) at the two walls.

Droplet Detection Algorithm

In the binarized image section in Figure 23b, three different objects are visible. There are droplets that have been successfully filled by the filling operation in the image preparation step. Some of the bigger droplets are though not fully inside the depth-of-field and are therefore only binarized as open arcs. The last class of objects are large filament like objects caused by the water film at the wall of the Venturi throat. Because the bigger droplets are mostly open arc objects due to their big reflection spot in the center, both, the filled and the open arc objects have to be detected to avoid a bias towards smaller droplets. The goal of the droplet detection algorithm is to distinguish both droplet objects from the liquid film fragments and discard the latter ones. Based on the results by Altheimer et al. [121] as well as Honkanen et al. [47], the method follows an ellipsoidal approach, i.e. the droplet shapes are approximated as ellipsoids. Hence, the droplet recognition can be reduced to an ellipse detection. Due to the different morphologies of the described droplet shapes, an algorithm was developed separately for each shape in order to increase the effectiveness and efficiency of the algorithm.

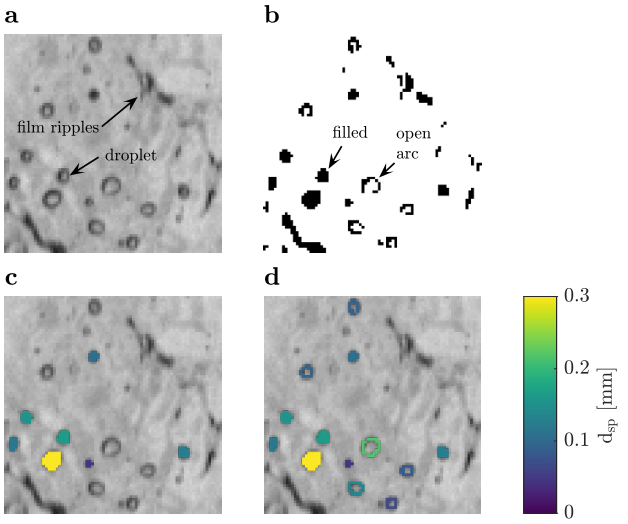

Figure 23: Droplet detection. (**a**) Raw grayscale image. (**b**) Binarized image including filling and gradient filter operations. (**c**) Detected droplets by the droplet detection module I including droplet sizes based on the equivalent droplet diameter (d_{sp}). (**d**) Detected droplets by both, the droplet detection modules I and II.

In the first detection module, a multivariate normal distribution fitting is applied to the labeled objects using the *regionprops* function provided by the image processing toolbox from MATLAB®. The toolbox determines the major and minor semi-axis a and b for each detected object by calculating the eigenvalues of the covariance matrix corresponding to the fitted normal distribution. Additional parameters such as the the eccentricity as defined in (2.21), the area, the extent and the solidity for each object are extracted as well. The area corresponds to the number of pixels of each object.

$$e = \sqrt{1 - \frac{b^2}{a^2}} \tag{2.21}$$

The extent of an object is defined as the ratio between the number of pixels of the object and the number of pixels contained in the smallest possible rectangular boundary box. The solidity is equal to the ratio between the number of pixels of an object and the number of pixels contained in the smallest possible convex hull approximated by a polygon. To discard the liquid film relics and the open arc objects, threshold values for each of the aforementioned parameter had to be set. As with the WMS data analysis, the selection of those threshold values is a trade-off between detection efficiency and droplet size accuracy. Due to the reduced dynamic range for very small droplets, the minimum area was set to six pixels. For an ideal ellipse, the extent and solidity are equal to $\pi/4$ and 1, respectively. However, because of the spatial discretization and morphological discrepancies, there are deviations from those values, especially for the smallest filled droplet objects. To account for these deviations, all numerical combinations with a minimum area of six pixels were analyzed and the thresholds were iteratively adapted to get reasonable droplet shapes considering the mentioned deviations.

In the second detection module, the least square fitting technique is used to detect the open arc objects and to extract the corresponding ellipses. The already detected filled droplet objects are first removed to not be counted twice. Similar to the first detection module, the area and eccentricity are extracted by the *regionprops* function to discard the film relic objects. In the next step, ellipses are fitted through each open arc object. The challenge of this second module is to reconstruct the ellipse from an open arc shape. A huge variety of different ellipse detection algorithms has been published in the literature in the past decades. Wong et al. [122] provided a review of the different ellipse detection techniques for images. The two main classes of techniques are Least Square methods (LS) and Hough Transform based techniques (HT). Due to its simplicity and low computational cost, the direct LS method developed by Fitzgibbon et al. [123] is applied. The last criterion was the computation of the root-mean-square error (RMSE) of the orthogonal distances between the object pixels and the ellipse fit for each object to obtain the goodness of fit as defined by Eberly [124]. Based on the RMSE, a threshold value of 0.5 pixel was selected to discard the fitted ellipses with large residuals. The droplets detected by the first two detection modules are shown for the already discussed image section in Figure 23c and d.

For the further droplet size analysis, similar to the analysis of the bubbles with the WMS, a volume equivalent diameter is defined for each detected droplet based on the extracted major and minor semi-axes. As the information in the third dimension, the third semi-axis c is not known, a spherical approach is chosen to reconstruct the third semi-axis. In contrast to a prolate

or an oblate spheroid approach as shown by Altheimer et al. [121], the spherical approach weights both semi-axes equally using the geometric mean as defined in (2.22).

$$c = \sqrt{ab} \tag{2.22}$$

The equivalent droplet diameter d_{sp} can be calculated based on the ellipsoidal droplet volume V_{eq} and the third semi-axis according to (2.22).

$$d_{eq} = \sqrt[3]{\frac{6V_{eq}}{\pi}} = \sqrt[3]{8abc} = 2\sqrt{ab} \tag{2.23}$$

In the context of mass transfer, surface area or volume-based probability density functions f_2 and f_3 are of most interest. Corresponding probability density functions can be estimated, following the expression (2.24) with n_i being the number of droplets in that size bin.

$$pdf_r(d_{eq}) \approx \frac{d_{eq}^r n_i(d_{eq})}{\sum_i d_{eq}^r n_i(d_{eq})} \tag{2.24}$$

Most of the collection efficiency models developed for Venturi scrubbers are based on a single representative droplet diameter even though Fathikalajahi et al. [125] have shown that a single parameter is not enough to describe complex droplet size distributions. Mugele and Evans [126] published a standardized formula to compute various mean diameters d_{pq} (2.25) such as the arithmetic mean d_{10}, the surface mean diameter d_{20} or the volume mean diameter d_{30}.

$$d_{pq} = \left(\frac{\int d_{eq}^p f_0(d_{eq}) dd_{eq}}{\int d_{eq}^q f_0(d_{eq}) dd_{eq}}\right)^{\frac{1}{p-q}} \approx \left(\frac{\sum_i d_{i,eq}^p n_i}{\sum_i d_{i,eq}^q n_i}\right)^{\frac{1}{p-q}} \tag{2.25}$$

In the context of collection efficiency models for Venturi scrubbers, the Sauter mean diameter d_{32} (2.26) is the preferred parameter due to its good representation of the volume to surface ratio of the underlying droplet size distribution, where V_{eq} and A_{eq} represent the equivalent volume and surface area, respectively.

$$d_{32} \approx \frac{\sum_i d_{i,eq}^3 n_i}{\sum_i d_{i,eq}^2 n_i} = \frac{6\sum_i^N V_{i,eq} n_i}{\sum_i^N A_{i,eq} n_i} \tag{2.26}$$

For droplet size distributions, various empirical probability density functions have been published. In this study, the empirical distribution published by Nukiyama and Tanasawa [127] has proven to be a good choice to describe the droplet size distributions in the presented Venturi scrubber with liquid film injection. This finding is agreeing with a systematic performance comparison of different empirical distribution models performed by Paloposki [128]. The Nukiyama-Tanasawa (NT) distribution (2.27) was presented by Nukiyama and Tanasawa in the context of a comprehensive study on liquid sprays.

$$pdf_0(d_{eq}) = \frac{\delta\theta^{\frac{3}{\delta}}}{\Gamma\left(\frac{3}{\delta}\right)} d_{eq}^2 e^{\left(-\theta d_{eq}^\delta\right)} \tag{2.27}$$

The probability density function is parametrized by the size parameter θ and the distribution parameter δ. The cumulative NT distribution function (2.28) can be derived by integrating the probability density function (2.24).

$$CDF_0(d_{eq}) = \frac{1}{\Gamma\left(\frac{3}{\delta}\right)} \Upsilon\left(\frac{3}{\delta}, \theta d_{eq}^\delta\right) \tag{2.28}$$

The gamma function Γ and the lower incomplete gamma function Y appearing in the distributions are defined as follows by (2.29) and (2.30) respectively.

$$\Gamma(y) = \int_0^\infty x^{y-1} e^{-x} dx \tag{2.29}$$

$$\Upsilon(y, z) = \int_0^z x^{y-1} e^{-x} dx \tag{2.30}$$

Based on equation (2.25), the descriptive mean diameters can be calculated analytically assuming a NT distribution and resulting in (2.31).

$$d_{pq} = \left(\frac{\theta^{-\frac{p-q}{\delta}} \Gamma\left(\frac{p+3}{\delta}\right)}{\Gamma\left(\frac{q+3}{\delta}\right)}\right)^{\frac{1}{p-q}} \tag{2.31}$$

For each measurement point, a nonlinear least square curve fit is performed using the NT distribution and the *fit* function provided by the curve fit toolbox from MATLAB®. One of the measurement points is exemplary plotted in Figure 24 with the number based probability function pdf_0 and the volumetric cumulative size distribution CDF_3. To account for the limited spatial resolution and the upper limit of the NT distribution model, only the experimental histogram data between the peak of the surface- or volume-based size distribution and the 99% percentile was used for the curve fit.

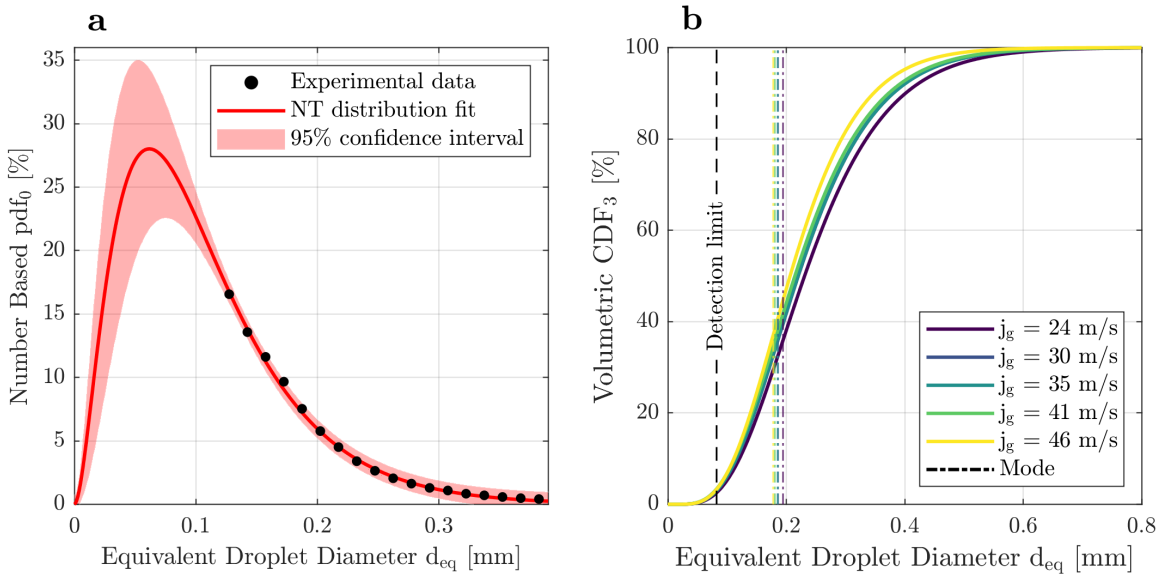

Figure 24: Distribution fit results. (a) Numerical fitting of the Nukiyama-Tanasawa (NT) number-based probability density distribution to the experimental data for the following exemplary operational conditions: j_g = 38.1 m/s, j_l = 0.335 m/s, H = 0.5 m. (b) NT volume based cumulative distribution function for a submergence level (H) of 0.5 m including the experimental detection limit and the analytical modes of the corresponding fitted NT volume-based probability density distributions.

In contrast to the empirical droplet size distributions, correlations for the Sauter mean diameter that were derived for Venturi nozzle scrubbers are scarce. One of the most extensively used correlations for Venturi nozzle was published by Nukiyama and Tanasawa [129] based on experimental data obtained by liquid spray experiments. The correlation (2.32) contains the superficial gas and liquid velocities j_g and j_l as well as the ratio of the gas and liquid volume flow rates Q_g and Q_l, also known as liquid loading, as operational input parameters, σ is the surface tension, ρ_l is the liquid mass density and μ_l the liquid dynamic viscosity.

$$d_{32} = \frac{0.858}{j_g - j_l}\sqrt{\frac{\sigma}{\rho_l}} + 1.683 \cdot 10^{-3}\left(\frac{\mu_l}{\sqrt{\sigma\rho_l}}\right)^{0.45}\left(\frac{1000Q_l}{Q_g}\right)^{1.5} \quad (2.32)$$

It worth highlighting that this correlation was developed for forced feed liquid spray injection in straight tubes and for a parameter range of 80 m/s for j_g, 250 m/s for j_l and liquid loadings Q_l / Q_g of 0.08 to 1 l/m^3. Another widely used correlation (2.33) was derived by Boll et al. [130] based on measurements in a Venturi scrubber operated in forced feed mode with rectangular cross-section and liquid spray injection.

$$d_{32} = \frac{4.22 \cdot 10^{-2}}{(j_g - j_l)^{1.602}} + \frac{5.77 \cdot 10^{-3}}{(j_g - j_l)^{1.602}}\left(\frac{1000Q_l}{Q_g}\right)^{1.922} \quad (2.33)$$

The operational parameter range for the superficial gas velocity was reported to be 30 – 122 m/s for j_g and a liquid loading Q_l / Q_g of 0.64 – 2.57 l/m^3. So far, no correlation could be found that was derived for self-priming Venturi scrubbers with liquid jet or film injection.

Considering the similarity between in the droplet generation by entrainment, five additional Sauter mean diameter correlations derived for annular flows in vertically oriented straight tubes are included in this work for comparison with the experimental data obtained in the Venturi nozzle. The correlations published by Tatterson et al. [131], Kataoka et al. [132], Kocamustafaogullari et al. [133] and Berna et al. [134] can all be standardized by (2.34) as introduced by Berna et al. with the parameters summarized in Table 6.

$$d_{32} = C \cdot D_h^{c_1} \cdot j_g^{c_2} \cdot j_l^{c_3} \cdot \rho_g^{c_4} \cdot \rho_l^{c_5} \cdot \mu_g^{c_6} \cdot \mu_l^{c_7} \cdot \sigma^{c_8} \quad (2.34)$$

The empirical constant C together with the exponents c_1 to c_8 are listed in Table 6 for all four correlations. A more simplified correlation (2.35) developed for an air-water annular two-phase flow in a vertical tube was introduced by Sarimeseli and Azzopardi [135].

$$d_{32} = \frac{\sigma}{\rho_g j_g^2}\left(0.069 j_g + 0.0187\left(\frac{\rho_l j_l}{\rho_g j_g}\right)^2\right) \quad (2.35)$$

All discussed empirical correlations describing the Sauter mean diameter were converted to SI units for consistency reasons.

3 TWO-PHASE FLOW EVOLUTION INSIDE COMMERCIAL WET SCRUBBERS WITH INTERNALS

The design of a nuclear wet scrubber is a very challenging task. The wet scrubbers can basically be seen as bubble column reactors with the aim to scrub radioactive gas and aerosols. The main difference to traditional bubble columns from the chemical sector is the transient operation mode and the wide range of injection velocities. In the work of Jacquemain et al. [4], the Swiss regulation is cited which requires a filter to be able to deal with flow rates that are for boiling water reactors being build up by 1 % of the reactor power and 0.5 % for pressurized water reactors. Depending on the venting moment, this can lead to quite high injection flow rates. The nuclear power plant Beznau, which serves here as a conservative example with the smallest thermal power, could evaporate at 0.5 % reactor power at a pressure range of 1 to 7 bar in a typical FCVS with an approximate diameter of 3 m enough steam to achieve superficial gas velocities of up to 0.15 m/s. Typical 1 GW class reactors would generate in PWRs more than double and in BWRs up to 6 times more steam which would hence increase the superficial gas velocity even beyond 0.15 m/s.

With increasing gas flow rate, the flow becomes more heterogeneous and turbulent. Shah et al. [136] quoted in their work a flow map as shown in Figure 25 on the dependence of the flow regime on the bubble column diameter and the superficial gas velocity for water and dilute aqueous solutions. Taking the previous example of Beznau and a bubble column of 3 m in diameter, the gas superficial velocity of 0.15 m/s would lie in the heterogeneous flow regime. From a soluble gas retention point of view, a small injection velocity is desirable to achieve a homogeneous flow with small bubbles rising slowly through the scrubber. A high bubble density with a small bubble diameter would lead to a high gas-liquid interface and the slow velocity to long residence times. The retention of particulate contaminants in the gas stream on the other hand benefits from fast flow direction and velocity changes in order to enhance the impaction deposition with the gas-liquid interphase. Such conditions are easier achieved in more turbulent flow conditions.

To solve this discrepancy in filtered containment venting systems based on wet scrubbers, internal structures are installed to enhance the retention of all contaminants. The nozzles are e.g. designed to increase the probability of aerosol particles hitting solid surfaces or the gas-liquid interphase while other structures slow down the gas flow and thereby increasing the residence time or breaking up the bubble sizes for a more intensive mass transfer for gaseous fission products.

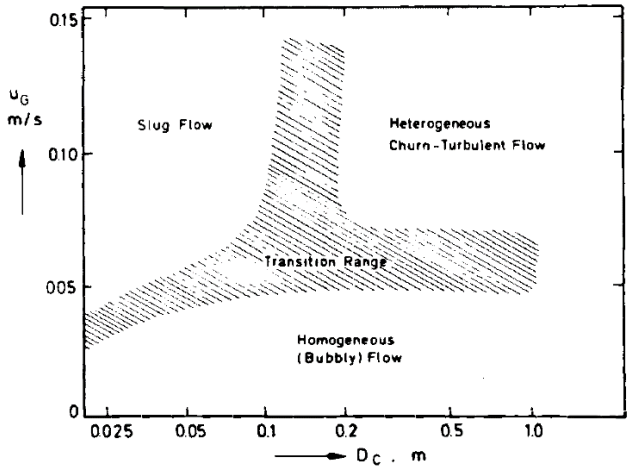

Figure 25: Approximate dependence of flow regime on gas velocity and column diameter (water and dilute aqueous solutions) [136].

In commercial FCVS designs that rely on wet scrubbers, two different nozzle types can be found that aim to deal with the aforementioned challenges. Simple nozzles with impaction plates and a mixing element are characteristic for IMI CCI filter designs, whereas multiple industrial vendors rely on Venturi nozzles to enhance the retention by droplet entrainment inside the nozzle.

The focus of this section will be laid on the hydrodynamic characterization of two commercial scrubber nozzle designs that are being used in real FCVS, the IMI-CCI design and a Venturi-based solution. All experiments are performed at adiabatic conditions with nitrogen or air as the gas phase and water without chemical additives as the liquid phase. The choice to use adiabatic conditions with non-condensable gases instead of a steam environment was made to study the flow fields that are being established by those nozzle designs. The results will support the outline of diffusive mass transfer tests which can in a

latter step be used to be compared with existing soluble gas models in the severe accident codes.

For the IMI-CCI design, the evolution of the flow over the column height will be analyzed for different flow rates. The effect of the bubble breaker in the column will also be looked at. For the Venturi nozzle, which has two different operating stages, the droplet generation in the throat of the nozzle will first be studied and in a second step the two-phase flow field above the outlet. As two different facilities were used for the two different scrubber designs, they will be introduced at the proper subsection with the nozzle geometry.

3.1 IMI Nuclear impaction plates and mixing elements

The IMI-Nuclear (former CCI AG) wet scrubber is one of the few that does not rely on Venturi inlet nozzles but follows a different approach. The scheme of the filter is illustrated in Figure 26. The contaminated incoming gas stream is forced through a series of nozzles at the bottom of the scrubber vessel. Three impaction plates with concentric holes are mounted on each nozzle above the outlet orifice as schematically shown in Figure 27. These plates enhance the retention of aerosols due to the impact of the flow and the resulting abrupt change of velocity and direction of the affected gas stream. At turbulent injection conditions, the bigger aerosol particles cannot easily follow the gas stream due to inertial effects and eventually hit either the plates or the gas-liquid interphase. The plates serve also as jet breaker at higher gas flow rates and supports the formation of smaller churns. A Sulzer Chemtech mixing element (cf. Figure 28) is placed above the gas injector to break up the remaining big gas plugs into finer bubbles.

In the real CCI-IMI scrubber, the mixing element does not cover the full cross section of the filter vessel. The perimeter of the mixing element is closed and leaves a small distance to the wall of the filter to form an annulus. The annulus serves as a downcomer for the displaced liquid by the incoming gas stream as indicated in Figure 29. This liquid carries over part of the small bubbles and creates a recirculation zone which is indicated in Figure 26 with the arrows. The recirculation is supposed to increase the residence time of the dragged bubbles and should thus help to increase the retention of gaseous contaminants. Upstream of the outlet of the filter, a moisture separator is holding back droplets that are formed at the pool surface from bursting bubbles or liquid that is directly carried over at higher gas velocities. Without this separator, contaminated liquid could be entrained and eventually released through the stack of the plant into the environment.

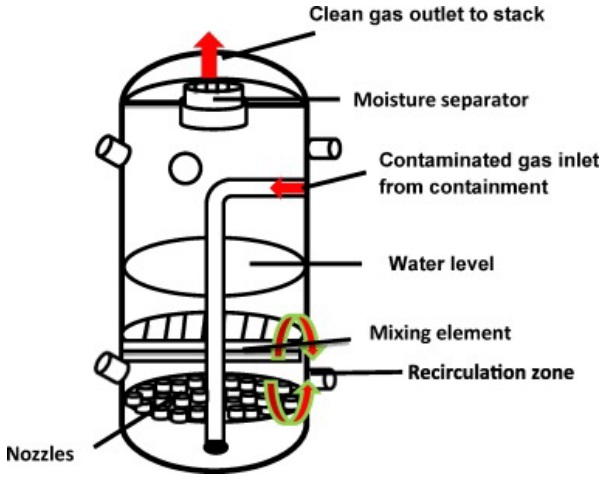

Figure 26: Schematic of the CCI-IMI-Nuclear scrubber as pictured in [4] with nozzles, mixing element, marked recirculation zone and moisture separator.

In the work of Beghi et al. [33], a scaled down facility called Mini-VEFITA was designed and assembled, replicating an IMI Nuclear wet scrubber with reduced height and width. The walls of the facility were made of borosilicate glass, which allowed to visually observe the flow structure and behavior for the different test conditions. The facility was used to determine iodine retention in the scrubber and was therefore equipped with instrumentation to measure the iodine concentration at the inlet and outlet of the test section. Except for the void fraction that was measured by the level swell and visual observations, no further instrumentation was in place to describe the two-phase flow in the facility.

ISOLDE Test Facility at PSI

The straight-forward method to investigate the effect of the flow regime would have been to instrument Mini-VEFITA with additional measurement techniques for the hydrodynamic quantities. Unfortunately, the limited space due to the already existing equipment, the safety precautions for dealing with iodine and the harsh

environment inside the facility, i.e. the high pH solution, temperature fluctuations and the corrosive nature of iodine, made the installation of further instrumentation very difficult.

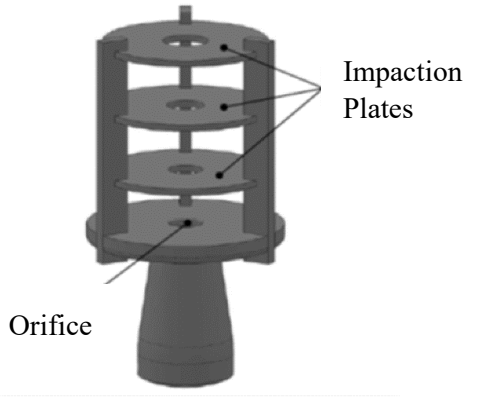

Figure 27: 3D schematic of the CCI injection nozzle with impaction plates

Figure 28: Picture of the Sulzer Chemtech mixing element mesh

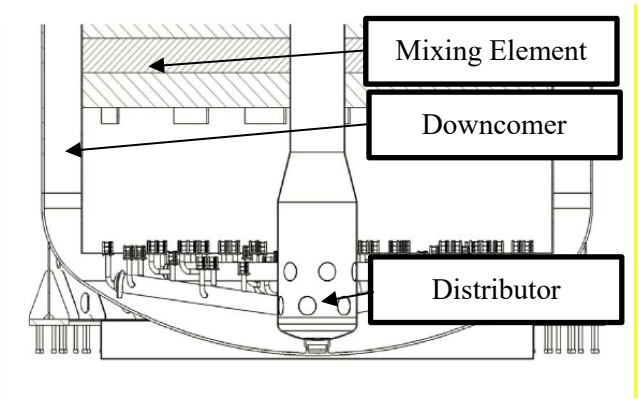

Figure 29: Detailed schematic of the bottom of the IMI-Nuclear-CCI Scrubber with gas distributor, mixing element and downcomer as presented by Grob [137].

The first idea to design a WMS made out of gold coated wires was given up. Even if the wires would withstand the scrubber solution and the iodine vapor, there was still no solution how to guide the wires out of the facility with a sealing method that is resistant to an iodine environment and ductile to close the gaps created by the wires. A preliminary test during the conceptual phase with a small WMS with steel wires also revealed high noise levels coming from the heaters that are necessary for the iodine vapor that could not be easily shielded off. Last but not least, the high pH caused by the scrubber solution increases the electrical conductivity of the liquid to values above the working range of the WMS.

As Mini-VEFITA could not be used for thermal-hydraulic tests, another solution had to be found. Eventually, a twin-unit to Mini-VEFITA was designed and assembled with focus on hydrodynamic instrumentation and easy handling.

The ISOLDE (**I**odine **S**crubbing and **O**ther **D**econtamination **E**xperiments) facility was built as a versatile, modular test facility for mid-scale two-phase flow measurements. Using easily available standard parts and building the facility at an elevated position allows for fast modifications on the facility, e.g. exchange of the nozzle type or internals, depending on the focus of the work. The facility was assembled at PSI with the same geometry and dimensions as Mini-VEFITA. The modularity was a result of the decision to mount a WMS at a fixed position and move the nozzle from the bottom instead. By moving the nozzle upwards to measure the two-phase flow properties at different elevations in the flow, the water level had to be adjustable to keep the same submergence level above the nozzle for all the measurements.

The facility dimensions, i.e. an inner diameter of 0.2 m and a minimum height of 1.5 m were taken from Mini-VEFITA. The wire-mesh sensor was the main instrumentation for the hydrodynamics of the facility. A small bypass tube was attached to measure the collapsed water level. Like in Mini-VEFITA, a 0.20 m tall mixing element was mounted about 0.38 m above the nozzle outlet. The facility could be fed from three different gas inlet sources. The inhouse dry nitrogen source was one of the two mainlines. On this mainline, a bypass connection was made to easily install further

pressurized gas bottles for tests with other gas mixtures in the future. The second gas line going into the manifold before the injection line was connected to the DRAGON steam generator [138] for future tests with saturated steam or steam/non-condensable mixtures. The overview of the test section of the facility with the WMS and the data acquisition is presented in Figure 30.

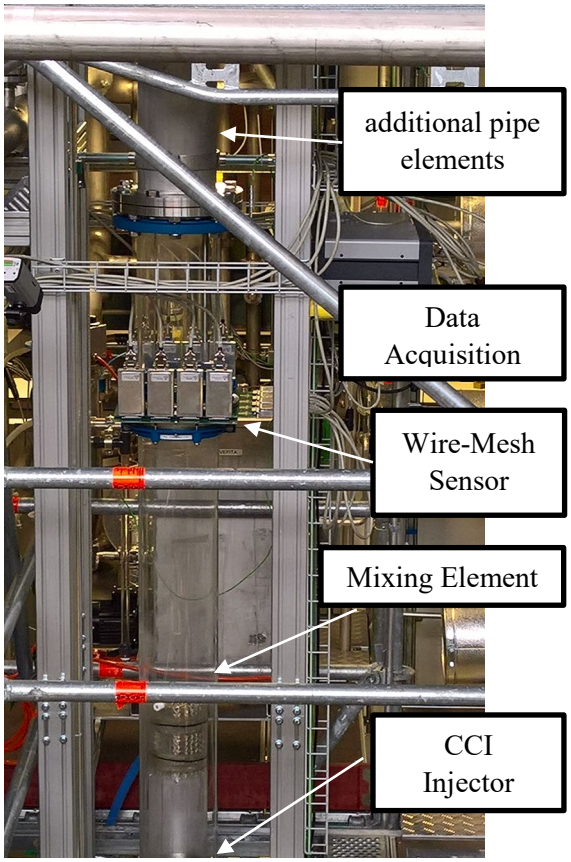

Figure 30: ISOLDE test facility with WMS data acquisition system, the CCI injector with mixing element and the additional pipe compartments on the top.

The three-layer sensor used in the ISOLDE facility was mounted between two flanges as depicted in Figure 31. On each layer, 64 stainless steel wires were soldered on a PCB with the soldering points lying on the inner side of the flange. This allowed to manufacture thinner sealing rings made out of white silicon with no carbon content. Dark sealing materials are usually darkened with carbon which is electrically conductive and causes crosstalk between the electrodes of the WMS. The sealing rings would be squeezed flat on the PCB without any wires underneath which prevents leak flow paths and stress on the wires. The pitch of the stainless-steel wires is 3 mm in lateral and 3.5 mm in axial direction with a wire diameter of 100 µm. The maximum measuring frequency in this configuration is 2500 Hz. In the analysis of this work, the data from the first two layers were used to determine the bubble size distribution and the interfacial area density whereas the information coming from the upper layer is used in the calculation of the bubble velocity.

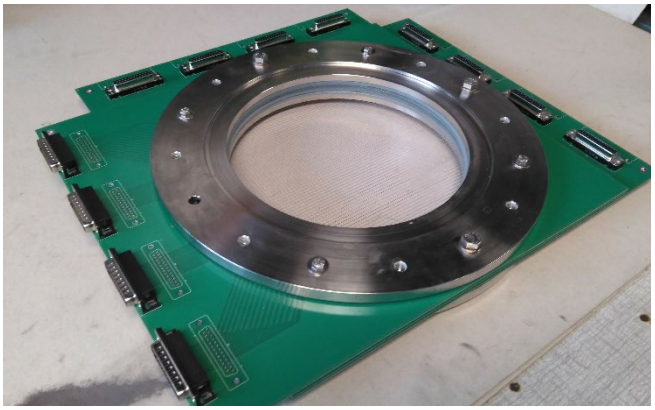

Figure 31: Three-layer wire-mesh sensor with 64 x 64 x 64 wires mounted between two flanges for easier installation.

A series of hydrodynamic tests was carried out at different measuring positions and gas injection flow rates, as described in Table 7. The nominal conditions for the Swiss power plants were summed up in the work of Hammer and Ritter [139] and are also shown in Table 7. The lowest distance of 143 mm was chosen as a compromise between capturing the effects of the injection zone and keeping a safety distance between the nozzle and the WMS. The safety distance was mainly needed to avoid an accidental contact during the maneuvering of the nozzle into position. The following two distances were split to 0.1 m steps up to 343 mm. The first measuring point above the mixing element is 0.1 m above the mesh and the furthest measuring distance was selected to have a good distance margin from the water surface to reduce pool surface effects on the bubble characteristics. The holding structure of the mixing element would not allow to position the WMS underneath it. In order to characterize the flow, any measurement below 388 mm, where the mesh is in place, was performed without it. This means, that at the distances of 143 mm, 250 mm and 343 mm above the nozzle, the mixing element was not installed. The

intrusiveness of the mixing element, i.e. the hindrance of the metal mesh, will most probably have an effect on the bubble sizes. Yet, the data should give a reasonable image of the situation up to the position where the flow enters the mesh.

The flow rates for the test matrix were chosen according to the conditions used in the work of Beghi et al. [33] to verify the observations on the flow regime. The submergence level of the injector was set to 900 mm for the tests with the mixing elements and only 700 mm for the measuring positions with the CCI injector only. The gas flow rates were increased, starting from 20 l_n/min up to 500 l_n/min resulting in superficial velocities of 0.012 – 0.29 m/s. As it can be seen in the test conditions in Table 7, a small amount of sodium sulfate was added to the water. Sodium sulfate in these small amounts is not known to affect the surface tension of the water too much as shown by dos Santos et al. [140]. It also has no corrosive effects on steel but increases the conductivity of the water to a level where the WMS can operate with a better signal to noise ratio and thereby making the data processing more accurate.

Limitations of the Facility and Measurements

As mentioned before, the facility is scaled down in width and height. While the height would have been easy to extend with additional pipe elements, the diameter of Mini-VEFITA and thus ISOLDE reached its limit with the borosilicate glass tubing which were important for visual observations in the studies of Beghi et al. [33]. The cross section of ISOLDE corresponds to half the area that is covered by one nozzle in an IMI-Nuclear wet scrubber with 112 nozzles. The flow in the near field will most probably replicate the real situation, whereas the far field would be influenced by the wall of the facility. It is worth noting that in a real FCVS configuration, due to the big number of nozzles, there would also be interactions of the bubbles from the neighboring nozzles in the far field as well, a detail that cannot be reflected by the scaled tests with a single nozzle.

Another issue that arose during the analysis of the WMS data of the measurements with the mixing element. The results were at first inconclusive for superficial velocities above 0.1 m/s. A deeper look in the raw data revealed the source of the error. The high bubble density and thereby resulting high void values

Table 7: Test conditions in the ISOLDE facility for the study of the hydrodynamics inside an IMI-Nuclear wet scrubber

	ISOLDE	**Nominal Values in Swiss Power Plants based on Hammer et al. [197]**
Superficial gas velocity [m/s]	0.012 – 0.29	0.2 – 0.25
Injection Flow Rate [l_n/min]	20 – 600	max. 1950*
Temperature [°C]	25 ± 2	max. 166 [131]
Gas mixture	Dry Nitrogen	Steam + Non-Condensables
Liquid phase	Demineralized Water	Thiosulfate + pH Buffer Solution
Na_2SO_4 concentration [g/L]	0.4 ± 0.1	0
Nozzle inner diameter [mm]	6	6
Water submergence [mm]	700 (CCI injector only) 900 (CCI + ME)	~3000
Measuring distance from nozzle edge [mm]	+143 (CCI injector only) +250 (CCI injector only) +343 (CCI injector only) +688 (CCI+ME) +730 (CCI+ME)	-

* based on a design with 112 nozzles and a filter diameter of 3.5 m according to the drawings of Grob [129] at nominal flow rates of Leibstadt according to Hammer and Ritter [197]

lead to a widening of the signal histogram that is used for calibration. In Figure 32, a histogram is exemplary shown for the center node at 688 mm distance from the nozzle and a superficial velocity of 0.29 m/s. The peak which was thought to be the liquid reference conductance is obtained at a too small value. Fortunately, the measurements at the smallest superficial velocities did not behave this way. The calibration matrix of the measurements at low flow rates were taken for all the other experiments to get interpretable results.

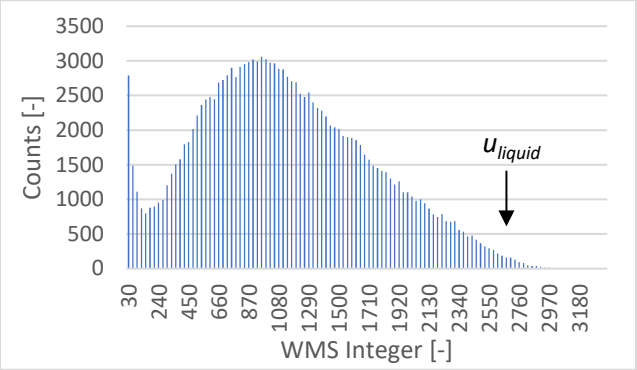

Figure 32: Exemplary WMS data histogram for measuring positions above the mixing element and superficial velocities above 0.1 m/s and indicator of the real liquid conductance u_{liquid}.

The drawback of this static calibration file is the lack of temporal effects. Such temporal effects can be temperature effects due to the forced evaporation by the dry nitrogen. Over a measuring day, the liquid temperature could drop by 5 °C which corresponds to a deviation of up to 10 % in the liquid conductance. However, this is captured in the 11 % error uncertainty of the void fraction.

Hydrodynamic Characterization of the Flow

The void fraction is the most reliable and accurate quantity coming from the WMS. In Figure 33, the cross-section average void fraction at each measuring position is plotted against the superficial gas velocity with the marked transition regime as seen in Figure 25 for a bubble column diameter of 200 mm according to Figure 25 from Shah et al. [136]. The void fraction is continuously growing with increasing superficial velocity with the expected bend in the transition regime. Beghi et al. [33] found the transition in Mini-VEFITA to lie at around 0.1 m/s and assumed that the mixing element had probably an influence on the delayed regime transition. Additionally, the facility was filled with a solution of 0.01 mol/l of sodium hydroxide and 0.06 mol/l of sodium thiosulfate which had an influence on the surface tension, too. In the present tests inside ISOLDE, the water was not loaded with any chemicals.

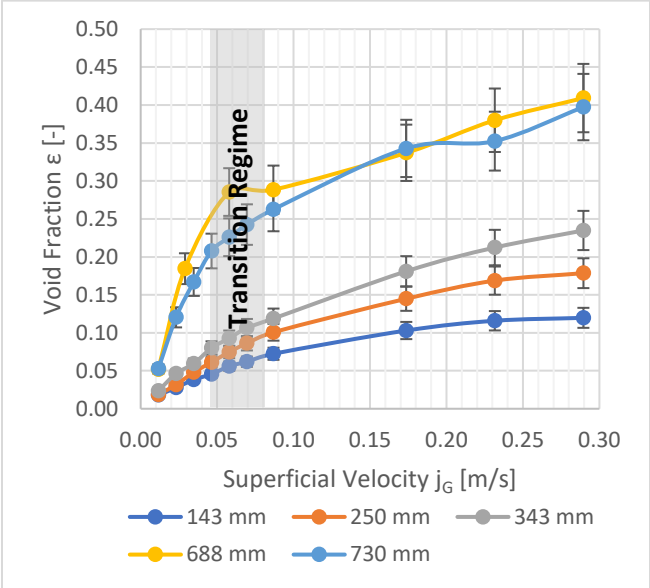

Figure 33: Average void fraction at different flow rates for the different measuring heights inside the ISOLDE facility with marked (gray bar) transition regime according to Shah et al. [136].

The bend at the flow transition in the void fraction data is more pronounced above the mixing element than below the mixing element. Furthermore, the void fraction for higher superficial velocities seems to be not that strongly depending on the axial measuring position. The trend of the void fraction over the column height is plotted in Figure 34 to better capture this observation. For the lowest flow rate at 0.012 m/s, the bubbles are slightly expanding with increasing column height due to the lower hydrostatic pressure. After the mixing element, the bubbles are broken up to a finer swarm, which is almost tripling the average void fraction, and they continue to rise along the height with no further disturbance. For superficial velocities between 0.058 m/s and 0.087 m/s, the void evolution over height shows a linear increase below the mixing element with a distinct increase in the profile visible after the element. This speaks for the mixing element to be still operational in this flow regime. For the two highest superficial velocities, the average void fraction

increases with almost a constant inclination through the mixing element and stagnates. The drop or stagnation of the void fraction could be caused by recoalescing of the fragmented bubbles or due to the flow evolution.

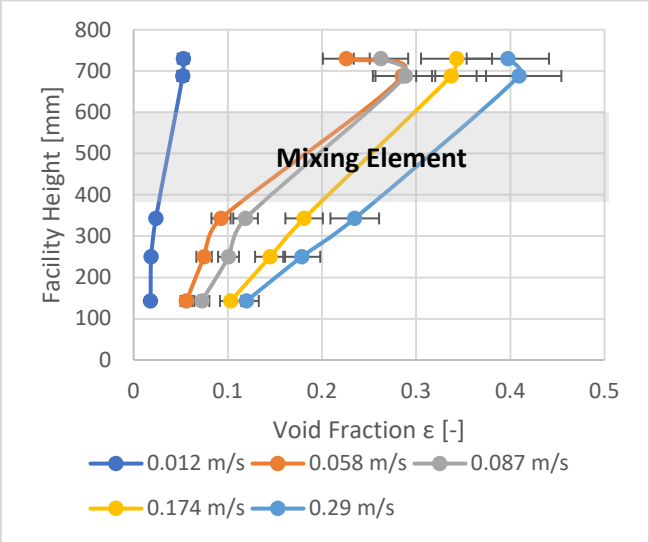

Figure 34: Average void fraction evolution over column height for different gas injection flow rates at ambient temperatures with the position of the mixing element marked in grey.

Besides averaged values, due to the tomographic ability of the wire-mesh sensor, the radial profiles of the void fraction can be processed and plotted as done in Figure 35. The radial profiles confirm the observations of the averaged values. In the bubbly flow regime, i.e. at 0.012 m/s, the bubbles are formed rather in the center, the nozzle position, and are broken up inside the mixing element to form a more uniform distribution over the whole cross-section. At 0.058 m/s and 0.087 m/s, the flow needs longer to develop as the radial profile is flattening only at 250 mm distance. Due to the gas injection in the center of the column, a toroidal vortex is formed that transports the gas faster than at the edges. With increasing height, this vortex dissipates in radial direction. As a result, the bubbles are distributed all over the cross section and are causing the void profile to flatten.

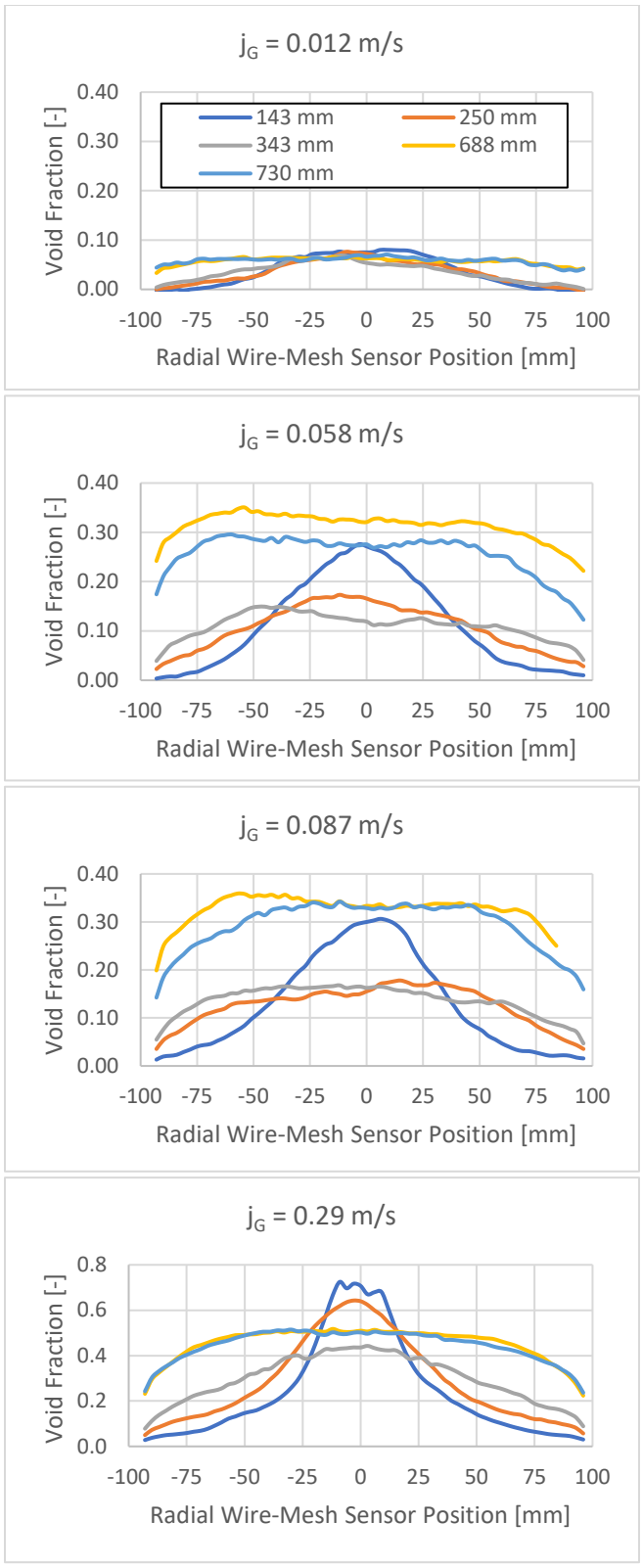

Figure 35: Radial void fraction at different elevations in the ISOLDE facility for different superficial gas velocities at ambient temperature.

Passing through the mixing element, the void fraction is increased significantly and stabilizes with the same radial distribution shape. At the highest flow rate, i.e. 0.29 m/s, the void profile needs a longer distance to flatten the centric peak as the momentum of the gas volumes is also higher. The mesh supports the flattening of the void distribution but the increase of the void fraction is quite small compared to the previous flow conditions.

The interfacial area density further completes the picture of the flow structure description so far. In Figure 36, the interfacial area density trend is shown for all injection flow rates and distances. As seen before with the void fraction over the height, also the interfacial area density experiences a significant jump after the mixing element between 343 mm and 688 mm. At the flow rates below the grey marked transition region, the interfacial area after the mixing element density gains a factor of 3 in value of the values before the element. This is an evidence for the strong bubble breakup inside the Sulzer Package. At flow rates in the heterogeneous regime beyond the transition, the interfacial area density still undergoes a significant increase, this increase is though only doubled. The smaller gain in interfacial area density indicates that the optimal working range for the Sulzer Chemtech mesh seems to lie in superficial velocities below the transition regime, i.e. below 0.09 m/s.

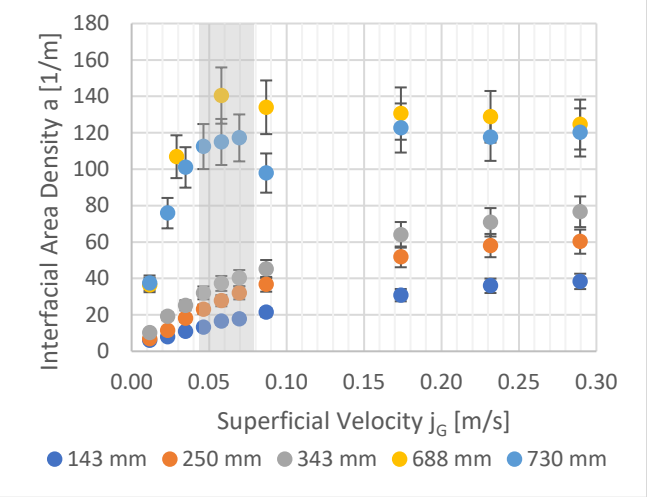

Figure 36. Interfacial area density for different injection flow rates at different measuring positions with the CCI injector and the mixing element at adiabatic temperature conditions with the marked grey transition region according to Shah et al. [136].

To better interpret the influence of the Sulzer packing on the interfacial area density, two additional measurements were performed at 644 mm and 722 mm distance without the element. The comparison between both positions with and without mixing element can be seen in Figure 37. In addition to the two far-field distances, the interfacial area density of the measurement position 343 mm is also plotted. The first observation in Figure 37 is the comparison between the distances 343 mm, 644 mm and 722 mm without the Sulzer mesh. It appears that the flow is developed after 343 mm as the interfacial area density is insensitive to the column height over the following 380 mm at all flow rates. At higher superficial velocities, this could also be explained with the impact of the wall of ISOLDE. At smaller flow rates though, i.e. below the transition regime, the flow is more homogeneous which speaks for a developed flow.

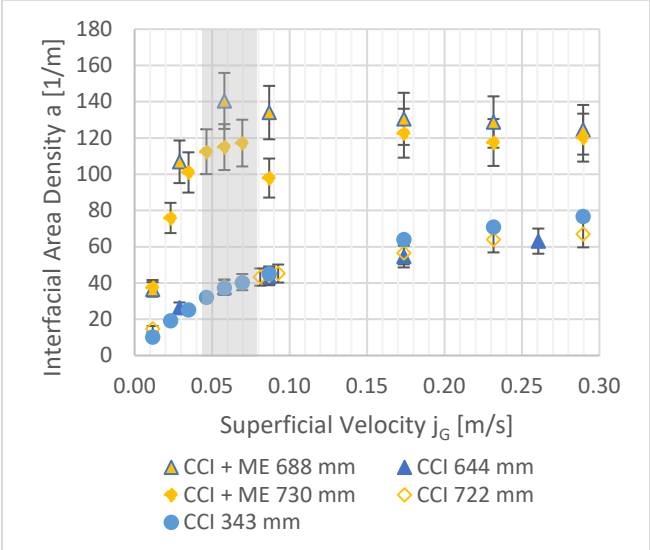

Figure 37: Comparing interfacial area density at the similar position with and without mixing element at different injection flow rates with the marked grey transition region from bubbly to churn-turbulent flow.

Secondly, the interfacial area density is, as seen before, experiencing a gain with the mixing element that is smaller than in the homogeneous regime but still quantifiable. The distance between the interfacial area density values with and without the mixing element are though coming closer with increasing superficial velocity. This would support the theory that in the heterogeneous regime, the bubble breakup is not as efficient as below the transition regime.

The further processed data allow to get an insight into the bubble size distributions as displayed in Figure 38. For the lowest superficial velocity, the bubble breakup can be observed over the height of the facility. Especially after the mixing element, the peak in the distribution is clearly shifted from roughly 30 mm bubbles close to the injection down to a bubble diameter of 10 mm. It is noteworthy, that even at this flow rate, the flow is not perfectly homogeneous. For all the flow rates, below the mixing element, i.e. 388 mm, the bubbles are rather big with a relative flat distribution profile. With higher superficial velocity, the bubbles after the injection become even bigger it can be seen at 0.058 m/s. The injected bubbles reach 60 mm in equivalent diameter as the flow starts to develop. The mixing element is here still capable to break up the quite

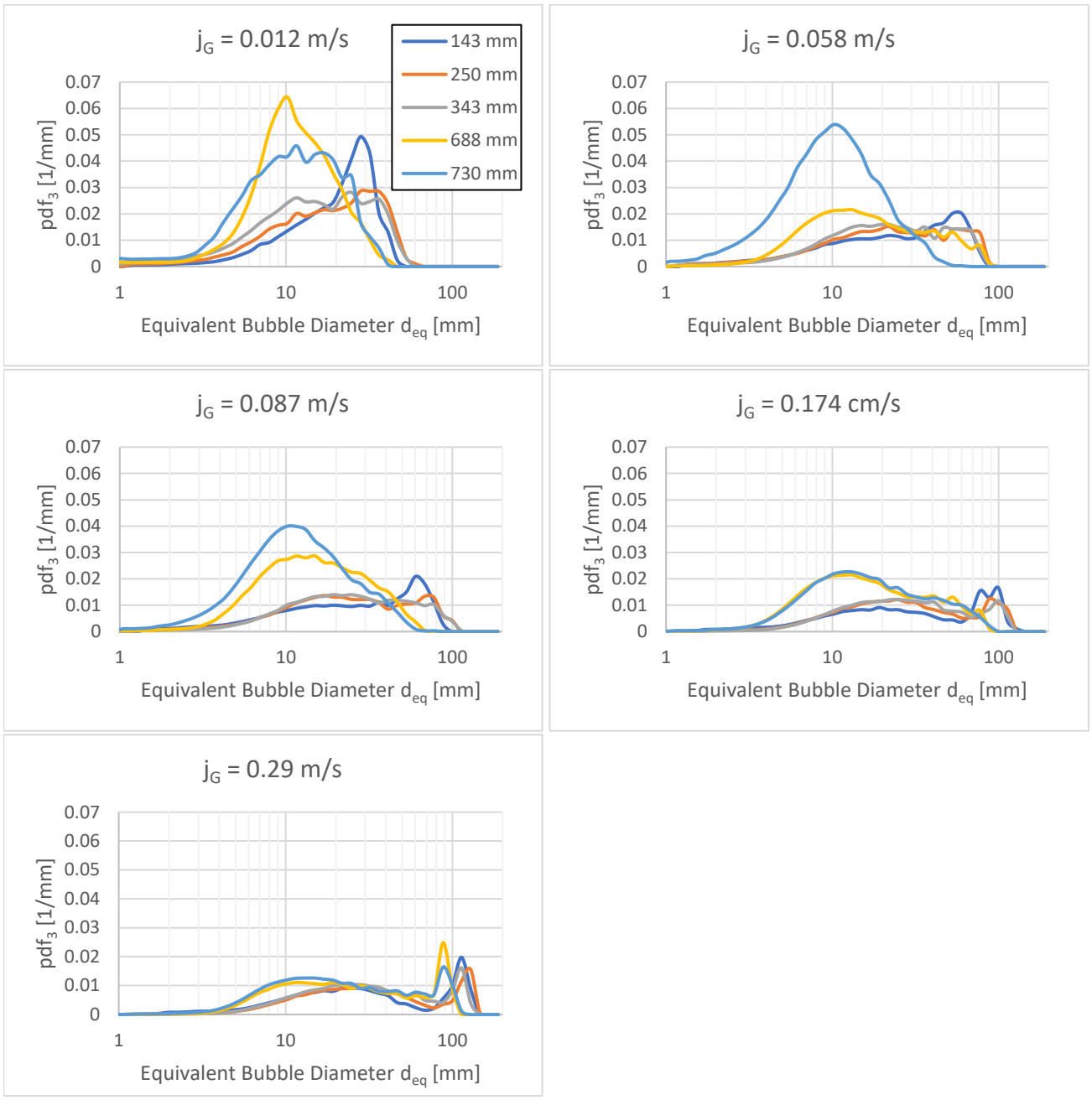

Figure 38: Volumetric share of the bubbles in dependence of the equivalent bubble diameter for superficial velocities of 0.012 m/s, 0.058 m/s, 0.087 m/s, 0.174 m/s and 0.29 m/s for different distances from the nozzle tip at ambient temperature.

big gas volume into 10 mm sized bubbles, although the distribution gets flatter.

The same behavior is visible at 0.087 m/s superficial velocity. Above the mixing element, judging by the bubble size distribution, the flow region would be seen as bubbly flow. For higher injection flow rates, the effect of the mixing element starts to decrease as shown at the superficial velocities at 0.29 m/s. The bimodal shape of the bubble size distribution persists even though the mixing element shifts both, the distinct peak and the flat peak by 20 mm. Based on observations during the tests, the mixing element is probably drying out the metal mesh so that there is no way for the liquid to entrain and break up the volumes.

Another way of getting insights of the flow structure and its evolution is to look at virtual side views of the void fraction distribution on the vertical central plane of the column. They are created by plotting a series of instantaneous one-dimensional void fraction distributions obtained along an electrode wire in the center of the measuring plane over time. In Figure 39, the virtual side views are displayed for the lowest superficial gas velocity of 0.012 m/s. At the distances before the mixing element, the formation of caps and oblate ellipsoids is clearly visible. The presence of the different sized caps explains why the bubble size distribution at 0.012 m/s does not show a sharp uniform peak but rather a flat profile. The situation changes after the mixing element where the bubble size is just about the resolution of the WMS. Some unified bubbles are still found which are better visible at 730 mm distance, but they are a clear minority at this flow rate.

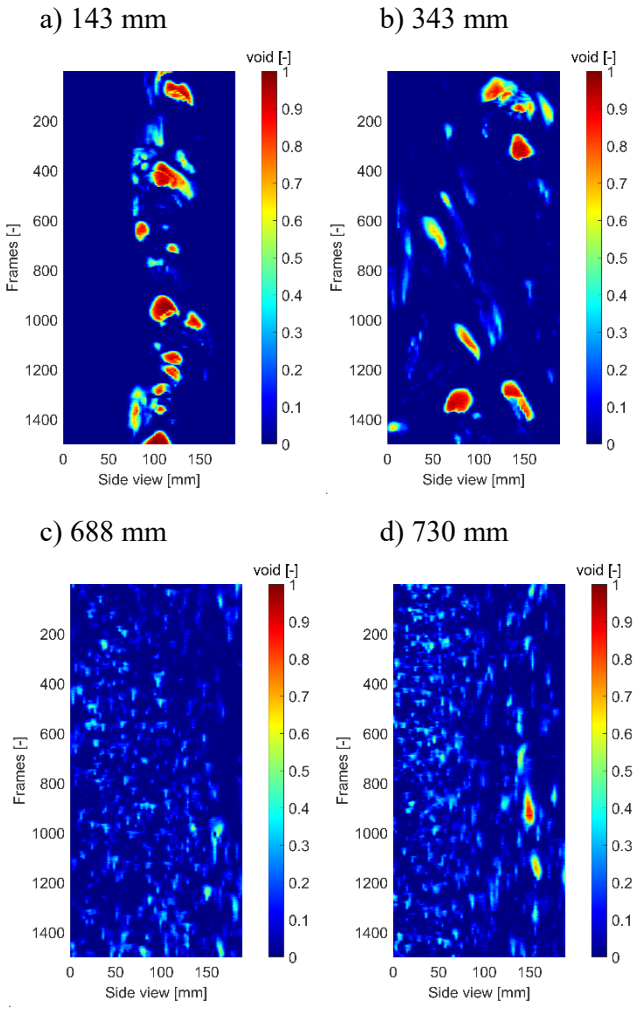

Figure 39: Virtual side views of the flow at the center of the column at 0.012 m/s superficial velocity at different measuring positions.

Increasing the flow rate gives bigger bubbles close to the nozzle as it can be seen in Figure 40 a). The big cap bubbles break up into smaller oblate ellipsoids on their way to the mixing element, Figure 40 b). After the mixing element, the bubbles are mostly dispersed with some bigger oblate ellipsoids still present.

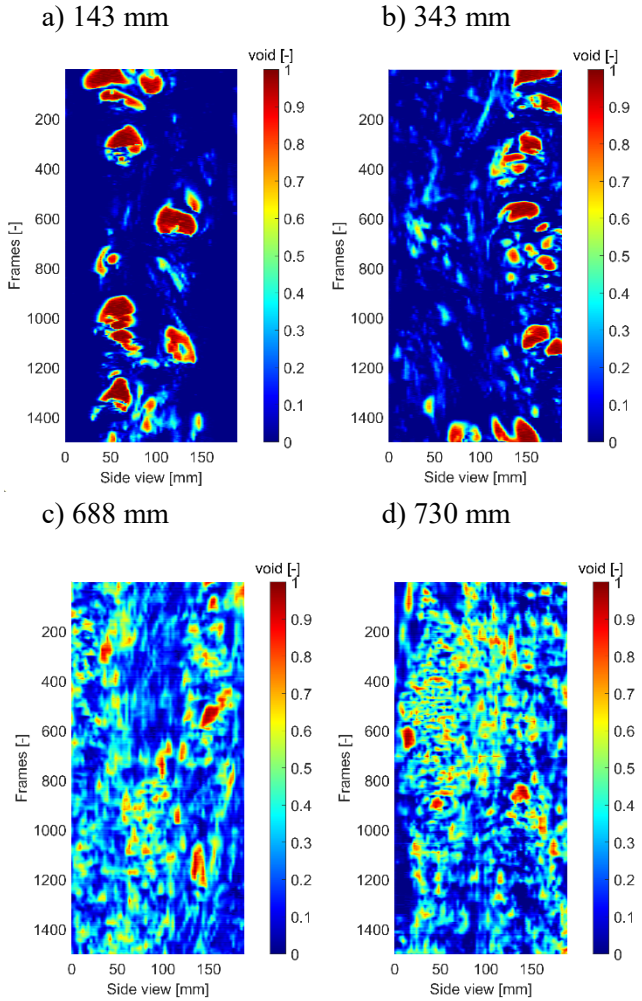

Figure 40: Virtual side views of the flow at the center of the column at 0.057 m/s superficial velocity at different measuring positions.

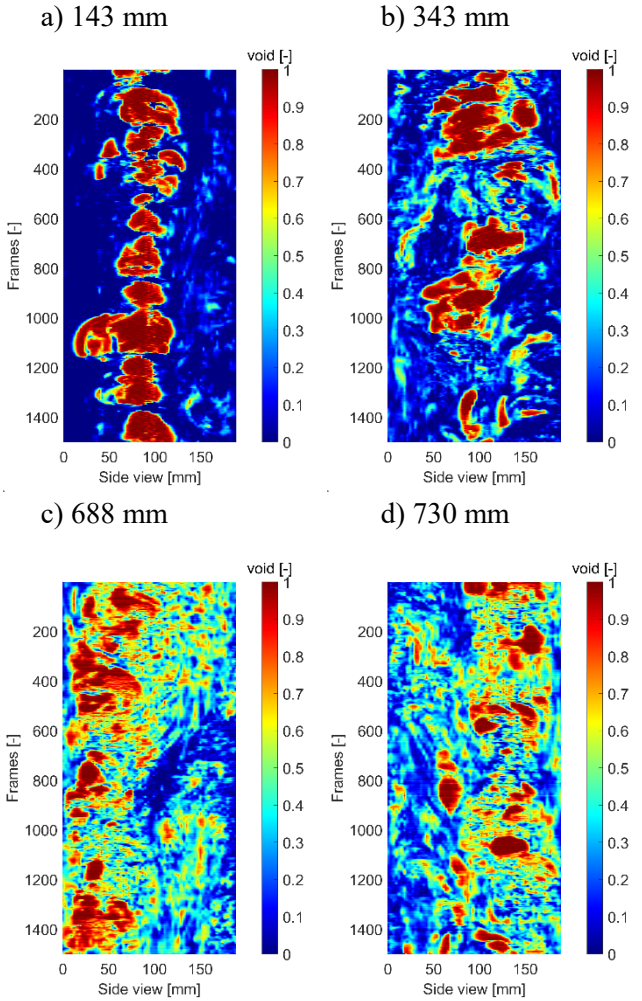

Figure 41: Virtual side views of the flow at the center of the column at 0.29 m/s superficial velocity at different measuring positions.

The most chaotic flow can be observed for the highest superficial gas velocity, 0.29 m/s, Figure 41. Close to the nozzle, the bubbles are being generated with a small liquid bridge between them. The nozzle is still bubble gassing as no jet is visible. This can be attributed to the impaction plates as their purpose is also to break a jet. The generated big Taylor bubbles do not survive too long as they can be easily broken down by the liquid force that is created due to the vortex that is established by the high gas velocities in the center of the column. At 343 mm distance, the flow can only be described as chaotic. Above the mixing element, a highly dense bubble swarm with many bigger churns can be identified.

Even at higher flow rates, the mixing element has an effect on the flow, but due to the high gas share and the dense bubble packing, the effect is less prominent. However, the breakup of the big volumes would increase the interfacial area, even if it would just be for a short time which could nonetheless enable a higher mass transfer rate.

Effect of FCVS Chemicals on the Hydrodynamics

One way to enhance the retention efficiency of wet scrubbers is to chemically trap the species in the liquid state by chemical bonds. Regarding iodine retention inside FCVS, usually sodium thiosulfate is added to the pool which is capable in reducing iodine to an ion for a better solubility in water. Furthermore, sodium hydroxide or sodium carbonate keep the pH high for

less revolatilization. The high pH induced by these chemicals will affect the surface tension of the liquid mixture and thereby the hydrodynamics. Beghi et al [33] used 0.06 mol/L of sodium thiosulphate and 0.01 mol/L of sodium hydroxide, which is the composition of commercially available scrubber solutions. Another option for the composition is 0.15 mol/L of sodium thiosulphate and 0.01 mol/L of sodium carbonate. The chemicals are widely available with small chemical safety requirements necessary.

The effect of chemicals was investigated using a WMS in a small table-top facility. Due to the high pH environment, the stability of the wire-mesh sensor electrodes, which were made of stainless steel, had to be verified first. For this purpose, a small table-top facility was assembled called Mini-ISOLDE as pictured in Figure 42. The facility was built from DN50 stainless steel tubes that were welded to two flanges between which the WMS was installed. From the bottom side, a 6 mm inner diameter nozzle was inserted about 5 cm above the bottom. The WMS used in this setup was a simple 1.55 mm PCB electronic plate with a 16x16 electrode configuration soldered on it.

For the tests, the facility was filled with the two scrubber solutions and left for 24 hours to observe the reactions on the soft spot of the sensor, the soldering points and the stainless-steel wires. At ambient temperature, the chemical stability of the sensor was no issue. In a second test, the lower part of Mini-ISOLDE was heated with a heating wire to 60 °C for half a day to replicate a typical test condition as performed by Beghi et al. [33]. At this elevated temperature, the chemicals had a strong corrosive effect on the soldered connections. Despite the sensor still being operational, the test was conducted without any gas injection, i.e. no mechanical loads on the wires. At that point, the assumption was made that this particular design would not suit for temperatures much higher than ambient in combination with chemical additives in ISOLDE.

Beside the corrosive nature of the chemicals, another issue arose from the electrical conductivity of the two scrubber solutions. The conductivity was found to exceed the conductivity limit that can be measured by an WMS even at ambient temperature. The signal acquisition unit of the sensor saturates at an electrical conductivity of 5 mS/cm electrical conductivity [81] which was exceeded by both solutions (with measured conductivities of 6 mS/cm and 15 mS/cm using a commercial conductivity probe).

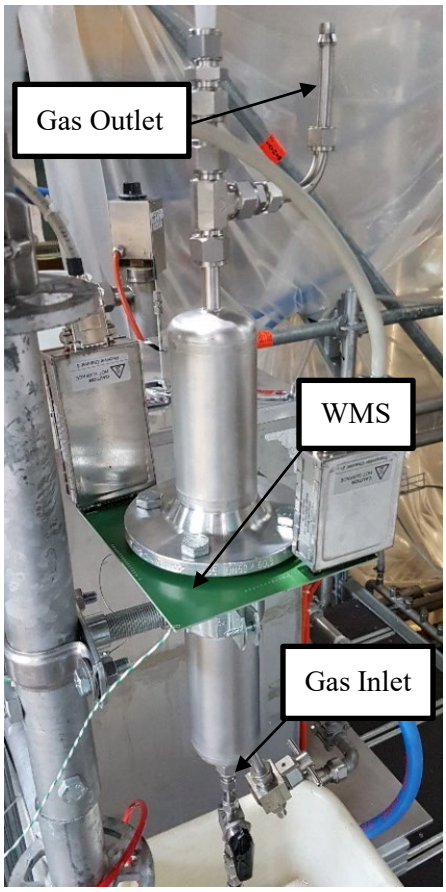

Figure 42: Mini-ISOLDE tabletop facility at PSI with a 16x16 WMS (green PCB) installed between the two flanges

To overcome this problem, the output voltage of the signal generator of the data acquisition was reduced with a voltage divider. Unfortunately, even though the electrical circuits were chosen to operate at the high frequencies of the WMS, the signal was distorted too heavily to be useful for the data processing. It turned out that a new signal acquisition with a lower impedance of driver circuits for both transmitter and receiver electrode wires would be required, a development that was started but finally had to be terminated due to efforts which were out of scope of this work.

The Mini-ISOLDE facility was used to give preliminary insights on the effect of the chemicals on the hydrodynamics using lower concentrations of chemicals than used in commercial scrubber solutions. The maximum measurable concentration of each

chemical in deionized water was determined for each one separately in 0.005 mol/L steps before the saturation conductivity of 5 mS/cm was reached. The results are summarized in Table 8. Additionally, the two chemicals of the two commercial solutions were prepared and diluted to the concentration where the WMS would be able to measure an interpretable signal.

The tests at Mini-ISOLDE are far from optimal since the facility was manufactured to perform simple tests on new WMS designs and endurance tests. The mesh of the sensor was also not fully covering the cross-section of the pipe. This will allow bubbles to pass through the open corners of the sensor and falsify the results. Also, the nozzle was arbitrary placed inside. Yet, the results can be compared to the tests performed with deionized water to see if there is a strong observable effect in the bubble formation with the chemical compounds up to the concentrations where the WMS can still operate. One additional test run was performed with a concentration of 0.005 mol/L sodium sulphate solution to verify that sodium sulphate has a negligible effect on the surface tension.

The cross-section averaged void fraction is plotted for different injection flow rates in Figure 43. The void fraction of the deionized water shows the highest values. Only the solution of sodium thiosulphate alone is within the measurement uncertainty of the deionized water. The void evolution curve of the sodium sulfate solution is also below the one for pure deionized water, being much closer to the chemical solutions. All solutions containing both types of standard additives show lower void fraction than the deionized water, an effect that is significant with regard to the error bars.

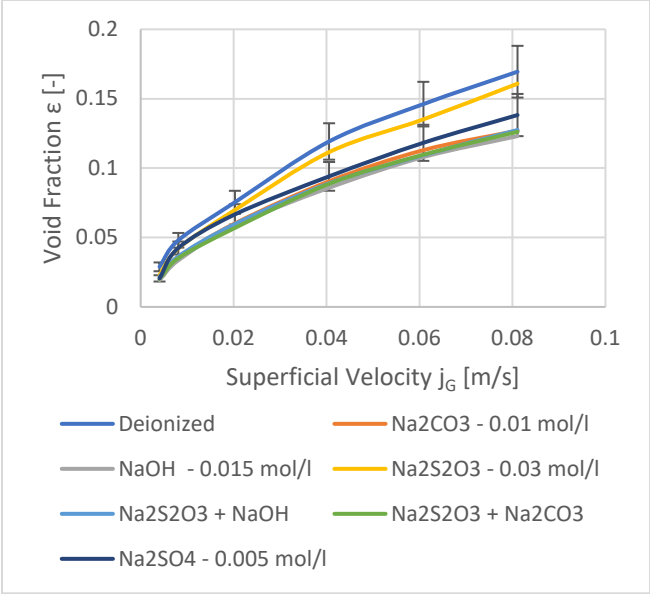

Figure 43: The effect of FCVS chemicals and sodium sulphate on the average void fraction inside Mini-ISOLDE for different superficial velocities.

The lower void fraction is an indication for an altered surface tension as expected. The thiosulfate alone in solution has interestingly no significant impact unlike the sodium carbonate or the sodium hydroxide. Furthermore, the sodium sulfate trend is much closer to the chemical additives than the pure deionized water. The effect could also be induced by a very poor signal to noise ratio in the deionized water environment that leads to noise induced noise artefacts. An insight in the bubble size distribution would help to investigate this but unfortunately, Mini-ISOLDE was manufactured for simple two-layer wire-mesh sensors. The simplicity of this sensors on single PCB boards were an added value for fast testing for their chemical resistivity, thermal

Table 8: Maximum concentrations of the chemicals used for FCVS applications before saturation was reached.

Chemical Compound	Maximum achieved Concentration [mol/L]	Conductivity measured [mS/cm]	Commercial Scrubber Solution [mol/L]
$Na_2S_2O_3$	0.03	4.19	-
Na_2CO_3	0.01	2.03	-
NaOH	0.015	3.14	-
$Na_2S_2O_3$ / Na_2CO_3	0.01 / 0.0066	3.64	0.15 / 0.01
$Na_2S_2O_3$ / NaOH	0.0025 / 0.0004	4.37	0.06/0.01

endurance or noise behavior but not for deep analysis. The third layer or a second sensor is missing to deduce the bubble velocity for a bubble size comparison.

The interfacial concentration on the other hand does not require any information on the bubble velocity and can be evaluated, as shown in Figure 44. The interfacial area density holds some information on the detected bubble interphase. As before, the deionized water and the sodium thiosulphate solution are slightly standing out whereas the rest is all within the uncertainty range. Judging on this preliminary data, the effect of the chemicals at these low concentrations measurable with a WMS are negligible. This does not mean that the chemicals at concentration levels found in the commercial solutions have no influence on the hydrodynamic quantities.

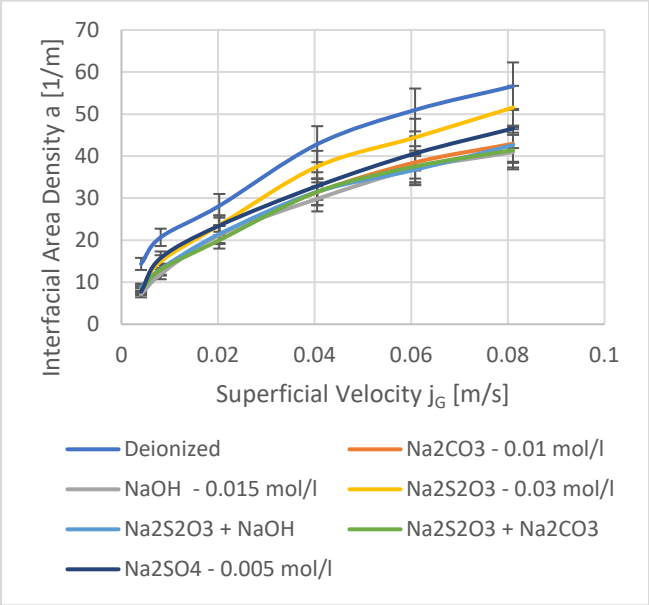

Figure 44: The effect of FCVS chemicals and sodium sulphate on the interfacial area density inside Mini-ISOLDE for different superficial velocities

Conclusions on the CCI-IMI-Nuclear Design

The CCI-IMI nozzle that has been optimized to enhance the aerosol retention, showed a typical flow evolution for a similar sized bubble column for flow rates that could be found in real FCVS scrubbers at different venting points in time. The nozzle does however not produce a fine bubbly flow even at very low injection rates that would be more beneficial for the scrubbing of gaseous components. This task is taken over by the Sulzer Chemtech mixing element above the nozzle. It was shown that up to the transition region from bubbly to the strongly heterogeneous churn-turbulent flow, i.e. up to a superficial velocity of 0.087 m/s, the mixing element performed as expected. The rather big cap bubbles and large gas plugs were broken down to smaller fragments, thus increasing the interfacial area density significantly. At higher injection velocities, the mixing element loses its efficiency. In this flow regime, it might help absorb aerosol particles through impaction on the metal mesh but the bimodal churn-turbulent flow regime travels through the full height of the column. The difficulty in the IMI-CCI design as a filtered containment venting system is the trade-off between the retention of aerosols and gaseous contaminants. For a high gas retention efficiency, a much finer nozzle would be required to form a homogeneous bubbly flow situation inside the liquid with the typical low rising velocity. This could on the other hand reduce the aerosol retention that profits from high acceleration, fast direction changes and impaction on flow obstacles.

The ISOLDE tests were all performed with demineralized with a small concentration of sodium sulphate to increase the electrical conductivity into the working range of the WMS. The addition of the commercial scrubber solution will influence the surface tension of the water but as Beghi et al. [33] observed in their studies, the heterogeneous flow persists at flow injection rates of 0.17 m/s superficial velocity and higher. A direct comparison of the results is hence difficult and should be made with caution. For the best utilization of the obtained results from ISOLDE, additional tests in Mini-VEFITA would be beneficial. The tests should be performed in pure water with iodine loaded nitrogen to replicate the test conditions in ISOLDE. The combination of both tests, the retention of iodine in water and the hydrodynamic data could be used to benchmark the soluble gas models in the system codes. Because in any case, the assumption of the bubbly or cap flow in the bubble rising zone after the injection zone as seen for example in BUSCA does not correctly account for the chaotic flow situation in a real FCVS scenarios.

Apart from the hydrodynamic observations, there have been some advancements on the instrumentation side worth noting. The WMS design of the facility, i.e.

to integrate the full PCB in the flange and thereby avoid the wiring to the outside of the facility showed a good operational behavior. The sealing forced to have a relatively big axial distance between the wire planes of 3.5 mm. This should be reduced in a second revision of the design. Another drawback was found in the measuring plane above the mixing element. Bubbles with an oblate ellipsoidal shape were formed with a very high density, which made the processing of the data very challenging. As Ito et al. [83] also noted in their work, the stagnant pool conditions are not very preferable to operate at with a WMS. A possible solution to this issue could be an idea that was studied at ETH Zürich for the characterization of a plunging jet. A movable WMS was manufactured and controlled by a linear motor to force the bubbles through the mesh. This step would require heavy modifications on the ISOLDE facility and a further development of the signal processing of the data as the position of the sensor would change during the measurement.

3.2 Venturi Nozzles Design

Venturi scrubbers are the most commonly used injection orifices in wet scrubbers used in filtered containment venting system as also noted by Bal et al. [141]. As the scrubber design is also used in other industries to scrub pollutants out of exhaust stream, it is not surprising to find a lot of research being done on venturi nozzles. The designs vary with respect to the operation mode, geometry and the liquid injection mechanism. The main parts of a Venturi are the reducer in which the contaminated gas is accelerated, the throat in which the liquid is injected and mixed with the gas stream, and the diffusor in which the gas velocity decreases and the major retention of aerosols and gas phase species takes place as depicted in Figure 45. The most common design in the nuclear wet scrubber design is the self-priming Venturi nozzle due to its passive operation mode. In a self-priming Venturi, the liquid that is surrounding the nozzle is sucked in by the pressure difference between the static pressure of the gas stream at the narrowest point and the hydrostatic pressure of the pool. If the scrubber is operated in fully submerged mode, i.e. the Venturi nozzle is also covered by the scrubber solution, the retention of the contaminated gas is acting in two stages. The first stage is the Venturi tube in which the injected liquid will form droplets and create a big interfacial area to retain the gas phase contaminants and aerosols. Once the gas stream leaves the diffusor, further scrubbing takes place in the bubble rising zone as the second retention stage. In other industries, the Venturi nozzles are usually operated in a forced feed mode, which means that the scrubbing liquid is actively pumped into the throat. During a postulated severe accident, the assumption has to be made that no power source is available which is why the self-priming operation was chosen.

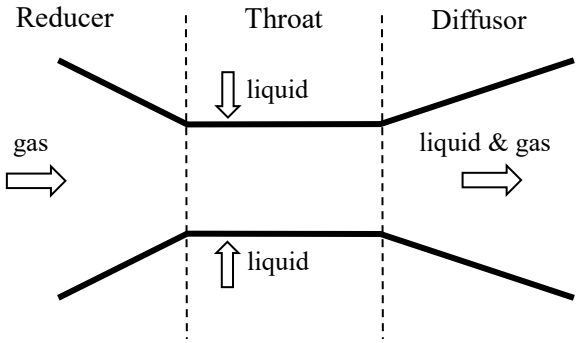

Figure 45: Generic schematic representation of a Venturi scrubber with reducer, injection and diffusor as presented by Breitenmoser et al. [107].

The operation mode is not the only characteristic of a Venturi scrubber. The liquid injection mechanism of the Venturi nozzle is also defining how the droplets are being formed. Three design categories can be found in industry, the film, the jet and the spray injection design as schematically shown in Figure 46. In the film injection design, the scrubbing liquid is introduced in the reducing section of the scrubber by slits. The liquid forms a film at the throat wall, i.e. an annular flow regime establishes in the throat. In the spray type, the liquid is introduced by spray nozzles. The spray injection mechanism, that has been studied by Gretzinger and Marshall [142] and Kim and Marshall [143], the liquid is atomized by pneumatic atomization. The jet injection type uses multiple orifices in the throat wall to inject the scrubbing liquid. The scrubbing liquid forms jets, which are initially oriented perpendicular to the main gas flow direction. For the film injection mechanism, liquid droplets are generated by entrainment from the liquid film as described by Parker and Cheong [144]. In the jet injection, the liquid is

atomized by jet breakup induced by capillary, acceleration and shear forces as found in the works of Atkinson and Strauss [109] and Roberts and Hill, [110].

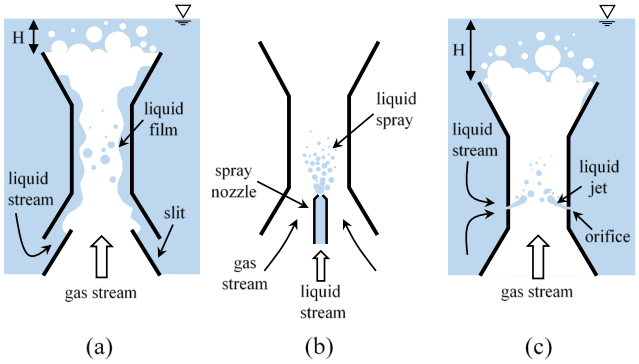

Figure 46: Schematic representation of different liquid injection mechanisms for Venturi scrubbers. (a) Film injection. (b) Spray injection. (c) Jet injection as presented by Breitenmoser et al. [107].

For the design and operation of Venturi scrubbers, the collection efficiency is of great importance and has therefore been extensively studied over the past seven decades, cf. Ali et al. [145]. These studies revealed a entangled dependency between the collection efficiency and various material, geometrical and operational parameters such as the liquid and gas flow rates, the specific geometry of the Venturi nozzle, the liquid injection mechanism, the spatial dispersion as well as the size distribution of the droplets within the throat or the material properties of the different phases, i.e. the pollutant, the carrier gas and the scrubbing liquid. These parameters themselves are based on different fundamental physical processes, e.g. inertial impaction, diffusion, absorption and condensation, among others, as investigated by Ali et al. [34].

In order to improve the understanding of the performance and the operation behavior of current FCVS designs under severe accident conditions, various experimental and numerical studies have been carried out over the past decade, e.g. by Bal et al., [141] and Dong and Yang, [146]. Based on the findings of these investigations, new wet scrubber based FCVS were developed. With respect to the Venturi scrubbers, liquid film injection together with self-priming operation have proven to be promising features for new FCVS with improved collection efficiency as presented by Lee et al., [147] and Y. Zhou et al., [148]. Due to the novel features, studies about multiphase flow dynamics in Venturi scrubbers with liquid film injection operated in self-priming mode are scarce and many research works, like Ali et al. [34, 35], Lee et al. [147] and Zhou et al. [148, 36] focused mainly on the collection efficiency for aerosols and gaseous iodine.

Based on earlier models developed for actively driven Venturi scrubbers with liquid jet or spray injection by Calvert [149], Boll [150], Yung [151] and Haller et al. [152], among others, Ali et al. and Zhou et al. derived new models for self-priming Venturi scrubbers with liquid film injection. For these new models, common droplet size correlations derived and validated for actively driven Venturi scrubbers with liquid spray injection have been used. Only four experimental studies have so far quantitatively investigated the droplet size distribution in Venturi scrubbers with film injection and published the results. All four studies were performed at adiabatic and ambient operational conditions with an air-water two-phase mixture with active liquid injection. The experimental details of these studies such as the hydraulic diameter D_H of the throat or the operational range of the superficial gas and liquid velocity j_g and j_l with respect to the throat cross-section are summarized in Table 9. The range of the superficial liquid velocity is given for a standard submergence level of 0.5 m.

Parker and Cheong [144] were the first one performing systematic droplet size distribution analysis in a film injection type Venturi scrubber. They used an impression method with magnesium oxide coated glass slides to quantify the droplet sizes at the outlet of the Venturi tube. Parker and Cheong concluded from their data that the peak of the droplet size distribution is located between 10 and 20 µm for the tested parameter range. Furthermore, they observed that droplets are generated by entrainment from the water film at the leading edge of the throat and that the droplets are further atomized in the gas core of the throat by aerodynamic forces down to the mentioned droplet sizes. They performed also spray injection experiments and did not find any significant difference between the droplet size distribution by film and spray injection at the outlet of the diffusor.

Table 9: Published experimental studies about droplet size distributions in film injection type Venturi scrubbers as presented by Breitenmoser et al. [89].

	Parker and Cheong [132]	**Teixeira et al. [143]**	**Alonso et al. [111]**	**Silva et al. [145]**	**Present work**
D_H [m]	0.025	0.019	0.019	0.123	0.026
Measurement Technique	Impression Method	Laser Diffraction	Laser Diffraction	Laser Diffraction	High-Speed Imaging
Operation Mode	Active	Active	Active	Active	Self-Priming
Liquid Injection	Porous Wall	Porous Wall	Porous Wall	Porous Wall	Slit
Main Flow Direction	Downward	Upward	Downward	Horizontal	Upward
Gas Superficial Velocity [m/s]	99	127 - 182	50 - 90	34 - 70	23 - 46
Liquid Superficial Velocity [m/s]	$(3.8 - 16)\cdot10^{-3}$	$(0.45\text{-}2.7)\cdot10^{-1}$	$(0.5 - 1.4)\cdot10^{-1}$	$(1.1 - 6.4)\cdot10^{-3}$	$(3.2 – 3.5)\cdot10^{-1}$
Temperature [°C]	Ambient*	Ambient*	Ambient*	Ambient*	25 ± 1
Throat Cross-Section	Circular	Circular	Circular	Circular	Rectangular

*no information given in the works on elevated temperature

Teixeira et al. [153] investigated the liquid entrainment and used laser diffraction techniques to measure droplet sizes in a Venturi scrubber. The goal of their work was to study the influence of a Venturi nozzle as an insert in a vertical tube on the annular flow. The liquid film injection was located more than 4.5 m upstream of the Venturi tube inlet. It is important to highlight that with this setup, droplets are generated already before the Venturi tube inlet by the liquid film entrainment mechanism. The resulting droplet size distribution at the outlet of the diffusor is therefore significantly different compared to droplets generated in the throat of a Venturi tube. Teixeira et al. could show with their data that the droplets formed in the Venturi tube are significantly smaller than the droplets created upstream in the vertical tube. They modelled the droplet size distribution with the Rosin-Rammler distribution [154]. Moreover, three additional findings were presented by Teixeira. First, their results showed that 50% of the total entrainment was caused by the Venturi tube. They thereby confirm the outcomes of Parker and Cheong, that the entrainment droplet generation mechanism was the driving force. Second, the entrained mass flow rate increases for an increase in the liquid flow rate, whereas the mean droplet diameter is not significantly changing with a variation of the liquid flow rate. Third, Teixeira et al. were able to confirm the empirical finding of Azzopardi and Govan [118] that the mean droplet diameter is decreasing with an increase in the gas flow rate which is a result of higher shear and turbulence.

Alonso et al. [119] also used the laser diffraction method to measure droplet size distributions in a laboratory-scale Venturi scrubber. The water was introduced by film and by jet injection. The droplet sizes were measured at three different locations along the Venturi scrubber height, i.e. two at the throat and one at the diffusor outlet. The resulting data showed that the Sauter mean diameter can be well described by the Boll correlation [150] and that the droplet size distribution can be modelled with the Rosin-Rammler distribution function. The correlation of Nukiyama and Tanasawa [127] significantly overpredicted the Sauter mean diameter, particularly for high gas velocities. It

was observed that the droplet size distribution gets wider and shifts to larger values as the droplets travel downstream in the Venturi scrubber. Furthermore, there was a significant difference between the droplet size distributions for the film and the jet injection at the two throat measurement locations, particularly at superficial gas velocities below 50 m/s. Alonso et al. concluded that the type of liquid injection has a strong influence on the drop size at the throat and therefore also the removal efficiency. Additionally, Alonso et al. confirmed Teixeira's experimental results that an increase in the gas flow rate causes a decrease in the Sauter mean droplet diameter and that the liquid flow rate is not strongly affecting the droplet size.

Silva et al. [155] performed droplet size measurements in an industrial large-scale Venturi scrubber with the laser diffraction method. There were also two different liquid injection mechanisms available in these experiments, i.e. film and spray injection. Similar to Alonso et al., Silva et al. measured at three different axial locations along the Venturi tube. The results showed that the droplet size distribution decreases to smaller values along the throat. In the diffusor, the opposite behavior was observed. Silva et al. concluded that the size of the throat and the diffusor possess a significant impact on the droplet atomization and coalescence mechanisms. Furthermore, they stated that the Boll correlation and the Rosin-Rammler distribution are not adequate measures to describe droplet size distributions in an actively driven industrial-scale Venturi scrubber with film injection. Like the three previously discussed studies, the same qualitative dependences between the Sauter mean droplet diameter and the liquid and gas flow rates were found.

The studies performed by Alonso et al. and Silva et al. have shown that the different liquid injection mechanisms have a strong effect on the droplet size distribution in the throat of Venturi scrubbers. Thus, the legitimate use of droplet size correlations to Venturi scrubbers with liquid injection systems other than the ones used to derive the correlation is not necessarily given. However, the findings of the discussed experimental studies have only a limited relevance for industrial Venturi scrubbers with liquid film injection operated in self-priming mode. All discussed studies performed measurements with actively driven Venturi scrubbers. Mayinger and Lehner [156, 157] showed in their studies that Venturi scrubbers operated in self-priming mode show a self-regulating performance, i.e. for an increase in the gas flow rate, the liquid flow rate is decreasing and vice versa. Although no significant difference in the underlying physical atomization processes between the self-priming and the forced feed mode for the same liquid injection mechanism was found, Venturi scrubbers operated in the self-priming mode possess distinct operational characteristics, e.g. comparatively high liquid flow rates at low gas flow rates. All four studies used porous walls to inject the liquid and create the liquid film. Azzopardi and Govan [118] as well as Silva et al. [155] showed also in their studies that scaling mathematical models for Venturi scrubbers of different sizes at constant gas and liquid flow rates does not produce good results.

At this state, there is a lack of experimental studies investigating droplet size distributions in full-scale Venturi scrubbers with liquid film injection operated in self-priming mode. The first aim of this section was to perform droplet size measurements in a full-scale replica of an industrial self-priming Venturi scrubber with liquid film injection by using high-speed imaging. The measured data could be compared to droplet size correlation derived for Venturi scrubbers to verify their applicability in this type of nozzle. In addition, the experimental data with the empirical droplet size distributions might be used in collection efficiency models and to understand the operational behavior of current industrial self-priming Venturi scrubbers with liquid film injection.

The second part was to investigate the evolution of the two-phase flow for the submerged operation of the Venturi nozzle with a WMS. Despite that a big portion of the scrubbing is taking place in the droplets due to their big interfacial area, the bubble rising zone in the pool is also contributing to the overall retention efficiency. Therefore, quantifying the two-phase flow structure can support the development of adjusted models specific to Venturi nozzles.

TRISTAN Test Facility at PSI

The experiments were performed in the TRISTAN (**T**ube **R**upture **I**n **S**team genera**T**or: multi-ph**A**se flow

iNvestigations) facility at the Paul Scherrer Institute. The facility is depicted in Figure 47. TRISTAN was designed to perform two-phase flow investigations in large diameter channels and tube bundles that are relevant for steam generator tube rupture (SGTR) accident scenarios. Betschart et al. [158] performed such experiments to get insights into the two-phase flow evolution along the tube height inside a steam generator tube bundle with different tube rupture openings and at different positions in the tube array. The exact details can be found in the work of Betschart [40].

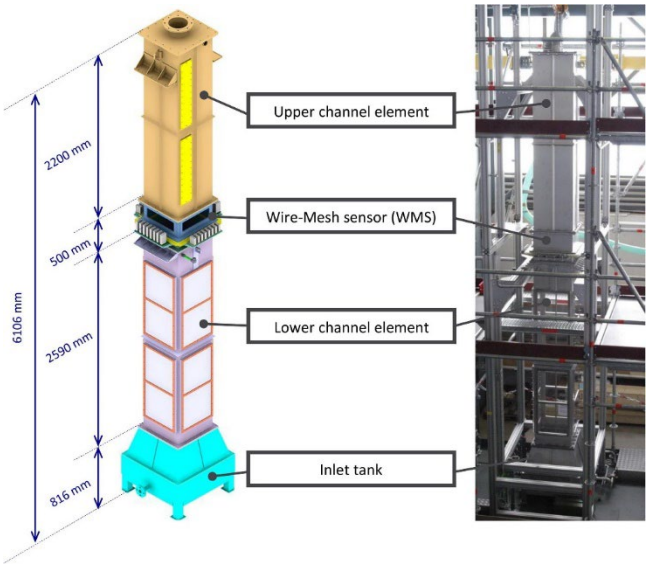

Figure 47: A schematic representation of the TRISTAN facility with its height dimensions and a photograph of the facility as presented by Betschart et al. [158]

The test section of the facility has a square cross-section of 0.5 x 0.5 m^2 and a total height of 6.1 m. The lower channel elements of the facility are equipped with acrylic glass windows, which allow optical access to the flow. The facility is operated at adiabatic conditions using pressurized air and water. A water heater is installed in the recirculation path between the pump and the water tank to run tests at elevated temperatures. The acrylic glass permits temperatures up to 40 °C. On the gas side, the pressurized air passes also through a gas heater. Like in ISOLDE, the WMS was installed at a fixed height. In order to measure at different positions in the two-phase flow mixture, the nozzle had to be positioned closer or further away from the nozzle. The liquid outlet flange can thus be adjusted to four predefined positions so the submergence above the nozzle stays constant with a maximum deviation of approximately 300 mm.

The Venturi nozzle, as schematically shown in Figure 48, has a total height of 700 mm with a throat height of 160 mm. The compression ratio of the areas of the converging and diffusor section is 19.45 for both parts. The nozzle has two suction slits on opposite sides that are 3.2 mm high. The rectangular shape of the facility, i.e. the transparrent acrylic glas windows were flat, and the rectangular flow cross-section of the nozzle made the image processing easier due to the evenly distributed magnification by the optical refraction in water.

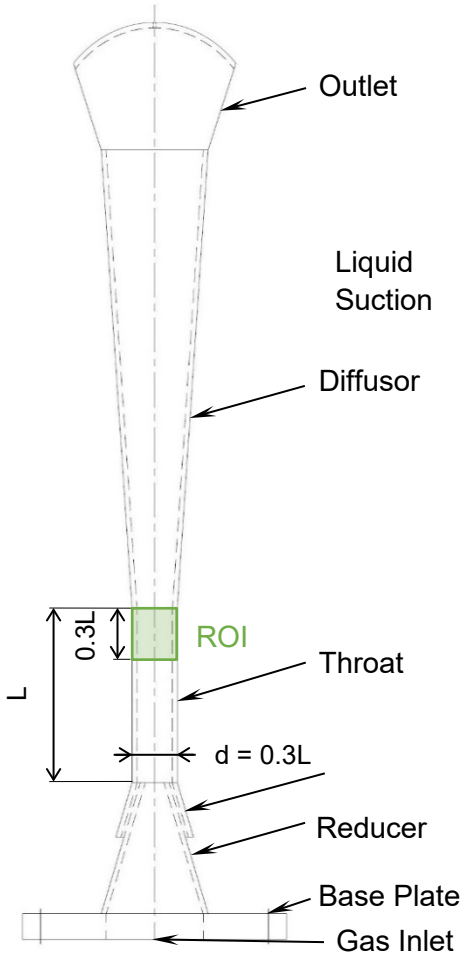

Figure 48: Venturi nozzle schematic as presented by Breitenmoser et al. [107] and the highlighted region of interest (ROI).

The main instrument for the droplet size estimation was a high-speed camera (HSC) from LaVision, the model HighSpeedStar 5.1. The camera was operated with the LaVision DaVis 8 software. The camera has a

maximum frame rate of 3 kHz at full resolution of 1024x1024 pixels. This leads to the aforementioned spatial resolution of 42 µm per pixel. The measuring time was set to 2 s with a frame rate of 2 kHz. The shutter speed was kept as low as possible, which was a trade-off between deteriorating the contrast and the sharpness of the droplets in the image. Since lightning conditions depend on the submergence, shutter speeds of 40 µs for the submerged and 33 µs for the unsubmerged operational conditions were chosen. A macro lens was used with a focal length of 105 mm and a lens apperture of f/2.8. The channel was illuminated from the back by an LED panel with a diffusive luminous flux of 4400 lm. The panel was attached on the rear acrylic glass window. The HSC was mounted in front with a distance of 50 cm from the front glass as shown in Figure 49. The distance was chosen so that the measurement section of the Venturi throat would be covering the whole image. The upper end of the acquired equilateral images was aligned to the start of the diffuser section as indicated in the schematic of the Venturi nozzle in Figure 48 with the square region of interest (ROI).

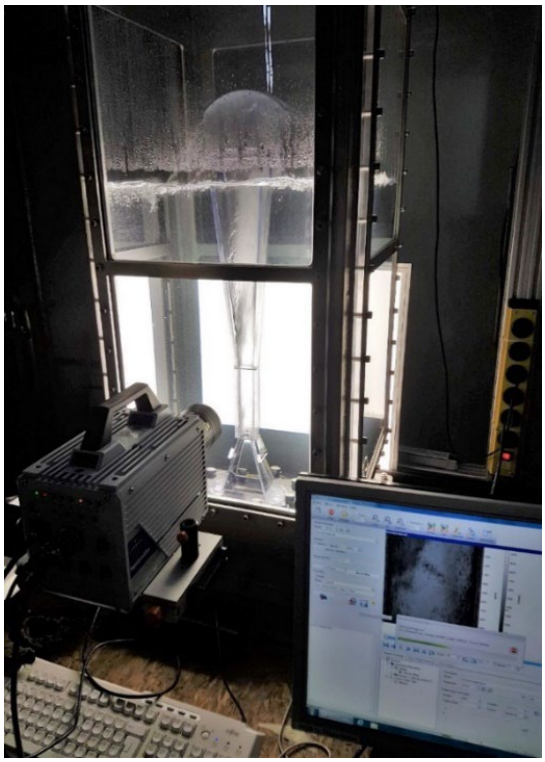

Figure 49: Venturi nozzle inside the TRISTAN facility with the high-speed camera system and data acquisition.

For the characterization of the two-phase flow once the gas enters the pool, the water submergence was set to 2.2 m above the nozzle exit. The gas flow rates were within the same range as the droplet size experiments as these would be realistic values for this type of FCVS nozzle. The details on the TRISTAN WMS can be found in the work of Betschart [40]. As mentioned before, the WMS was designed to be installed at a fixed position but should be easily removable for maintenance. The sensor was thus mounted on a flange element of the facility which could be installed with the same equipment as the rest of the facility. A 3D model of the WMS is shown in Figure 50. The tube support grid was not required in this work and was hence removed. The main features of the WMS in TRISTAN were a lateral pitch of 3.4 mm with an axial pitch of 2 mm, built with 100 µm stainless steel wires in a 128 x 128 configuration. At a distance of 50 mm, a second 128 x 128 WMS was installed for the possibility to correlate the signals for the determination of bubble velocities. Due to the long distance of the wires, a spring system was elaborated that permitted to prestress the wires without putting too much load on the soldering points of the PCB. The details of the design can be found in the work of Betschart [40].

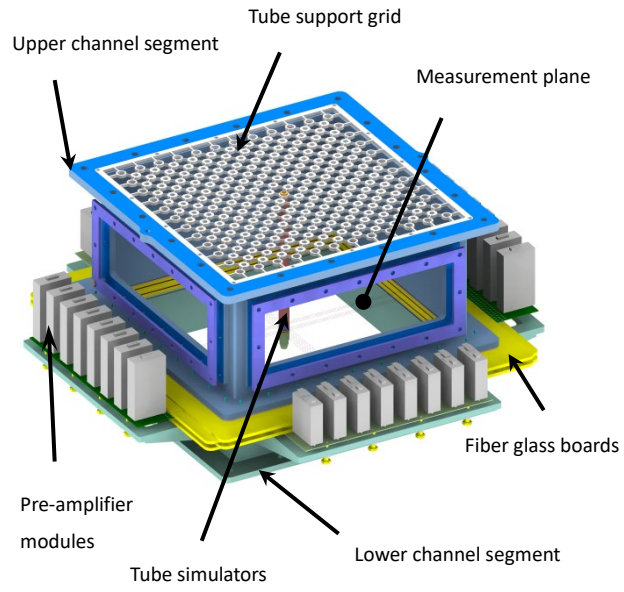

Figure 50: A 3D computer model of the WMS of the TRISTAN facility as used in the work of Betschart et al. [40, 158]

Table 10: Test conditions in the TRISTAN facility for the study of the droplet sizes in the Venturi throat and the pool hydrodynamics

Droplet Size Distribution		
	TRISTAN	**Nominal conditions based on the tests from Jung et al. [198] and Kim et al. [199]**
Superficial gas velocity in the throat [m/s]	23 – 46	up to 52
Temperature [°C]	25 (gas) 25 (liquid)	150
Gas mixture	Compressed Air	Steam and Non-Condensables
Liquid	Demineralized Water	Thiosulfate + pH Buffer Solution
Water submergence [m]	0, 0.5, 1.2	3
Hydrodynamics in the Pool		
Superficial gas velocity in the pool [m/s]	0.1 – 0.2	up to 0.16
Temperature [°C]	35 (gas) 35 (liquid)	150
Gas mixture	Compressed Air	Steam and Non-Condensables
Liquid	Demineralized Water	Thiosulfate + pH Buffer
Na_2SO_4 concentration [g/L]	0.1 ± 0.01	-
Measurement Positions [$L/D_{H,outlet}$]	1, 2, 3, 4, 5	-

The water and gas temperature were slightly higher than ambient, i.e. 35°C to avoid heat transfer between the gas and the liquid phase and to reduce the temperature decrease of the water due to forced evaporation. The position of the Venturi nozzle was varied to have a dimensionless distance to the WMS of 1 – 5 $L/D_{H,\,outlet}$ from the nozzle exit, with D_H being the hydraulic outlet diameter of the Venturi nozzle exit. At higher elevations, the wall of the TRISTAN facility became more prominent in the interaction with the flow which is why no further tests were analyzed for the interpretation. All test conditions for the droplet size experiments and the two-phase flow experiments in the pool are summarized in Table 10. Furthermore, the nominal conditions for this type of nozzle were also added that were deduced from the tests of Jung et al. [159] and Kim et al. [160] to put the experimental condition into perspective. The real wet scrubber holds 60 Venturi nozzles which corresponds to an average cross-section area of approximately 0.1 m^2 per nozzle. The cross-section of TRISTAN has 0.25 m^2 which leads to the same conclusion as with the CCI nozzle, i.e. the near field hydrodynamics should be relatively accurate while the far-field will experience disturbances also from the neighboring nozzles in the real-world application.

For the estimation of the bubble sizes, the average gas phasic velocity was taken as bubble velocity. The chaotic flow situation and the relatively big distance between both WMS in TRISTAN only yielded reasonable bubble velocities for the bigger bubbles. Besides this limitation, one of the amplifiers quit service during the measurement campaign which lead to the loss of 16 wires on the second WMS. Thus, one part of the facility would be blinded which supported to the decision to scale the bubbles with the average phasic velocity.

Droplet Size Distribution inside the Venturi

A total amount of 27 droplet size tests was carried out at the TRISTAN experimental facility by varying submergence levels and gas flow rates. The superficial gas velocity j_g with respect to the throat cross-section was varied between 23 and 46 m/s. The superficial liquid velocity j_l was determined by linear interpolation and extrapolation based on the experimental data of Lee

et al. [147] that used the same Venturi nozzle geometry. Three different submergence levels were tested, i.e. 0, 0.5 and 1.2 m. The ambient temperature was kept constant at 25 °C and the local pressure varied between 1.01 and 1.15 bar according to the gas flow rate.

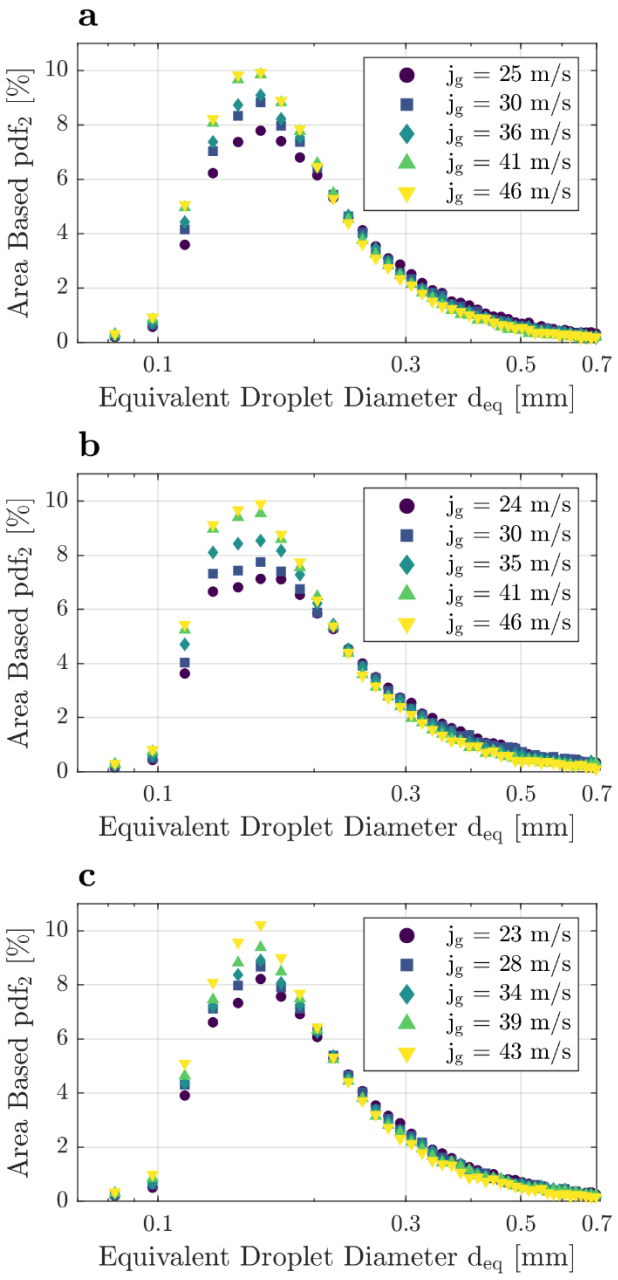

Figure 51: Surface-area based probability density function (pdf_2) as a function of the equivalent droplet diameter (d_{eq}) for different submergence levels (H). (a) H = 0 m. (b) H = 0.5 m. (c) H = 1.2 m as presented by Breitenmoser et al. [107].

The surface area-based probability density pdf_2 as a function of the equivalent droplet diameter d_{eq} is presented in Figure 51 for varying superficial gas velocities j_g and submergence levels H. The surface area-based probability density function is selected due to its importance as a measure of the interfacial area needed for mass transfer. For all submergence levels, the same qualitative droplet size distribution characteristics can be observed, i.e. a right skewed unimodal distribution with a mode between 0.1 mm and 0.2 mm. Increasing the superficial gas velocity causes an increase of the peak and at the same time a slight decrease of the bigger droplets. The mode is though staying relatively constant over all the measurements.

Based on equation (2.26), the Sauter mean diameter D_{32} is calculated for all performed measurements. The results are presented in Figure 52. The Sauter mean diameter is located between 0.15 and 0.3 mm for all test conditions. As expected also from other studies, D_{32} decreases with an increase in the superficial gas velocity. The limited spatial resolution for droplets smaller than 120 µm of the high-speed camera lead unfortunately to considerably big error bars. Nevertheless, the results give an estimate on the expected droplet size and can hence be used for comparison with other works or correlations. Taking the uncertainty limits into account, no significant difference between the tested submergence levels can be observed. Therefore, the following discussion will focus on the measurements performed for a submergence level of 0.5 m.

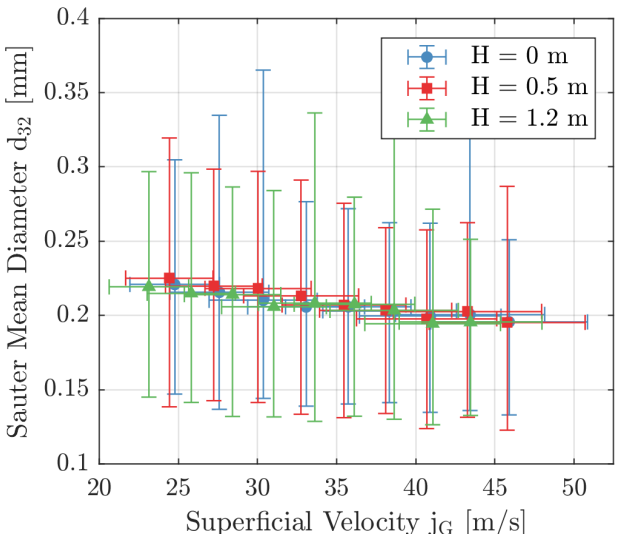

Figure 52: Sauter mean diameter (D_{32}) of the droplet size distribution as a function of the superficial gas velocity (j_g) for different submergence levels (H) as presented by Breitenmoser et al. [107].

In Figure 53, the measured Sauter mean diameters for a submergence level of 0.5 m are compared with the results obtained by Teixeira et al. [153], Alonso et al. [119] and Silva et al. [155]. The measurements of Silva et al. are the only ones which are within the range of the experimental superficial gas velocity applied in this work. Considering the error bars, the experimental results agree with the results obtained by Silva et al. The measurements performed by Alonso et al. and Teixeira et al. were all at higher superficial gas velocities. However, assuming that the dependence of the Sauter mean diameter on the superficial gas velocity is similar, Alonso et al. found smaller droplet sizes compared to the experimental results of Silva et al. and those of this study. A comparison between the data is in any case rather difficult. First, for all three studies, no uncertainty analysis was performed and thus the statistical significance of the different results cannot be interpreted. Second, as shown by Azzopardi and Govan [118] as well as Silva et al. [155], different physical processes drive the droplet size dynamics in different scaled Venturi scrubbers, e.g. turbulent breakup or coalescence. A direct comparison of Venturi scrubbers with a significantly different throat size might therefore not be possible. Compared to the other studies, the Venturi scrubber used for this study is also operated in a self-priming mode.

As discussed previously, the superficial liquid velocity in a self-priming Venturi is linked to the superficial gas velocity, i.e. an increase of the gas flow rate causes a decrease of the liquid flow rate and vice versa. Despite the superficial liquid velocity varying only slightly in the experimental range of this study, it is important to compare this quantity with actively driven Venturi scrubbers. A last point worth noting is the fact that Teixeira et al. [153] and Alonso et al. [119] performed the droplet size measurements at the outlet of the Venturi nozzle, i.e. at the end of the diffusor section, whereas the measurements performed by Silva et al. [155] and this study are carried out at the end of the Venturi throat section. Unfortunately, the study performed by Parker and Cheong did not report any quantitative mean droplet diameter parameters. Therefore, their data cannot be included in the comparison presented here.

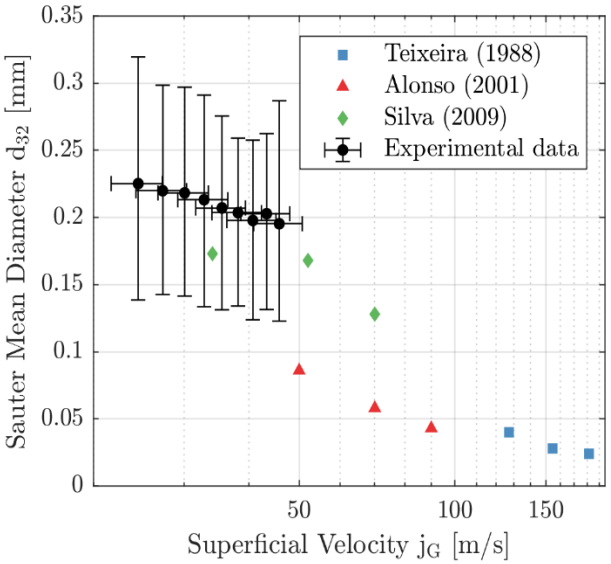

Figure 53: Experimental Sauter mean diameter (D_{32}) obtained by Teixeira et al. [153] for j_l=0.23 m/s, Alonso et al. [119] for j_l=0.1 m/s and Silva et al. [155] for j_l=3,2·10^{-3} m/s together with the present experimental results for 0.5 m submergence level (H) as a function of the superficial gas velocity in the throat (j_g) as presented by Breitenmoser et al. [107].

The experimental results are also used to assess Sauter mean diameter correlations. Two of the most used correlations for collection efficiency models developed for industrial Venturi scrubbers with liquid film injection, as they were used by Ali et al. [34], [35], [145] or Zhou et al. [36] for their studies are the

Nukiyama and Tanasawa and the Boll correlation. Based on the equations (2.32) and (2.33) and the operational parameters applied in this study, the two correlations are plotted together with the experimental Sauter mean diameter data in Figure 54 for a submergence level of 0.5 m. Both correlations overestimate the experimental results excessively.

This overestimation might come from the fact, that both correlations, Nukiyama and Tanasawa as well as Boll, limited their correlations to a specific operational range. Especially the liquid flow rate in this work is well above the range of the two correlations, owed to the self-priming operation mode. Additionally, in both correlations, the dimensions of the Venturi scrubber and more specifically the throat section are not represented, although it was shown by various studies that the Venturi size has a significant impact on the droplet size distribution, i.e. by Azzopardi and Govan [118] and Silva et al. [155]. Last but not least, both correlations were developed for liquid spray injection. Hence, an incorrect droplet generation process is assumed by using these correlations, which would be the pneumatic atomization. In film injection type Venturi scrubbers, entrainment is the dominant process by which droplets are generated within the throat section. Consequently, by assuming spray injection for a liquid film injection type Venturi scrubber, the liquid load in the throat is significantly overestimated and thus the Sauter mean diameter. This is mostly visible at low gas and high liquid flow rates, which are characteristic operational conditions for self-priming Venturi scrubbers.

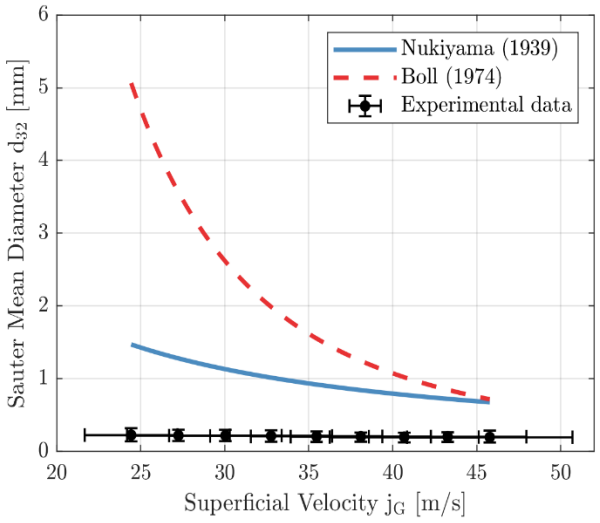

Figure 54: Sauter mean diameter (D_{32}) according to the correlation developed by Nukiyama and Tanasawa [129] and the correlation published by Boll [150] together with the present experimental results for 0.5 m submergence level (H) as a function of the superficial gas velocity in the throat (j_g) as presented by Breitenmoser et al. [107].

If the droplet formation mechanism is the leading driver for the Sauter mean diameter, annular flow correlations developed for straight tubes might agree much better with the experimental data obtained in this study. For both, the Venturi scrubber with liquid film injection as well as annular flows in straight tubes, droplet entrainment from a surface of a liquid film is the dominating droplet generation process as documented by Berna et al. [134]. Additionally, most of the annular flow correlations account for the hydraulic diameter of the corresponding flow.

In Figure 55, five common droplet size correlations for vertically oriented straight tubes are plotted together with the experimental data for a submergence level of 0.5 m. The order of magnitude between the experimental data and the annular flow correlations is much better compared to the two correlations discussed before. The correlation developed by Kocamustafaogullari et al. [133] shows the lowest deviation from the experimental data with a root mean square error of 0.04 mm. The correlations developed by Tatterson et al. [131], Kataoka et al. [132] and Sarimeseli and Azzopardi [135] agree also quite well with the experimental data. The slight overestimation of the correlation published by Berna et al. [134] might be explained by the wider applicability range, i.e. Berna et

al. considered many more fluids and broader operational conditions compared to the other four correlations, which are mainly limited to air-water two-phase flows for ambient conditions.

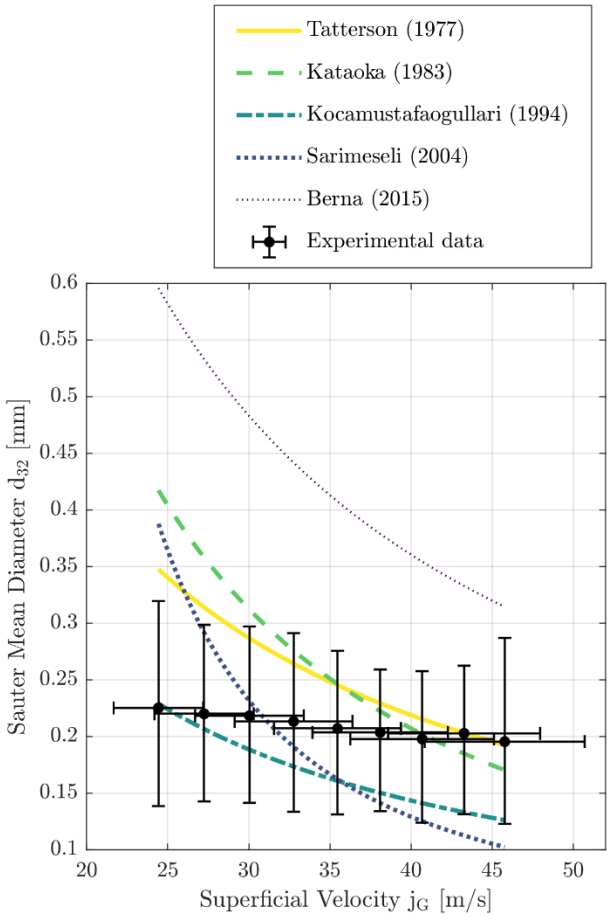

Figure 55: Sauter mean diameter (D_{32}) according to common correlations for straight tubes together with the present experimental results for a submergence level (H) of 0.5 m as a function of the superficial gas velocity (j_g) as presented by Breitenmoser et al. [107].

However, the pronounced decreasing trend of droplet size with increasing gas superficial velocity, seems to be weaker in the experimental results than predicted by the annular flow correlations. This weaker trend might be a result of the significant differences between the geometry as well as the operation of the Venturi scrubber and the vertical tubes related to the annular flow correlations. The measurements were performed with a Venturi scrubber operated in self-priming mode. As mentioned earlier, Venturi scrubbers in self-priming operation show a self-regulating behavior, i.e. for an increase in the gas flow rate, the liquid flow rate is decreasing and vice versa.

Lehner [157] and Mayinger and Lehner [156] could show experimentally that this behavior results in an almost constant scrubbing efficiency over large ranges of gas flow rates. This stable retention performance of the self-priming Venturi scrubber could be a result of the observed weak trend in droplet size as a function of the gas flow rate. Second, in contrast to the pipes with a circular cross-section adopted for the annular flow correlations, the presented Venturi scrubber had a rectangular cross-section and a slit-type injection. Parker and Cheong [144] observed a strong importance of the leading edge of the throat in the droplet generation and might also explain the difference between the experimental data and the correlations. In addition, the experimental results published by Costa et al. [161], who also analyzed the droplet size distribution in a rectangular Venturi scrubber, seem to confirm the weak trend observed in the measurement data. The ratio between the throat length and the hydraulic diameter was relatively small, i.e. only about three, which could be another reason for the weak tendency. Although the measurements were performed at the end of the throat, the flow is not expected to be fully developed. The difference in the trend might therefore also come from the difference of the non-developed flow in the measurements and the assumed fully developed flow in the annular flow correlations.

Although there is a clear difference in the trend, the general agreement in magnitude between the annular flow correlations and the experimental data compared to the correlations by Nukiyama and Tanasawa as well as by Boll et al. is significantly better and confirms the assumption that the physical droplet generation process is essential in correlating descriptive mean droplet diameters in Venturi scrubbers.

Two-Phase Flow Evolution in the Pool

The film and droplets are as mentioned earlier only one stage of the retention qualities of a Venturi scrubber. If the nozzle is operated in submerged mode, the two-phase flow mixture in the nozzle is injected into the pool. There, it forms a heterogeneous flow with a very chaotic structure where gas bubbles can be further scrubbed. The quantification of this flow condition will

be valuable for further model development of the bubble rising zone with Venturi nozzles.

At first, the void fraction evolution over the dimensionless distance is plotted for the five measured superficial gas velocities in Figure 56. Similar to the liquid suction flow rate and the droplet size distributions, the average void fraction is not strongly affected by the gas flow rate. The void is steadily increasing over height which is attributed to the flow evolution and the fragmentation of the bigger bubbles that are injected into the pool. After 3 L/D_H, considering the error bars, the average void fraction remains relatively stable which could be an indication for a steady flow situation.

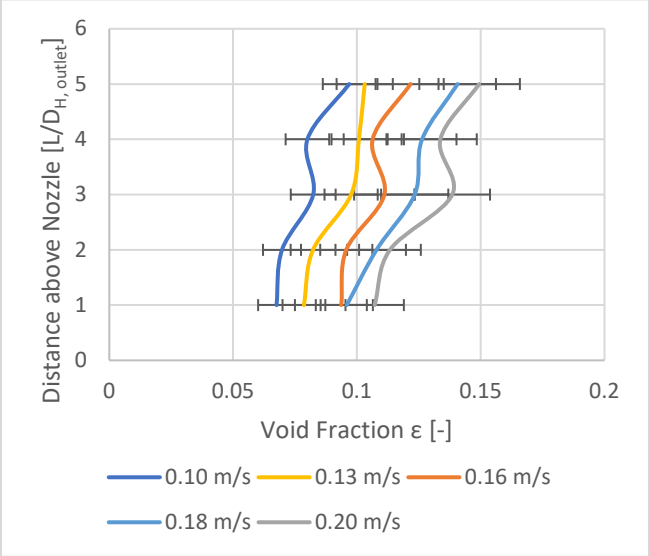

Figure 56: Void fraction evolution above the Venturi nozzle exit for typical gas flow rates inside the TRISTAN facility.

Using the tomographic abilities of the WMS, the void fraction can be averaged over time to have a closer look to the void fraction distribution across the channel area. As the Venturi has two opposite exits, it is not surprising that the void fraction distribution would show two distinctive peaks as shown in Figure 57 at the closest distance. With increasing height, these two peaks are blurring and a more uniform distribution is developing.

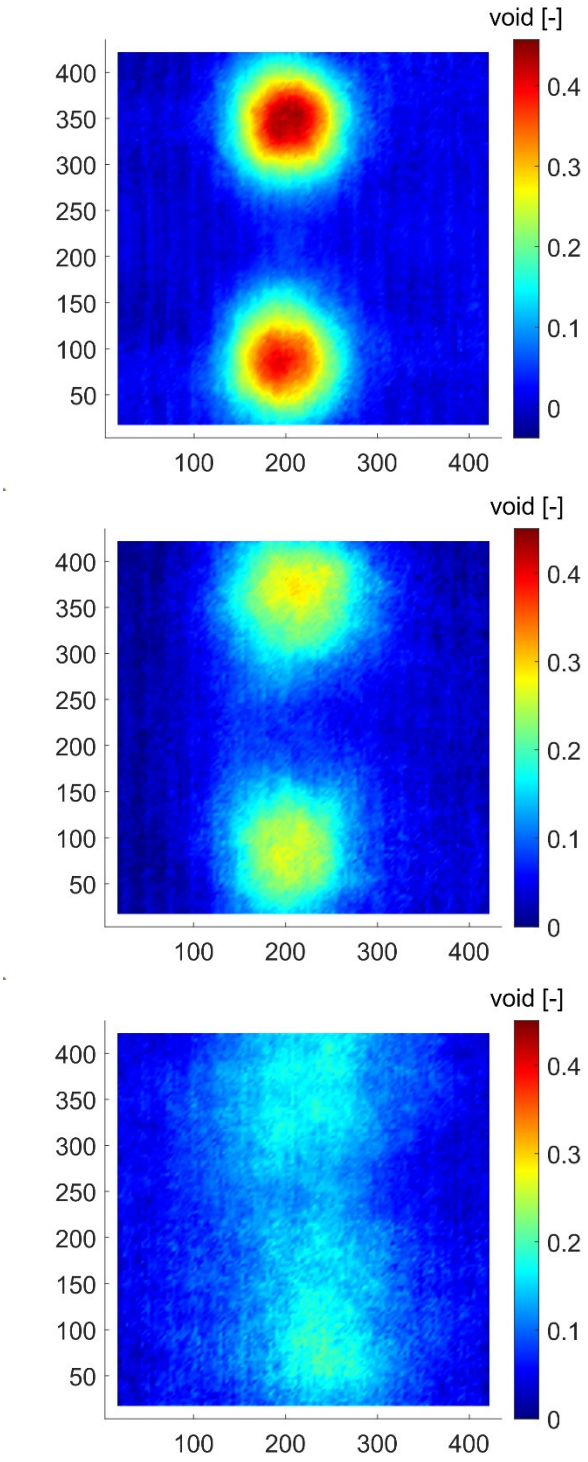

Figure 57: Void fraction distribution over the whole test cross-section of the facility at 0.1 m/s superficial gas velocity at distances 1 L/D_H, 3 L/D_H and 5 L/D_H from top to bottom.

These profiles are also agreeing to the observations of the average void fraction in Figure 56. The void

fraction had for all gas flow rates two distinct peaks at the closer three measuring points, which were exactly above the laterally oriented outlets of the Venturi nozzle (cf. Figure 48). Further away from the nozzle, the peak widened as the gas volume is distributed over a bigger part of the cross section of the facility. The dilution of the peak becomes less from 3 L/D_H onwards.

The bubble side distributions in Figure 58 should give more information on the made assumptions. As it can be seen, the trend follows a trimodal distribution which is seldomly seen in two-phase flows. The injection method of a two-phase flow mixture from a Venturi diffusor is on the other hand also quite unusual. The cut-off at around 2 mm was done by the recognition algorithm as it discards all bubbles that are smaller than half the pitch in compliance with the validation work of the sensor. It appears that at first, a very high share of big gas volumes is formed. With growing distance from the nozzle, a clear increase over the height of the bubbles with an equivalent diameter of 15 mm can be observed. For the smaller flow rate, i.e. 0.1 m/s superficial velocity, the bubble size distribution remains the same after 3 L/D_H. The shift of the smaller peak for the furthest distance is probably attributed to the decreasing gas phase velocity which was used for the analysis of the bubble volumes. At the highest measured superficial velocity, 0.2 m/s, the bubble breakup process is not done after 3 L/D_H. The peak for the smaller sizes keeps increasing up to the furthest distance even though the change from 4 L/D_H to 5 L/D_H is only minor. The main difference between both flow rates is the volumetric share of the bigger bubbles at the closest distance. The additional gas flow is stored in the big gas churns and not finely dispersed which explains why the void fraction in Figure 56 is not varying that much. However, the big gas volumes are fragmented fast as the peak is decreasing in height and comes closer to the distribution of the smaller flow rate. Nonetheless, the flow remains very heterogeneous up to the furthers measured distance with the smaller bubbles dominating in volume but with good share of big churns still present.

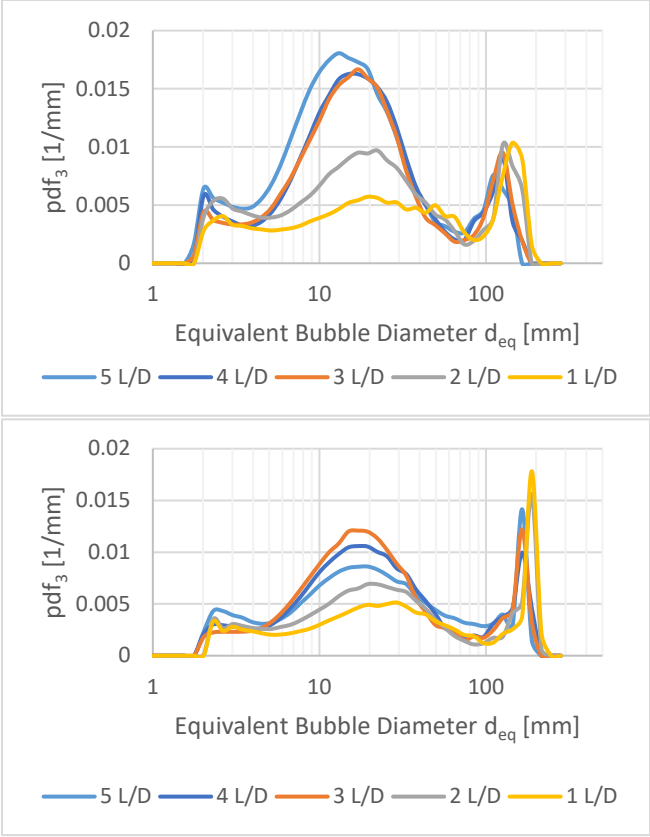

Figure 58: Bubble size distributions at different pool height positions for 0.1 m/s (top) and 0.2 m/s (bottom) superficial velocity

The virtual side view of the center through the two gas streams above the Venturi nozzle are shown for a superficial velocity of 0.1 m/s in Figure 59. At the closest distance, i.e. Figure 59 a), the big churns and the first fragmented gas bubbles can be found. The two distinctive streams can be followed over the height up to 3 L/D_H in Figure 59 c). At 4 L/D_H, the streams are less pronounced as the bubbles are spread over the whole length of the WMS. This is in agreement with the diluted void fraction peaks in Figure 57.

The virtual side view also confirms the trimodal shape the bubble size distribution. At all four distances, there are three types of bubbles visible. The most dominant are the big gas volumes which are less numerous but would hold a big share of volume. The second type are the fragmented churns which are the most frequent type in the side views. The last type are the very small bubbles with the size of a couple of millimeters, seen as dots in the side view. They are very few at the closest distance but grow in number as the

flow develops. Yet, their volumetric contribution is rather small but they cannot be neglected from a scrubbing point of view as they increase the interfacial area.

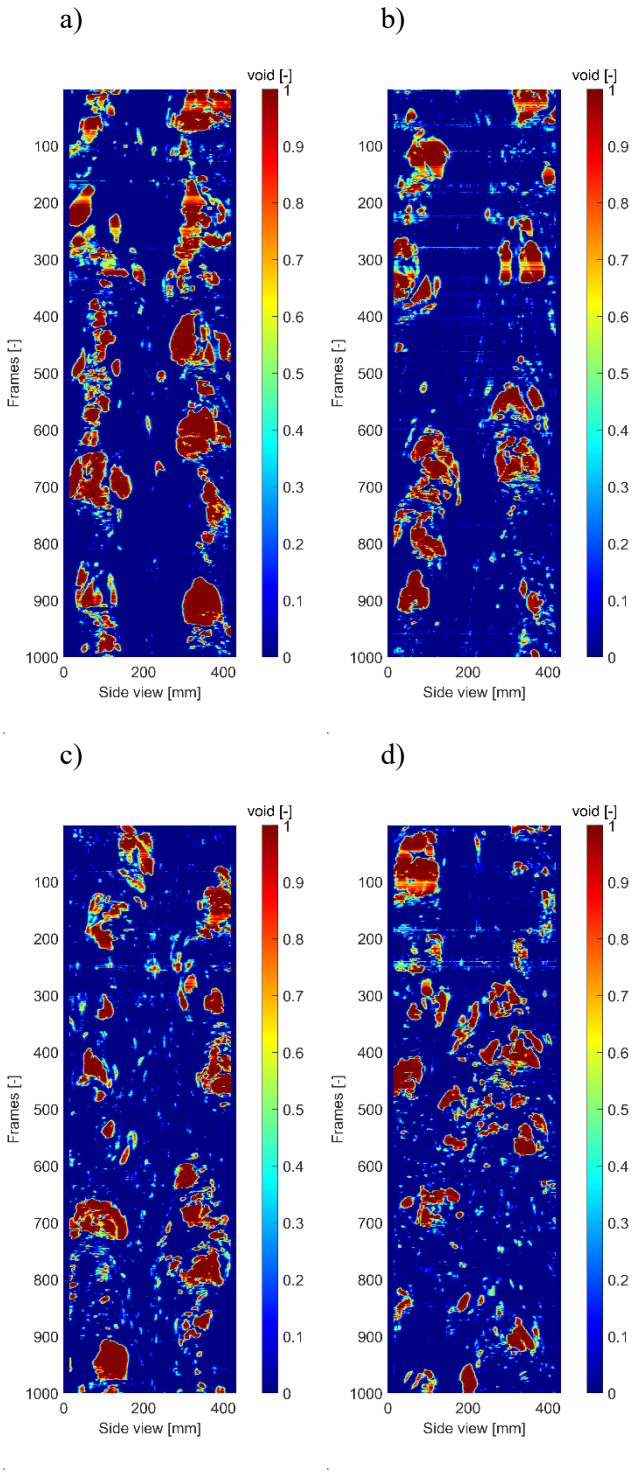

Figure 59: Virtual side projection of the flow evolution of the Venturi nozzle at 0.1 m/s superficial velocity for a) 1 L/D_H b) 2 L/D_H c) 3 L/D_H d) 4 L/D_H.

As the interfacial area density can now be assessed without the information of the bubble velocity, the previously observed flow development should also be seen in this quantity. The evolution of the interfacial area density is plotted in Figure 60. As seen in the average void evolution, the steadiness of the Venturi nozzle stands out. Almost independent of the injection flow rate, the interfacial area density is increasing only over the facility height and thereby almost doubling in value. Also, in the interfacial area density progression, the flow seems to develop after a distance of 3 to 4 L/D_H away from the nozzle as the values stay within the uncertainty margin.

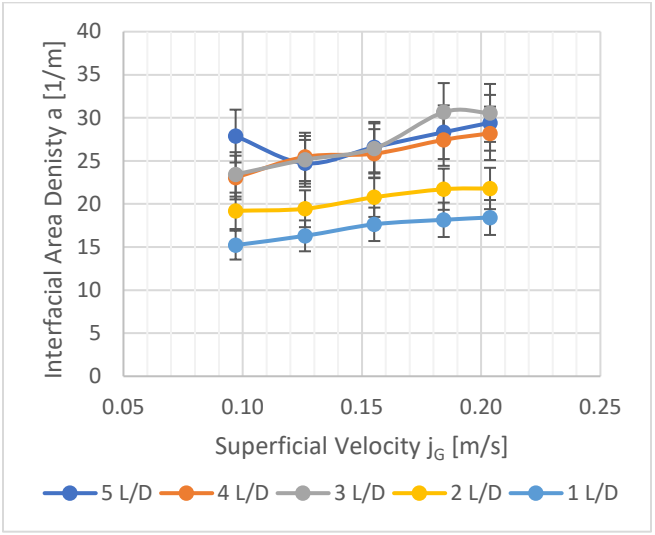

Figure 60: Interfacial area density at different positions above the Venturi nozzle at different superficial velocities.

During the analysis of the droplet size estimation, the steadiness of the droplets was already noticed. And as also mentioned by Lehner [157] and Mayinger and Lehner [156], the Venturi nozzle has an almost constant scrubbing efficiency over a variety of gas injection flow rates. The same behavior was observed for this nozzle in the interfacial area density. The bubble size distribution in Figure 58 is giving a possible reason for this. At higher superficial velocities, the additional gas volume was mostly stored in the already quite big bubbles. By increasing their size, the interfacial area is increasing slower than the volume which could explain why there was only a small change observable. Only by breaking up during the rise in the pool, the interfacial area density gained substantially in value.

Conclusions on the Venturi Nozzle

The Venturi nozzle is complex and difficult to design and even more difficult to model. Compared to a traditional gas injector design, where gas is injected into a pool and rises towards the pool surface, the Venturi nozzle adds another region which is the flow situation inside the throat and diffusor of the nozzle. The droplet sizes inside the throat as the two-phase flow situation in the pool were both investigated at ambient temperature conditions.

In nowadays simulations, the droplet size estimation for FCVS related activities is performed by the application of correlations derived from the chemical process engineering. These nozzles are actively driven Venturi tubes and cannot be applied to self-priming ones as used in the nuclear field without validation. This could be shown by using direct high-speed imaging shadowgraphy on a full-scale commercial Venturi nozzle used in FCVS. Unfortunately, the resolution limitations from the used camera equipment lead to relatively big error bands and most likely to an overestimation of the droplet sizes as droplets below 120 µm would not be captured. Yet, even with these uncertainty levels, the values were significantly smaller than the predicted Sauter mean diameters determined by the aforementioned correlations. The high liquid load primarily resulting from the self-priming operation mode overpredicts the droplet sizes by an order of magnitude. Given that fact, it is important to further assess the droplet sizes experimentally to decrease this discrepancy. One idea for the future model improvement was to look into correlations that are based on the same droplet formation mechanism, i.e. liquid entrainment. Annular flow correlations were taken that were established for similar sized round pipes and the results agree much better to the real values, even though they cannot fully capture the trend. The diffusor exit and the short length of the throat certainly were localized to probably have their contribution to this discrepancy. Furthermore, the uncertainty resulting from the resolution limitation of the high-speed camera makes a trend detection rather difficult and could only be improved with a new test series with a higher resolving camera. Unfortunately, the limitation of the adiabatic conditions will persist as the method relies on transparent materials for optical access and major modifications would be required to use steam and non-condensable mixtures.

Operating in submerged mode, the scrubbing goes on in the liquid bulk of the pool where the morphology of the two-phase flow is changed in a continuous liquid with dispersed bubbles. At realistic gas flow rates, the obtained void fraction was analyzed and did not show a strong dependency on the gas flow rate, similar to the droplet size distribution. The same was true for the interfacial area density. The only difference could be found in the bubble size distribution where the volumetric share of the globule bubbles increased with higher flow rates. This particular design proved that if the gas flow rate stays within its specification, the hydrodynamic quantities have nearly no dependence from the gas flow, being it droplets or bubbles. In other works, the constant scrubbing efficiency was also highlighted that showed no significant change over various gas flow rates which could be due to the steady hydrodynamics.

Looking only into the two-phase flow evolution in the pool, a comparison between the IMI-Nuclear CCI nozzle and the Venturi design is possible. The interfacial area density of the bubbles achieved by the Venturi nozzle for the same superficial velocities was in the same order of magnitude as the CCI nozzle with the impaction plates. This advantage persists only until the flow reaches the mixing element, which doubles to triples the value of the interfacial area density depending on the gas flow rate. However, the Venturi nozzle benefits from additional interfacial area density in the throat and diffusor coming from the droplets and the liquid film.

From a modeling aspect, the existing system codes with their assumption of the three distinct regions for pool scrubbing, will not be easily applicable for wet scrubber based FCVS. Even though a breaking up of the globule bubbles after the injection region could be observed in all cases, the flow remained in the heterogeneous churn-turbulent region with smaller bubbles dominating in volume share. SPARC compared to BUSCA considers at least a globule bubble share, but not the heterogeneity of the remaining bubbles in the two-phase flow. The results of both nozzles suggest that separate models should be considered to predict the retention efficiency more accurately.

4 DIFFUSIVE MASS TRANSFER IN BUBBLY AND SLUG FLOW

In process engineering, two-phase flows are widely applied for mass transfer and chemical reactions between gas and liquid phase or even with particulate matter. The application of bubble columns as chemical reactors is widespread, e.g. for gas purification of flue gas lines from coal combustion as studied by Hutson et al. [162] or Paul et al. [163] or the scrubbing of NO_x and SO_2 gases with a new electrochemical approach as reported by Pillai et al. [164]. Bubble columns operate even in three-phase-flows, for example in slurry applications in waste water treatment for the production of biofuels as presented by Chaudhary et al. [165]. Depending on its purpose, different phases are interacting with each other in a process of mass exchange, with or without the purpose of running a chemical reaction or heat transfer between the phases. The design of such columns is often quite simple since no moving parts are necessarily required, the efficiency of the reactors is well-studied, and the upscaling is easily achieved by setting up cascades or parallel columns. The lack of moving elements in the simplest bubble column designs makes the maintenance simple too.

Containment venting filters based on wet scrubbers are bubble columns operating often at untypically high flow rates. The relevant internals of these scrubbers consist mostly of a special nozzle and in some cases a bubble breaker mesh which makes the scrubbers rather simple columns. Unlike the chemical reactors where the flow can be controlled and adjusted to optimize the desired product output, the passive design of the nuclear filter designs will activate at elevated pressures which requires the ability to operate in a wide range of volumetric flow rates. As seen in section 3, these high flow rates lead to the formation of heterogeneous, chaotic flow conditions. The chemical sector has extensively studied bubble columns, they are however acting mostly in the homogeneous bubbly flow regime. Nonetheless, the similarity of the transfer process as described by the gas solubility models in the pool scrubbing codes, the research from the chemical field could be looked into to improve those aforementioned models. Consequently, the most established correlations should be investigated for their applicability for nuclear wet scrubbers.

In two-phase flow mass transfer, there are different assumptions in order to model the diffusion between the two phases. A very common approach is the two-film two-resistance theory as firstly introduced by Lewis and Whitman [166]. The underlying concept of their theory assumes that on both sides of the gas-liquid interphase, there is a thin boundary layer of gas and liquid which is not influenced by the convective mixing effects of the flow. As a consequence of this hypothesis, the transfer of mass in both ways, i.e. absorption or desorption of gas, is limited only by the diffusion processes in both phases as the films are free of convection. Thus, the two films can be interpreted as resistances that control the mass transfer rate, described by two individual mass transfer coefficients. Depending on the solubility of the gas, one of the two sides will be the dominating resistance. A lot of works in the past have focused on studying the liquid side mass transfer, mostly because the gas side mass transfer is not relevant in pure gas scenarios or because the limiting absorption was more limiting.

Starting chronologically, one of the earlier works on mass transfer in bubble columns was performed by Hughmark [167] who correlated the gas hold up and bubble sizes on the liquid side coefficient with his own data but also with other publications dealing with bubble swarms. He found in his work that smaller bubbles tend to have a higher liquid side mass transfer coefficient and proposed a correlation for the Sherwood Number Sh (4.1) that he derived from his results with a dependency of the bubble diameter. The correlation is based on the Schmidt number Sc and the Reynolds number Re, the liquid side diffusion coefficient D_L and the bubble diameter D_P (4.2) that requires the surface tension σ and the liquid density ρ_L to calculate.

$$Sh = \frac{k_L * D_P}{D_L} = 2 + 0.061 * Re^{0.484} * Sc^{0.339} * \left(\frac{D_P * g^{\frac{1}{3}}}{D_L^{\frac{2}{3}}} \right)^{1.61} \tag{4.1}$$

$$D_p = \frac{0.25}{12} * \left(\frac{\sigma}{72} \right)^{0.6} * \left(\frac{62.4}{\rho_L} \right)^{0.2} \tag{4.2}$$

A very widely used model comes from the studies of Akita et al. [168, 169]. In both works, they obtained

a model for the average void fraction ε (4.3), the volumetric mass transfer coefficient k_La (4.4) and, via the Sauter mean diameter d_{32}, the liquid-side mass transfer coefficient k_L (4.5). Unlike the correlations of Hughmark (4.1), Akita et al. included the column diameter D_{ch} through the Eötvös number *Eö*, the Galileo number *Ga*. Their medium-sized bubble column had an inner diameter of 15.2 cm that was fed from a gas chamber at the bottom with a 5 mm single hole as an injector. The Sauter mean diameter was measured by direct imaging techniques where the bubble sizes were obtained by the analysis of single images. Assuming a homogeneous flow pattern with spherical shaped bubbles, the interfacial area can be derived from the Sauter mean diameter as presented in (4.6).

$$\frac{\varepsilon}{(1-\varepsilon)^4} = 0.2 * E\ddot{o}^{\frac{1}{8}} * Ga^{\frac{1}{12}} * Fr; \quad (4.3)$$

$$k_La = 0.6 * \frac{D_L}{D_{ch}^2} * Sc^{0.5} * E\ddot{o}^{0.62} * Ga^{0.31} * \varepsilon^{1.1} \quad (4.4)$$

$$\frac{k_L * d_{32}}{D_L} = 0.5 * Sc^{0.5} * Ga^{0.25} * E\ddot{o}^{0.375} \quad (4.5)$$

$$a = \frac{6*\varepsilon}{d_{32}} \quad (4.6)$$

Hikita et al. [170, 171] did similar tests in two different columns with 0.1 m and 0.19 m inner diameter and different single nozzles, between 9 mm and 36.2 mm inner diameter. In their work, they came up with the expression (4.7) for the void fraction and (4.8) for the volumetric mass transfer coefficient k_La (4.7).

$$\varepsilon = 0.672 \left(\frac{j_G \mu_L}{\sigma_L}\right)^{0.578} \left(\frac{\mu_L^4 g}{\rho_L \sigma_L^3}\right)^{-0.131} \left(\frac{\rho_G}{\rho_L}\right)^{0.062} \left(\frac{\mu_G}{\mu_L}\right)^{0.107} \quad (4.7)$$

$$k_La = 14.9 \left(\frac{j_G * \mu_L}{\sigma_L}\right)^{1.76} \left(\frac{\mu_L^4 * g}{\rho_L * \sigma^3}\right)^{-0.248} \left(\frac{\mu_G}{\mu_L}\right)^{0.243} \left(\frac{\mu_L}{\rho_L D_L}\right)^{-0.604} \quad (4.8)$$

Deckwer et al. [172] did very extensive research in quantifying also the hydrodynamics in the column. Two columns were used, one with an inner diameter of 0.2 m and one with 0.15 m. As spargers, a cross with 56 nozzles of 1 mm in diameter and a glass sintered porous plate with a pore diameter of 150 µm were used in each column respectively. Their empirical correlation (4.9) was only dependent on the superficial gas velocity and two constants that would change with the nozzle geometry and the used liquid and gas.

$$k_La = b_0 * j_g^{b_1} \quad (4.9)$$

Calderbank and Moo-Young [173] agreed in their work to the observation of Hughmark [167] that smaller bubbles have a higher liquid-side mass transfer coefficient k_L but that the coefficient would stay constant beyond a certain threshold. The boundary was found to be around a Sauter mean diameter of 2.5 mm. Their mass transfer coefficient would be a pure function of material and the gravitational constant (4.10).

$$k_L = 0.42 \left(\frac{\Delta\rho * \mu_l * g}{\rho_l^2}\right)^{\frac{1}{3}} \left(\frac{\mu_l}{\rho_L * D_L}\right)^{-\frac{1}{2}} \quad (4.10)$$

The range of the operational parameters of all the presented correlations can be found in Table 11. These studies focused mostly on the mass transfer and used the instrumentation available at that time to determine

Table 11: Experimental range of the compared correlations of Hikita et al., Deckwer et al., Akita et al., Hughmark, Calderbank and Moo-Young as found in literature and this work.

	Hikita et al. [171]	Deckwer et al. [172]	Akita et al. [168]	Hughmark [167]	Calderbank and Moo-Young [173]	This work
Dynamic viscosity [Pa·s]	0.001 – 0.019	-	0.00058 – 0.021	0.0009 – 0.152	0.0006 – 0.0897	0.001
Liquid density [kg/m^3]	998 – 1230	-	800 - 1600	768 – 1698	1000 - 1178	998
Surface tension [N/m]	0.038 – 0.755	-	0.022 – 0.0742	0.025 – 0.076	-	0.072
Facility Diameter [m]	0.1 0.19	0.15 0.2	0.154 0.6	0.025	-	0.05
Nozzle Diameter [m]	0.013 0.0206 0.0362	$150 \cdot 10^{-6}$ 0.001	0.005	-	-	0.004

hydrodynamic quantities, e.g. using the swell level to measure the average void fraction or evaluating photographs by image processing methods, which work well in the bubbly flow region but suffer from a high uncertainty in more heterogeneous flows. This is in particular true for the interfacial area density, which was estimated in many works, e.g. Akita et al. [169], by using the Sauter mean diameter and assuming homogeneous flow conditions. This assumption can be made in low superficial gas velocity ranges but is prone to bigger uncertainty in the transition regimes. The bubble sizes were obtained using stationary photographs, not considering the temporal changes of the bubble sizes due to the progressing absorption and desorption of the gaseous phase. Most of the works also stayed in the bubbly or cap flow regime since the characterization of the required parameters like interfacial area density or void fraction is quite difficult for the heterogeneous regime.

Some works used literature correlations instead of measurements to quantify their flow regime inside the column, i.e. for void fraction or interfacial area density. The concentrations of the absorbed gas in the liquid for the determination of the mass transfer coefficient were usually measured with chromatographs, the Winkler method or an oxygen sensor and verified by checking the global mass balance of the incoming and outgoing gas stream. The difficulty in analyzing flow regimes beyond bubbly flow and the limited applications of heterogeneous flow regimes in process engineering led to little work existing in these flow regimes like Krishna et al. [174] or Vandu et al. [175], Vermeer et al. [176].

The two-phase flow regime in wet scrubbers as studied in the previous section showed that there is a need to measure mass transfer effects also in the churned-turbulent flow regime. As part of this work, the aim in this section is to establish and assess a new measuring technique and perform a generic study on the effect of the flow regime on the mass transfer. To achieve this, the hydrodynamics were fully characterized and a new method was established by using wire-mesh sensor technology and carbon dioxide as a model gas, mixed with nitrogen as carrier gas in some of the tests to characterize the flow structure and measure instantaneous gas concentrations dissolved in the liquid phase at the same time and in high resolution in space and time.

The choice of carbon dioxide as a model substance deserves explanation. A flow of steam and air mixture loaded with small concentrations of iodine would have been a more realistic condition found during severe accidents. Unfortunately, iodine is a difficult gas to deal with due to its highly corrosive properties on any steel surface, even on stainless steel. Furthermore, the development of a new measurement methodology requires validation data performed with established techniques or literature to be compared with. The amount of iodine mass transfer tests is rather small which made it not an optimal candidate to start with. In this sense, a favorable substitute for iodine loaded nitrogen is CO_2. Carbon dioxide is widely available, has been extensively used by others, has no corrosive properties and gas flow controllers can be easily calibrated. The diffusion coefficients of molecular iodine and carbon dioxide have the same order of magnitude. The maximum iodine uptake of water is though, judging by the Henry constant, two orders of magnitude higher than for carbon dioxide (iodine: 3.1 mol/m^3 at 1 atm, carbon dioxide: $3.4 \cdot 10^{-2}$ mol/m^3 at 1 atm [177]).

However, the main idea of the experiments conducted in this section is to gain basic understanding of the gas-liquid mass transfer in bubble columns with a new proposed method that should get a first impression on the thermal-hydraulic impact on the mass transfer and should simplify future experiments.

4.1 Extended Methodology for Mass Transfer Measurements using WMS

The first aim was to take a deeper look into the influence of the two-phase flow on the diffusion processes within a bubble column for different flow regimes. Carbon dioxide absorption measurements were carried out in a rectangular column of 50 x 50 mm^2 cross section, instrumented with a WMS. The calibration and data processing required for the hydrodynamic characteristics of the two-phase flow from primary WMS signal have been described in section 2.1. For the quantification of the mass transfer from the gaseous to the liquid phase, the increase of the electrical conductivity of the liquid by the dissolved

CO_2 was evaluated. It can be distinguished from the presence of gas in the measuring plane, since the latter reduces the conductance signals.

Dissolution of Carbon Dioxide in Water

Carbon dioxide has a considerable physical solubility in water that is proportional to the partial pressure of CO_2 in the gaseous phase as described by Henry's Law. After dissolution, carbon dioxide can chemically react with water to form carbonic acid, bicarbonates or carbonates depending on the acidity of the aqueous solution. The carbonic acid from CO_2 with water is formulated in (4.11) and the dissociation reaction of carbonic acid can be found in (4.12).

$$CO_{2(aq)} + H_2O \Leftrightarrow H_2CO_{3(aq)} \tag{4.11}$$

$$H_2CO_{3(aq)} \Leftrightarrow H_3O^+_{(aq)} + HCO^-_{3(aq)} \tag{4.12}$$

In the pH range of this work, i.e. around 7, the reaction rate of carbonic acid is according to Housecroft and Sharpe [178] slow, whereas the dissociation is very fast. Therefore, it can be assumed that the majority of the formed carbonic acid is present in its dissociated form as ions in the water. Demineralized water itself has a low electrical conductivity. The only ions in pure water are the result of the self-ionization of water by dissociating 2 water molecules into H_3O^+ and OH^- (4.13). The presence of additional ions in demineralized water will increase the electrical conductivity significantly.

$$2\,H_2O \Leftrightarrow H_3O^+_{(aq)} + OH^-_{(aq)} \tag{4.13}$$

The use of higher conductive water, e.g. by adding salt to demineralized water or using tap water, would make the data processing of the WMS raw data for the hydrodynamics easier. However, the dissolved impurities could buffer the ion formation from the dissociation equation (4.12). Carbonates or sulfates could take up hydrogen ions to form bicarbonates or bisulfates and thereby dampen the increase of electrical conductivity in the liquid. The detection of dissolved gas would be thus very difficult and the resolution would drop significantly.

Furthermore, as only a fraction of CO_2 dissolved in pure water reacts with water, most of the dissolved carbon dioxide stays in its molecular form. The increase of the conductivity can be interpreted as dissolved carbon dioxide in aqueous solution. Henry's Law can be hence applied to convert the gas streams into dissolved equilibrium concentrations C_{CO2} in water (4.14). The partial pressure of carbon dioxide can be derived using the molar flow rates of CO_2 ($\dot{n}_{CO_2}$) and N_2 ($\dot{n}_{N_2}$).

$$C_{CO_2} = k\frac{\dot{n}_{CO_2}}{\dot{n}_{CO_2}+\dot{n}_{N_2}}P_{atm} \tag{4.14}$$

The gas solubility in water is temperature dependent, therefore, the Henry constant He as it is given for 298.15K has to be corrected for the temperature condition T of the measurement (4.15).

$$He(T) = \left(He_0 \cdot e^{\left(\frac{-\triangle_{sol}H}{R}\left(\frac{1}{T}-\frac{1}{298.15}\right)\right)}\right) \tag{4.15}$$

$$He_0 = 3.3\times10^{-4}\ \frac{mol}{m^3Pa}, \frac{-\triangle_{sol}H}{R} = 2400\ K$$

Modified WMS Calibration

The dependency of the liquid conductivity from the amount of dissolved carbon dioxide requires a modification of the WMS signal processing. The data have to be segregated to distinguish between instants in which the presence of the gas phase reduces the measured conductance from the increase of the conductance due to dissolved CO_2. Additionally, the signal component containing the information on the electrical conductivity of the liquid phase has to be processed with a calibration curve that yields the concentration of the dissolved gaseous species, which characterizes the intensity of the mass transfer. In this particular case, the calibration curve has to assign a carbon dioxide concentration in aqueous solution to a measured electrical conductivity that is higher than the average reference liquid conductivity σ_L.

An existing calibration data set found in literature by Light et al. [179] used ultrapure water, which would not be easily applicable in the existing facilities. The aforementioned high susceptibility for buffer effects of the formation of carbonic acid and its dissociation can shift the equilibrium and have thus an influence on the electrical conductivity. Since ultrapure water was not available in quantities sufficient for conducting experiments, a calibration with the water of the available quality was inevitable. A calibration matrix had to be obtained for desalinated water of the laboratory faucet at ETH Zürich. This was done in a small dedicated set of measurements. A table-top

facility that followed the design idea of Light et al. [179] was assembled for this purpose as illustrated by Figure 61. The main idea was to create different equilibrium states of carbon dioxide in demineralized water by injecting a mixture of the carbon dioxide concentration with nitrogen as an inert gas. After a settling time allowing the mixture to reach an equilibrium state, the electrical conductivity and temperature were measured simultaneously.

Real in-situ conductivities are needed, whereas commercial conductometers usually apply a temperature compensation to display a value normalized to a standard temperature, e.g. of 25 °C. In the calibration measurements, the temperature compensation of the electrical probe was turned off to replicate the in-situ values the WMS would also measure in the bubble column.

The different molar fractions of CO_2 were reached by adjusting the two flow rates coming from a carbon dioxide and a nitrogen gas tank. As it can be seen in Figure 61, the incoming gas mixture was injected through a glass frit [c] with a P 250 porosity into a three-neck flask [a] filled with demineralized water from the laboratory socket with a base conductivity of around 1 µS/cm. Two out of three necks were sealed to avoid air ingress and the third was left open to release the stream of the undissolved gas and avoid a pressure build up inside the glass flask. A conductivity probe (Greisinger GMH 3400 series) and a thermocouple [b] were placed in each of the side necks to track the evolution of the values. A magnetic stirrer [d] in the flask would make sure that the dissolved gas distributed evenly in the liquid and avoid local build-ups of mass concentrations that might have biased the measurement. The flask was fixed in position by a retort stand.

In a first step, the flask was sparged with pure nitrogen to desorb the atmospheric carbon dioxide and oxygen that is inevitably present in the demineralized water supplied by the centralized system. The conductivity level of the water reached a minimum value of 1.0 ± 0.6 µS/cm [180]. The high uncertainty came from the measuring range of the conductivity probe. In the range below 1 µS/cm, small impurities can strongly affect the electrical conductivity. Subsequently, the nitrogen and carbon dioxide volumetric flow rate were adjusted to create a CO_2 gas concentration in the feed that was increased in steps of 1% in the range below 10% and in steps of 5% until pure carbon dioxide was reached. After each increase of carbon dioxide, the electric conductivity was monitored for 10 minutes until it converged to a stable value. The magnetic stirrer would create a perfectly mixed liquid and the atmospheric mixture in the flask would eventually reach the mole fraction of the incoming gas stream. Therefore, an equilibrium concentration could be established with the atmosphere in the flask. The exchange with the atmosphere would be minimized by having only the small side neck open where the injected gas would eventually escape.

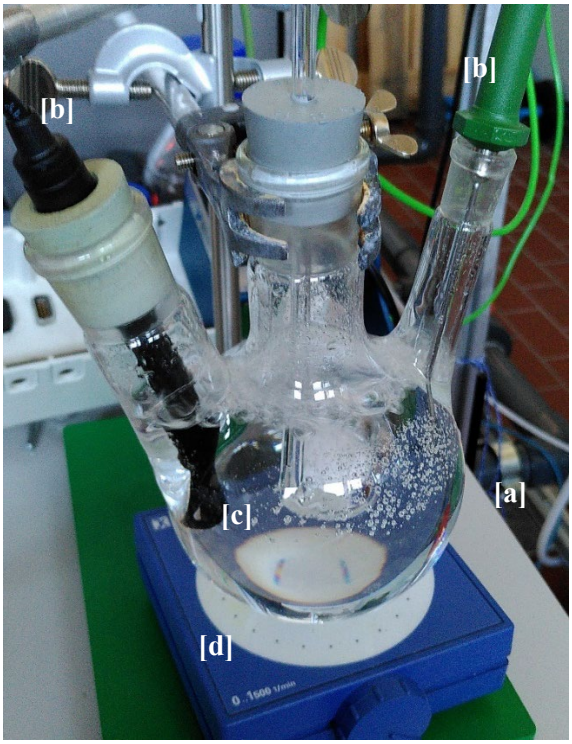

Figure 61: Calibration setup with sealed conductivity probe and thermo couple to quantify the different parameters. [a] 3-neck-flask [b] conductivity probe and thermocouple [c] gas sparger [d] magnetic stirrer

The results of the recorded electrical conductivity data are depicted in Figure 62. The ordinate has already been converted from gas flow rate to dissolved gas concentration in the water. The curve shows as known from literature an exponential function that converges towards a saturation value which would lie at 1720 ± 34.4 ppm at 20°C (cf. Sander [177]). The accuracy of the conductivity measurement device is ±0.3% of the full scale which would correspond to ±0.6 µS/cm. The

reading accuracy of the volumetric flow controller is 1.0% of full scale [181]. For comparison reasons, the data of the studies of Light et al. [179] is also plotted in Figure 62. In their work, the base conductivity at 20 °C was 0.04 µS/cm and they stayed for their studies in a very low concentration region.

The calibration curve can be used in this form to convert electrical conductivity values into carbon dioxide concentration in aqueous solution for measurements performed with carbon dioxide in the gas mixture of the gas phase.

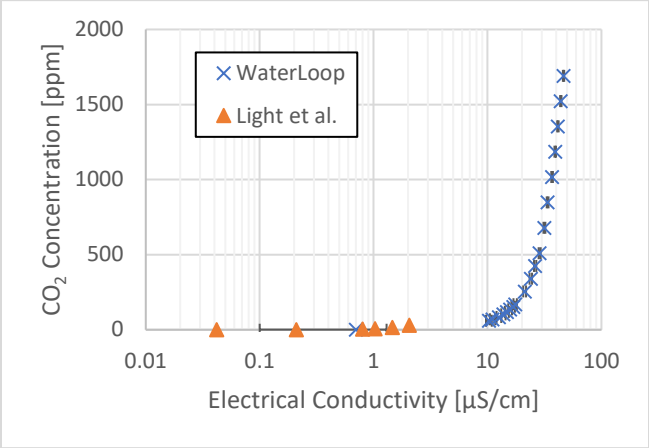

Figure 62: Calibration curve for CO_2 in water in demineralized water at a base conductivity of 0.7 µS/cm at 23 °C and the values of Light et al. [179] at 20 °C.

It has to be kept in mind that the raw data of the WMS do not represent conductivities directly. The stored values are conversion results of the internal analog-digital converters, i.e. 12-bit or WMS integers, from which is known that they are proportional to the instantaneous conductance sampled at the given crossing point of the WMS electrodes. Thus, two additional modifications of the raw data were necessary. The raw signal of a WMS crossing point during a measurement with carbon dioxide injection is shown in Figure 63. At the beginning of the test run, the WMS is recording the base conductivity of the liquid without any gas injection. A similar signal sample without gas injection was also recorded at the end of each experiment. At the same time, the electrical conductivity was measured from a sample that was taken from the facility close to the WMS position with the conductivity meter was used in the calibration experiments. This allowed to correlate the WMS raw signal to an electrical conductivity value for all WMS nodes and deduce the so-called cell constant. Over all measurements, it turned out that the cell constant of the WMS would lie in a narrow range between 0.0142 – 0.016 µS/cm per WMS integer.

After knowing the dependency of the WMS integers from the local instantaneous conductivity at the electrode crossing points of the sensor, the decomposition of the WMS signals into void and CO_2 concentrations can be accomplished. A raw signal stemming from one crossing point recorded during a CO_2 injection test is shown in Figure 63. It is visible that the dips in the signal caused by the passage of bubbles have a much lower characteristic time constant than the continuous growth due to the carbon dioxide dissolution. This difference in the characteristic frequency of both contributions to the total WMS signal allows to obtain short-term averages of the liquid conductivity by the histogram method described in section 2.1, i.e. histograms similar to the one in Figure 6 are calculated around each instant in time. The time over which histograms were accumulated was chosen such that it lied between the characteristic time of signal changes due to bubbles and due to the gas dissolution. For the evaluation of the experiments performed at the WaterLoop facility at ETH Zürich, described later, histograms for the instant t were built from data out of the time interval [t - 0.5 s, t + 0.5 s].

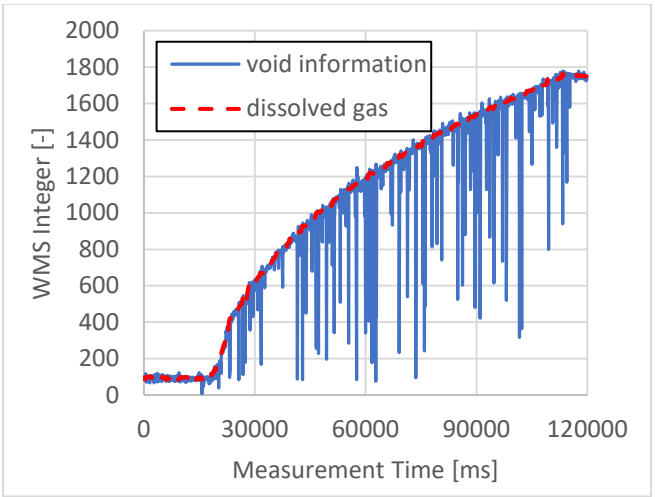

Figure 63: Typical WMS signal trend during a 2-minute recording with carbon dioxide as gas phase with the correction factor overlay in red.

In order to apply the set of routines that were developed for the signal processing of WMS data in experiments with constant conductivity, it was decided to convert the raw signals from the CO_2 tests with the use of a correction factor that eliminates the influence of the CO_2 in the liquid phase. After normalizing the signal with the correction factor, a raw signal corrected to a virtual constant liquid conductivity is found that can be processed by the normal WMS signal processing methods presented in section 2.1. An example of the corrected raw signal is shown in Figure 64. The high noise level at the beginning of the measurement comes from the very low conductivity of the demineralized water at the start of the test. The raw signal has at this stage a low amplitude which is close to the signal noise level. Since the noise amplitude stays approximately constant, the spurious fluctuations of the corrected signal decrease in course of the CO_2 injection, because the correction factor decreases with growing conductivity to 5 – 10 % of the signal amplitude, as known from tests without CO_2 injection. Note, that the fluctuations are not only caused by electric noise, but there is also a contribution from physically explainable signal overshoots. Due to the high initial noise levels, for the hydrodynamic analysis, the first 5 seconds of the measurement were usually dropped from the interpretation.

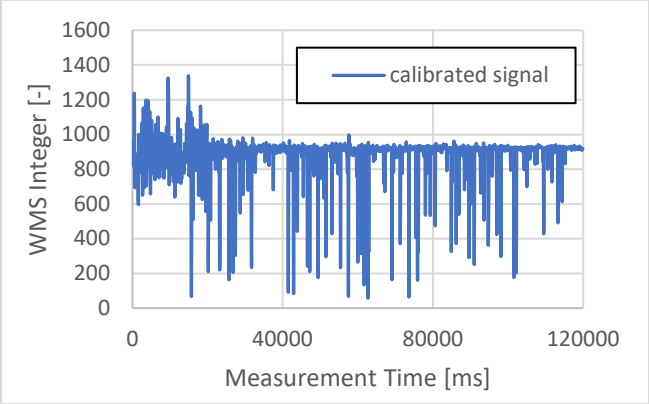

Figure 64: WMS of carbon dioxide injection after applying the correction factor.

The time history of the correction factor is directly used with the cell constant to derive electrical conductivity values which can be converted with the calibration curve of Figure 62 to determine the average gas content in the liquid with very little computational effort. The areal average over the WMS cross-section gives an estimate on the gas concentration in the liquid bulk. The downside of this calculation method is the loss of the high temporal and spatial resolution of the sensor, which is in principle able to visualize local accumulations of higher CO_2 concentrations, e.g. in the wake of the bubbles. Nonetheless, quantities like the lumped mass transfer coefficient and the trend of the gas absorption can be obtained. The analysis of the time and space resolved quantities can be done in a future step to study unexplainable phenomena.

Experimental Facility at ETH Zürich

The facilities TRISTAN and ISOLDE were intended for tests in more industrial scale with proven measuring techniques. Both setups were designed to allow for modifications but their sizes bring challenges in the validation work of new instrumentation methods. The WaterLoop facility at ETH Zürich was initially used for simple two-phase flow experiments primarily for educational purposes. The core of the test channel is a square cross section with a side length of 5 cm and a total height of about 2 m, which was found to be sufficient for the CO_2 injection experiments. The test section is made of acrylic glass for optical access with multiple positions where the WMS can be installed, two of which were used in this measurement campaign.

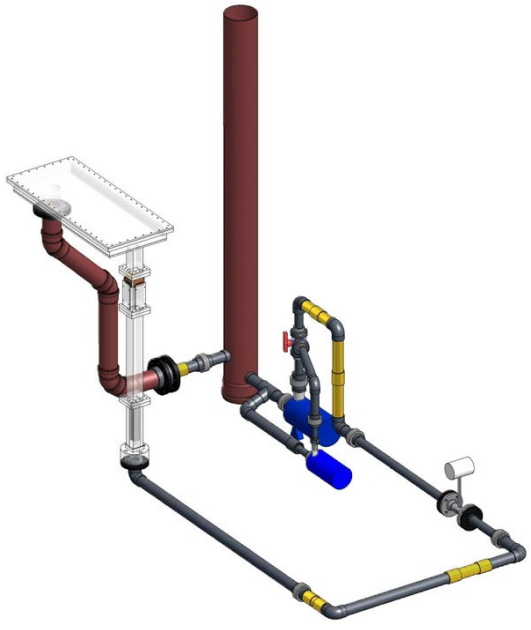

Figure 65: Water Loop facility at ETH Zürich with the water tank, deaerator and test section [94]

A water pump connected to an open water tank can be used for forced liquid circulation which was not necessary for this work. The test section was thus operated without a water circulation as a simple bubble column. The gas injection nozzle has an inner diameter of 4 mm and can be supplied with pressurized air from the laboratory supply and dry nitrogen or dry carbon dioxide from gas cylinders. At the outlet of the test bench, a simple separator has been installed to avoid pressurization of the system. The injected gas is released into the ambient through an opening on top of this separator. Figure 65 shows a simplified 3D view on the facility, whereas Figure 66 gives a schematic view on the facility.

For the tests conducted in this section, the WMS was either placed 27±1 cm or 127±1 cm above the gas injection nozzle which results in a difference between both measuring positions of 100 cm. The installed 3-layer sensor is equipped with 16 central transmitting wires and surrounded by two layers of 16 receiving electrodes each with a lateral pitch of 3.0 mm, an axial pitch of 1.5 mm and a wire diameter of 125 µm. The sensor was originally used for the work of Ito et al [94]. The sampling frequency of the sensor was set to 5000 Hz with a total measurement time of 120 seconds.

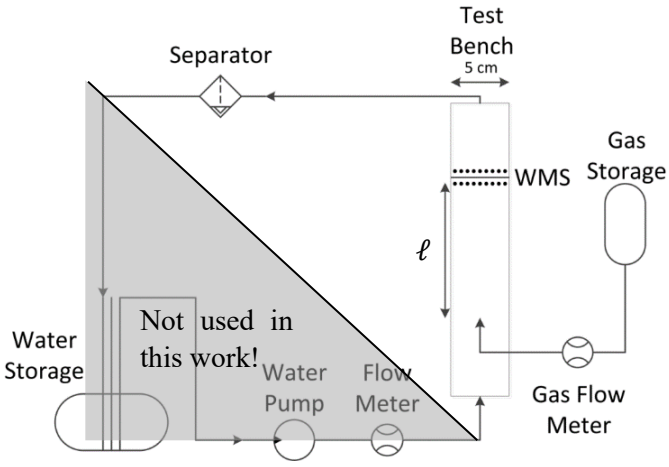

Figure 66: Scheme of the WaterLoop facility at ETH Zürich with a marking of the deactivated section for the present tests.

For each test, the facility was filled with demineralized water up to the level of the separator, resulting in a nozzle submergence of 1.57 ± 1 m that remained constant. The piping from the pump to the test channel was isolated with a valve after the liquid flow meter from the rest of the column. A small outlet was installed in the middle of the test section to take water samples. The samples were required to measure the electrical conductivity and temperature before and after each experiment for the calibration of the WMS data. The tests were started by first sparging dry nitrogen for at least 10 minutes at a flow rate of 1 ln/min to strip any previously present oxygen and carbon dioxide in the demineralized water. Similar to the calibration tests described before, the electrical conductivity of the water would drop to 0.7 to 1.2 µS/cm at the beginning of the test.

After the stripping, the WMS recording was run for 10 seconds before and after the measurement without any gas injection to acquire liquid conductivity values with the WMS. Therefore, with a measurement time of 120 seconds, the total gas injection time lasted around 90 seconds for each measurement. The choice of the gas flow rates in the test matrix in Table 12 was mostly limited by the gas flow meters for carbon dioxide and nitrogen. The range of the mass flow controller was 0.25 – 20 ln/min for carbon dioxide and 0.1 – 7 ln/min for nitrogen. For the pure carbon dioxide tests, the full range of the mass flow controller was exploited but for the gas mixtures, the combined flow range was restricted to 1 – 10 ln/min, corresponding to a superficial velocity of 0.007 – 0.07 m/s. Other than the limitation of the flow meters, it was important to perform experiments in the bubbly and the more heterogeneous slug flow region. This would allow to study the potential influence of the flow transition on the dissolved mass concentration or the mass transfer coefficient.

Table 12: Measurement conditions for all conducted mass transfer experiments using carbon dioxide in the WaterLoop facility

Measuring positions above nozzle tip [m]	0.27 ± 0.01 1.27 ± 0.01
Water submergence [m]	1.57
Injection nozzle inner diameter [m]	0.004
Superficial gas velocity [m/s]	0.002 – 0.145
Volumetric CO_2-N_2 Gas Mixtures [-]	0.25, 0.5, 0.75, 1.0
Temperature range during measurements [°C]	25 ± 2
Base conductivity of demineralized water after N_2 sparging [µS/cm]	0.7 – 1.2

For the tests with nitrogen, the conductivity of the demineralized water was an issue and caused a very bad signal-to-noise ratio. The addition of chemical additives like sodium sulfate could have left residuals in the piping and hence have an influence on the later carbon dioxide tests. Thus, the nitrogen tests were performed at elevated concentrations of dissolved carbon dioxide. During the nitrogen tests, the liquid conductivity was decreasing and needed to be compensated with the same procedure as done for the carbon dioxide tests. The initial carbon dioxide concentration was set arbitrarily, as the focus was mainly laid on the WMS signal to be around 60 % of the full measuring range.

4.2 Hydrodynamic Quantities

Before entering into the mass transfer quantities liked dissolved mass concentrations or mass transfer coefficients, the flow field can be looked at from a bubble characteristic point of view to study potential effects of the two-phase flow field during two-phase flow mass transfer. In order to obtain reference data without mass transfer, the first tests were conducted with dry nitrogen. The very small solubility of nitrogen at atmospheric pressure allows to neglect the reduction of the gas superficial velocity over the column height due to its dissolution in the water. Measurements were performed up to superficial velocities of 0.044 m/s. The transition regime for bubble columns with a hydraulic diameter of 0.05 m should be found at superficial velocities between 0.035 and 0.047 m/s. The average void behavior for the top and bottom measuring position in Figure 67 show the typical void trend for increasing superficial velocities.

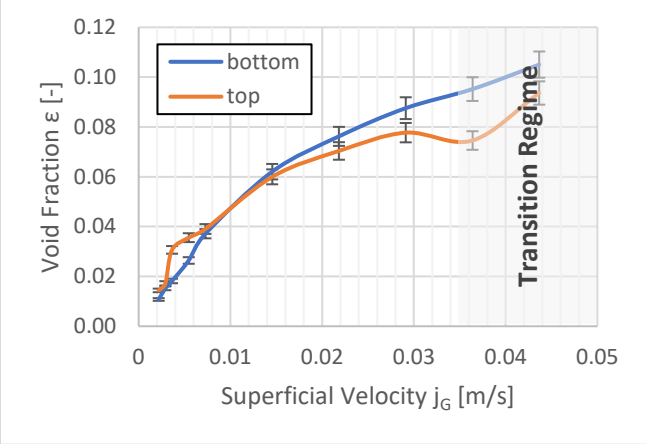

Figure 67: Average void fraction of the bottom and top position of the WMS for dry nitrogen with the transition regime marked according to Figure 25.

The increasing trend is interrupted at the top of the column which could be interpreted as transiting into the slug or churn-turbulent flow regime. The marked transition regime from Shah et al. [136] that can be found in Figure 25 for a 0.05 m bubble column would agree quite well with the experimental data and could be confirmed by more nitrogen tests with higher injection flow rates. The dip in the trend was though only observed at the upper measuring position which can be explained by the necessity of a sufficient inlet length for the evolution of the heterogeneous flow regime.

Fortunately, the tomographic ability of the WMS can be used to create virtual side projections with the void information data. The calibrated void measurement matrix can be collapsed in the viewing direction by searching the maximum void. This method corresponds to what the flow would look like standing in front of the facility in the viewing direction. Figure 68 gives an insight into the flow situation for the bottom and top position, respectively for the four superficial gas velocities 0.002 m/s, 0.007 m/s, 0.029 m/s and 0.044 m/s. Even at the smallest flow rate, the coalescing bubbles can be observed between the bottom and the top position. At the bottom, single bubbles are passing through the sensor whereas at the top, first cap like objects already arrive. At 0.03 m/s, the caps grow and appear already at the bottom measuring position and coalesce to first smaller slugs. At 0.044 m/s, small slugs are already visible at the bottom measuring position. At the top, the tail bubbles are much finer and the flow

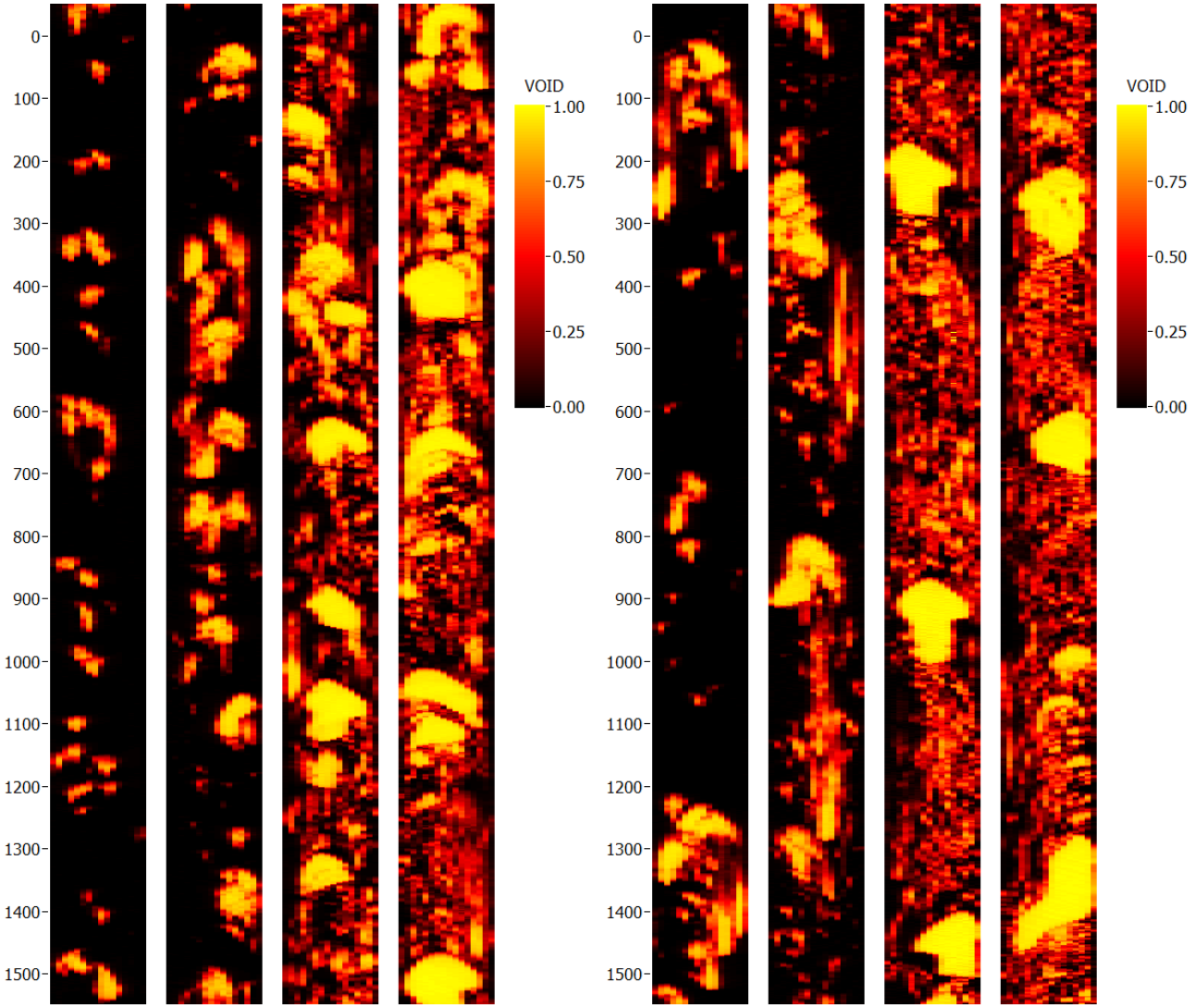

Figure 68: Virtual side projections of the bottom (left) and top (right) measuring position using the void fractions for 0.002 m/s, 0.007 m/s, 0.03 m/s and 0.044 m/s from left to right.

seems to be more developed. The side projections support the void fraction evolution of Figure 67 on the transition regime. The discovery of cap flows at the top position even at smaller flow rates could also explain the small bump at the top position in the void fraction at 0.004 m/s.

The void information of the nitrogen tests confirms that both flow structures, bubbly and slug flow, can be reached with the superficial gas velocities in the test matrix in Table 12 for all gas mixtures. The nitrogen results can also be used for comparison of the pure carbon dioxide tests to verify if there is a change in the bubble characteristics.

For the data evaluation, the total measurement period was split in three sections, each one 30 seconds long starting from 5 seconds after the injection. The first 5 seconds were discarded due to the bad signal-to noise ratio as it was explained in the previous section. In the figures to follow, the three phases are labeled “start”, “middle” and “end” for simplicity. 30 seconds would give a reasonable amount of data for statistically stable averages of the secondary measuring quantities. To get a first overview over the whole range of the measurements, the averaged void fractions are plotted in Figure 69 and Figure 70 for both bottom and top measuring positions.

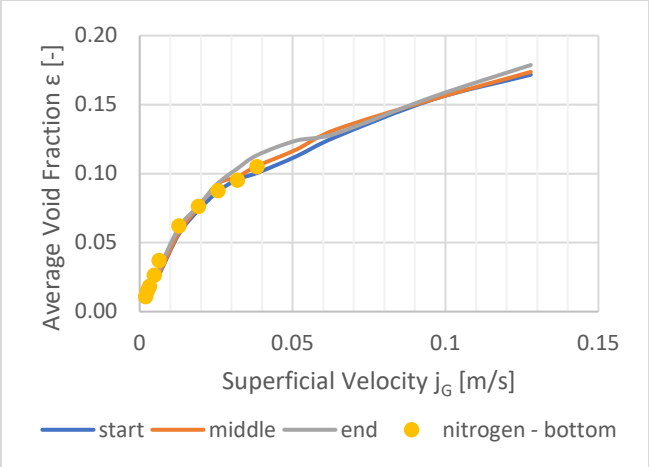

Figure 69: Average void fraction at different time sections in the measurement at the bottom measuring position.

The bottom measurement seems to be unaffected by the absorption of carbon dioxide in all three time spans as the average void does not only stay the same but also follows the values measured in the tests with nitrogen. Judging by the trend of the void fraction, the transition regime would lie between 0.03 m/s and 0.05 m/s of superficial gas velocity which agrees with the findings of Shah et al. [136]. The top measuring position reveals a stronger effect of the reacting gas. At lower flow rates, the values for the three time intervals group together on a level significantly below the void during nitrogen injection. This difference is due to the absorption of CO_2, which reduces the superficial velocity of the gas over height. At superficial velocities above 0.06 m/s, the absorption effect vanishes after the first 30 seconds which is a result of the liquid approaching the saturation with CO_2. Therefore, the absorption decreases and the void fraction histories converge in these cases.

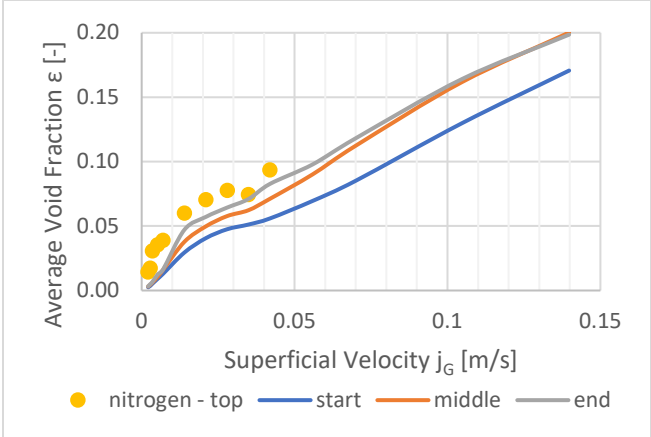

Figure 70: Average void fraction at different time sections in the measurement at the top measuring position.

A very similar picture can be observed in the evolution of the interfacial area density. In Figure 71, no difference is visible at the bottom of the column between the different time windows and between tests with CO_2 and nitrogen tests.

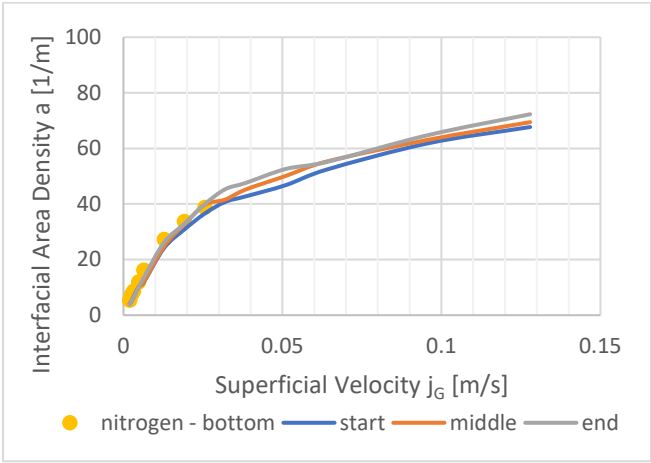

Figure 71: Interfacial area density evolution with increasing superficial velocity at different time sections in the measurement at the bottom measuring position

At the top position on the other hand, the interfacial area density is growing during the measurement for superficial velocities below 0.06 m/s. The values stay below the nitrogen values which would mean that during the 90 seconds of test duration, the liquid saturation value was not completely reached. Above 0.06 m/s, only the first 30 seconds show a significant difference in the interfacial area density. As before, the assumption that the liquid became saturated with carbon

dioxide is supported by the observation that the bubble sizes were no longer reduced by absorption.

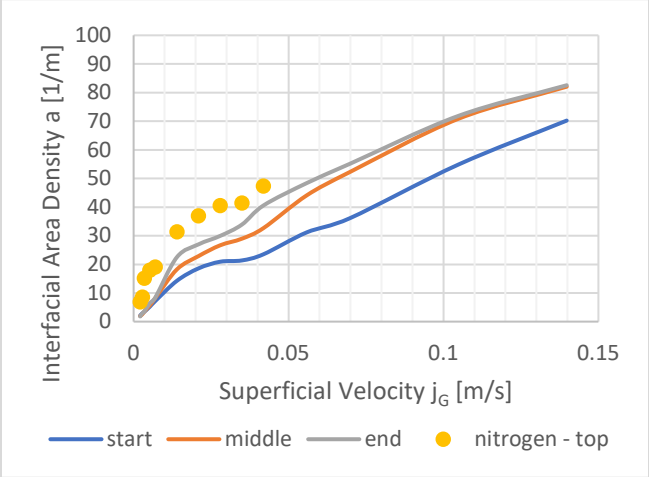

Figure 72: Interfacial area density evolution with increasing superficial velocity at different time sections in the measurement at the top measuring position.

With the outcome of this quick global overview on the measurement data, the more detailed analysis can be separated into the two flow regimes of interest, bubbly/cap flow and slug flow.

Bubbly and Cap Flow

As mentioned earlier, most of the correlations in the bubble rising zone designed for severe accident system codes are assuming a homogeneous bubbly flow structure in suppression pools and wet scrubbers. Therefore, it is worth starting with the analysis of this flow regime. Optical observations and the side projections in Figure 68 found the transition to cap flow to start as early as 0.007 m/s superficial velocity with first smaller slugs being formed at the top of the column around 0.02 m/s. Therefore, the superficial velocities for the bubbly flow experiments in the test matrix would lie in the range between 0.002 and 0.005 m/s.

At first, the void fraction history was determined by averaging the cross-sectional void fraction over short intervals of ±0.5 s around the interrogated instant. For a clearer visibility of the global trends, linear fits of the fluctuating data are added in the plots. Figure 73 and Figure 74 show the temporal evolution of the void fraction for the bottom position with the lowest and highest injection flow rates in a bubbly flow for carbon dioxide and nitrogen. For the bottom case in Figure 73, the trend lines display only weak changes for both flow rates and gases. The void fractions observed during nitrogen injection are always slightly higher than the CO_2 which corresponds to the tendencies shown above in the plots of the time averaged data. The missing changes in the trends for the carbon dioxide injection cases indicate again that the concentration of the dissolved CO_2 did not reach levels where the gradient between bubble surface and liquid bulk starts causing a decline of the mass transfer, thus the bubble volumes change over height but not over time.

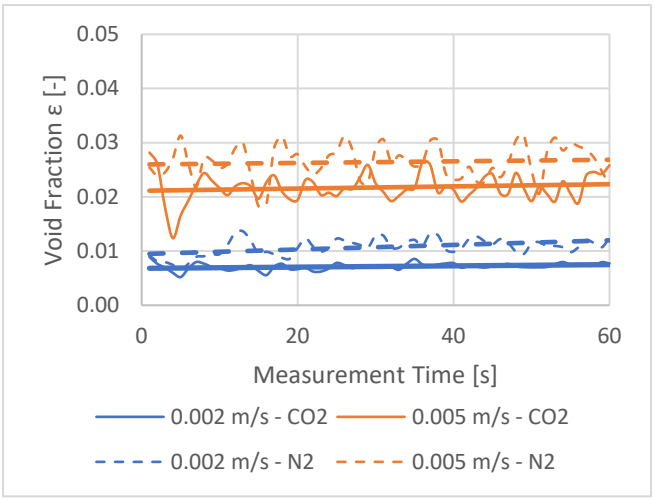

Figure 73: Void fraction evolution (with trend lines) at the bottom measuring position during 60 seconds of experiments for the lowest (0.002 m/s) and highest (0.005 m/s) flow rate in the bubbly flow regime.

The signals from the top of the column shown in Figure 74 are much more interesting to interpret. Compared to the bottom (Figure 73) at both flow rates, the void fraction dropped significantly. This is particularly visible for the higher gas flow rate, i.e. for 0.005 m/s in the pure bubbly flow regime. The drop in void fraction can be explained by the shrinkage of the bubbles while rising from the lower to the upper measuring positions. The ratio of the nitrogen void fractions to the carbon dioxide ones is about 4.5 for the superficial velocities at the injection of 0.002 m/s and 3.5 for 0.005 m/s respectively. This could be a first indication for a decrease of the mass transfer with increasing superficial velocity due to the formation of bigger bubbles, as Hughmark [167] concluded in his research.

The void fractions of the N_2 measurements were slightly higher at the top of the column compared to the

bottom (Figure 73) which can be explained by the expansion of the gas while rising in the column, experiencing a 100 mbar hydrostatic pressure drop and the developing length of the flow field.

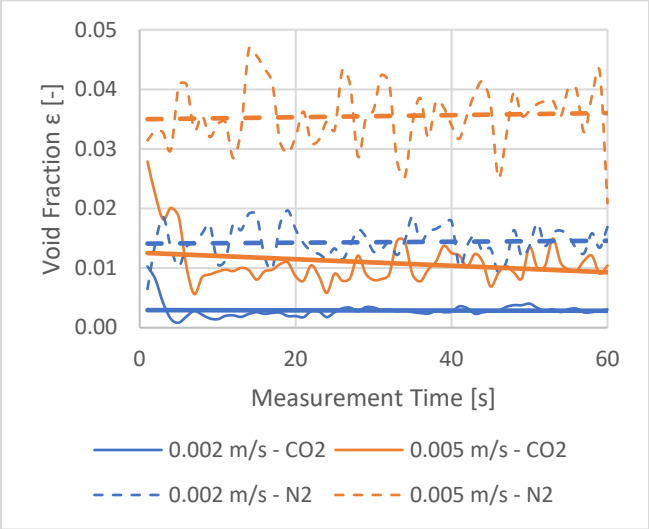

Figure 74: Void fraction evolution (with trend lines) at the top measuring position during 60 seconds of experiment for the lowest and highest flow rate in the bubbly flow regime

The bubble size distribution for the lowest superficial flow rate is depicted in Figure 75 for both measuring positions and both gases. The CO_2 curves are taken from the middle time window. The nitrogen data show a weak coalescing behavior of the flow, resulting in a small side peak next to the main peak. As expected from the results from the void fraction and the interfacial area density, the bubble sizes at the bottom are basically the same for nitrogen and carbon dioxide. Only a small quantity of the injected gas is scrubbed in this flow setting between the nozzle and the bottom measuring position. During the rise of the bubbles towards the upper measuring position, the bubbles lose volume which can be seen in the significantly smaller bubble diameter in the size corresponding distribution. The behavior of the bubble size follows the same trend for all the flow rates in the bubbly flow regime up to 0.005 m/s, regardless the time period considered.

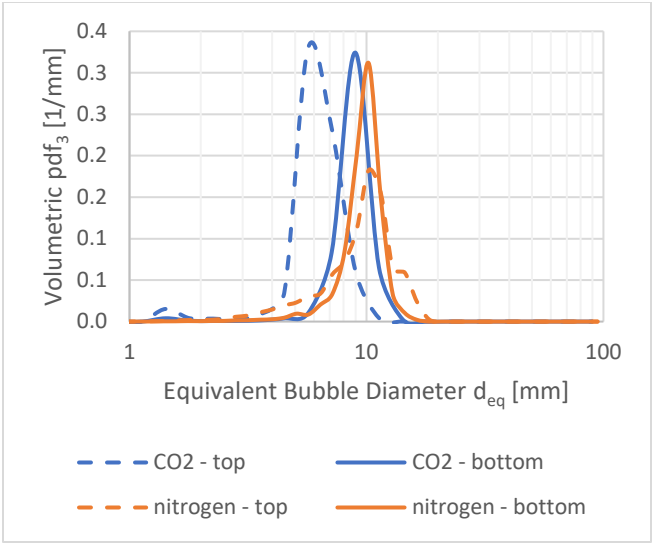

Figure 75: Bubble size distribution of the nitrogen and carbon dioxide tests for a superficial velocity of 0.002 m/s during the middle time window.

The cap flow regime is not very easy to be distinguished from the slug flow region at the upper boundary. As said before, slugs start to be formed through coalescence at the top of the facility from a superficial velocity of 0.029 m/s and onwards. The void fraction evolution at the bottom position at the lower flow rate shows in Figure 76 no difference to the bubbly flow behavior. The two trend curves differ by 1 % on average from each other with a relative constant value. At 0.029 m/s, the void fraction of the carbon dioxide injection is steadily increasing with time whereas the nitrogen declines with time. The CO_2 curve can be explained with a decreased mass transfer rate due to the absorbed gas in the liquid reaching higher levels which causes for a smaller concentration difference between the bubble interphase and the liquid bulk.

The nitrogen behavior is most probably an effect of the decreasing desorption of carbon dioxide in the column. At higher gas flow rates and depending on the amount of dissolved CO_2 concentration, it appears that a significant share of the carbon dioxide was desorbed into the gas stream which could be detected by the WMS. With the carbon dioxide concentration decreasing in the liquid, less gas would be desorbed and thus the void would decrease. Nonetheless, the void fraction values are within the same order of magnitude.

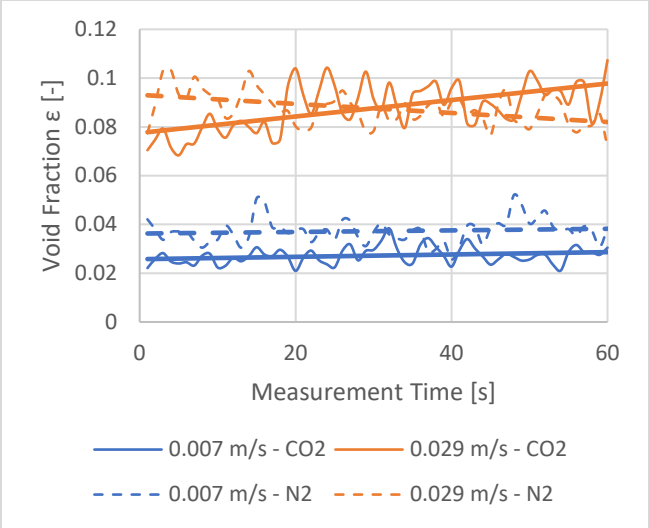

Figure 76: Void fraction evolution (with trend lines) at the bottom measuring position during 60 seconds of experiment for the lowest and highest flow rates in the cap flow regime.

At the top position, as seen in Figure 77, the void ratio between the nitrogen and the CO_2 gas injection decreased further to about 3.2. For the flow rate at 0.029 m/s, the same inclining gradient in void fraction can be found for carbon dioxide at the top as at the bottom. At the top position though, the void fraction does not completely reach the value of the nitrogen test which has again a decreasing trend line. This would mean that the liquid at the bottom region was faster saturated than at the top measuring position.

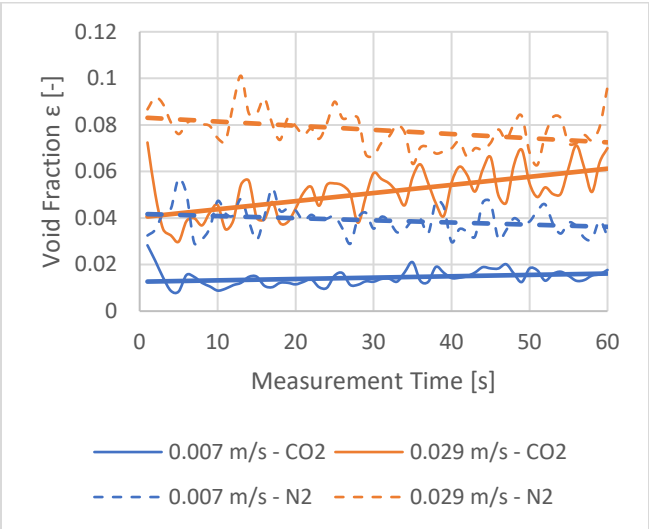

Figure 77: Void fraction profiles (with trend lines) at the top measuring position during 60 seconds of experiment for the lowest and highest flow rates in the cap flow regime.

The bubble size distribution of the carbon dioxide injection for the flow rate of 0.007 m/s in Figure 78 follows the same trend as in the bubbly flow regime. A single peak that is decreasing in bubble size over the facility height indicates mass transfer activity between the two measuring positions. The nitrogen injection starts with a unimodal peak at a relatively big bubble diameter which forms again a more identifiable side peak at the upper position. The absence of this side peak in the carbon dioxide distribution leads to two possible explanations. Either the mass transfer rate is so strong that the coalesced bubbles could not form bigger sized bubbles or the surface tension at the interphase of the CO_2 bubbles is due to the slight acidification changed and the bubbles are less prone to coalescence at this flow rate.

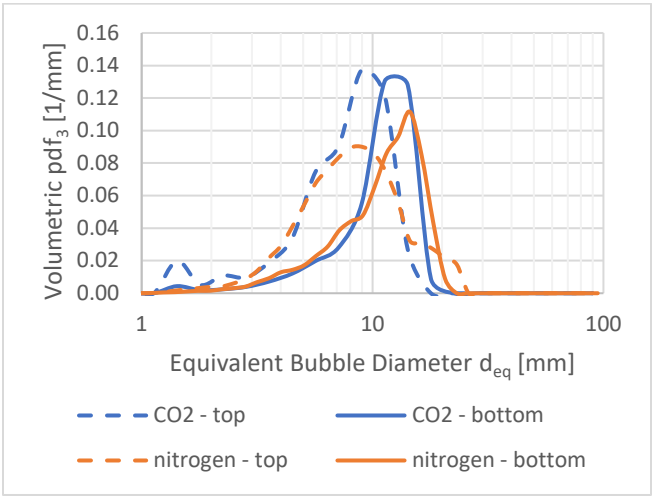

Figure 78: Bubble size distribution of the nitrogen and carbon dioxide tests for 0.007 m/s superficial velocity during the middle time window.

At a flow rate of 0.029 m/s, the bubble size distribution in Figure 79 is clearly showing at both measuring positions the typical bimodal distribution of the slug or churn-turbulent flow. The bottom size distribution for both gases is basically identical with a small shift in the bigger peak towards a smaller bubble size. The top case shows an interesting phenomenon that highlights the importance for adjusting in gas soluble retention models that are solely based on residence time and uniform bubble sizes. The bigger peak is nearly identical for both gases. For the smaller peak, a significant decrease in volume share is noticeable. This difference can be explained by the

absorption of the gas in the liquid bulk but would also mean that the bigger gas volumes are almost not contributing at all on the mass transfer. The bigger caps and smaller slugs were rising with a relative high velocity through the facility, having a relatively small residence time. The smaller bubbles that are broken off or are dragged with in the tails travel a bigger distance as they are moved also laterally in a chaotic way but also downwards with the liquid that is displaced by the gas slugs. Hence, there is no uniform residence time and the gas amount of the bigger bubbles is basically leaving the column with very little scrubbing.

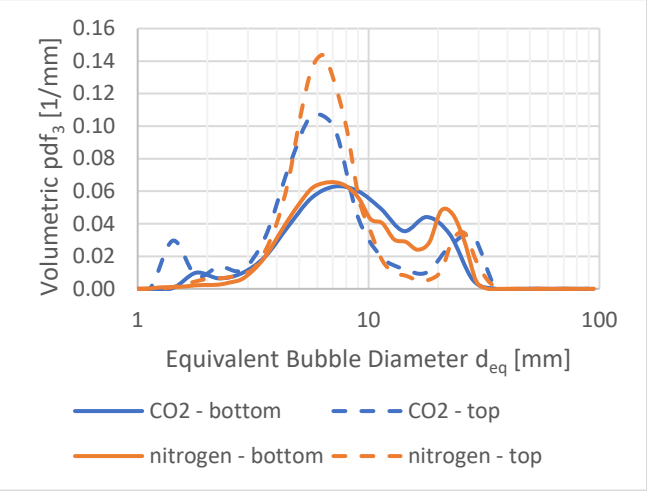

Figure 79: Bubble size distribution of the nitrogen and carbon dioxide tests for 0.029 m/s superficial velocity during the middle time window.

Slug and Heterogeneous Flow

Above 0.029 m/s, the two-phase flow mixture is completely in the slug flow regime. The limitation of the nitrogen mass flow controller was given at 0.044 m/s which is why the void fraction evolution is shown for this flow rate in Figure 81. The higher flow rates for the pure carbon dioxide tests of the test matrix, i.e. up to 0.14 m/s, showed basically the same behavior. As seen before at 0.029 m/s, the bottom curves are principally overlapping. This means that either no mass transfer is happening at all at this position or the more prevalent theory also by other research works that a lot of absorption is very quickly occurring at the injection zone. As before, part of the carbon dioxide is being transferred on the way to the upper measuring position but due to the faster saturating of the liquid, the void is constantly increasing even at the top and would eventually reach the same value as in the non-active nitrogen case.

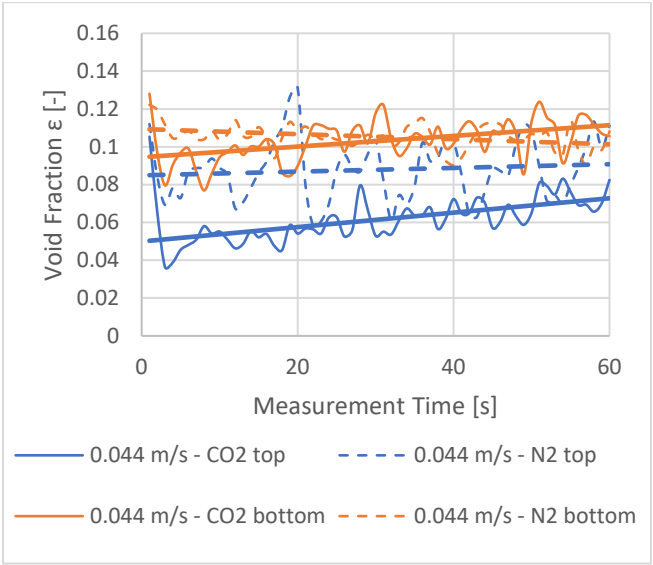

Figure 80: Void fraction evolution (with trend lines) at the bottom and top measuring position during 60 seconds of experiment for an injection superficial gas velocity of 0.044 m/s.

The bubble size distribution in Figure 81 is verifying the observations of before. The size distribution at the bottom is completely the same for the nitrogen and carbon dioxide test. Only at the top, a difference is again visible at the smaller peak, repeating the phenomenon for the 0.03 m/s flow rate.

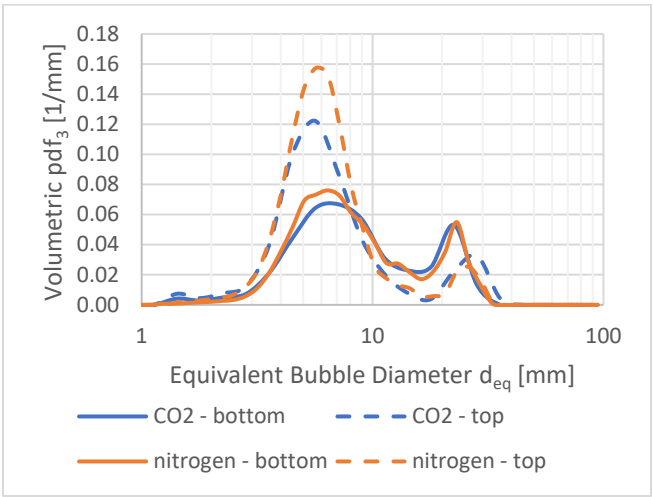

Figure 81: Bubble size distribution of the nitrogen and carbon dioxide tests for 0.044 m/s superficial velocity during the middle time window.

Conclusions from the Hydrodynamics

Two main phenomena can already be extracted from the analysis of the hydrodynamic characteristics of the two-phase flow structure without looking into the absorbed mass in the liquid bulk. The first conclusion was made at the very beginning in the bubbly and cap flow regime. The bubbles in this flow region are shrinking while traversing through the bubble column. This indicates a clear transfer of gas mass to the liquid bulk as no similar trend could be observed with the test series with nitrogen gas. In system codes, the bubble swarm is assumed to have a constant bubble size. As the concentration of iodine is relatively small, the absorption into the liquid will not have a significant effect on the bubble diameter. With higher flow rates and thus growing and coalescing bubbles into caps, the ratio of the average void fraction between the CO_2 and N_2 data was decreasing. This can be interpreted as a decreasing mass transfer as bigger bubbles in this size range are rising faster. This observation can even support the hypothesis for computer model development to take the shape and size of the bubbles into account in the modelling of the retention efficiency as it is done in BUSCA with the bubble angle.

The second conclusion in the hydrodynamics was made in the heterogeneous flow regime. In the comparison of the bubble size distributions, only the share of the small CO_2 bubbles decreased whereas the share of Taylor bubbles remained the same. This could on the one hand be an effect of the heterogeneous residence time, i.e. the Taylor bubbles pass through the column quite fast and the smaller bubbles are caught in the wake of large gas plugs. Or on the other hand, the bubble break-up into smaller fragments is increasing the interfacial area which enhances the mass transfer. The SPARC model of the decontamination factor of iodine as shown in (1.10) is in fact dividing the bubbles in the rising zone by their share into globules and smaller bubbles. A higher share of globules, i.e. of bigger bubbles, is decreasing the overall DF. This concept should be further looked into for heterogeneous mass transfer modelling.

4.3 Dissolved Carbon Dioxide in Water

For the first time in this work, the WMS was used to determine the dissolved concentration of a soluble species in the liquid. This extends the applicability of the instrument methodology of the WMS considerably by providing simultaneous measurement of the two-phase flow hydrodynamics and the concentration of the dissolved mass to verify the made interpretations so far. In Figure 82, the carbon dioxide concentration is plotted against the measurement time for the lower superficial velocities attributed to the bubbly flow regime. At this flow conditions, a constant difference between the top and the bottom position establishes after 10 – 20 seconds. This could come from the shrinkage of the bubbles when they reach the top position, which leads to less bubble surface and thus to less absorbed CO_2. As the extension of the interface between the liquid and the gas is decreasing, the mass transfer rate is also decreasing. Furthermore, the concentration difference between the interface and the bulk of the liquid is still big enough to not be the limiting factor. A discrepancy can be found at the superficial velocity of 0.005 m/s. The difference between the top and bottom position is smaller compared to the other flow rates. This flow rate seems to behave more like the following curves in the cap flow regime.

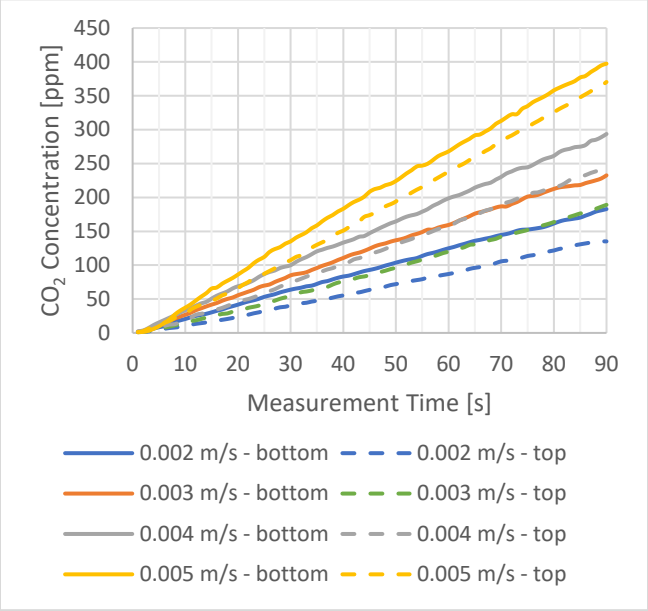

Figure 82: Measurement of the relative dissolved carbon dioxide concentration in water at different flow rates in the bubbly flow regime for both measuring positions.

The concentration behavior at higher flow rates in the cap flow region is displayed in Figure 83. The straight increase of the bubbly flow is with increasing

injection superficial gas velocity transforming to a concave shape. For the two higher flow rates, the top concentration is catching up with the bottom position even though both curves still operate at undersaturated conditions. In order to achieve this, an additional effect has to be present at this flow condition.

In order to explain this phenomenon, a partially backmixed liquid phase over height is proposed. Due to the big gas plugs, the liquid is no longer perfectly mixed and an axial concentration gradient is being established. This phenomenon can be evaluated by means of the axial dispersion model. The axial dispersion of the liquid is promoted by the rising gas phase. Deckwer et al. [182] focused in their work on the applicability of axial dispersion and state that in columns smaller than 30 cm or with a height to diameter ratio that is larger than 3, axial concentration gradients can establish and dispersion should not be neglected. The presented column fulfils the conditions with a hydraulic diameter of 0.05 m and a diameter-to-height ratio of 30. The observed trends qualitatively agree with those published in their works.

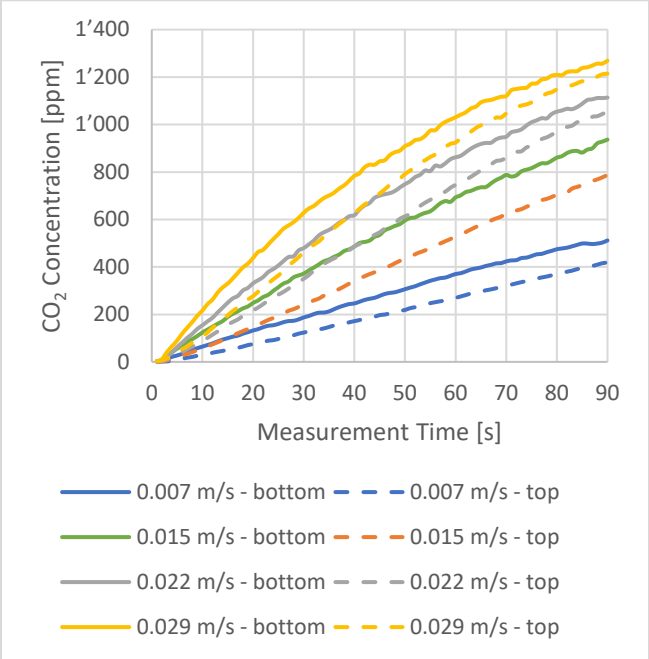

Figure 83: Measurement of the relative dissolved carbon dioxide concentration in water at different flow rates in the cap flow regime for the both positions.

The axial dispersion gets even stronger in the slug flow region. The bottom concentration curves in Figure 84 follow a logarithmic trend whereas the top measurements show an initial delay in their gas mass uptake. This information is crucial for modelling that is later carried out for the determination of the mass transfer coefficient of the bubble column, as the axial dispersion term has to be taken into account in the model. At the highest superficial velocity, i.e. at 0.073 m/s, the concentration profile is even hitting saturation within the measurement time, first at the top, then also at the bottom measuring position. The axial carryover of the transferred mass is very strong at this flow rate. As the big gas slugs are covering most of the cross section of the channel, it is not surprising that they are pushing the liquid ahead of them and thereby carrying the water with the dissolved mass into the higher section of the facility.

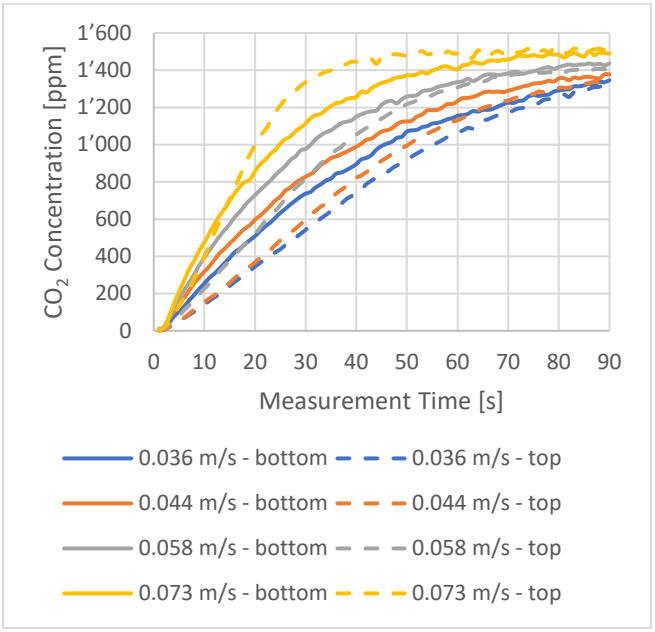

Figure 84: Measurement of dissolved carbon dioxide in water at different flow rates in the slug flow regime for both measuring positions.

4.4 Effect of gas mixtures on mass transfer

The possibility to inject a mixture of carbon dioxide and nitrogen allows to study the effect of partial pressure and gas concentration gradients on the mass transfer. Shah et al. [136] stated in their summary that the gas side resistance becomes important only in highly soluble gases like ammonia in water, where the gas side resistance is limiting the mass transfer rate. Danckwerts [183] also described in his work, that the

transfer of carbon dioxide to plain liquid in a bubble column without packing is limited by the liquid side mass transfer rate due to the slow absorption. Thus, the assumption could be made that there should be no strong influence of the nitrogen in the gas mixture in the bubble column.

The curves of the normalized concentrations of dissolved CO_2 in Figure 85 measured at a superficial velocity of 0.007 m/s allow the conclusion that the influence of gas-side resistance is minor at both measuring positions. Keeping in mind, that the equilibrium concentration used for the normalization is proportional to the partial pressure of CO_2, i.e. the absolute concentrations of dissolved CO_2 are growing with increasing CO_2 concentration in the gas. A small difference is noticeable for the 25% gas concentration case. This difference could hint that despite the suggestions of literature, there is a gas side resistance acting.

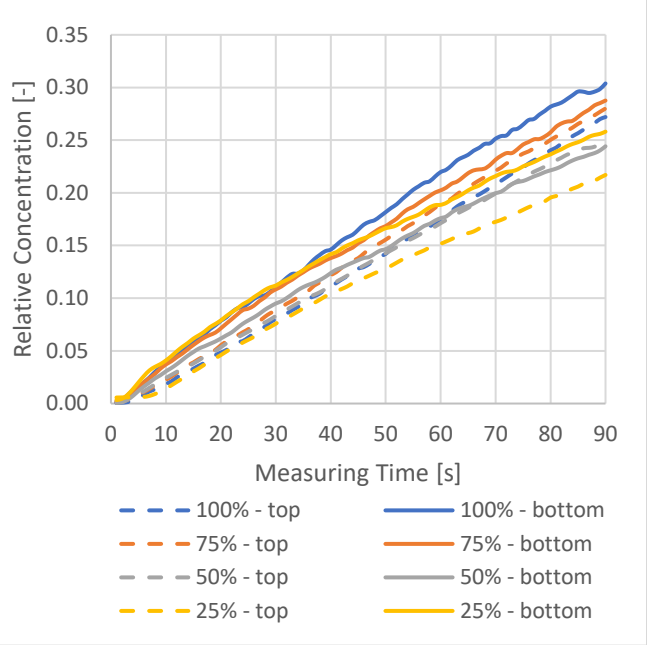

Figure 85: Relative dissolved carbon dioxide concentration over time for different gas mixtures at a superficial velocity of 0.007 m/s at both measuring positions.

Looking at the hydrodynamic data, there is no big discrepancy that would justify a different absorption rate. With increasing nitrogen content, the bubble size distribution in Figure 86 is getting closer to the size distribution of the pure nitrogen, which is explained by the decreasing rate of CO_2 dissolution.

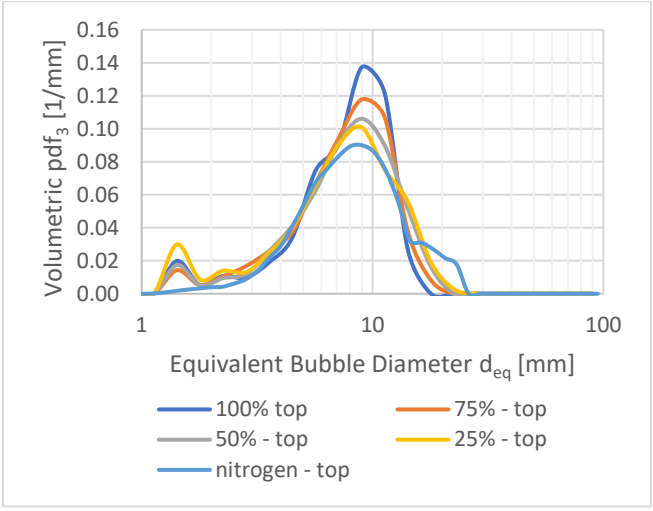

Figure 86: Bubble size distribution at the top position for 0.007 m/s superficial velocity during the middle time window for all gas concentrations.

The concentration profiles for the slug flow region at the highest measured combined superficial velocity of the gas mixture of 0.044 m/s are depicted in Figure 87. In the slug flow domain, a clear discrepancy between the different histories of dissolved CO_2 concentration is visible already at 75% gas concentration. At the top position, a 25% nitrogen content is not yet really noticed compared to the pure carbon dioxide. The 50% and the 25% CO_2 containing gas mixtures on the other hand show a significant drop in mass transfer rate. The gas concentration also has a stronger influence at the bottom of the column. Here, already at 75% CO_2 a small difference to the pure carbon dioxide case is visible and at 50% and 25% CO_2 content in the gas, the dissolution rate is increasingly deteriorated.

The values in the slug flow regime seem to stabilize also at a value below the saturation concentration of the specific partial pressure. The small contact time between the gas and the liquid due to the high velocity with a gas-side resistance due to the inert gas could explain why the converging starts at a lower level. It could also be, that with a much longer measuring time, the values would eventually reach the saturation at the given partial pressure.

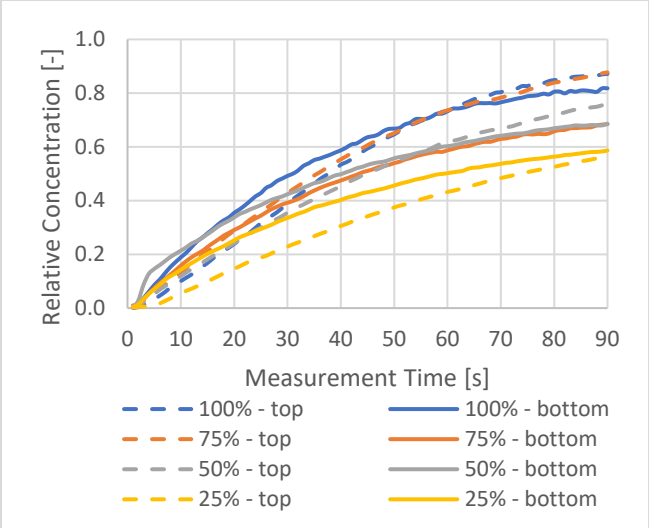

Figure 87: Relative dissolved carbon dioxide concentration for different gas mixtures for 0.044 m/s at both measuring positions.

As already observed with the smaller flow rate, the higher nitrogen share leads to the bubble size distribution getting closer to the pure nitrogen data, as shown in Figure 88. So again, the bubble sizes are not the reason for a different behavior in the mass transfer.

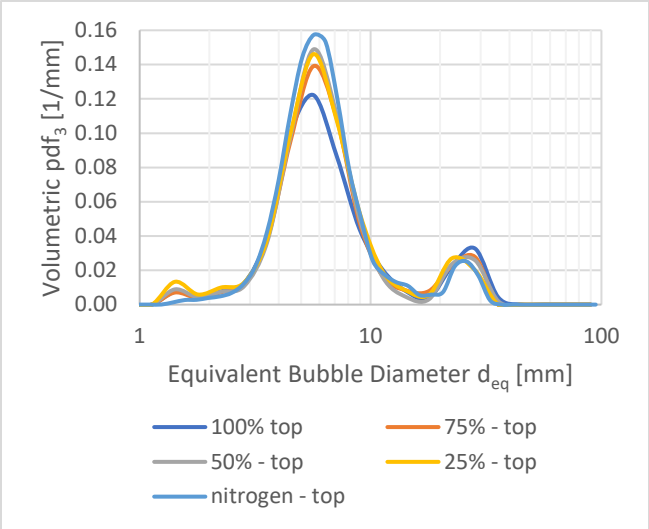

Figure 88: Bubble size distribution at the top position for 0.044 m/s superficial velocity during the middle time window for all gas concentrations.

4.5 Determining Mass Transfer Coefficients

As already mentioned, mass transfer from gas to liquid can be described by the two-film two-resistance theory according to Lewis and Whitman [166]. The mass transfer rate can then be described with (4.16) with k as the volumetric mass transfer rate, A the interfacial area, p as the gas partial pressure and c as the gas concentration in the liquid. The subscripts g, L and i refer respectively to the state inside the gas, in the liquid bulk or at the interface.

$$\frac{dm}{dt} = k_G \cdot A \cdot (p_g - p_i) = k_L \cdot A \cdot (c_i - c_L) \qquad (4.16)$$

Depending on the solubility of the gas in the liquid phase, the equation can be further simplified. If a gas is highly soluble in the liquid phase, e.g. ammonia in pure water, then the gas side diffusion will be the limiting side. Therefore, the liquid side can be neglected in the expression (4.16) and the equation is reduced to the first half. The opposite is true for gases that have a low solubility. As also backed by the work of Danckwerts [183], carbon dioxide in water, as used in this work, is a low soluble gas with a very low gas side resistance compared to the liquid side. The equation (4.16) can hence be simplified to (4.17).

$$\frac{dm}{dt} = k_L \cdot A \cdot (c_i - c_L) \qquad (4.17)$$

Furthermore, as Lewis and Whitman explained, with the gas diffusion being significantly higher, the gas concentration at the interface is reaching values that are very close to the partial pressure inside the gas phase. The rate equation (4.17) becomes then independent of the concentration in the gas film (4.18). Dividing both sides of (4.18) by the liquid volume (4.19) and taking the void fraction in the equation (4.20), i.e. $V_L = (1-\varepsilon) \cdot V_{tot}$, leads to the so-called CSTR (continuously stirred tank reaction) model (4.21) where the interfacial area A becomes the interfacial area density a and c^* represents the saturation concentration at the given gas partial pressure.

$$\frac{dm}{dt} = k_L \cdot A \cdot (c^* - c_L) \qquad (4.18)$$

$$\frac{dm}{dt} \cdot \frac{1}{V_L} = k_L \cdot \frac{A}{V_L} \cdot (c^* - c_L) \qquad (4.19)$$

$$\frac{dc}{dt} = k_L \cdot \frac{A}{(1-\varepsilon) \cdot V_{tot}} \cdot (c^* - c_L) \qquad (4.20)$$

$$\frac{dc}{dt} = \frac{k_L a}{1-\varepsilon} \cdot (c^* - c_L) \qquad (4.21)$$

The reason to convert the interfacial area A to the density a and the mass transfer rate to a concentration rate dc/dt is the simplification in the measurement

instrumentation for the estimation of the volumetric mass transfer coefficient k_La. To further elaborate this, the differential equation (4.21) has to be solved with the assumption that k_La is constant and c^i as the initial dissolved gas concentration in the liquid which yields the equation (4.22). The liquid side mass transfer coefficient k_L can in this form only be obtained if the interfacial area density a is known. The interfacial area density is though not always easy to measure, especially with the given measuring techniques of the time of many aforementioned works. On the other hand, the instrumentation to estimate k_La reduces to a measurement of the instantaneous concentration *c(t)* and the average void fraction ε which were widely available techniques when the first studies were conducted to develop correlations.

$$k_La = \frac{1-\varepsilon}{t} ln(\frac{c^*-c^i}{c^*-c(t)}) \qquad (4.22)$$

The basic concept of the CSTR is a perfectly mixed liquid phase and does not reflect any diffusion and advection effects inside the bubble column. The effect of this neglection can be profoundly seen in the work of Manjrekar et al. [184]. They studied the mass transfer and hydrodynamics in three-phase flow for biofuel applications, using a bubble column of 10 cm radius and 115 cm height, resulting in an L/D ratio of over 11. They at first used the CSTR model to obtain the volumetric mass transfer coefficient k_La and calculated the concentration with the expression (4.21). As they also stated in their work, the fit as shown in Figure 89 could not capture the trend curve correctly. The delayed increase of the measured concentration in the first 20 seconds of the measurement could not be reproduced with the logarithmic function of (4.22). It can rather be explained by a series connection of a certain number of continuously stirred tanks, for which analytical solutions exist as well. In a bubble column however, the situation is more complex, since the two reactants do not stream through the system with equal mass flows and back mixing can take place.

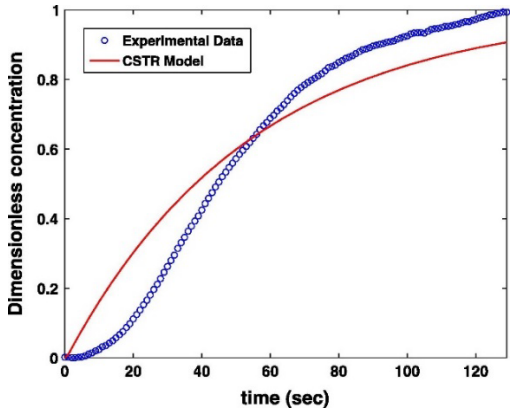

Figure 89: Poor fit of the CSTR model on the experimental data from the work of Manjrekar et al. [184] inside their tall bubble column

This shape tendency shown in Figure 89 was also previously observed in the carbon dioxide experiments in the bubble column at the top measuring position in the cap and slug flow region (cf. Figure 84), even though not as strongly developed as in the work of Manjrekar et al. [184]. For tall bubble columns, especially at higher gas velocities, the one-dimensional ADM (axial dispersion model) as presented in (4.23) and (4.24) has been commonly used. The coefficients D_z are here the axial dispersion coefficient for the liquid and gas, respectively. The axial dispersion

$$\frac{dc_L}{dt} = D_{z,L}\frac{d^2c_L}{dz^2} + \frac{k_La}{1-\varepsilon}(He \cdot c_G(t,z) - c_L(t,z)) \qquad (4.23)$$

$$\frac{dc_G}{dt} = D_{z,G}\frac{d^2c_G}{dz^2} - j_g\frac{dc_G}{dz} - \frac{k_La}{\varepsilon}(He \cdot c_G(t,z) - c_L(t,z)) \qquad (4.24)$$

For the determination of the volumetric liquid side mass transfer coefficient k_La, most of the previous works [172, 182, 171] neglected the gas-phase dispersion $D_{z,G}$ and the change in the gas concentration, since the dispersion term in the gas phase for low soluble gas would be small. This would justify to reduce the axial dispersion model with no liquid circulation to (4.23).

Regarding the liquid axial dispersion coefficient, the literature offers a number of correlations. Ohki and Inoue [185] looked into the longitudinal mixing of the liquid phase with tracer injections. Their bubble column worked in the bubbly flow and the coalesced bubble-slug flow conditions with different sized bubble columns and gas injection diameters. They derived a liquid-phase axial dispersion coefficient correlation for

both flow regions, the bubbly flow (4.25) and slug flow (4.26)

$$D_{z,L} = 0.3 \cdot d_c^2 j_G^{1.2} + 170 \cdot d_n \qquad (4.25)$$

$$D_{z,L} = \frac{14 d_c}{(1-\varepsilon)^2} \qquad (4.26)$$

A few years later, Deckwer et al. [172] also looked into the liquid axial dispersion inside their bubble columns. They concluded that their data correlated well with an adjusted expression (4.27) they took over from Towell et al. [186].

$$D_{z,L} = 2.7 \cdot d_c^{1.4} \cdot j_G^{0.3} \qquad (4.27)$$

One-Dimensional Model to obtain k_La and k_L

A computer code was developed to solve (4.23) numerically as a function of the height of the bubble column. For this purpose, the column is discretized in a series of cells in axial direction. Besides the concentrations of the dissolving component in the gas and the liquid phases, the void fraction ε and the superficial gas velocity j_g as well as a pressure and temperature corrected Henry constant *He* are functions of time *t* and height *z*. The volumetric mass transfer coefficient k_La is also not a constant value since the interfacial area density is developing in the flow path. Previous studies from Akita et al. [168] or Hikita et al. [13] concluded in their studies that the mass transfer coefficient is depending on fluid properties (cf. (4.4) and (4.7)), e.g. density or the diffusion coefficient of the gas but also on void fraction or superficial gas velocity. The latter two are varying over the column height. The mass transfer coefficient can thus either be iterated to achieve a good match of the model predictions with the measurements or correlations taken from the literature can be validated.

In a strict sense, both mass transfer coefficients k_L and k_G are functions of local values characterizing the interaction of the gaseous and the liquid phases, in particular, bubble size, void fraction, drift velocity and the turbulence intensity. However, the proposed one-dimensional modeling is not sensitive enough to allow a detailed parametrization of the mass transfer coefficients with these quantities as inputs, since the dependencies are weak. It was therefore decided to keep k_L constant over the height, whereas the interfacial concentration was updated over height, since it decreases with progressing CO_2 dissolution. The product k_La is therefore changing over height due to the continuous decrease of the interfacial area concentration. The value of k_L that is found by the iterative fit of the model results to the measured concentration histories is thus an average of the given test conditions and is obtained as function of the injected gas flow. The analyzed measurement data matrix in Table 12 delivered the gas concentrations in the liquid, void fractions and interfacial area densities at two different heights of the bubble column which were used as criterion for the best choice of the mass transfer coefficient.

The code is initialized by assigning the physical constants like densities at norm conditions for CO_2 and N_2 and the reference temperature of the experiments. Further inputs are the collapsed height *H* before the start of the gas injection and the axial sensor positions and the hydraulic diameter of the column d_c. With the node height of *dz*, the column is subdivided into $n = H/dz$ cells.

The mass transfer coefficient k_L is also defined as a constant in this section. The previous works of Calderbank and Moo-Young [173] found a constant behavior of k_L for bubble sizes relevant to this work as shown in the expression (4.9). Hughmark [167] and Akita et al. [169] have in their correlations (cf. (4.1) and (4.5)) a weak dependency on the Sauter mean diameter. The relative change of the bubble sizes during one measurement would not have a significant impact on the mass transfer coefficient and would therefore justify to keep k_L constant throughout the routine. The constant was adjusted until the CO_2 concentration curves agreed with the experimental data as good as possible, i.e. the shape and the final values.

The second step as described in Figure 90 was to adapt the flow quantities originating from the mass flow controllers at norm conditions (0 °C, 1 atm) to the boundary conditions of the experimental bubble column and convert the inputs into mass flow rates of the different mixtures with the carbon dioxide concentration in the total gas stream *x* and the average gas density ρ_{g0} at the bottom of the column.

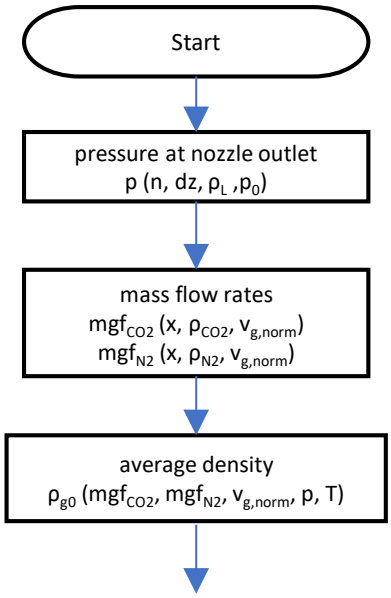

Figure 90: Calculation of the two independent gas mass flow rates and the average gas density

With the averaged density ρ_{g0} and the volumetric flow rates, the superficial velocity j_{g0} is calculated which is the input for the void estimation using the drift flux model of Zuber and Findlay [187]. The void ε_0 at the bottom was required to calculate the gas volume v_{g0} at the lowest cell but also the initial bubble size d_{b0} with the correlation from Akita et al. [169]. The hydrodynamic results in the bubbly flow regime allowed to start with the assumption of a homogeneous and monodispersed flow which kept the code simple to start with. The wide range of variation of the superficial gas velocities allowed to cover heterogeneous flow conditions, as well, as it is done in system codes, like BUSCA, and observe the influence of the flow regime. The total number of bubbles n_{b0} is deduced as function of bubble size and void fraction, as presented in Figure 91, whereby it is assumed that all bubbles have the same diameter.

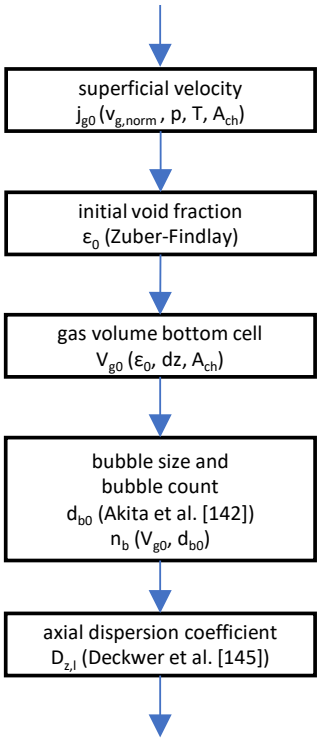

Figure 91: Estimation of initial void ε_0, initial bubble size d_{b0} and bubble count n_{b0}.

With **Error! Reference source not found.**both code segments executed, all initial conditions are given to determine the mass transfer coefficient from the gas to the liquid phase. At this point, the concept of the virtual height was implemented to deal with the axial expansion of the volume inside the virtual column, caused by the gas injection. The presence of gas bubbles will swell the height of each cell according to the local void fraction. In a Eulerian meshing, it would theoretically be needed to model the corresponding advection of liquid from one cell to another, requiring the introduction of a mass conservation equation for the liquid phase. This can be avoided by using a Lagrangian approach for the liquid phase. The concept of the virtual height axis z_i is illustrated in Figure 92. In this coordinate system, node boundaries are shifted upwards with growing void fraction, with the consequence, that the liquid inventory in each cell stays unchanged if the void fraction changes. The height z_i was calculated using the void fraction information in a way that the liquid phase is always kept in each cell at its initial volume before the start of the gas injection, while all

other variables, like the interfacial area density and the measuring position of the sensor, used the dynamic coordinate system as exemplary shown at the right side of Figure 92. Note that in this approach, the sampling points for comparison with the wire-mesh sensor data are not at a constant position with regard to the virtual z axis. The real height of each computational cell has to be found by integration the volumetric fraction of liquid over height and the sampling of calculated void fractions and CO_2 concentrations has to be done at the real height, which has to be updated at each time step. Since the position of the WMS cannot be made coinciding accurately with a center of a computational cell anymore, an interpolation between the two closest cells was made.

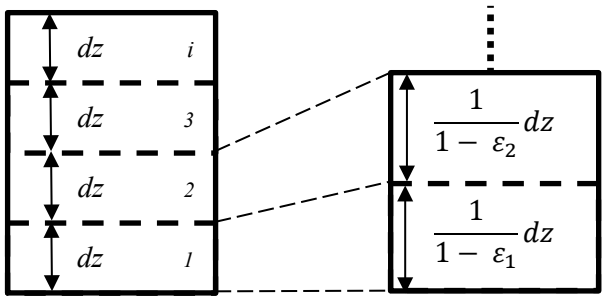

Figure 92: Schematic difference between the spatial nodalization (left) and the virtual height (right) for the estimation of the mass transfer coefficient.

The next code segment, given in Figure 93, iterated in an inner loop over the axial height through each cell and in an outer loop over time *dt*. For numerical stability reasons, the timestep *dt* had to be smaller than $0.5 \cdot dz^2$. In the inner loop, the pressure *p*, mass flow rate *mgf* and partial pressure *y* were calculated for each cell. As the carbon dioxide traversed through the column, a part of its mass was retained in the liquid which decreased the available gas volume over height.

The integration over time is only used to compute the evolution of the concentration profiles. The superficial gas velocity, as well as all other quantities linked to it by closure relations, are calculated in a quasi-steady-state manner. This means that the transit time of the gaseous phase through the column is assumed to be negligible compared to the characteristic time constant of the concentration changes, which is notably the case. The transition of the gas phase through the column of about 1.7 m height takes at typical velocities only few seconds, whereas the concentration buildup continues for the entire run time of the experiments.

Regarding void fraction, one out of three different correlations from literature were tested. The first void correlation is again the drift flux model of Zuber and Findlay [187]. The second void correlation (4.3) was proposed by Akita et al. [168]. The last correlation (4.6) came from the work of Hikita et al. [170]. An accurate void fraction was necessary as the void fraction $\varepsilon(i)$ of cell *i* was used for the calculation of the mixture volume v_{node} and thus the diameter of the bubbles d_b and their total surface A_b. The total surface A_b and volume v_{node} were both elements of the volumetric mass transfer coefficient k_La. A strong mismatch of the void had a direct influence on k_La which would lead to a wrong adjustment of k_L.

Eventually, all quantities to feed the axial dispersion model were assessed. The partial pressure *y* was used to calculate the saturation concentration c_{eq} at the bubble boundary in line with the two-resistance theory for low soluble gases. To calculate the new concentration of the cell *i*, the explicit forward Euler method is used, whereas the central differences are calculated to obtain the second derivative of the concentration for the axial dispersion model. The local instantaneous mass transfer rate is a source term in the balance equation for the dissolved CO_2 integrated over time and a sink term in the balance equation of the superficial liquid velocity, integrated over height, the latter, as mentioned above, in a quasi-steady-state fashion. The sum of all the transferred gas mass at cell *i* was stored in *mg(i)* as shown in Figure 93.

With this one-dimensional model, the evolution of the concentration in the liquid bulk and the void fraction can be calculated. The last step was to iterate through the full virtual height and store the quantities at the two measuring positions of the sensor for verification against the experimental data.

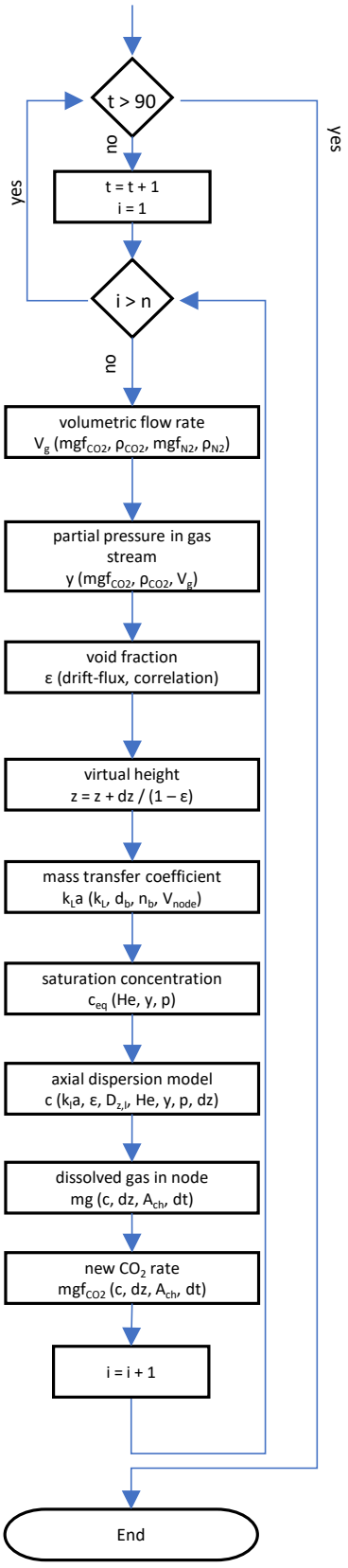

Figure 93: Iterative determination through time and nodes of the mass flow coefficient and the transferred mass

Validation of the One-Dimensional Model

In Figure 94, the void fraction evolution from the measured data is plotted against the models for all injection superficial gas velocities. In the bubbly flow regime, the data is agreeing very well as also the assumption of a unimodal bubble size distribution is correct. The best agreeing void model in this regime is the drift flux model from Zuber and Findlay [187]. In the transition region, the drift flux model starts to overpredict the void fraction. In this region, the void correlation from Hikita et al. showed a much better agreement between the calculated and the experimental void. As mentioned before, the correct estimation of the void fraction is important as the void fraction is one of the parameters in the equation for determining the mass transfer coefficient. A big deviation in the void fraction will inevitably lead to a wrong mass transfer coefficient.

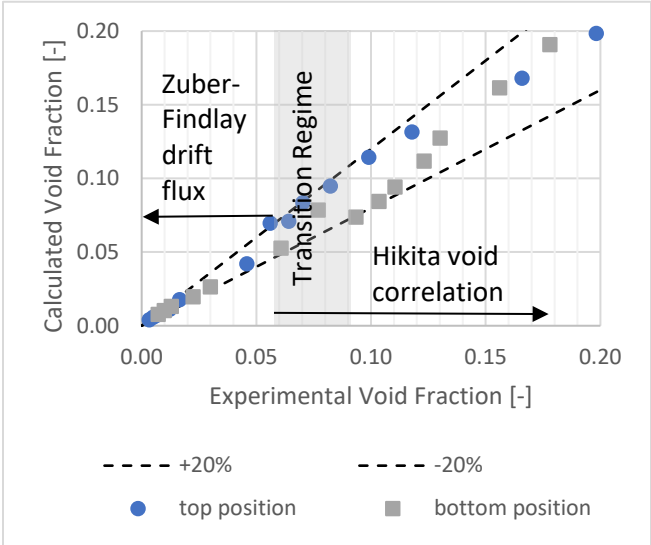

Figure 94: Comparison of the experimental void fraction against the calculated void fraction resulting from correlations of the last 30 seconds of the measurement.

For the dissolved gas concentrations in the liquid, the results were again split into the three flow regions bubbly, cap and slug flow. The calculated carbon dioxide concentrations in the bubbly flow region were expected to agree the best with the measurement data as the model assumes a homogeneous monodispersed two-phase flow. The model prediction in Figure 95 did show a good agreement as the error stays within a 10 % error band. One exception is the bottom measurement position at the higher flow rate. The lower values

correspond to the beginning of the measurement where for the bottom measuring position some transient or flow developing effects are still acting which are not captured by the model. Nonetheless, as many one-dimensional models, it does not aim to reproduce the full details of the flow situation but rather a good average situation.

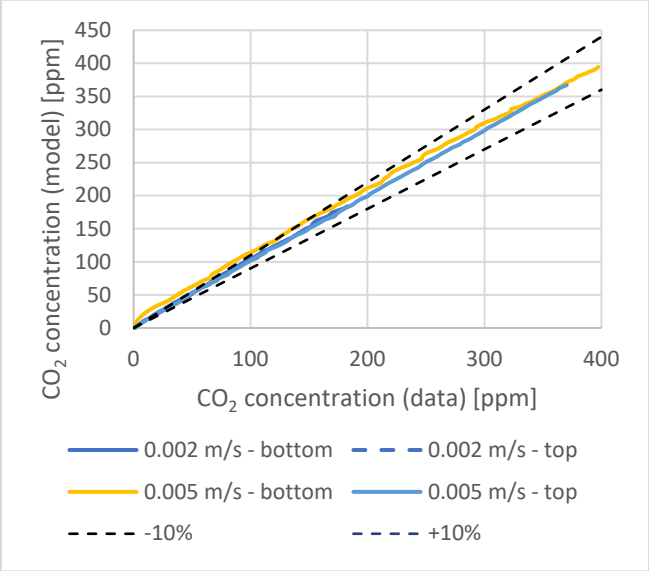

Figure 95: Comparison of the experimental and calculated dissolved CO_2 concentrations in the liquid for 0.002 m/s and 0.005 m/s injected superficial gas velocities.

The dissolved CO_2 concentration calculation in the liquid is still performing well in the cap flow respectively the transition regime, cf. Figure 96. At the higher superficial velocity, which is close to the slug flow regime, the calculated concentration overshoots at the lower values but meets the experimental value at higher concentrations. The model is still not perfectly able to capture the delay of the concentration uptake at the top which is why there is a bigger discrepancy at that point.

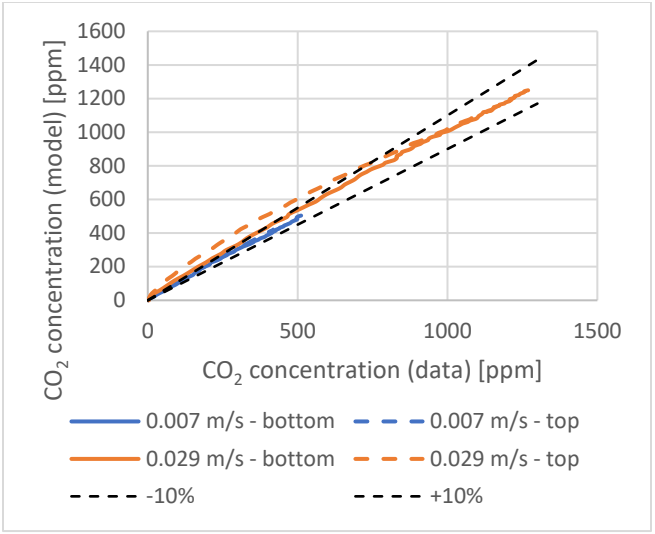

Figure 96: Comparison of the experimental and calculated dissolved CO_2 concentrations in the liquid for 0.007 m/s and 0.029 m/s injected superficial gas velocities.

Surprisingly enough, even in the higher superficial velocities of 0.109 m/s, the model prediction for the absorbed mass with a constant k_L and a monodispersed gas phase did work quite well. As before, the top data is overpredicting the concentration at lower concentration values, which is the early phase of the experiment. But all in all, considering that the heterogeneous flow regime is represented by the Sauter mean diameter, the values are quite good for a first try.

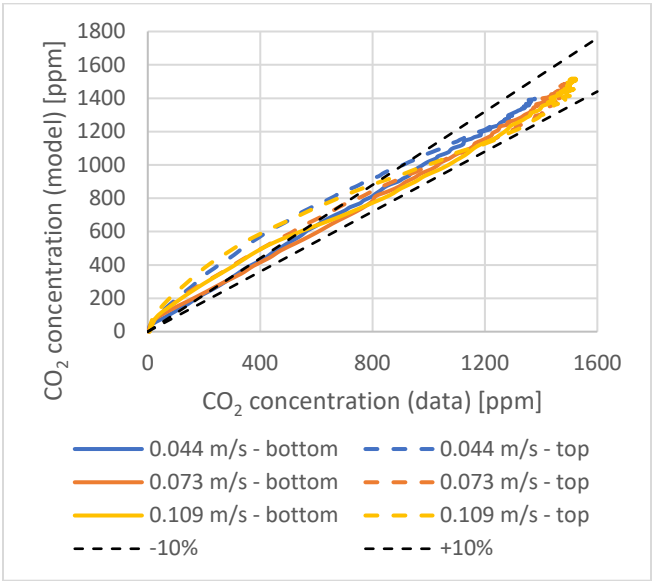

Figure 97: Comparison of the experimental and calculated dissolved CO_2 concentrations in the liquid for 0.044 m/s, 0.073 m/s and 0.109 m/s injected superficial gas velocities.

Liquid Side Mass Transfer Coefficient

The liquid-side mass transfer coefficients k_L that were found as a best fit of the model to the experimental data are put against the superficial velocity in Figure 98 for the experiments with a pure CO_2 injection. When the superficial gas velocity is increased, the mass transfer coefficient makes a dip between 0.005 and 0.03 m/s. At the latter velocity, the minimum value is overcome and the mass transfer coefficient increases again with higher superficial velocities to reach a stable level with only few outliers. This is in-line with the findings of Hughmark [167] as well as Calderbank and Moo-Young [173]. The interpretation here would be that in the undisturbed wobbling of the single bubbles at very low superficial velocities, a lot of mass can be transferred between the two phases as the bubble excitation at the interface renews the liquid at the surface. In the swarm or more chaotic flow, the swarm hindrance forces the bubble to rise in a straighter direction upwards which decreases the mass transfer rate. For flow rates above 0.04 m/s, i.e. in the slug flow regime, the volumetric liquid mass transfer coefficient remains pretty stable. This would also go well with Calderbank and Moo-Young [173] that formulated a constant k_L correlation independent of the gas injection flow rate.

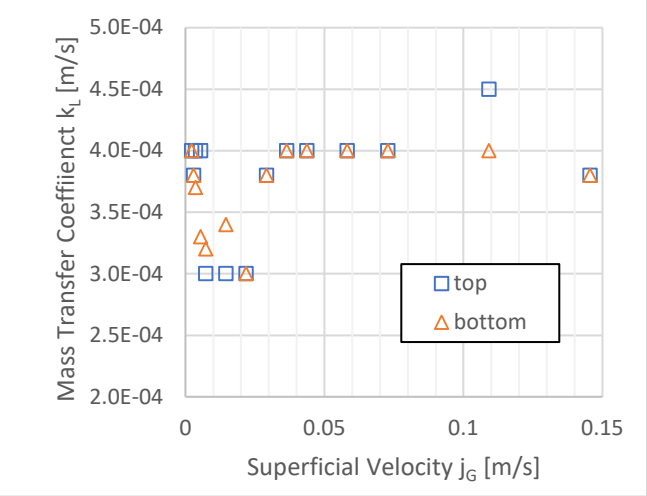

Figure 98: Volumetric liquid-side mass transfer coefficient for both measuring positions and 100% CO_2 feed inlet.

Consequently, if the k_L is practically constant, the volumetric mass transfer coefficient k_La will follow the trend of the interfacial area density. As it can be observed in Figure 99, this is especially true for the bottom measuring position. At the top position, the mass transfer coefficient follows a rather linear increase with higher superficial velocities.

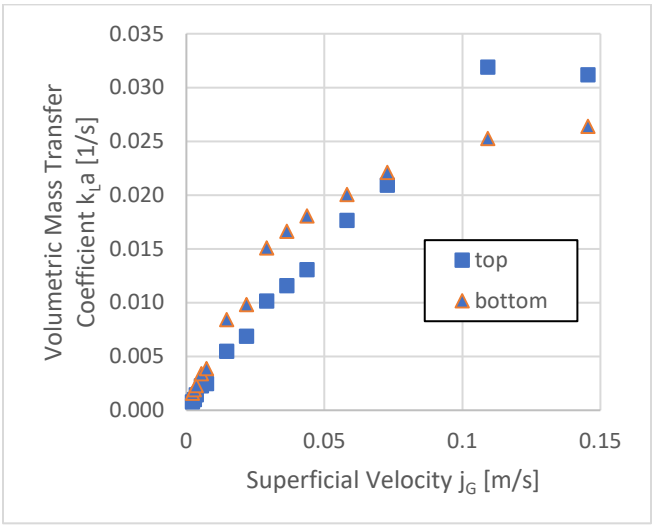

Figure 99: Liquid side mass transfer coefficient for both positions for the 100% CO_2 feed gas stream.

At the beginning of this section, the idea was postulated to evaluate existing mass transfer correlations from the literature for the formulation of a new model. In Figure 100, the experimental data of the pure gas injection at all flow rates are plotted against three of the most prominent correlations from Hughmark [167], Akita et al. [169] as well as Calderbank and Moo-Young [173] for the top measuring position since the flow is more developed there. Unfortunately, the agreement is not that overwhelming. The correlations of Akita et al. [169] and Calderbank and Moo-Young [173] stay constant over the all injection flow rates which is why the calculated k_L with their calculation is basically on a horizontal line. The data of Hughmark [167] on the other hand underestimate the mass transfer coefficient for a wide range of the measurements. The trend as such is not represented by either of the three liquid mass transfer correlations.

The reason for this big discrepancy is manifold. The correlations were all derived for different sized facilities with nozzles more used in the chemical sector that are designed to form a fine bubble swarm. The nozzle used for this work had the similar dimension of a nozzle that could be used in a wet scrubber which is rather big in

dimension, i.e. in the millimeter range. Furthermore, the mass transfer coefficient k_L was also estimated in those works by the determination of k_La and the interfacial area density. The latter was mostly done through optical imaging methods. The tomographic abilities of the WMS give a much clearer image of the flow situation which result in values with higher accuracy. A similar sized facility with a similar nozzle would be needed to replicate the flow situation to validate the proposed correlations.

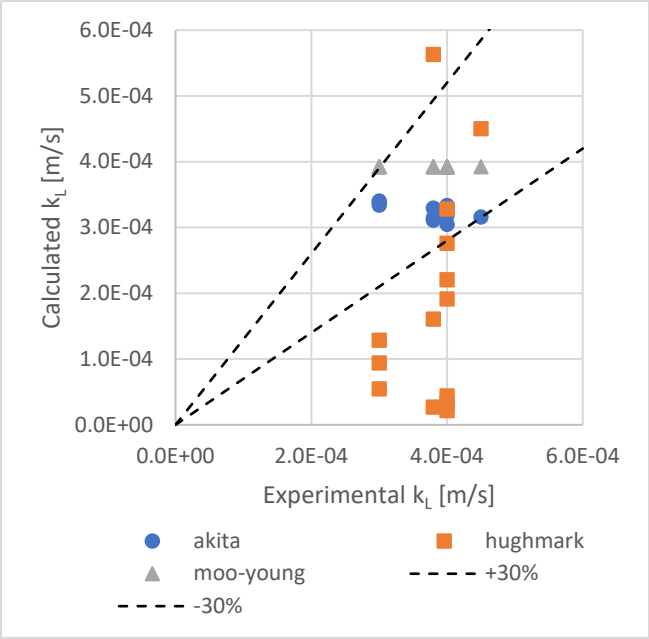

Figure 100: Estimated liquid-side mass transfer coefficients compared with three correlations at the top measuring position.

More correlations exist for the calculation of the volumetric liquid side mass transfer coefficient k_La than for k_L alone as k_La can be easier measured. Three of the most used industrial k_La correlations were compared with the retrieved experimental data in Figure 101. The correlation presented by Akita et al. in the earlier work [168] did after all show a great performance for both positions. At higher flow rates, the discrepancy grew, which can be explained by the different flow regime due to the different facility dimension and nozzle geometry, but compared to the pure k_L correlation, the results were in much better agreement. The correlation of Deckwer et al. [172] produces values on the upper limit of the 30 % error band while Hikita et al. [13] is constantly overpredicting.

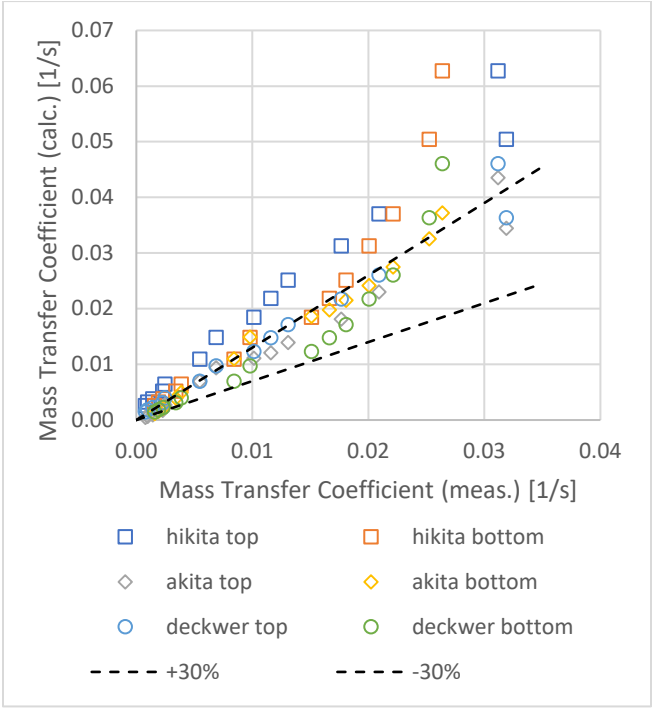

Figure 101: Comparison of three correlations for the volumetric liquid-side mass transfer coefficients for the pure CO_2 gas inlet tests at both positions against correlations from Hikita et al. [13], Akita et al. [168] and Deckwer et al. [172].

Continuing with the application of the correlation developed by Akita et al. to the gas mixture tests revealed to not show as good agreement as the pure gas experiments. Despite the fact that Akita et al. used gas mixtures themselves, the discrepancy between the measured values and the calculated got worse with decreasing carbon dioxide content in the gas stream. According to literature, the gas side transfer coefficient is not known to have an influence on the mass transfer with carbon dioxide, as the liquid side is more limiting. If this information is neglected, it would be possible to calculate the gas side mass transfer coefficient to verify if this could have an effect on the calculated mass transfer coefficients.

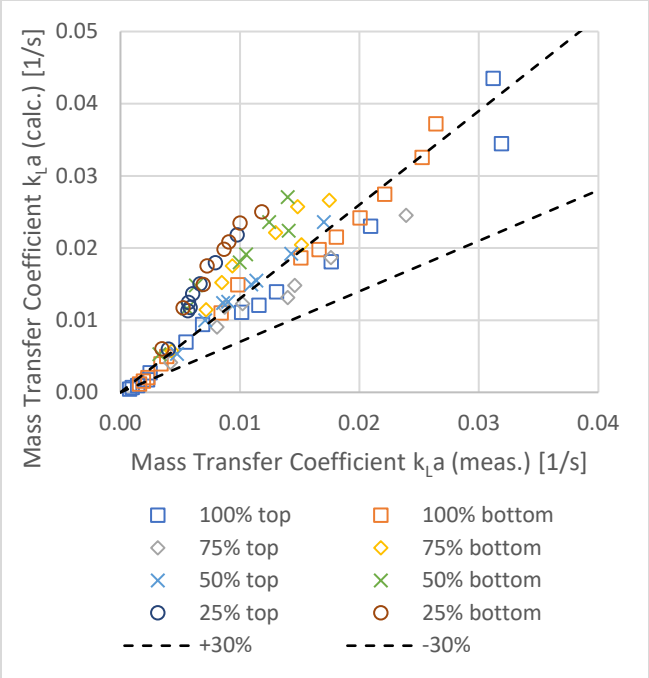

Figure 102: Comparing the calculated liquid-side mass transfer coefficient from the Akita et al. correlation [168] with the measured values.

In the pure CO_2 environment, no gas diffusion can cause a resistive force on the interphase transfer. The combined transfer coefficient K_L would be the estimated mass transfer coefficient for the gas mixture tests whereas k_L is the liquid side mass transfer of the pure carbon dioxide measurements. *He'* is the dimensionless Henry constant, which is the Henry constant multiplied by the temperature and the universal gas constant. With these quantities and the two-resistance theory equation (4.28), the gas side mass transfer coefficient k_G can be obtained.

$$\frac{1}{K_L} = \frac{1}{k_L} + \frac{He'}{1/k_G} \tag{4.28}$$

Knowing the gas side mass transfer coefficient, the new combined volumetric mass transfer coefficient can be calculated by using the mass transfer coefficient from the correlations. Since the correlation for k_La showed the best performance in the pure gas environment, the formula (4.29) is slightly modified to take interfacial area density into account.

$$\frac{1}{K_L a_{mod}} = \frac{1}{k_L a_{Akita}} + \frac{He'}{k_G \cdot a_{meas}} \tag{4.29}$$

The new combined mass transfer coefficient K_La_{mod} is plotted against the measured value for each concentration which yields the results in Figure 103. The mass transfer coefficients for 75% gas concentration were already before very close to ones of the pure gas, which is why no effect could be observed. But for 50% and less, the discrepancy got significantly smaller with one exception being the 50 % gas concentration measurements at the bottom position.

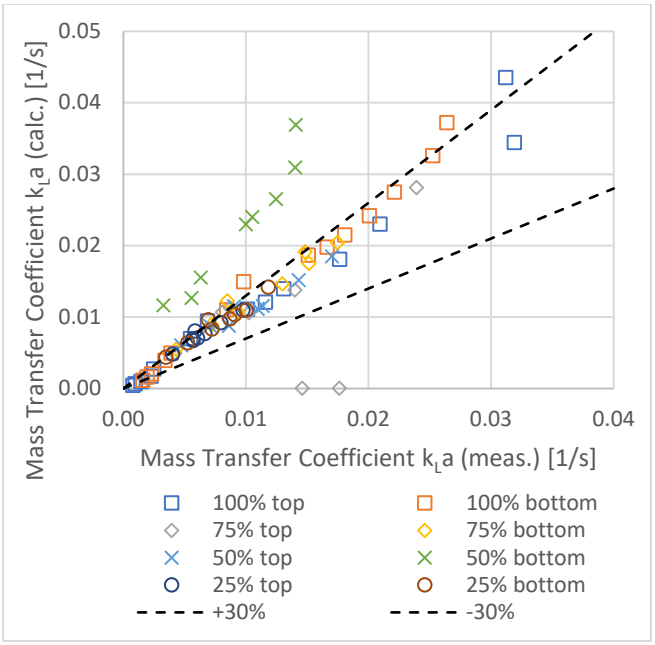

Figure 103: Comparing modified Akita et al. correlation with measured liquid-side mass transfer coefficient.

As the 75 % gas concentration did not give any values for the gas side mass transfer coefficients, only two gas concentrations were left to be investigated at two measuring positions. This is unfortunately not enough to correlate the values or find any physical dependency as it can be seen in Figure 104. For most of the test cases, the values of the gas side mass transfer coefficient stay relative constant for superficial velocities above 0.02 m/s. Lower superficial velocities result in slightly higher value. Regarding the flow behavior, the opposite would have been expected. At higher superficial flow rates, the flow gets more chaotic and should cause more circulation inside the gas phase, which would increase the diffusivity. As mentioned, further tests, especially at lower gas concentrations would be required to study the effect of the gas side mass transfer more analytically.

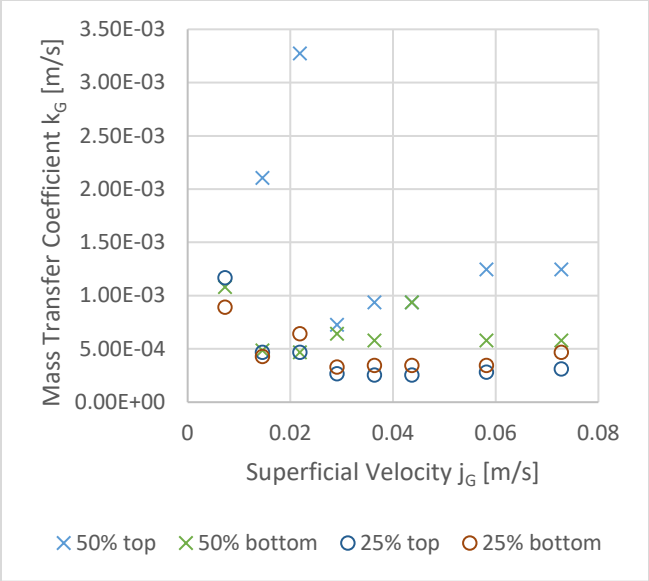

Figure 104: Estimated volumetric gas side mass transfer coefficient at different superficial velocities for 50% and 25% concentration of CO_2 in the gas stream.

Last but not least, the one-dimensional code allows for the calculation of the retention values in the present bubble column. As the concentration profiles and void fractions were replicated within a good margin, the total scrubbed mass can be compared to the total injected mass. In Figure 105, the collection efficiency is plotted for 8 different flow rates against the simulation time. Since the higher flow rates came close to the saturation values in the liquid, the collection efficiency would drop very fast. The gas is at this point traversing through the liquid without interaction. The curves in Figure 105 support this for the superficial velocities above 0.03 m/s. In the bubbly and cap flow regime, i.e. up to 0.007 m/s, a longer experiment would not have a strong impact on the measured collection efficiency. In the heterogeneous flow regime, the efficiency drops very fast to very low values. This information is also important in the preparation of a test series with absorbing gases in order to avoid to run into the saturation region.

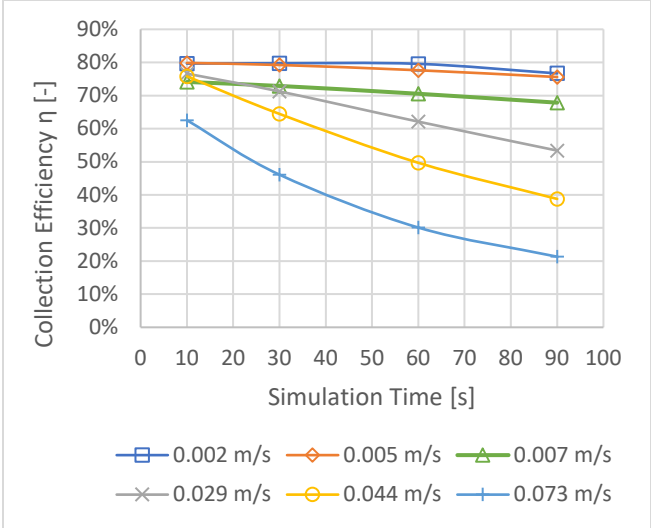

Figure 105: Collection efficiency at different injection flow rates at different simulation times.

Running the one-dimensional code for all the flow rates used in the experiments over the full 90 seconds yields the collection efficiency curve in Figure 106. The results have a certain similarity to those of Beghi et al. [33]. At small superficial velocities, the collection efficiency is rather high whereas beyond the transition region in the slug flow region, the values seem to be almost independent of the injection flow rate.

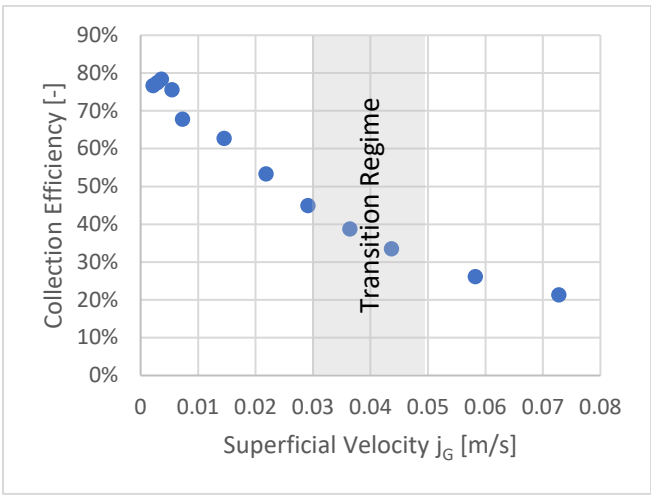

Figure 106: Simulated collection efficiency for all the flow rates of the presented experiments after 90 seconds of simulation time.

4.6 Conclusions on Diffusive Mass Transfer Tests

The wire-mesh-sensor has been used in the past for the analysis of many two-phase flow structures. Bubble

reconstructions, interfacial area determination and bubble size estimations were studied thoroughly in different fields. In the mass transfer tests with carbon dioxide as the gas-phase, the hydrodynamics revealed the shrinking of the bubbles over bubble height for the bubbly flow regime and a higher contribution of the smaller bubbles in bimodal bubble sizes to the transferred gas mass. In this work, for the first time, the WMS was able to detect not just the bubbles but also the mass transferred from the gas to the liquid phase. The additional information gained by the dissolved gas concentration showed that axial dispersion in more heterogeneous flow with Taylor or bigger cap bubbles can play an important role in the two-phase flow diffusion depending on the facility size. The formulation of a one-dimensional model linked with the experimental liquid concentration data made the determination of the mass transfer coefficient possible and the hydrodynamic information, i.e. the interfacial area density, allowed for the estimation of the liquid-side mass transfer coefficient k_L without the need of assumptions based on the Sauter mean diameter or literature correlations.

In the pure carbon dioxide tests, most of the phenomena observed could be backed up with literature and previous observations. The use of carbon dioxide in a mixture with nitrogen however, showed that the gas side mass transfer coefficient could play a small role even if the liquid side is the more limiting factor. Unfortunately, only a small set of gas mixture experiments were performed as the limiting liquid side coefficient was assumed to be more relevant. Further tests in the low concentration region, i.e. 10 – 40% CO_2 gas concentration with a finer stepping in the gas flow rate could give more insight into this phenomenon.

The results gained by the carbon dioxide tests give a picture of general mass transfer phenomena. In situations relevant to real wet scrubbers, the high steam content and the low iodine concentration in the gas will have a strong impact on the retention. With lower gas concentrations, the gas side mass transfer coefficient will definitely play a role. Nevertheless, the studied range gave first impressions on mass transfer effects worth looking deeper into. More verification tests for which a lot of literature values are also available, could be performed with the use of oxygen as it also reacts with pure water and increases the electrical conductivity of water. For the study of the gas-side resistance, ammonia could be an interesting candidate as it is very soluble in water. Expanding the test matrix with more gases could also show if the results could be easily transferred, eventually also to iodine tests cases.

Outlook on Iodine Scrubbing

The developed one-dimensional code was applied only for carbon dioxide measurements. Theoretically, with a small adjustment of the Henry constant, the diffusion coefficient and the solubility limit, the model can be modified to estimate iodine retention for water conditions. Beghi et al. [33] not only used chemicals in the water which could be modeled with an enhancing reaction factor as explained by Danckwerts [183]. The use of the internals makes a benchmark of the code obsolete as the effect of the internals are partly known only on the hydrodynamics. However, Lind et al. [188] have presented preliminary test results of a couple of experiments in Mini-VEFITA that have been conducted with iodine loaded nitrogen (150 ppm), pure water and a generic nozzle with 6 mm diameter and 30 minutes of feeding time. The data is scarce but all the quantities are known for a calculation with the BUSCA code and the newly adapted computer model.

In the one-dimensional code, the axial dispersion coefficient was turned off as in Mini-VEFITA, the filling height of 700 mm to 200 mm diameter would be just within the specification recommended by Deckwer et al. [182] on the applicability of the CSTR model without axial dispersion. The volumetric liquid side mass transfer coefficient k_L was calculated with the correlation of Akita et al. and multiplied with the interfacial area density obtained from complementary measurements in ISOLDE. The combined value k_La was then given as an input as the code could not determine the interfacial area density correctly, i.e. the calculated interfacial area density is double the measured one in ISOLDE.

The experimental data points from Lind et al. are plotted in Figure 107 against the BUSCA calculation and the adjusted CSTR model. The BUSCA model heavily overpredicts the retention in the bubbly flow regime as it assumes a homogeneous bubble swarm with a decent residence time. The CSTR on the other

hand underpredicts for the lowest flow rate but is in the proximity of the experimental data. Obviously, the values were slightly adjusted with experimental known parameters to get the correct k_La whereas in the carbon dioxide tests, only k_L was used as a constant value. But the data would anyway not allow any further conclusions as five data points are too few to judge the quality of a model. Yet, with more experimental data in the low gas concentration region and a deeper look into more sophisticated interfacial area density correlations, it could be a possible way to enhance the one-dimensional code for a model suggestion in severe accident system codes.

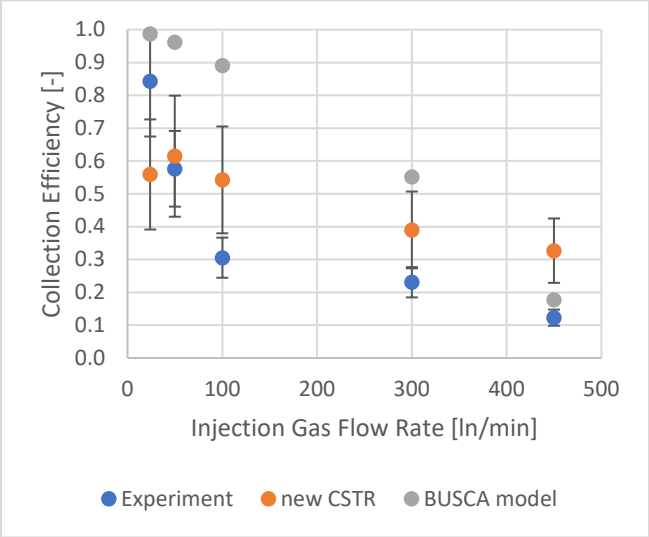

Figure 107: Collection efficiency determined from preliminary tests from MiniVEFITA [188], the BUSCA model and the adapted CSTR model.

5 CONCLUSION AND OUTLOOK

The retention of radioactive material released from the nuclear fuel during a severe accident is a challenging task. Especially, the retention of iodine is difficult as it can exist as both aerosols and gas phase species in the containment. The most common gas phase species are molecular iodine and organic iodides which can be formed inside the containment during a severe accident. Thanks to existing installations, the release of radioactivity in the form of iodine can be drastically reduced. Suppression pools, steam generators but also filtered containment venting systems based on wet scrubbers all hold liquid inventory that can retain part of the iodine and trap it, before it manages to escape in a possible flow path to the environment. In case of the wet scrubber filters, they are even loaded with chemical additives to enhance the chemical reaction that leads to the absorption of iodine species.

As part of the safety analysis, nuclear power plants are using commercial system codes to study the accident consequences. The codes that are available today for the calculation of postulated severe accident events and the assessment of possible releases contain models that deal with the various transport and retention mechanisms. Regarding the diffusion of the gaseous iodine compounds in the two-phase flow regime through the gas-liquid interface, the retention of the gas phase iodine species in the liquid pools can be modelled using the so-called soluble gas model. To model scrubbing of the gaseous contaminants in a liquid pool, the codes typically define three zones, for which models of the mass transfer process are needed. These are the injection region, the bubble rising zone and the pool surface. Regarding the bubble rising zone, a homogeneous bubble swarm of unimodal sized ellipsoids or cap bubbles is assumed in most of the codes. Considering the fact that a pressure build-up might thus require a fast depressurization of the containment, the volumetric flow rates can reach very high values.

This work was launched with the scope to experimentally characterize the two-phase flow structure in water pools relevant to wet scrubbers and to verify the hydrodynamics against the assumptions in the soluble gas models of the system codes. The performance of the two most widespread types of injection nozzles applied in Filtered Containment Venting Systems as well as the effect of a static mixing packing were studied in an experimental pool and laboratory bubble columns. The wire-mesh sensor was chosen as the main instrumentation technique in order to determine bubble sizes. To complement the hydrodynamic studies, a new method was developed to measure gas-liquid mass transfer for soluble gases. The mass transfer coefficient of a soluble gas in a simple geometry was investigated to get a first impression on the effect of the hydrodynamics on the mass transfer.

For this work, two-fold development of the analytical methods to interpret wire-mesh sensor data needed further development to obtain robust results for a very difficult measuring regime for the WMS, the stagnant pool condition. It is known that the wire-mesh sensor disturbs the flow in a bubble column more than in a two-phase flow with a positive net liquid flow rate. The newly established routines coping with these problems showed overall a good performance, including a new filtering technique, the use of the Maxwell-Hewitt instead of the linear calibration and the compensation of overshoot signals that are caused by the disturbance of the electrical field at the gas-liquid interphase. Also, a new method was derived for the determination of the interfacial area density that is independent of the bubble velocity and can thus be used with the measurement data of one sensor layer only.

The first part of the thesis is dedicated to the hydrodynamics of the two-phase flow generated by injection nozzles applied in real wet scrubbers under adiabatic conditions, i.e. with no steam content in the gas mixture. A single cylindrical injection nozzle (CCI IMI Nuclear design) was tested in a 200 mm diameter bubble column. The nozzle design consists of a generic 6 mm nozzle and is equipped with three impaction plates with central holes of 6 mm. Tests were performed with and without a static mixing element, a so-called Sulzer packing, placed above the nozzle outlet. In a real FCVS the packing serves as a bubble breaker and mass transfer intensifier.

Bubble size distributions and interfacial area concentration were measured above the nozzle and downstream of the packing. The studies revealed for the

mixing element to be the most efficient in breaking the bubbles in the bubbly flow regime up to the transition regime with cap flow. In this flow region, the interfacial area density is amplified by the mixing element by a factor of 3 to 4. The bigger bubbles are fragmented to smaller ones, thus creating a more homogenized bubble size distribution. This will have a positive influence on the mass transfer rate as smaller bubbles have a higher residence time and a better surface to volume ratio. Beyond the transition regime, gas trapped in the packing is forming bigger Taylor bubbles and the bigger gas bubbles are not affected too much by the mixing element, resulting into a very heterogeneous flow condition which is not addressed by existing system codes that assume a homogenous residence time of bubbles of uniform size. This leads to an overestimation of the retention in the state-of-art models in this flow regime.

The chemical solutions that are used to enhance the retention of molecular iodine are known to have an effect on the surface tension. Tests with chemicals were conducted for practical reasons in a smaller table-top column of 50 mm diameter. The concentration of scrubbing agents was varied up to the operational limits of the data acquisition system of the WMS. Within the limits of the achievable concentrations of the additives (0.015 mol/L NaOH, 0.03 mol/L $Na_2S_2O_3$, 0.01 mol/L Na_2CO_3, which is between 4 and 66 % of the maximum concentration applied in real filters, depending on the chemical composition), no significant difference to the pure water tests were observed.

A Venturi nozzle used in a commercial FCVS design was tested as the second nozzle type in submerged and non-submerged mode in an experimental pool of 0.5 x 0.5 m^2 in lateral dimensions. With the use of a high-speed camera, a new method based on shadowgraphy was developed to determine the droplet size inside the throat of a Venturi nozzle type sparger. The results made clear that, despite the probable overprediction of the droplet sizes, the use of the commonly known correlations used by literature for the estimation of the Sauter mean diameter, the main parameter, is not suitable. These correlations developed within the chemical sector, i.e. by Nukiyama-Tanasawa and Boll, refer to actively driven Venturi tubes, in which the liquid is injected in a controlled way and mostly sprayed into a gas stream through fine orifices. The own experiments showed that these correlations overestimate the Sauter mean diameter compared to the self-priming passive designs of the Venturi nozzle used in FCVS. The used Venturi design relied on the suction of the liquid through slits that caused an untypically high liquid to gas ratio compared to the actively driven Venturi nozzles of the chemical sector. Since the liquid to gas ratio has a strong weight in both correlations, the calculated droplet diameter grew accordingly.

Existing annular flow correlations on the other hand, where the droplet formation mechanism is due to entrainment from a liquid film at the wetted walls, which is similar to the functioning of self-priming Venturi nozzles, gave droplet sizes in the same order of magnitude. A change to the application of such correlations in the established codes could be considered if more experimental data could be provided, i.e. different Venturi design and wider gas injection range. For the further development in this area, a high-speed camera with a higher resolution would be desirable or, alternatively, the use of inline holography to capture also droplet sizes in the 100-micron region and reduce the measurement uncertainty.

The bubble rising zone above a Venturi nozzle that is operated fully submerged was characterized by wire-mesh sensors. The specific Venturi design studies showed a relatively constant interfacial area density and void fractions in the rising zone, almost independent of the injected gas flow rate. A similar behavior was observed for the droplet size distribution which lead to the conclusion that the Venturi nozzle performs relatively constant in the designed operation range, making the modeling aspect easier. Despite the fact that the initial big globule bubbles are fragmented in their flow path, the flow regime remains heterogeneous with a typical bimodal churn-turbulent size distribution. Again, the codes would not take this effect of two differently fast rising bubble size classes into account.

Comparing both nozzles, the IMI-Nuclear design manages to create a higher interfacial area density in the pool and would at first seem to be the better choice. The Venturi tube on the other hand benefits from the droplet generation in the throat and diffusor section with a high liquid renewal rate. The effectiveness of each design would need to be tested by injecting a soluble gas and

measure the concentration of the dissolved gas in the pool.

In real life scenarios, the gas mixture entering the FCVS will contain a significant amount of steam at elevated temperatures which was not taken into account in this work. Beside the increased difficulty in the analysis due to the temperature fluctuations in the liquid, the main aim of this work was to study the gas solubility model. The main idea was to isolate the diffusion process before going into more complex situations where temperature effects will also play a role. Combining adiabatic thermal-hydraulic tests with adiabatic mass transfer measurements would thus be an optimal start. Another limitation in the nozzle characteristics came from the facility dimensions. The cross-section of the facilities is down-scaled and corresponds to half and double the actual cross-section of the CCI and the Venturi nozzle respectively. The results in the near field will though still be valid as the far field will also experience disturbances from the adjacent nozzle in a real wet scrubber which was mostly studied in this work.

In order to look deeper into the mass transfer phenomena from the gaseous phase into the liquid and its dependency on the flow structure, the WMS was further developed to be applicable in mass transfer experiments. One requirement is the use of a reactive gas that dissolves in the liquid phase, causing a significant increase of the electrical conductivity of its aqueous solution compared to pure water. Carbon dioxide was chosen as a substitute to replicate the gas mixture containing contaminants that are to be removed in a wet scrubber. The experimental studies were carried out in a small rectangular bubble column (50 x 50 mm^2, height of 1.7 m) with pure water. The model gas carbon dioxide would allow to verify the results with literature correlations and assess the use of the new developed method for future tests.

The novel measuring technique consisted of a separation of the information on the dissolved gas quantity from the signal components originating from the gaseous phase, which is causing a decrease of the local instantaneous conductance at the affected sensor electrodes. This allowed for the first time a simultaneous quantification of the gas dissolution process together with the characterization of the topology of the gas-liquid interface in a high spatial and temporal resolution.

Experiments carried out applying the novel signal processing method revealed that in the heterogeneous flow regime, it is mostly the small bubbles that are being scrubbed whereas the Taylor bubbles and churns are traversing through the bubble column without too much retention. The information from the liquid concentration showed though that these bigger bubbles are also contributing to the distribution of the dissolved gas by axial dispersion. Axial concentration gradients have thus to be taken into account for small-scale facilities with high L/D ratios. Axial dispersion models are then needed to predict the concentration distribution correctly, since the ideally mixed reactor model is not applicable. In FCVS wet scrubbers, this should be less relevant as the filters have rather big diameters.

The CO_2 dissolution experiments conducted at the small bubble column were additionally analyzed using a one-dimensional dynamic model that resolves the column by a nodalization in axial direction. The comparison between model and experiment allowed to identify values of the overall liquid-side mass transfer coefficient k_La. The fact that the processing of the wire-mesh sensor signals yields the interfacial area density gave the possibility to extract the liquid-side mass transfer coefficient k_l, whereas numerous researchers in the past were only able to present the volumetric liquid-side mass transfer coefficient k_La. The results of both, k_La and k_L, are in good agreement with the empirical correlations proposed by Akita and Yoshida even though their experiments where performed under more homogenized flow conditions.

The tests performed with gas mixtures using nitrogen to reduce the partial pressure of the dissolving gas did not behave as expected from literature. Even though the liquid side mass transfer coefficient is known to be the limiting one for carbon dioxide diffusion, the gas mixtures with a carbon dioxide content of 50% or less did react significantly slower with the liquid bulk. The preliminary addition of a gas side mass transfer coefficient to form an overall mass transfer coefficient K_La consistent with the two-resistance theory improved the comparison with correlations from literature. More detailed experimental information is needed for the development of reliable

models of the gas-side mass transfer, which is a task remaining for the future.

A simplified extrapolation using known kinetic coefficients of the reaction of iodine with water, i.e. liquid side diffusion coefficient and solubility limit, allowed to provide first estimates of the scrubbing efficiency. The test conditions of preliminary iodine retention tests being conducted in the Mini-VEFITA facility were used as input parameters. The ideally mixed reactor model used the k_L correlation of Akita and Yoshida and the experimental interfacial area density data from the WMS at the specific test condition to form an average mass transfer coefficient k_La. The results of this model were much closer to the experimental retention data than the state-of-the-art model implemented in BUSCA. However, the model still required the interfacial area density as an input parameter which should be in a further step replaced by an empirical model as well. More detailed experimental retention data would also be necessary to assess the model uncertainty.

For the future work in this field, it is recommended to design an improved WMS for bubble column experiments. A finer distance in lateral and mostly axial direction would be desirable to get a better resolution on the dense bubble swarms related to the mixing element. For experiments with high concentrations of chemicals prompting the iodine scrubbing, the electronic signal acquisition system of the WMS has to be perfected. In particular, the impedance of transmitter and receiver cascades had to be further reduced in order to improve the signal quality in case of a high electrical conductivity of the liquid phase. With a finer sensor and a new data acquisition system, the effect of the scrubber solution on the two-phase flow structure could be studied at real conditions. Furthermore, carbon dioxide tests are suggested to be performed in a more realistic scaling compared to industrial geometries. On top of that, more mixture tests would be beneficial with a reduced concentration of the dissolving gas component in the range between 10 and 40 % to further shed light on the effect of the gas side resistance. Tests with other gases, like oxygen or ammonia, could also be made in order to verify the carbon dioxide results and validate if the found correlations and models can be transferred to other gases, like eventually iodine.

6 BIBLIOGRAPHY

[1] S. Bouckaert, A. Fernandez Pales, C. McGlade, U. Remme, B. Wanner, L. Varro, D. D'Ambrosio and T. Spencer, *Net Zero by 2050: A Roadmap for the Global Energy Sector,* International Energy Agency, 2021.

[2] I. E. Agency, World energy outlook 2020, 2020.

[3] IAEA, Defence in Depth in Nuclear Safety, Vienna: INTERNATIONAL ATOMIC ENERGY AGENCY, 1996.

[4] D. Jacquemain, S. Guentay, S. Basu, M. Sonnenkalb, L. Lebel, J. Ball, H. J. Allelein, M. Liebana, B. Eckardt, N. Losch and others, "OECD/NEA/CSNI status Report on filtered Containment Venting," 2014.

[5] L. Soffer, S. B. Burson, C. M. Ferrell, R. Y. Lee and J. N. Ridgely, "Accident source terms for light-water nuclear power plants. final report," 1995.

[6] J. L. Collins, M. F. Osborne, R. A. Lorenz and A. P. Malinauskas, "Fission Product Iodine and Cesium Release Behavior Under Light Water Reactor Accident Conditions," *Nuclear Technology,* vol. 81, p. 78–94, April 1988.

[7] C. Hillrichs, D. Vignon and P. Felten, "Review of European filtered containment venting systems," *European Nuclear Society (ENS),* p. 9–12, 2012.

[8] M. J. Crick and G. S. Linsley, "An Assessment of the Radiological Impact of the Windscale Reactor Fire, October 1957," *International Journal of Radiation Biology and Related Studies in Physics, Chemistry and Medicine,* vol. 46, p. 479–506, January 1984.

[9] H. R. Diffey, C. H. Rumary, M. J. S. Smith and R. A. Stinchcombe, "Iodine clean-up in a steam suppression system," in *CONF-65047*, 1965.

[10] J. Hillary, J. C. Taylor, F. Abbey and H. R. Diffey, "Iodine removal by a scale model of the SGHW reactor vented steam suppression system," *No. TRG Report,* vol. 1256, 1966.

[11] J. J. Hillary, L. F. Gate and K. Gurney, "Experience in testing installed fission product trapping plant with methyl iodide," July 1967.

[12] L. E. Stanford and C. C. Webster, "ENERGY SUPPRESSION AND FISSION PRODUCT TRANSPORT IN PRESSURE-SUPPRESSION POOLS.," Office of Scientific and Technical Information (OSTI), 1972.

[13] H. Hikita, S. Asai, K. Tanigawa, K. Segawa and M. Kitao, "The volumetric liquid-phase mass transfer coefficient in bubble columns," *The Chemical Engineering Journal,* vol. 22, pp. 61-69, 1981.

[14] D. P. Siegwarth and M. Siegler, "SCALE MODEL TESTS OF FISSION-PRODUCT REMOVAL IN SUPPRESSION POOLS.," January 1971.

[15] S. Güntay, "Experiment poseidon: Elemental iodine retention in water pools," *Transactions of the American Nuclear Society,* vol. 62, 1990.

[16] A. T. Wassel, A. F. Mills, D. C. Bugby and R. N. Oehlberg, "Analysis of radionuclide retention in water pools," *Nuclear Engineering and Design,* vol. 90, p. 87–104, November 1985.

[17] S. A. Ramsdale, S. Güntay and H.-G. Friederichs, "BUSCA-JUN91. Reference manual for the calculation of radionuclide scrubbing in water pools," 1995.

[18] P. C. Owczarski and K. W. Burk, "SPARC-90: A code for calculating fission product capture in suppression pools," Office of Scientific and Technical Information (OSTI), 1991.

[19] L. E. Herranz, M. J. Escudero, V. Peyrés, J. Polo and J. López-Jiménez, "Review and assessment of pool scrubbing models," 1996.

[20] K. Fischer, *Pool scrubbing models for iodine components,* 1996.

[21] S. A. Ramsdale, Status of research and modelling of water-pool scrubbing: final report, City: Commission of the European Communities, 1992.

[22] N. A. Fuchs, R. E. Daisley, M. Fuchs, C. N. Davies and M. E. Straumanis, "The mechanics of aerosols," *Physics Today,* vol. 18, p. 73, 1965.

[23] T. Lind, A. Dehbi and S. Güntay, "Aerosol retention in the flooded steam generator bundle during SGTR," *Nuclear Engineering and Design,* vol. 241, p. 357–365, January 2011.

[24] A. Dehbi, D. Suckow, T. Lind, S. Guentay, S. Danner and R. Mukin, "Key Findings from the Artist Project on Aerosol Retention in a Dry Steam Generator," *Nuclear Engineering and Technology,* vol. 48, p. 870–880, August 2016.

[25] S. I. Kim, J. Y. Oh, B. H. Lee and S. H. Hong, "Aerosol Retention Test in Dry Steam Generator during Steam Generator Tube Rupture Accident Condition," in *Transactions of the Korean Nuclear Society Spring Meeting, Jeju, Korea*, 2021.

[26] H. Diao, Y. Zhou, H. Gu, Y. Li and C. Yan, "Experimental study on the scrubbing efficiency of aerosols contained in horizontal and vertically downward submerged gas jet," *Progress in Nuclear Energy,* vol. 126, p. 103406, August 2020.

[27] L. E. Herranz, C. Lopez and J. Penalva, "Investigation on jet scrubbing in nuclear reactor accidents: From experimental data to an empirical correlation," *Progress in Nuclear Energy,* vol. 107, p. 72–82, August 2018.

[28] K. Fujiwara, W. Kikuchi, Y. Nakamura, T. Yuasa, S. Saito, A. Kaneko and Y. Abe, "Experimental study of single-bubble behavior containing aerosol during pool scrubbing," *Nuclear Engineering and Design,* vol. 348, p. 159–168, July 2019.

[29] L. E. Herranz, R. D. Tardáguila, T. Berschart, T. Lind and S. Morandi, "Remaining issues on pool scrubbing: Major drivers for experimentation within the EU-PASSAM project," in *Proceedings of ICAPP*, 2014.

[30] T. Albiol, L. Herranz, E. Riera, C. Dalibart, T. Lind, A. D. Corno, T. Kärkelä, N. Losch, B. Azambre, C. Mun and L. Cantrel, "Main results of the European PASSAM project on severe accident source term mitigation," *Annals of Nuclear Energy,* vol. 116, p. 42–56, June 2018.

[31] D. Suckow, M. Furrer, J. Yang, B. Jäckel and T. Lind, "Investigation of iodine retention in a filtered containment venting system in the VEFITA test program," in *Proceedings of the International OECD-NEA/NUGENIA-SARNET Workshop on the Progress in Iodine Behaviour for NPP Accident Analysis and Management*, 2015.

[32] T. Lind, D. Suckow and J. Yang, "Characterization of the Performance of Wet Scrubbers Used in FCVS," *IAEA TECDOC SERIES,* p. 210, 2015.

[33] I. Beghi, T. Lind and H.-M. Prasser, "Experimental studies on retention of iodine in a wet scrubber," *Nuclear Engineering and Design,* vol. 326, p. 234–243, January 2018.

[34] M. Ali, C. Yan, Z. Sun, H. Gu and J. Wang, "Study of iodine removal efficiency in self-priming venturi scrubber," *Annals of Nuclear Energy,* vol. 57, p. 263–268, July 2013.

[35] A. L. I. MAJID, Y. A. N. CHANGQI, S. U. N. ZHONGNING, G. U. HAIFENG, W. A. N. G. JUNLONG and K. H. U. R. R. A. M. MEHBOOB, "IODINE REMOVAL EFFICIENCY IN NON-SUBMERGED AND SUBMERGED SELF-PRIMING VENTURI SCRUBBER," *Nuclear Engineering and Technology,* vol. 45, pp. 203-210, 2013.

[36] Y. Zhou, Z. Sun, H. Gu and Z. Miao, "Performance of iodide vapour absorption in the venturi scrubber working in self-priming mode," *Annals of Nuclear Energy,* vol. 87, p. 426–434, January 2016.

[37] N. P. Gulhane, A. D. Landge, D. S. Shukla and S. S. Kale, "Experimental study of iodine removal efficiency in self-priming venturi scrubber," *Annals of Nuclear Energy,* vol. 78, p. 152–159, April 2015.

[38] L. E. Herranz, J. Fontanet and L. Cantrel, "Modeling liquid–gas iodine mass transfer under evaporative conditions during severe accidents," *Nuclear Engineering and Design,* vol. 239, p. 728–734, April 2009.

[39] K. Fischer, M. Freitag and H. S. Kang, "Mechanistic model of iodine mass transfer at pool surfaces," *Nuclear Engineering and Design,* vol. 278, p. 627–631, October 2014.

[40] T. Betschart, "Two-Phase Flow Investigations in Large Diameter Channels and Tube Bundles," 2015.

[41] S. Gupta and L.E. Herranz and J.-P. Van Dorsselaere, "Integration of Pool scrubbing Research to Enhance Source-term Calculations (IPRESCA)," *8th european review meeting on severe accident research,* 2017.

[42] B. Rosenberg, "The drag and shape of air bubbles moving in liquids," 1950.

[43] O. Levenspiel, "Collapse of steam bubbles in water," *Industrial & Engineering Chemistry,* vol. 51, p. 787–790, 1959.

[44] R. C. Kintner, T. J. Horton, R. E. Graumann and S. Amberkar, "Photography in Bubble and Drop Research," *The Canadian Journal of Chemical Engineering,* 1961.

[45] K. Nishino, H. Kato and K. Torii, "Stereo imaging for simultaneous measurement of size and velocity of particles in dispersed two-phase flow," *Measurement Science and Technology,* vol. 11, p. 633–645, 5 2000.

[46] Y. Murai, Y. Matsumoto and F. Yamamoto, "Three-dimensional measurement of void fraction in a bubble plume using statistic stereoscopic image processing," *Experiments in Fluids,* vol. 30, p. 11–21, 1 2001.

[47] M. Honkanen, P. Saarenrinne, T. Stoor and J. Niinimäki, "Recognition of highly overlapping ellipse-like bubble images," *Measurement Science and Technology,* vol. 16, p. 1760–1770, July 2005.

[48] D. Bröder and M. Sommerfeld, "Planar shadow image velocimetry for the analysis of the hydrodynamics in bubbly flows," *Measurement Science and Technology,* vol. 18, p. 2513–2528, 7 2007.

[49] M. Lichti and H.-J. Bart, "Bubble size distributions with a shadowgraphic optical probe," *Flow Measurement and Instrumentation,* vol. 60, p. 164–170, 4 2018.

[50] S. Beucher, "The watershed transformation applied to image segmentation," *Scanning Microscopy,* vol. 1992, p. 28, 1992.

[51] F. D. Nunno, F. A. Pereira, F. Granata, G. de Marinis, F. D. Felice, R. Gargano and M. Miozzi, "A shadowgraphy approach for the 3D Lagrangian description of bubbly flows," *Measurement Science and Technology,* vol. 31, p. 105301, 7 2020.

[52] Y. Murai, K. Inaba, Y. Takeda and F. Yamamoto, "Backlight imaging tomography for slug flows in straight and helical tubes," *Flow Measurement and Instrumentation,* vol. 18, p. 223–229, 10 2007.

[53] A. Dasgupta, D. K. Chandraker, S. Kshirasagar, B. R. Reddy, R. Rajalakshmi, A. K. Nayak, S. P. Walker, P. K. Vijayan and G. F. Hewitt, "Experimental investigation on dominant waves in upward air-water two-phase flow in churn and annular regime," *Experimental Thermal and Fluid Science,* vol. 81, p. 147–163, 2 2017.

[54] B. J. Thompson, "Diffraction by Opaque and Transparent Particles," *Optical Engineering,* vol. 2, 1 1964.

[55] B. J. Thompson, J. H. Ward and W. R. Zinky, "Application of Hologram Techniques for Particle Size Analysis," *Applied Optics,* vol. 6, p. 519, 3 1967.

[56] B. J. Thompson, "Holographic particle sizing techniques," *Journal of Physics E: Scientific Instruments,* vol. 7, p. 781–788, 10 1974.

[57] G. Haussmann and W. Lauterborn, "Determination of size and position of fast moving gas bubbles in liquids by digital 3-D image processing of hologram reconstructions," *Applied Optics,* vol. 19, p. 3529, 10 1980.

[58] W. Lauterborn and W. Hentschel, "Cavitation bubble dynamics studied by high speed photography and holography: part one," *Ultrasonics,* vol. 23, p. 260–268, 11 1985.

[59] W. Lauterborn and W. Hentschel, "Cavitation bubble dynamics studied by high speed photography and holography: part two," *Ultrasonics,* vol. 24, p. 59–65, 3 1986.

[60] Y. J. Lee and J. H. Kim, "A Review of Holography Applications in Multiphase Flow Visualization Study," *Journal of Fluids Engineering,* vol. 108, p. 279–288, 9 1986.

[61] O. Feldmann, "Short-Time Holography and Holographic PIV Applied to Engineering Problems," in *Applied Optical Measurements*, Springer Berlin Heidelberg, 1999, p. 263–278.

[62] S. Shao, C. Li and J. Hong, "A hybrid image processing method for measuring 3D bubble distribution using digital inline holography," *Chemical Engineering Science,* vol. 207, p. 929–941, 11 2019.

[63] G. F. Hewitt and D. N. Roberts, "Studies of two-phase flow patterns by simultaneous x-ray and flast photography," 2 1969.

[64] O. C. Jones and N. Zuber, "The interrelation between void fraction fluctuations and flow patterns in two-phase flow," *International Journal of Multiphase Flow,* vol. 2, p. 273–306, 12 1975.

[65] U. H. H.-M. Prasser, "Anordnung zur Röntgentomographie mit einem elektronisch abgelenkten Elektronenstrahl". Patent DE 103 56 601.5, 2003.

[66] F. Fischer, D. Hoppe, E. Schleicher, G. Mattausch, H. Flaske, R. Bartel and U. Hampel, "An ultra fast electron beam x-ray tomography scanner," *Measurement Science and Technology,* vol. 19, p. 094002, 7 2008.

[67] M. Banowski, U. Hampel, E. Krepper, M. Beyer and D. Lucas, "Experimental investigation of two-phase pipe flow with ultrafast X-ray tomography and comparison with state-of-the-art CFD simulations," *Nuclear Engineering and Design,* vol. 336, p. 90–104, 9 2018.

[68] S. Banerjee, E. Hussein and D. A. Meneley, "Simulation of a neutron scattering method for measuring void fraction in two-phase flow," *Nuclear Engineering and Design,* vol. 53, p. 393–405, August 1979.

[69] R. H. Bossi, A. H. Robinson and J. P. Barton, "High-Speed Motion Neutron Radiography," *Nuclear Technology,* vol. 59, p. 363–374, November 1982.

[70] J.-S. Chang and G. D. Harvel, "Determination of gas-liquid bubble column instantaneous interfacial area and void fraction by a real-time neutron radiography method," *Chemical Engineering Science,* vol. 47, p. 3639–3646, September 1992.

[71] K. Mishima, T. Hibiki and H. Nishihara, "Visualization and measurement of two-phase flow by using neutron radiography," *Nuclear Engineering and Design,* vol. 175, p. 25–35, November 1997.

[72] R. Zboray and H.-M. Prasser, "Measuring liquid film thickness in annular two-phase flows by cold neutron imaging," *Experiments in Fluids,* vol. 54, September 2013.

[73] R. Zboray and P. Trtik, "800 fps neutron radiography of air-water two-phase flow," *MethodsX,* vol. 5, p. 96–102, 2018.

[74] R. Zboray and P. Trtik, "In-depth analysis of high-speed, cold neutron imaging of air-water two-phase flows," *Flow Measurement and Instrumentation,* vol. 66, p. 182–189, April 2019.

[75] C. Lani and R. Zboray, "Development of a high frame rate neutron imaging method for two-phase flows," *Nuclear Instruments and Methods in Physics Research Section A: Accelerators, Spectrometers, Detectors and Associated Equipment,* vol. 954, p. 161707, February 2020.

[76] L. R. Price, "Electrical Impedance Computed Tomography (ICT): A New CT Imaging Technique," *IEEE Transactions on Nuclear Science,* vol. 26, p. 2736–2739, April 1979.

[77] J. Lattimer, D. W. Fitting and L. Adler, "Ultrasonic dynamic imaging (UDI) system to determine the size and velocity of large spherical simulated bubbles in liquids. [LMFBR]," January 1979.

[78] H.-M. Prasser, A. Böttger and J. Zschau, "A new electrode-mesh tomograph for gas–liquid flows," *Flow Measurement and Instrumentation,* vol. 9, pp. 111-119, 1998.

[79] H.-M. Prasser, "Wire-Mesh Sensors and Cognate Measuring Techniques," WORLD SCIENTIFIC, 2018, p. 139–264.

[80] H. F. V. Peña and O. M. H. Rodriguez, "Applications of wire-mesh sensors in multiphase flows," *Flow Measurement and Instrumentation,* vol. 45, p. 255–273, 10 2015.

[81] M. Trepte, "WMS200 Manual," 2008.

[82] H.-M. Prasser, D. Scholz and C. Zippe, "Bubble size measurement using wire-mesh sensors," *Flow Measurement and Instrumentation,* vol. 12, pp. 299-312, 2001.

[83] D. Ito, H.-M. Prasser, H. Kikura and M. Aritomi, "Uncertainty and intrusiveness of three-layer wire-mesh sensor," *Flow Measurement and Instrumentation,* vol. 22, pp. 249-256, 2011.

[84] L. Sigrist, O. Dossenbach and N. Ibl, "On the conductivity and void fraction of gas dispersions in electrolyte solutions," *Journal of Applied Electrochemistry,* vol. 10, p. 223–228, 3 1980.

[85] D. L. George, J. R. Torczynski, K. A. Shollenberger, T. J. O'Hern and S. L. Ceccio, "Validation of electrical-impedance tomography for measurements of material distribution in two-phase flows," *International Journal of Multiphase Flow,* vol. 26, p. 549–581, 4 2000.

[86] J. C. Maxwell, A treatise on electricity and magnetism, vol. 1, Oxford: Clarendon Press, 1873.

[87] G. F. Hewitt, "Measurement of two phase flow parameters," *NASA STI/Recon Technical Report A,* vol. 79, p. 47262, 1 1978.

[88] R. E. D. L. Rue and C. W. Tobias, "On the Conductivity of Dispersions," *Journal of The Electrochemical Society,* vol. 106, p. 827, 1959.

[89] H.-M. Prasser and R. Häfeli, "Signal response of wire-mesh sensors to an idealized bubbly flow," *Nuclear Engineering and Design,* pp. -, 2017.

[90] H.-M. Prasser, M. Beyer and D. Lucas, "Improvement of topflow void fraction data using potential field simulations of the wire-mesh sensor response," in *Specialists Workshop on Advanced Instrumentation and Measurement Techniques for Experiments Related to Nuclear Reactor Thermal Hydraulics and Severe Accidents (SWINTH-20*, 2019.

[91] M. B. Horst-Michael Prasser, "Bubble recognition algorithms for the processing of wire-mesh sensor data," in *6th International Conference on Multiphase Flow - ICMF2007*, Leipzig, 2007.

[92] V. Brankov, "MATLAB Toolbox for Wire-Mesh Sensor Data Processing," 2020.

[93] H.-M. P. Marco Simiano, "Estimation of individual bubble velocities in a gas-liquid flow using wire-mesh sensors," in *International Conference on Multiphase Flow ICMF 2007*, 2007.

[94] D. Ito, H. Kikura, M. Aritomi and H.-M. Prasser, "Bubble velocity estimation with three-layer wire-mesh sensor," in *International Symposium on Flow Visualization - ISFV13*, 2008.

[95] D. Hoppe, A. Grahn and P. Schütz, "Determination of velocity and angular displacement of bubbly flows by means of wire-mesh sensors and correlation analysis," *Flow Measurement and Instrumentation,* vol. 21, pp. 48-53, 2010.

[96] T. Kanai, M. Furuya, T. Arai, K. Shirakawa and Y. Nishi, "Three-dimensional phasic velocity determination methods with wire-mesh sensor," *International Journal of Multiphase Flow,* vol. 46, pp. 75-86, 2012.

[97] M. Furuya, T. Kanai, T. Arai, H. T. H.-M. Prasser, U. Hampel and E. Schleicher, "Three-Dimensional Velocity Vector Determination Algorithm for individual Bubble identified with Wire-Mesh Sensors," in *Proceedings of SWITH-2016*, 2016.

[98] M. Furuya, T. Kanai, T. Arai, H. Takiguchi, H.-M. Prasser, U. Hampel and E. Schleicher, "Three-dimensional velocity vector determination algorithm for individual bubble identified with Wire-Mesh Sensors," *Nuclear Engineering and Design,* vol. 336, p. 74–79, September 2018.

[99] H.-M. Prasser, "Evolution of interfacial area concentration in a vertical air–water flow measured by wire–mesh sensors," *Nuclear Engineering and Design,* vol. 237, pp. 1608-1617, 2007.

[100] H.-M. Prasser, S. Stucki, T. Betschart and J. Eisenberg, "Interfacial Area Density Measurement using a Three-Layer Wire-Mesh Sensor," in *16th International Topical Meeting on Nuclear Reactor Thermal Hydraulics*, 2015.

[101] C. E. Clifford, N. E. MacDonald, H.-M. Prasser and M. L. Kimber, "Robust computational framework for wire-mesh sensor potential field calculations," *Flow Measurement and Instrumentation,* vol. 67, p. 107–117, 6 2019.

[102] Ag2gaeh, *Ellipsoide,* 2021.

[103] S. Richter, M. Aritomi, H.-M. Prasser and R. Hampel, "Approach towards spatial phase reconstruction in transient bubbly flow using a wire-mesh sensor," *International Journal of Heat and Mass Transfer,* vol. 45, pp. 1063-1075, 2002.

[104] H.-M. Prasser and M. Beyer, "Bubble recognition algorithms for the processing of wire-mesh sensor data," in *Proceedings of 6th International Conference on Multiphase Flow*, 2007.

[105] K. Baur, "Development of a three-layer WMS withoptical access for the validation ofhydrodynamic parameters in bubblyflows using a high-speed camera_," 2016.

[106] C. Tompkins, H.-M. Prasser and M. Corradini, "Wire-mesh sensors: A review of methods and uncertainty in multiphase flows relative to other measurement techniques," *Nuclear Engineering and Design,* vol. 337, p. 205–220, 10 2018.

[107] D. Breitenmoser, P. Papadopoulos, T. Lind and H.-M. Prasser, "Droplet size distribution in a full-scale rectangular self-priming Venturi scrubber with liquid film injection," *International Journal of Multiphase Flow,* vol. 142, p. 103694, September 2021.

[108] J. L. York and H. E. Stubbs, "Photographic analysis of sprays," 1951.

[109] D. S. F. Atkinson and W. Strauss, "Droplet Size and Surface Tension in Venturi Scrubbers," *Journal of the Air Pollution Control Association,* vol. 28, p. 1114–1118, November 1978.

[110] D. B. ROBERTS and H. I. L. L. JAMES C., "ATOMIZATION IN A VENTURI SCRUBBER," *Chemical Engineering Communications,* vol. 12, p. 33–68, October 1981.

[111] X. Gamisans, M. Sarrà, F. J. Lafuente and B. J. Azzopardi, "The hydrodynamics of ejector-Venturi scrubbers and their modelling by an annular flow/boundary layer model," *Chemical Engineering Science,* vol. 57, p. 2707–2718, July 2002.

[112] J. B. Blaisot and J. Yon, "Droplet size and morphology characterization for dense sprays by image processing: application to the Diesel spray," *Experiments in Fluids,* vol. 39, p. 977–994, September 2005.

[113] N. Fdida, L. Vingert, A. Ristori and Y. L. Sant, "DROPLET SIZE AND VELOCITY MEASUREMENTS IN A CRYOGENIC JET FLAME OF A ROCKET-TYPE COMBUSTOR USING HIGH-SPEED IMAGING," *Atomization and Sprays,* vol. 26, p. 411–438, 2016.

[114] A. Lecuona, P. A. Sosa, P. A. Rodríguez and R. I. Zequeira, "Volumetric characterization of dispersed two-phase flows by digital image analysis," *Measurement Science and Technology,* vol. 11, p. 1152–1161, July 2000.

[115] S. Y. Lee and Y. D. Kim, "Sizing of spray particles using image processing technique," *KSME International Journal,* vol. 18, p. 879–894, June 2004.

[116] S. Rezayat, M. Farshchi, H. Karimi and A. Kebriaee, "Spray Characterization of a Slinger Injector Using a High-Speed Imaging Technique," *Journal of Propulsion and Power,* vol. 34, p. 469–481, March 2018.

[117] Y. Zhou, Z. Sun, H. Gu and Z. Miao, "Experimental research on aerosols collection performance of self-priming venturi scrubber in FCVS," *Progress in Nuclear Energy,* vol. 85, p. 771–777, November 2015.

[118] B. J. Azzopardi and A. H. Govan, "The modelling of venturi scrubbers," *Filtration & separation,* vol. 21, p. 196–200, 1984.

[119] D. F. Alonso, J. A. S. Gonçalves, B. J. Azzopardi and J. R. Coury, "Drop size measurements in Venturi scrubbers," *Chemical Engineering Science,* vol. 56, p. 4901–4911, August 2001.

[120] N. Otsu, "A Threshold Selection Method from Gray-Level Histograms," *IEEE Transactions on Systems, Man, and Cybernetics,* vol. 9, p. 62–66, January 1979.

[121] M. Altheimer, R. Häfeli, C. Wälchli and P. R. von Rohr, "Shadow imaging in bubbly gas–liquid two-phase flow in porous structures," *Experiments in Fluids,* vol. 56, September 2015.

[122] C. Y. Wong, S. C. F. Lin, T. R. Ren and N. M. Kwok, "A survey on ellipse detection methods," in *2012 IEEE International Symposium on Industrial Electronics*, 2012.

[123] A. Fitzgibbon, M. Pilu and R. B. Fisher, "Direct least square fitting of ellipses," *IEEE Transactions on Pattern Analysis and Machine Intelligence,* vol. 21, p. 476–480, May 1999.

[124] D. H. Eberly, "3D Game Engine Design (Second Book)," *North Carolina,* 2007.

[125] J. FATHIKALAJAHI, M. TAHERI and M. R. TALAIE, "THEORETICAL STUDY OF NONUNIFORM DROPLETS CONCENTRATION DISTRIBUTION ON VENTURI SCRUBBER PERFORMANCE," *Particulate Science and Technology,* vol. 14, p. 153–164, April 1996.

[126] R. A. Mugele and H. D. Evans, "Droplet Size Distribution in Sprays," *Industrial & Engineering Chemistry,* vol. 43, p. 1317–1324, June 1951.

[127] S. NUKIYAMA and Y. TANASAWA, "An Experiment on the Atomization of Liquid : 3rd Report, On the Distribution of the Size of Droplets.," *Transactions of the Japan Society of Mechanical Engineers,* vol. 5, p. 131–135, 1939.

[128] T. Paloposki, "Drop size distributions in liquid sprays," *Acta Polytechnica Scandinavica, Mechanical Engineering Series;(Finland),* vol. 36, 1994.

[129] S. NUKIYAMA and Y. TANASAWA, "An Experiment on the Atomization of Liquid. : 4th Report, The Effect of the Properties of Liquid on the Size of Drops.," *Transactions of the Japan Society of Mechanical Engineers,* vol. 5, p. 136–143, 1939.

[130] R. H. Boll, L. R. Fiais, P. W. Maurer and W. L. Thompson, "Mean Drop Size in a Full Scale Venturi Scrubber via Transmissometer," *Journal of the Air Pollution Control Association,* vol. 24, p. 934–938, October 1974.

[131] D. F. Tatterson, J. C. Dallman and T. J. Hanratty, "Drop sizes in annular gas-liquid flows," *AIChE Journal,* vol. 23, p. 68–76, January 1977.

[132] I. Kataoka, M. Ishii and K. Mishima, "Generation and Size Distribution of Droplet in Annular Two-Phase Flow," *Journal of Fluids Engineering,* vol. 105, p. 230–238, June 1983.

[133] G. Kocamustafaogullari, S. R. Smits and J. Razi, "Maximum and mean droplet sizes in annular two-phase flow," *International Journal of Heat and Mass Transfer,* vol. 37, p. 955–965, April 1994.

[134] C. Berna, A. Escrivá, J. L. Muñoz-Cobo and L. E. Herranz, "Review of droplet entrainment in annular flow: Characterization of the entrained droplets," *Progress in Nuclear Energy,* vol. 79, p. 64–86, March 2015.

[135] A. Sarimeseli and B. J. Azzopardi, "Correlating drop sizes in annular gas/liquid flows in vertical and horizontal pipes," *Proceedings of ILASS (Europe), Pg,* vol. 248, p. 253, 2004.

[136] Y. T. Shah, B. G. Kelkar, S. P. Godbole and W.-D. Deckwer, "Design parameters estimations for bubble column reactors," *AIChE Journal,* vol. 28, p. 353–379, 1982.

[137] D. Grob, "Filtered Containment Venting System," in *IMI Nuclear Presentation at NRC Public Meeting*, 2012.

[138] A. Dehbi, D. Suckow and S. Guentay, "Aerosol retention in low-subcooling pools under realistic accident conditions," *Nuclear Engineering and Design,* vol. 203, p. 229–241, January 2001.

[139] J. Hammer and A. Ritter, "Filtered Containment Venting Systems at Swiss NPPs and KKL in particular," in *ALARA Symposium*, 2014.

[140] A. P. dos Santos, A. Diehl and Y. Levin, "Surface Tensions, Surface Potentials, and the Hofmeister Series of Electrolyte Solutions," *Langmuir,* vol. 26, p. 10778–10783, April 2010.

[141] M. Bal, R. C. Jose and B. C. Meikap, "Control of accidental discharge of radioactive materials by filtered containment venting system: A review," *Nuclear Engineering and Technology,* vol. 51, p. 931–942, July 2019.

[142] J. Gretzinger and W. R. Marshall, "Characteristics of pneumatic atomization," *AIChE Journal,* vol. 7, p. 312–318, June 1961.

[143] K. Y. Kim and W. R. Marshall, "Drop-size distributions from pneumatic atomizers," *AIChE Journal,* vol. 17, p. 575–584, May 1971.

[144] G. J. Parker and K. C. Cheong, "Air-water tests on a venturi for entraining liquid films," *International Journal of Mechanical Sciences,* vol. 15, p. 633–641, August 1973.

[145] M. Ali, Y. C. Qi and K. Mehboob, "A review of performance of a venturi scrubber," *Research Journal of Applied Sciences, Engineering and Technology,* vol. 4, p. 3811–3818, 2012.

[146] S. Dong and J. Yang, "Overview of the experimental studies and numerical simulations on the filtered containment venting systems with wet scrubbers," *Annals of Nuclear Energy,* vol. 132, p. 461–485, October 2019.

[147] H. C. Lee, D. Y. Lee, W. Y. Jung, J. C. Lee and G. T. Kim, "Thermal-Hydraulic Performance of Scrubbing Nozzle Used for CFVS," 2016.

[148] Y. Zhou, Z. Sun, H. Gu and Z. Miao, "Experimental research on aerosols collection performance of self-priming venturi scrubber in FCVS," *Progress in Nuclear Energy,* vol. 85, p. 771–777, November 2015.

[149] S. Calvert, "Venturi and other atomizing scrubbers efficiency and pressure drop," *AIChE Journal,* vol. 16, p. 392–396, May 1970.

[150] R. H. Boll, "Particle Collection and Pressure Drop in Venturi Scrubbers," *Industrial & Engineering Chemistry Fundamentals,* vol. 12, p. 40–50, February 1973.

[151] S.-C. Yung, S. Calvert and H. F. Barbarika, "Venturi scrubber performance model," *Environmental Science & Technology,* vol. 12, p. 456–459, April 1978.

[152] H. Haller, E. Muschelknautz and T. Schultz, "Venturi scrubber calculation and optimization," *Chemical Engineering & Technology - CET,* vol. 12, p. 188–195, 1989.

[153] J. C. F. Teixeira, B. J. Azzopardi and T. R. Bott, "The effect of inserts on drop sizes in vertical annular flow," in *Second UK Conference on Heat Transfer*, 1988.

[154] A. G. Bailey, W. Balachandran and T. J. Williams, "The rosin—rammler size distribution for liquid droplet ensembles," *Journal of Aerosol Science,* vol. 14, p. 39–46, January 1983.

[155] A. M. Silva, J. C. F. Teixeira and S. F. C. F. Teixeira, "Experiments in large scale venturi scrubber," *Chemical Engineering and Processing: Process Intensification,* vol. 48, p. 424–431, January 2009.

[156] F. Mayinger and M. Lehner, "Operating results and aerosol deposition of a venturi scrubber in self-priming operation," *Chemical Engineering and Processing: Process Intensification,* vol. 34, p. 283–288, June 1995.

[157] M. Lehner, "Aerosol Separation Efficiency of a Venturi Scrubber Working in Self-Priming Mode," *Aerosol Science and Technology,* vol. 28, p. 389–402, January 1998.

[158] T. Betschart, T. Lind and H.-M. Prasser, "Investigation of two-phase flow hydrodynamics under SGTR severe accident conditions," *Nuclear Engineering and Design,* vol. 366, p. 110768, September 2020.

[159] J. Jung, J. B. Lee and H. Y. Kim, "Experimental Investigation of Iodine Decontamination Performance of a Filtered Containment Venting System in ARIEL Facility," in *Proceedings of the 26th International Conference Nuclear Energy for New Europe, Bled, Slovenia*, 2017.

[160] S. I. Kim, J. B. Lee, J. H. Jung, K. S. Ha, H. Y. Kim and J. Song, "Introduction of filtered containment venting system experimental facility in KAERI and results of aerosol test," *Nuclear Engineering and Design,* vol. 326, p. 344–353, January 2018.

[161] M. A. M. Costa, P. R. Henrique, J. A. S. Gonçalves and J. R. Coury, "Droplet size in a rectangular Venturi scrubber," *Brazilian Journal of Chemical Engineering,* vol. 21, p. 335–343, 2004.

[162] N. D. Hutson, R. Krzyzynska and R. K. Srivastava, "Simultaneous Removal of SO2, NOX, and Hg from Coal Flue Gas Using a NaClO2-Enhanced Wet Scrubber," *Industrial & Engineering Chemistry Research,* vol. 47, p. 5825–5831, June 2008.

[163] T. Paul, A. Sinharoy, K. Pakshirajan and G. Pugazhenthi, "Lipid-rich bacterial biomass production using refinery wastewater in a bubble column bioreactor for bio-oil conversion by hydrothermal liquefaction," *Journal of Water Process Engineering,* vol. 37, p. 101462, October 2020.

[164] K. C. Pillai, S. J. Chung, T. Raju and I.-S. Moon, "Experimental aspects of combined NOx and SO2 removal from flue-gas mixture in an integrated wet scrubber-electrochemical cell system," *Chemosphere,* vol. 76, p. 657–664, July 2009.

[165] R. Chaudhary, A. K. Dikshit and Y. W. Tong, "Carbon-dioxide biofixation and phycoremediation of municipal wastewater using Chlorella vulgaris and Scenedesmus obliquus," *Environmental Science and Pollution Research,* vol. 25, p. 20399–20406, June 2017.

[166] W. K. Lewis and W. G. Whitman, "Principles of Gas Absorption.," vol. 16, p. 1215–1220, December 1924.

[167] G. A. Hughmark, "Holdup and Mass Transfer in Bubble Columns," *Industrial & Engineering Chemistry Process Design and Development,* vol. 6, p. 218–220, 4 1967.

[168] K. Akita and F. Yoshida, "Gas holdup and volumetric mass transfer coefficient in bubble columns. Effects of liquid properties," *Industrial & Engineering Chemistry Process Design and Development,* vol. 12, p. 76–80, 1973.

[169] K. Akita and F. Yoshida, "Bubble size, interfacial area, and liquid-phase mass transfer coefficient in bubble columns," *Industrial & Engineering Chemistry Process Design and Development,* vol. 13, p. 84–91, 1974.

[170] H. Hikita, S. Asai, K. Tanigawa, K. Segawa and M. Kitao, "Gas hold-up in bubble columns," *The Chemical Engineering Journal,* vol. 20, pp. 59-67, 1980.

[171] H. Hikita and H. Kikukawa, "Liquid-phase mixing in bubble columns: Effect of liquid properties," *The Chemical Engineering Journal,* vol. 8, p. 191–197, 1 1974.

[172] W.-D. Deckwer, R. Burckhart and G. Zoll, "Mixing and mass transfer in tall bubble columns," *Chemical Engineering Science,* vol. 29, pp. 2177-2188, 1974.

[173] P. H. Calderbank and M. B. Moo-Young, "The continuous phase heat and mass-transfer properties of dispersions," *Chemical Engineering Science,* vol. 16, p. 39–54, December 1961.

[174] R. Krishna and J. M. van Baten, "Mass transfer in bubble columns," *Catalysis Today,* Vols. 79-80, p. 67–75, 4 2003.

[175] C. O. Vandu, K. Koop and R. Krishna, "Volumetric mass transfer coefficient in a slurry bubble column operating in the heterogeneous flow regime," *Chemical Engineering Science,* vol. 59, p. 5417–5423, 11 2004.

[176] D. J. Vermeer and R. Krishna, "Hydrodynamics and mass transfer in bubble columns in operating in the churn-turbulent regime," *Industrial & Engineering Chemistry Process Design and Development,* vol. 20, p. 475–482, July 1981.

[177] R. Sander, "Compilation of Henry\textquotesingles law constants (version 4.0) for water as solvent," *Atmospheric Chemistry and Physics,* vol. 15, p. 4399–4981, 4 2015.

[178] C. Housecroft, Inorganic chemistry, Upper Saddle River, N.J: Pearson Prentice Hall, 2005.

[179] T. S. Light, E. A. Kingman and A. C. Bevilacqua, "The conductivity of low concentrations of CO2 dissolved in ultrapure water from 0-100°C," in *Proceedings of the 209th American Chemical Society National Meeting*, Anaheim, 1995.

[180] G. M. GmbH, "Operating manual GMH 3431".

[181] A. G. Vögtlin Instruments, "red-y smart series operating instructions," 4147, 2012.

[182] W.-D. Deckwer, K. Nguyen-Tien, B. G. Kelkar and Y. T. Shah, "Applicability of axial dispersion model to analyze mass transfer measurements in bubble columns," *AIChE Journal,* vol. 29, p. 915–922, 11 1983.

[183] P. Danckwerts, Gas-liquid reactions, New York: McGraw-Hill, 1970.

[184] O. N. Manjrekar, Y. Sun, L. He, Y. J. Tang and M. P. Dudukovic, "Hydrodynamics and mass transfer coefficients in a bubble column photo-bioreactor," *Chemical Engineering Science,* vol. 168, p. 55–66, 8 2017.

[185] Y. Ohki and H. Inoue, "Longitudinal mixing of the liquid phase in bubble columns," *Chemical Engineering Science,* vol. 25, p. 1–16, 1 1970.

[186] G. D. Towell, C. P. Strand and G. H. Ackerman, "Mixing: theory related to practice," in *AIChE-I. Chem. E. Symp. Ser.*, 1965.

[187] N. Zuber and J. A. Findlay, "Average Volumetric Concentration in Two-Phase Flow Systems," *Journal of Heat Transfer,* vol. 87, p. 453–468, 11 1965.

[188] T. Lind, S. Tietze and P. Papadopoulos, "Retention of gas phase iodine species in a wet scrubber," *International severe accident management conference (ISAMC 2018),* 2018.

[189] Y. J. Choi, D. H. Kam, P. Papadopoulos, T. Lind and Y. H. Jeong, "Experimental investigation on bubble behaviors in a water pool using the venturi scrubbing nozzle," *Nuclear Engineering and Technology,* vol. 53, p. 1756–1768, June 2021.

[190] Z. Zhang, M. Bieberle, F. Barthel, L. Szalinski and U. Hampel, "Investigation of upward cocurrent gas–liquid pipe flow using ultrafast X-ray tomography and wire-mesh sensor," *Flow Measurement and Instrumentation,* vol. 32, p. 111–118, August 2013.

[191] M. Yang, H. I. Schlaberg, B. S. Hoyle, M. S. Beck and C. Lenn, "Real-time ultrasound process tomography for two-phase flow imaging using a reduced number of transducers," *IEEE Transactions on Ultrasonics, Ferroelectrics and Frequency Control,* vol. 46, p. 492–501, May 1999.

[192] L.-J. Xu and L.-A. Xu, "Ultrasound tomography system used for monitoring bubbly gas/liquid two-phase flow," *IEEE Transactions on Ultrasonics, Ferroelectrics and Frequency Control,* vol. 44, p. 67–76, January 1997.

[193] S.-Q. Wang, K.-W. Xu and H.-B. Kim, "Slug flow identification using ultrasound Doppler velocimetry," *International Journal of Heat and Mass Transfer,* vol. 148, p. 119004, February 2020.

[194] L. A. Ux, D. Leonard and R. G. Green, "A pulsed ultrasound transducer system for two component flow," *Journal of Physics E: Scientific Instruments,* vol. 18, p. 609–613, July 1985.

[195] P. Seleghim and E. Hervieu, "Direct imaging of two-phase flows by electrical impedance measurements," *Measurement Science and Technology,* vol. 9, p. 1492–1500, September 1998.

[196] S. P. Pellegrini, F. C. Trigo and R. G. Lima, "Adaptive Kalman filter-based information fusion in electrical impedance tomography for a two-phase flow," *Mechanical Systems and Signal Processing,* vol. 150, p. 107326, March 2021.

[197] Y. Murai, Y. Tasaka, Y. Nambu, Y. Takeda and A. S. Roberto Gonzalez, "Ultrasonic detection of moving interfaces in gas–liquid two-phase flow," *Flow Measurement and Instrumentation,* vol. 21, p. 356–366, September 2010.

[198] O. C. JONES, L. I. N. J.T. and L. OVACIK, "INVESTIGATION OF ELECTRICAL IMPEDANCE IMAGING RELATIVE TO TWO-PHASE, GAS-LIQUID FLOWS," *Chemical Engineering Communications,* vol. 118, p. 299–325, November 1992.

[199] O. C. Jones, J.-T. Lin, L. Ovacik and H. Shu, "Impedance imaging relative to gas-liquid systems," *Nuclear Engineering and Design,* vol. 141, p. 159–176, June 1993.

[200] M. Ingram, C. Mineo, A. Gachagan, A. J. Mulholland, A. Nordon and M. Hegarty, "Determination of Bubble Size Distribution Using Ultrasound Array Imaging," *IEEE Transactions on Ultrasonics, Ferroelectrics, and Frequency Control,* vol. 67, p. 1424–1437, July 2020.

[201] E. M. A. Hussein, D. A. Meneley and S. Banerjee, "Single-exposure neutron tomography of two-phase flow," *International Journal of Multiphase Flow,* vol. 12, p. 1–34, January 1986.

[202] E. Hussein, S. Banerjee and D. Meneley, "A new fast neutron scattering technique for local void fraction measurement in two-phase flow," in *Thermal hydraulics of nuclear reactors*, 1983.

[203] U. Hampel, D. Hoppe, K.-H. Diele, J. Fietz, H. Höller, R. Kernchen, H.-M. Prasser and C. Zippe, "Application of gamma tomography to the measurement of fluid distributions in a hydrodynamic coupling," vol. 16, p. 85–90, April 2005.

[204] R. K. Das and S. Pattanayak, "Electrical impedance method for flow regime identification in vertical upward gas-liquid two-phase flow," *Measurement Science and Technology,* vol. 4, p. 1457–1463, December 1993.

[205] S. L. Ceccio and D. L. George, "A Review of Electrical Impedance Techniques for the Measurement of Multiphase Flows," *Journal of Fluids Engineering,* vol. 118, p. 391–399, June 1996.

[206] C. F. Weber, E. C. Beahm and T. S. Kress, "Models of iodine behavior in reactor containments," Office of Scientific and Technical Information (OSTI), 1992.

[207] H. L. E. P. V. Polo and M. Escudero, *Removal of volatile iodine from gas bubbles rising in water pools: review and assessment of pool scrubbing codes,* 1996.

[208] T. Lind, S. Guentay, L. E. Herranz and D. Suckow, "A summary of the ARTIST: Aerosol retention during SGTR severe accident," *Annals of Nuclear Energy,* vol. 131, p. 385–400, September 2019.

[209] J.-L. Lachaume, D. Miller, G. Rzentkowski, N. Lahtinen, K. Valtonen, L. Foucher, S. S. Harikumar, T. Yamada, R. Sharafutdinov, M. Kuznetsov and others, "Implementation of defence in depth at nuclear power plants. lessons learnt from the fukushima daiichi accident," 2016.

[210] IAEA, External man-induced events in relation to nuclear power plant design : a safety guide, Vienna: International Atomic Energy Agency, 1996.

[211] L. E. Herranz, V. Peyrés, J. Polo, M. J. Escudero, M. M. Espigares and J. López-Jiménez, "Experimental and Analytical Study on Pool Scrubbing Under JET Injection Regime," *Nuclear Technology,* vol. 120, p. 95–109, November 1997.

[212] L. E. Herranz, "Pool Scrubbing in Severe Accident Sequences: Identification of Key Boundary Conditions," *IPRESCA Kick off Meet,* 2017.

[213] L. E. Herranz, R. Iglesias and J. Fontanet, "Mitigation of source term in suppression pools: Large uncertainties in predictability," *Annals of Nuclear Energy,* vol. 120, p. 509–515, October 2018.

[214] M. Gouëllo, J. Hokkinen, T. Kärkelä, P. Rantanen and A. Auvinen, "Development and qualification of an innovative wet electrostatic precipitator in view of gaseous iodine filtration on laboratory-scale," *Nuclear Engineering and Design,* vol. 327, p. 7–21, February 2018.

[215] B. Clément, L. Cantrel, G. Ducros, F. Funke, L. Herranz, A. Rydl, G. Weber and C. Wren, "State of the art report on iodine chemistry," 2007.

[216] M. Berzal, State-of-the-art review on fission products aerosol pool scrubbing under severe accident conditions : final report, City: European Commission, 1995.

[217] C. Berna, A. Escrivá, J. L. Muñoz-Cobo and L. E. Herranz, "Enhancement of the SPARC90 code to pool scrubbing events under jet injection regime," *Nuclear Engineering and Design,* vol. 300, p. 563–577, April 2016.

7 APPENDIX

7.1 CO2 ADM Pseudo Code

```
% pressure at nozzle outlet height (bottom)
p = n*dz*ρ1*g+p0;
% normalized gas flow at 0°c
vg,norm = gflow/(60*1000);
% CO2 volumetric flow rate at the bottom
vg,norm,co2 = x*vg,norm;
% N2 volumetric flow rate at the bottom
vg,norm,n2=(1-x)*vg,norm;
% CO2 mass flow rate at the bottom
mgf0,co2 = ρg0,co2*vg,norm,co2;
% N2 mass flow rate at the bottom
mgf0,n2=ρg0,n2*vg,norm,n2;
% Total mass flow rate at the bottom
mgf0 = mgf0,co2 + mgf0,n2;
% Average density at the bottom
ρg0 = mgf0/vg,norm)*p/p0*T0/T;

% Superficial velocity at the bottom
jg0 = (vg,norm*T/T0*p0/p)/Ach;
% Drift velocity at the bottom using Zuber and Findlay [187]
dw0 = 1.41*(((ρ1-ρg0)*σ1*g)/(ρ1^2))^0.25;
% Void at the bottom using Zuber
ε0 = jg0/(dw0+1.13*jg0);

% Initial gas volume at the bottom cell
vg0=ε0/(1- ε0)*dz*Ach;
% Bubble size using Akita et al. [169]
db0 =  26*((g*dc^2*rl)/σ1)^(-0.5)*(g*dc^3/ν1^2)^(-0.12)*(jg0/sqrt(g*dc))^(-0.12)*dc;
% Total number of bubbles
nb0=vg0/(db0^3*pi/6);
% Axial Dispersion Coefficient by Deckwer et al. [172]
Dz,1 = 2.7*dc^(1.4)*jg0^(0.3);

% Loop through time for 90 seconds with timestep dt
for t=1:90/dt
% Initial mass flow rate at the bottom
mgfco2 = mgf0,co2;

% Iterate axially through the cells
for i=1:n
% Pressure at cell i
p=(n-i)*dz*ρ1*g+p0;
% Total mass flow rate
mgf=mgfco2+mgf0,n2;
% Volumetric flow rate of CO2
vg,co2=(mgfco2/ρg0,co2)*p0/p*T/T0;
% Volumetric flow rate of N2
vg,n2=(mgf0,n2/ρg0,n2)*p0/p*T/T0;
% Combined volumetric flow rate
vg=vg,co2+vg,n2;
% Partial content CO2 in gas stream
```

```
y=v_g,co2/v_g;
% Mixture density
ρ_g=(y*ρ_g0,co2+(1-y)*ρ_g0,n2)*p/p_0* T_0/T;
% superficial velocity
j_g=v_g/A_ch;

% Void correlation
if ε_model == 1
   % Zuber and Findlay drift flux model
elseif ε_model == 2
   % Akita et al. correlation for ε
elseif ε_model == 3
   % Hikita et al. correlation for ε
end

% Mixture volume
V_node=1/(1-ε(i))*dz*A_ch;
% Average bubble diameter
d_b=((V_node*ε(i)/n_b0)*6/pi)^(1/3);
% Bubble surface
A_b=n_b0*pi*db.^2;
% Virtual height of the cell i
z(i+1) = z(i) + dz/(1 - ε(i));
% Liquid side mass transfer coefficient
k_La = k_L*(A_b/V_node);

% Saturation concentration using Henry's Law
c_eq=He*p*y;

% New concentration in cell i at time t with k_La and axial dispersion with D_z,L
c(i,t)=c(i,t-1)+ dt*(D_z,L*(c(i+1,t-1)-2*c(i,t-1)+c(i-1,t-1))/(dz^2)+k_La/(1-ε(i))*
(c_eq-c(i,t-1)));

% Mass transfer rate between two time steps
mgt = (c(i,t)-c(i,t-1))*dz*A_ch/dt;

% New mass flow rate of CO2 for the next cell
mgf_co2 = mgf_co2 - mgt;

% Cumulated CO2 at cell i
mg(i) = mg(i) + mgt*dt;
end
end
```